Design strategies towards $SrTiO_3$ based perovskite nanostructures for environmental catalysis

Dissertation

zur Erlangung des Grades

Doktor der Naturwissenschaften (*Dr. rer. nat.*)

an der Fakultät für Mathematik,
Informatik und Naturwissenschaften

Fachbereich Chemie
Universität Hamburg

Buğra Kayaalp

aus Ankara

Hamburg, März 2019

Die vorliegende Arbeit wurde in der Zeit von Oktober 2014 bis Dezember 2018 in der Arbeitsgruppe von JProf. Dr. Simone Mascotto am Institut für Anorganische und Angewandte Chemie der Universität Hamburg angefertigt.

Hiermit versichere ich an Eides statt, die vorliegende Dissertation selbst verfasst und keine anderen als die angegebenen Hilfsmittel benutzt zu haben. Die eingereichte schriftliche Fassung entspricht der auf dem elektronischen Speichermedium. Ich versichere, dass diese Dissertation nicht in einem früheren Promotionsverfahren eingereicht wurde.

Hamburg, den 12.03.2019

Buğra Kayaalp

1. Gutachter:	JProf. Dr. Simone Mascotto
2. Gutachter:	Prof. Dr. Michael Fröba
Mündliche Prüfung am:	26.04.2019

Acknowledgements

First and foremost I would like to thank my supervisor Prof. Simone Mascotto for his unwavering guidance and support through all stages of my PhD studies. I am grateful that I could pursue this very inspiring topic in a dynamic and close environment while greatly benefiting from his scientific and professional expertise. I greatly appreciate his guidance and contributions to manuscript preparation and paper submission process.

I am grateful to Prof. Michael Fröba for his strong support of our research group, engaging discussions and continual cordiality. Also, I would like to thank him for being the second reviewer of my dissertation.

I'd like to thank Prof. Dorota Koziej and Prof. Carmen Herrmann for agreeing to be in the examination board of my disputation.

My sincere thanks go to Prof. WooChul Jung from Korea Advanced Institute of Science and Technology (KAIST) for giving me the opportunity to do a research stay at his group, his excellent guidance and willingness to sustain our collaboration as well as for letting me use their outstanding experimental facilities. In this respect, I would like to specially thank Siwon Lee for his great expertise and contributions in oxidation catalysis studies as well as always finding the time for our thoughtful discussions. I'd like to also thank Jongsu Seo for performing the XPS measurements on the $La_{0.3}Sr_{0.7}Ti_{1-x}Fe_xO_{3\pm\delta}$ oxides. Along with Siwon and Jongsu; I am thankful to Yoonseok, Han Gil, Bonjae, NoWoo, JeongDo, SeungJin, YeonJu and Jun Kyu who took very good care of me despite my short time there. I miss you guys very much, also the great food and Norebang!

I'd like to acknowledge MIN Graduate School of Hamburg University for awarding me fellowships for a research stay abroad and conference participation which allowed me to pursue a research stay at KAIST as well as to present my findings at an international conference.

I am thankful for my group members Jonas Scholz and Kurt Klauke for being my companions in this long and challenging path. I appreciate your friendship and support very much.

I'm grateful to Elisa Poffe for her camaraderie that made work less stressful. Moreover, I'd like to thank our recent and former group members: Galina, Janina, Benedikt, Benjamin, as well as my bachelor and intern students; Tassos, Christian, Manuel, Dominik, Ralf, Anton and Tobias. Thank you very much for the good times!

I'd like to thank Prof. Massimiliano D'Arienzo for kinetic tests on $SrTiO_3$ photocatalysts and ESR measurements, Dr. Andreas Kornowski for providing excellent TEM, SEM and EDX mapping images as well as deep discussion of the data. I'm grateful to Dr. Luca Nodari for his Mössbauer spectroscopy analysis on $La_{0.3}Sr_{0.7}Ti_{1-x}Fe_xO_{3\pm\delta}$ samples. I thank Mattia Biesuz and Prof. Vincenzo Sglavo for performing flash sintering on $La_{0.1}Sr_{0.9}TiO_{3+\delta}$. I'm thankful to Dr. YoungJoo Lee for the NMR measurements as well as her sincere interest in the progression of my studies. Furthermore, I'd like to thank Sandra König, Uta Sazama and Isabelle Nevoigt for performing characterization of my samples. I'm grateful for your contributions to this dissertation.

I'd like to thank members of AK Fröba: Dr. Frank Hoffmann, Dr. Felix Brieler, Matthias, Malina, Ruben, Tamas, Timo, Julia, Jan, Benedikt, Eva, Patrick, Norman, Dawid and all others for providing a positive atmosphere at the workplace through their warmth and friendliness.

I wish to express my gratitude to my teachers at the Chemistry Department of Middle East Technical University as well as to the lecturers of Advanced Materials Science master program in Munich and Augsburg, who have stimulated my interest in science and helped me lay the foundations necessary to pursue PhD studies. In the same respect, I'd like to thank my former industry supervisors Dr. Sabine Thiemann-Handler and Dr. Stefan Maurer.

Finally, I'd like to express my gratitude to my family and friends in Turkey for their encouragements from afar. My parents, Hayati and Efsun, my sister Damla and my aunt Burcu thank you for being there for me. My dear Eunyoung, thank you for your love and perseverance that provides me meaning.

Abstract

In this work, a comprehensive design approach towards high performance perovskite oxide catalysts is presented. Variation of porosity, composition and defect structure were investigated over a $SrTiO_3$ based system and the structure – function relationships were identified via catalytic tests of model reactions relevant for environmental catalysis.

A facile cooperative assembly route which employs alkoxysilane endotemplating within a simple variation of polymer complex synthesis approach was developed to prepare mesoporous perovskite oxide powders. Modification of porosity was achieved by varying the amount of alkoxysilane template in the synthesis. Increasing template loads resulted in a gradual decrease in grain size and increase in porosity of the final $SrTiO_3$ powders with well interconnected mesopores and substantial specific surface areas of up to 240 $m^2\ g^{-1}$. Superior performance of mesoporous $SrTiO_3$ photocatalysts due to mutual variation of porosity and nanostructure were demonstrated via photocatalyzed methylene blue dye degradation tests.

Influence of composition variation on the material's functionality was investigated by cationic co-substitution in the $SrTiO_3$ lattice. Phase-pure, mesoporous $La_{0.3}Sr_{0.7}Ti_{1-x}Fe_xO_{3\pm\delta}$ (LSTF, $0 \leq x \leq 0.5$) solid solutions were prepared with a template free route to reach an effective compromise between stability and performance through La- and Fe- substitution respectively. Increase in iron substitution within the mesoporous structure led to substantially higher catalytic performance than of similar iron-based perovskite catalysts reported in literature. Composition dependent contributions of suprafacial and intrafacial reaction mechanisms to the overall catalyst activity were identified via kinetic studies of CH_4 and CO oxidation over $La_{0.3}Sr_{0.7}Ti_{1-x}Fe_xO_{3\pm\delta}$ oxides.

Simultaneous incorporation of chemical and textural complexity to the catalyst design was investigated by employing cooperative assembly route to prepare perovskites with $La_{0.3}Sr_{0.7}Ti_{0.5}Fe_{0.5}O_{3-\delta}$ nominal stoichiometry. Highly porous phase-pure LSTF solid solutions were successfully obtained, despite the failure in attaining precise stoichiometry. Promising

application potential of highly porous LSTF as active support was demonstrated via CO oxidation tests over LSTF supported Pt nanoparticles, where Pt/LSTF system showed superior performance than commonly employed Pt/CeO_2.

Modification of defect structure was investigated over an insulator $La_{0.1}Sr_{0.9}TiO_{3+\delta}$ nanoparticulate system. Concentration of ionic defects in donor substituted $SrTiO_3$ was successfully increased by simultaneous heat treatment and electric field exposure, which promoted catalyst's reactivity towards high temperature CH_4 oxidation reaction.

The multifaceted design strategies and structure – function studies presented in this work provide insights towards the conception of complex perovskite oxide nanoarchitectures with tailored functional properties that can ultimately be utilized in commercial applications.

Zusammenfassung

In dieser Arbeit wird ein umfassender Ansatz zur Entwicklung von Hochleistungskatalysatoren aus Oxiden des Perowskits vorgestellt. Dabei wurden die Variation der Porosität, der Zusammensetzung und der Defektstruktur an einem $SrTiO_3$-System untersucht. Zusätzlich wurden die Struktur-Eigenschafts-Beziehungen mittels katalytischer Tests von Modellreaktionen, die eine Relevanz für die Umweltkatalyse besitzen, ermittelt.

Eine unkomplizierte Syntheseroute zur Herstellung mesoporöser Perowskitoxid-Pulver wurde entwickelt. Die Syntheseroute basiert auf kooperativer Selbstanordnung und der Verwendung von Alkoxysilan-Endotemplaten im Rahmen einer Anpassung des Polymer-Komplex-Ansatzes. Die Porosität wurde modifiziert, indem die Menge an Alkoxysilan-Templat variiert wurde. Eine Erhöhung der Templatmenge führte zu einer sukzessiven Abnahme der Korngrößen und einer Zunahme der Porosität der erhaltenen $SrTiO_3$ Pulver. Die Pulver wiesen miteinander verbundene Mesoporen und spezifische Oberflächen von bis zu 240 $m^2 g^{-1}$ auf. Eine gesteigerte Aktivität von mesoporösen $SrTiO_3$-Photokatalysatoren durch Variation der Porosität und der Nanostruktur konnte anhand von photokatalytischen Zersetzungsreaktionen von Methylenblau-Farbstoff nachgewiesen werden.

Der Einfluss unterschiedlicher Zusammensetzungen auf die Materialfunktionalität wurde durch kationische Co-Substitution des $SrTiO_3$-Gitters untersucht. Phasenreine mesoporöse $La_{0.3}Sr_{0.7}Ti_{1-x}Fe_xO_{3\pm\delta}$ (LSTF, $0 \leq x \leq 0.5$) Mischkristalle wurden in einer templatfreien Synthese hergestellt. Die La- und Fe-Substitution sollte einen Kompromiss aus Stabilität und Aktivität darstellen. Eine Zunahme der Eisensubstitution innerhalb der mesoporösen Struktur resultierte in eine deutlich gesteigerte katalytische Aktivität verglichen mit literaturbekannten, eisenbasierten Perowskit-Katalysatoren. Der von der Zusammensetzung abhängige Beitrag von suprafacialem und intrafacialem Reaktionsmechanismus auf die katalytische Aktivität wurde mittels kinteischer Studien von CH_4- und CO-Oxidation an $La_{0.3}Sr_{0.7}Ti_{1-x}Fe_xO_{3\pm\delta}$-Oxiden bestimmt.

Die gleichzeitige Integration chemischer und struktureller Komplexizität bei der Katalysatorentwicklung wurde untersucht, indem eine kooperative Selbstanordnung als Syntheseroute für die Herstellung von Perowskiten mit der nominellen Stöchiometrie $La_{0.3}Sr_{0.7}Ti_{0.5}Fe_{0.5}O_{3-\delta}$ gewählt wurde. Hochporöse, phasenreine LSTF Mischkristalle konnten erfolgreich synthetisiert werden, auch wenn die exakte Stöchiometrie nicht eingehalten wurde. Das vielversprechende Anwendungspotential dieser hochporösen LSTF als aktiver Träger wurde mit Hilfe von CO-Oxidation an LSTF kombiniert mit Pt-Nanopartikeln nachgewiesen. Dabei zeigten die Pt/LSTF-Systeme eine deutlich höhere Aktivität als üblicherweise verwendetes Pt/CeO_2.

Die Modifikation der Defektstruktur wurde an dem nanopartikulären Isolator $La_{0.1}Sr_{0.9}TiO_{3+\delta}$ untersucht. Dabei konnte die Konzentration der ionischen Defekte im Donor-substituierten $SrTiO_3$ durch gleichzeitige thermische Behandlung und Nutzung eines elektrischen Feldes erfolgreich gesteigert werden. Dadurch konnte die katalytische Reaktivität der Hochtemperaturreaktion der CH_4-Oxidation erhöht werden.

Die vielfältigen Entwicklungsstrategien und Struktur-Eigenschafts-Beziehungen, die im Rahmen dieser Arbeit vorgestellt werden, liefern wertvolle Informationen hinsichtlich der Bildung komplexer Perowskitoxid-Nanostrukturen mit maßgeschneiderten funktionellen Eigenschaften, die langfristig für kommerzielle Anwendungen genutzt werden können.

Parts of this work were previously published in:

Kayaalp, B.•; Lee, S. •; Klauke, K.; Seo, J.; Nodari, L.; Kornowski, A.; Jung, W.; Mascotto, S.: Template-free mesoporous $La_{0.3}Sr_{0.7}Ti_{1-x}Fe_xO_{3\pm\delta}$ for CH_4 and CO oxidation catalysis. ***Appl. Catal., B.*** (2019), DOI: 10.1016/j.apcatb.2018.12.077.

• These authors equally contributed to the realization of this work.

Kayaalp, B.; Lee, Y.J.; Kornowski, A.; Gross, S.; D'Arienzo, M.; Mascotto, S.: Cooperative assembly synthesis of mesoporous $SrTiO_3$ with enhanced photocatalytic properties. ***RSC Adv.***, (2016) DOI: 10.1039/C6RA13800D

Catalytic CO and CH_4 oxidation studies presented in this work were performed at KAIST in collaboration with the research group of Prof. WooChul Jung and through important contributions of Siwon Lee. As part of the collaboration, the author of this dissertation had a research stay at KAIST for 3 months between January – March 2017.

Table of contents

Chapter 1

Introduction

Meeting the growing global energy demand while reducing the emissions of greenhouse gases (GHG) and toxic side-products remains one of the greatest social and environmental challenges of the early 21st century. According to U.S. Energy Information Administration, currently about 80% of the global energy consumption of 575 quads (1 quad = 10^{15} BTU = 293 TWh) is originated from non-renewable fossil fuels and the global energy demand is projected to increase 22% by the year 2040 [1]. Perpetuating fossil fuel use to fulfil the rising energy demand risks exacerbating the pollution problem and the adverse effects of global warming. In recent decades substantial efforts have been allocated to the development of carbon-neutral energy storage and conversion systems capable of taking on these challenges. As a result, renewables today are the fastest-developing global energy source with a steady 2.6% growth per year on average. Although, renewables will account for a sizable portion in the global energy mix in near future (Fig. 1.1), currently they only fulfill 3.6% of world energy consumption [2]. The intermittent nature of renewable energy generation which necessitates an arduous transition into smart grid infrastructures as well as insufficient conversion efficiencies and volatile material costs are the major challenges that must be overcome for a successful shift towards a carbon-neutral energy economy. Moreover, cost-effective and matured technologies for large scale energy storage are still yet to be achieved.

Considering the obstacles faced by renewable energy integration, natural gas is deemed as the bridge fuel for the transition into low-carbon energy economy due to its abundant reserves, lower carbon print and high energy density compared to other fossil fuels [3]. Total annual consumption of natural gas is projected to increase by ~36 % by 2040, whereas its share of 23.4% in the global energy mix is not expected to shift significantly [2,4]. Notwithstanding its

high consumption rates, conversion efficiency of natural gas to electricity in the widely employed steam turbines is typically limited to ~ 30% and more efficient conversion technologies with easy GHG emission control are highly desirable [3].

Environmental catalysis research plays a central role in addressing these challenges through development of cost-effective, efficient and emission-reduced fuel conversion processes as well as pollution abatement technologies like automotive exhaust emission control and wastewater treatment. An optimal catalyst for these applications should be highly active, stable and comprised of earth-abundant materials. In these regards, perovskite oxide family with general formula ABO_3 is a favorable class of materials. The capability of the perovskite crystal structure to accommodate a wide range of different compositions leads to an immense scope of possible physicochemical properties enabling the materials to be tailored for specific applications [5–9]. Combining this advantage with their exceptional stability and abundance of forming elements, perovskite oxides hold promise to find wide commercial utilization in environmental catalysis [5].

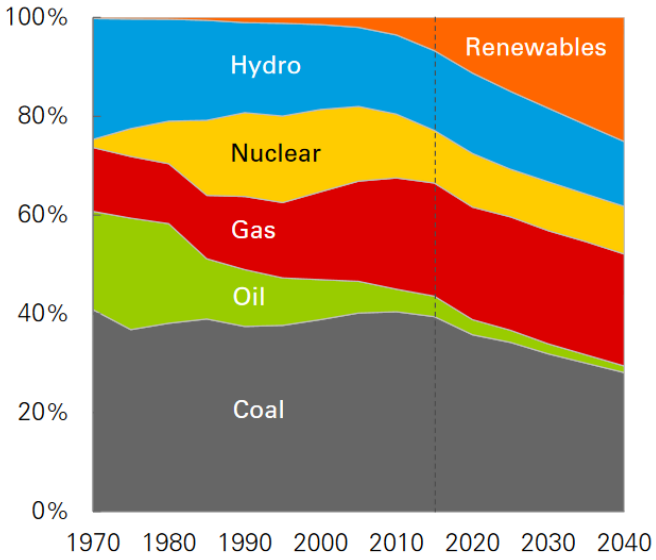

Figure 1.1: Global shares for total power generation [4].

Rational design of high-performance perovskite oxide catalysts requires a comprehensive and multifaceted approach that draws upon the fundamental structure-function relationships in the material. Chemical composition undoubtedly forms the foundation in deciding the overall feasibility of the material towards the designated catalytic application. In this respect,

substitution of native lattice sites of perovskite oxides by foreign atoms is an established strategy in literature to tailor their functional properties towards the specific reaction [10–13].

Nanostructure and morphology are as crucial as chemical composition in designating the overall physicochemical parameters and pertaining catalytic performance of the perovskite oxide. Mesoporous nanostructures possess numerous advantages to bulk counterparts due to their high surface areas, shortened diffusion pathways and higher separation efficiency of charge carrier pairs, which can cumulatively lead to superior reactivity and number of active sites [5,14,15]. Moreover, exploitation of nanoconfinement and quantum size effects in these systems can engender extraordinary functional properties that are fundamentally different than of the bulk material [3,16–18].

In addition to the design strategies with regard to bottom-up preparation of perovskite oxides, post-processing of the material (e.g. heat treatment) can significantly alter the catalytic performance by modification of numerous parameters, such as charge transport or nanostructure [19].

$SrTiO_3$ is a wide band-gap (~3.2 eV) photocatalytically active material with mixed ionic electronic conductivity (MIEC) and excellent structural stability [20–22]. Thanks to these attractive properties and well-established defect chemistry, $SrTiO_3$ and related perovskite oxides are utilized in a wide range of applications [5,15,23–26]. Although, in its pristine state strontium titanate does not show substantial performance in most thermally activated catalytic reactions, cationic substitution can promote material's activity [27]. These characteristics render $SrTiO_3$ a suitable model system for investigation of perovskite catalyst development towards environmental applications. In this work, design strategies of $SrTiO_3$ based perovskite catalysts with tailored porous nanoarchitecture, composition and defect structure was presented.

Novel synthesis strategies based on established polymer complex and solvothermal routes were developed to obtain perovskites with desired textural properties. Porosity and nanostructure tuning of the $SrTiO_3$ based systems were realized through a facile inorganic endotemplating route integrated into the modified polymer complex synthesis. Chemically complex perovskite oxides were prepared by La- and Fe- co-substitution in the $SrTiO_3$ lattice to form $La_{0.3}Sr_{0.7}Ti_{1-x}Fe_xO_{3\pm\delta}$ solid solutions with a composition variation between $0 \leq x \leq 0.5$. The choice of cationic substituents was based on the compromise between stability and performance characteristics. Fe is an earth-abundant element which is completely soluble in

cubic strontium titanate lattice and can provide excellent reactivity to the perovskite oxide system in thermally activated catalytic reactions [28,29]. La-substitution, on the other hand, can significantly improve the thermal and phase stability of the material without significantly altering the catalytic performance [30–32]. Finally, triggering the catalytic activity through pre-treatment of material was investigated by simultaneous electric field exposure and heat treatment on a nanoparticulated $La_{0.1}Sr_{0.9}TiO_{3+\delta}$ system. Assessment of the structure – function relationships that govern the catalytic performance of the tailored catalyst systems was achieved by thorough characterization and catalytic investigations via model reactions.

The multistep material development perspective of this work aims to present complex functional nanoarchitectures with tuned bulk and nanoscale properties as a forward-looking strategy towards high performance perovskite oxide catalysts.

Chapter 2

Theoretical Background

In this chapter, theoretical background on the structure, physicochemical properties and synthesis strategies of $SrTiO_3$ based perovskite oxides is presented. Moreover, state-of-art in the design and application of these materials in environmental catalysis is described. Finally, defect structure of $SrTiO_3$ based perovskites was discussed in detail.

2.1 Perovskite crystal structure

The $CaTiO_3$ mineral, perovskite, was discovered in 1839 in Ural Mountains and named after Russian mineralogist Count Lev Aleksevich von Perovski [33]. Perovskite crystal structure was first described in 1926 by Victor Goldscmidt and later adopted as the general name for ABX_3 type crystal structure family [34]. In the perfect cubic perovskite lattice with space group Pm3-m, each cation is in direct contact with the anions around them to form the ideal close packed arrangement. Smaller B-site cations are VI-fold coordinated and occupy the center position of the octahedra formed by X-site anions, whereas the larger A-site cations possessing XII-fold coordination sit in the interstitials formed by corner-sharing BX_6 octahedra (Fig 2.1a).

In perovskite structure, significant divergence from ideal stoichiometry can be accommodated within the framework without loss of structural integrity. Moreover, size variations of A- and B- site cations are tolerated and the long-range order is preserved notwithstanding lattice distortions in varying degrees [25]. Due to these characteristics of the framework, about 90% of metallic elements in the periodic table are capable of forming this phase. The divergence

from the ideal cubic crystal structure due to size effects can be described by a parameter, t, known as the Goldschmidt tolerance factor [34]:

$$t = \frac{r_A + r_X}{\sqrt{2}(r_B + r_X)} \tag{2.1}$$

where r_X is the radius of the anion, r_A and r_B are the radii of the A and B cations respectively.

The changes in the lattice symmetry for different t values were experimentally determined [35]. According to these findings, t values close to unity ($0.9 < t < 1.0$) are assigned to cubic perovskites, whereas in the range $0.71 < t < 0.9$ orthorhombic or rhombohedral symmetries are observed. Lower t values occur when the relative size of A-site cation is not large enough compared to the B-site cation. In such case, the BX_6 octahedra tilt to fill the empty space in between and lose some degree of symmetry as a result. The bending of the octahedra about the b and c axes creates an orthorhombic structure (space group Pnma) as shown on Fig. 2.1b, whereas bending about each axis leads to a rhombohedral one (space group R3c) [36].

Hexagonal or tetragonal symmetries of the perovskite structure are stable for tolerance factors higher than unity, where A-site cation is too large compared to the B-site cation. Fig. 2.2 presents common lower symmetry derivatives of cubic perovskite structure for varying tolerance factors.

Thanks to the flexibility of perovskite phase, in many cases, deviation from ideal cubic symmetry is rather slight and a minor tilting of the anionic octahedra can be even desirable for tailoring the electronic and dipole properties of the material as well as B-X bond length and strength [8].

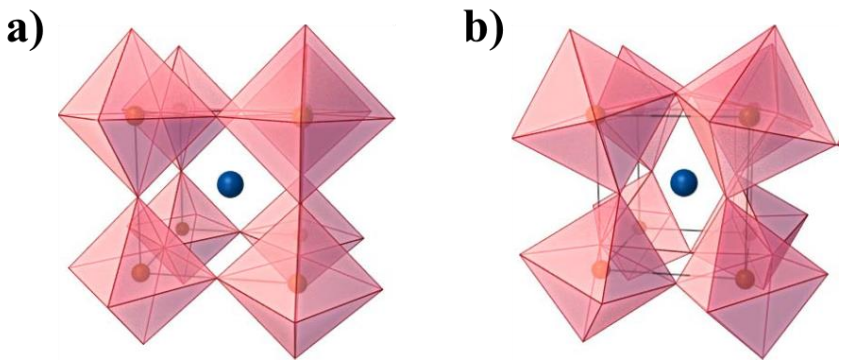

Figure 2.1: Perovskite lattice distortion from (a) cubic to (b) orthorhombic [33].

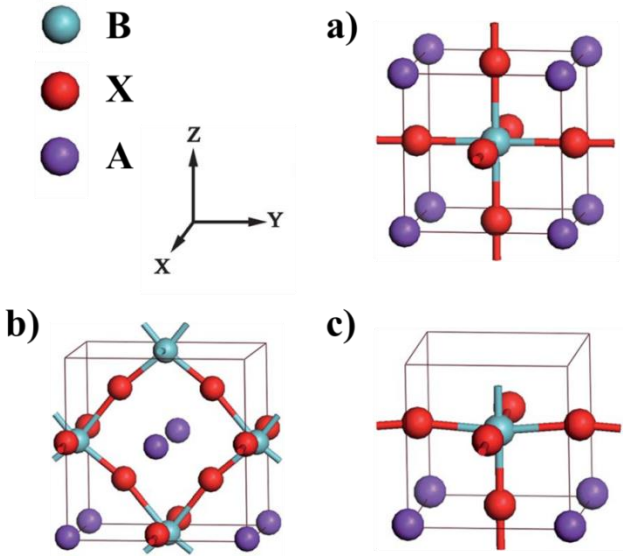

Figure 2.2: Schematic representations of ABX_3 perovskite crystal structure (a) cubic (b) orthorhombic (c) tetragonal. Adapted from [37].

Partial replacement of A- and B-sites of the ABX_3 lattice with foreign cations can be accommodated within the perovskite structure without undermining the long-range order. These foreign cations are conventionally called dopants if their concentration does not surpass 1 %, whereas the term 'substitution' can be conveniently used for any amount of replacement. When the foreign cations are of the same valence as the native species they replace in the perovskite lattice, the substitution is called isovalent. In such case, the change in material properties is mainly due to size effects. Acceptor or donor substitution refers to replacement of native sites with foreign cations of lower or higher valence respectively. Together, such replacement is termed aliovalent substitution.

The empirical Hume-Rothery solubility rules postulated for metal alloys also apply for ionic substitution in inorganic and mineral systems. In a hypothetical $M_xA_{1-x}BX_{3\pm\delta}$ perovskite system where M cations substitute native A-sites, likelihood of forming a substitutional solid solution is highest if [38]:

- MBX_3 and ABX_3 parent phases crystallize in identical structure.
- The ionic radii and electronegativity values of the M and A cations are similar.
- The cations M and A are of same valence.

When these conditions are fully followed, a continuous solid solution in the whole range ABX_3 – MBX_3 is likely formed where native and substituent (solute) cations are distributed

randomly in the designated sites in a single perovskite phase. On the other hand, if the conditions are partially fulfilled, solid solution may be observed only up to a certain degree of substitution, above which a phase transition or segregation may occur. This is the common case for aliovalent substitution where an extra charge is created that must be counterbalanced. In ionic solids, this extra charge is mainly compensated by formation of defects in the crystal, such as vacant sites in normally occupied lattice positions. Since diffusion of any charged or neutral species over crystalline solids is directly dependent on the type and number of the defects accommodated in the lattice, modifications in the defect structure by rational substitution of A- and B-site cations can have substantial implications on the material's functional properties. With respect to these aspects, the flexibility of the perovskite structure offers broad possibilities for material engineering in environmental catalysis.

2.2 Strontium titanate

$SrTiO_3$ is a well-known ideal cubic perovskite with a lattice parameter **a** = 3.905 Å and a mass density **ρ** = 5.12 g cm^{-3} at room temperature in its synthetic form [39]. Naturally occurring $SrTiO_3$ mineral was first discovered as late as 1982 in Siberia and was named tausonite after the Russian geochemist Lev Vladimirovich Tauson [40].

Small amounts of deviation from nominal stoichiometry are tolerated within $SrTiO_3$ cubic lattice. It is known that small excesses of strontium in the structure can be accommodated as local Ruddlesden-Popper phases with general composition $Sr_{n+1}Ti_nO_{3n+1}$ and tetragonal symmetry group I4/mmm (Fig 2.3) or as oxygen rich extended defects [41,42].

The cubic symmetry of $SrTiO_3$ lattice is retained up to its melting point of 2080 °C [39]. Transitions of $SrTiO_3$ cubic phase into lower symmetries can occur upon cooling as well as doping the material with foreign ions. $SrTiO_3$ crystals are reported to have tetragonal symmetry between 110 K – 65 K range [43], orthorhombic between 55 K – 35 K and possibly rhombohedral at temperatures below 10 K [44]. In its cubic form $SrTiO_3$ is a charge symmetric, paraelectric material, whereas with the tetragonal phase transition it gains a dipole moment and approaches ferroelectricity. Its already high dielectric permittivity, ε, increases linearly following the Curie-Weiss law from 370 up to ~ 10^4 as the temperature is lowered to 1.4 K [45]. At these extremely low temperatures (~ 1 K), doped $SrTiO_3$ can exhibit superconducting properties. Furthermore, $SrTiO_3$ substrates show excellent suitability for epitaxial growth of high-temperature superconductors [46].

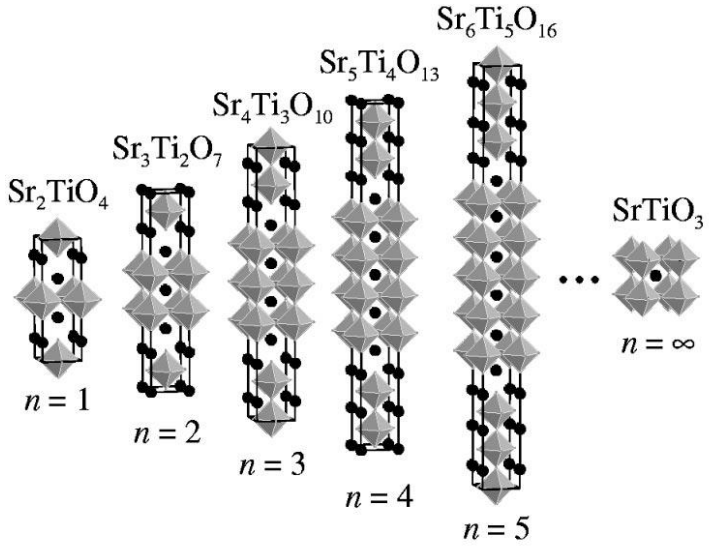

Figure 2.3: Unit cells of $Sr_{n+1}Ti_nO_{3n+1}$ homologous series. n = ∞ corresponds to $SrTiO_3$ [47].

In $SrTiO_3$ lattice, the bonds between Sr^{2+} and O^{2-} ions show ionic character, whereas between Ti^{4+} and O^{2-} ions the hybridization of O-2p states with Ti-3d states leads to bonds with covalent character [22]. Sr^{2+} cations don't play a direct role in the electronic structure due to their strong electropositivity. The valence band of $SrTiO_3$ is formed by oxygen 2s and 2p states at the highest occupied molecular orbitals (HOMO) and the conduction band is formed by degenerate Ti-3d states at the lowest unoccupied molecular orbitals (LUMO). The energy difference between HOMO and LUMO states amount to an indirect band-gap of 3.25 eV, which enables the material to show wide-gap semiconducting behavior [48].

Moreover, $SrTiO_3$-based perovskites belong to the class of mixed ionic-electronic conductors (MIECs) and show outstanding stability in various atmospheres [20]. Thus, $SrTiO_3$ is rendered a model material whose defect chemistry has been thoroughly investigated in last decades [21,26,49]. Thanks to these attractive properties, $SrTiO_3$-based perovskites find use in a wide range of applications, such as solar cells, H_2 production, oxygen sensors, fuel cell electrodes, oxide electronics and oxygen separation membranes [5,15,23–26].

2.2.1 Acceptor substitution: $SrTi_{1-x}Fe_xO_{3-\delta}$

$SrTi_{1-x}Fe_xO_{3-\delta}$ perovskites (STF for short) with the end members $SrTiO_3$ – $SrFeO_{3-\delta}$ form a continuous solid solution in the entire composition range $0 \leq x \leq 1$ [50]. Intermediate STF compositions possess purely cubic crystal structure, whereas end member strontium ferrite at

reducing conditions and high temperature goes through a phase transition from a cubic perovskite with disordered vacancy structure ($SrFeO_{3-\delta}$, $\delta \approx 0$) to a vacancy ordered brownmillerite phase, $SrFeO_{2.5}$ ($SrFeO_{3-\delta}$, $\delta = 0.5$) [51,52]. Vacancy ordering in this case refers to the distribution of oxygen vacancies in the anionic sublattice. Thus, the brownmillerite structure for $SrFeO_{2.5}$ can be described as a series of alternating layers of FeO_6 octahedra and FeO_4 tetrahedra sandwiched by Sr atoms as shown on Fig. 2.4. This order – disorder transition prevents the utilization of $SrFeO_{3-\delta}$ perovskites in many electrochemical and catalytic applications. On the other hand, intermediate compositions of $SrTi_{1-x}Fe_xO_{3-\delta}$ stabilizes the cubic structure without significant impediment in the material's MIEC properties and thus are desirable for a wide range of applications [53].

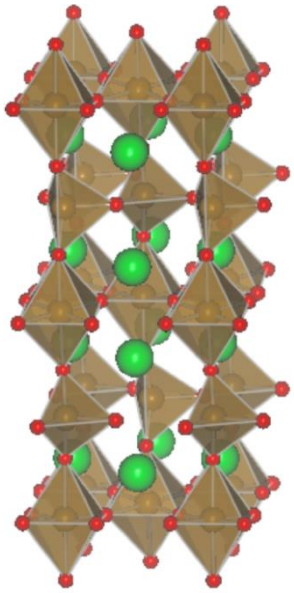

Figure 2.4: $SrFeO_{2.5}$ brownmillerite structure [54].

Notwithstanding some works reporting the presence of negligible amounts of Fe^{2+} and Fe^{5+}, the consensus in literature is that iron in $SrTi_{1-x}Fe_xO_3$ solid solutions mainly shows Fe^{3+} and Fe^{4+} valence states [55–57]. The ratio of Fe^{4+}/Fe^{3+} is dependent on a wide range of synthesis and treatment conditions. For small amounts of Fe substitution, Fe^{3+} is mainly formed due to thermodynamically stable half-filled sub-shell configuration of the cation (3d5). Moreover, unoccupied oxygen sites in the perovskite lattice favor Fe^{3+} rather than Fe^{4+} as the nearest neighbor for charge compensation [53,56]. Thus, for low amounts of iron substitution, the extra negative charge is mainly compensated by creation of anionic vacancies, since other

defect species such as cationic interstitials are energetically not favorable. At higher iron contents, Fe^{4+} valence state is mainly formed with an extent depending on oxygen partial pressure during material preparation [55,57].

As the composition of STF approaches the $SrFeO_{3-\delta}$ end-member, the material shows progressively increasing MIEC conductivity approaching to metallic-like behavior [58,59]. In such case, with increasing iron amount, Fe^{3+}/Fe^{4+} centers start to interact with each other and their 3d states form a continuous band which overlaps with O-2p states in the valence band, narrowing the band gap down to 1.9 eV [53,60,61]. Along with this decreasing trend in the band gap, oxygen surface exchange capability of the material is progressively enhanced [60].

Due to their attractive MIEC properties and stability, STF family of materials are rendered promising candidates for solid oxide fuel cell (SOFC) electrodes, oxygen sensors and oxygen permeation membranes [62–64]. Additionally, thanks to their close relation to $SrTiO_3$ with well-established defect chemistry, STF oxides are considered as ideal model systems for charge transport process investigations of complex mixed ionic-electronic conductors that are utilized in industrial applications.

2.2.2 Donor substitution: $La_{1-y}Sr_yTiO_{3+\delta}$

Donor substitution in strontium titanate is a widely employed strategy for improving the material's n-type conductivity [65–67]. La^{3+} (r = 1.36 Å) can substitute Sr^{2+} sites (r = 1.44 Å) without significant structural distortion due to the similar ionic radii of the cations. Various studies showed that lanthanum is completely soluble in $La_ySr_{1-y}TiO_{3+\delta}$ lattice up to $y \leq 0.4$ [68–70]. Around y = 0.5, slight distortions of the cubic crystal structure is observed, which then leads to a transition to orthorhombic crystal phase upon further La substitution.

While $La_ySr_{1-y}TiO_{3\pm\delta}$ (LSTO) is an insulator in oxidizing conditions, its heat-treatment under reducing atmosphere can induce substantial n-type conductivity [67]. In this case, La^{3+} ions compensate their extra charge by creation of electrons; Ti^{4+} is reduced to Ti^{3+} and Fermi level shifts further into the conduction band. Band gap of the material on the other hand stays essentially constant [71–73].

Preparation route and pre-treatment play a significant role in deciding the final physicochemical properties of donor substituted $SrTiO_3$ systems. Lanthanum substituted $SrTiO_3$ can be prepared either in compliance with cationic or oxygen stoichiometry. Cation-

stoichiometric LSTO with general formula $La_ySr_{1-y}TiO_{3+\delta}$, possesses an oxygen excess illustrated by the positive δ value to compensate the additional positive charge introduced by the donor substituent. In the $La_ySr_{1-y}TiO_{3+\delta}$ formula, δ value can reach as high as $y/2$ and remains essentially positive under operation conditions of solid oxide fuel cell anode [74]. Only at extremely reducing conditions, δ can be zero or negative. The extra oxygen in this structure is thought to be accommodated in secondary Ruddlesden-Popper phases or oxygen rich extended defects [75,76].

Alternatively, the extra positive charge from the donor can be compensated by creation of additional strontium vacancies through A-site deficiency, leading to an oxygen stoichiometric perovskite. The excessive amount of strontium vacancies impedes the formation of secondary SrO-rich phases. The suppression of these phases is beneficial, since they can inhibit the grain growth during sintering and their solution/dissolution during the oxidation – reduction cycle can be harmful for material performance. As a result, A-site deficient LSTO shows superior mechanical properties and redox stability than oxygen excess compositions [77]. On the other hand, A-site deficiency can promote an undesired TiO_2 segregation tendency under reducing conditions [78]. Thus, the preparation and treatment conditions should be chosen carefully to reach desired defect chemical properties.

Along with enhanced electronic properties, a major benefit of La substitution is the improvement of dimensional and chemical stability of the material in both reducing and oxidizing atmospheres [79,80]. Matsushima et al. demonstrated that La substitution leads to strengthened Ti – O bonds improving structural stability of the material [81]. Several researchers reported improved phase stability in reducing conditions and impediment of thermal expansion when $SrTi_{1-x}Fe_xO_{3-\delta}$ solid solutions were doped with La [32,82–84].

2.3 Environmental catalysis with $SrTiO_3$ based perovskites

Catalytic processes are at the center of modern society with about 35% of world's gross domestic product is estimated to arise from them [85]. Environmental catalysis research, which involves development of efficient pollution abatement and green energy conversion systems, carries tremendous relevance for attainment of global energy production goals and minimization of harmful gas emissions. Historically noble metals have been widely employed for such applications, but in recent decades perovskite oxides emerged as potential alternatives for noble metal catalysts due to their lower cost, decent activity, excellent stability

and tunable material properties. In this section, the environmental catalysis applications in which $SrTiO_3$ based perovskite oxides are utilized will be briefly described and the state of the art will be summarized.

2.3.1 Photocatalysis – wastewater depollution

Among the candidate energy sources to replace fossil fuels, solar energy is globally most favored option thanks to its inherent availability, cleanliness and inexhaustible nature. Total annual global energy consumption is currently around 600 exajoules (1 EJ $= 10^{18}$ J) and projected to reach 750 EJ by 2040 according to the assessments of EIA [86]. The irradiation of the earth by the sun amounts to about 4,000,000 EJ of energy reaching earth annually of which at least 50,000 EJ is easily harvestable [87]. Thus, utilizing only a tiny fraction of this solar energy would suffice to meet the global energy demand. Along with photovoltaics, photocatalytic methods such as CO_2 reduction to produce CO and CH_4 fuels [88] or water splitting to produce H_2 fuel [89], are the main strategies for harvesting solar energy. Despite promising developments, acceptable efficiencies for commercialization of these processes are still yet to be realized.

A crucial contemporary application of photocatalysis which already starts to play a role in modern wastewater treatment technologies is the degradation of organic pollutants. The shortage of clean water as well as pollution of the existing water sources due to rapid industrialization has raised the importance of wastewater recycling dramatically. Organic dyes are one of the largest groups of pollutants in wastewater. About 15% of the total amount of produced dyes in textile industry is lost as effluents in the process [90]. Another important concern is the increasing occurrence of antibiotics and other pharmaceuticals in water sources, which can have important impacts on public health [91,92]. Traditional water treatment technologies, such as adsorption and filtration based processes are relatively ineffective in purifying water contaminated by chemically stable compounds such as aromatic organic solvents, organic dyes and pharmaceuticals [93]. An effective approach to remove these pollutants is utilization of photocatalytic oxidation, which can lead to total mineralization of these organic compounds [94,95].

Photocatalytic redox processes are initiated by the excitation of the photocatalyst valence electrons to the conduction band via solar irradiation (Fig. 2.5). Electron-hole pairs are consequently formed, which migrate on the catalyst surface and can directly or indirectly

facilitate respective reduction and oxidation reactions [96,97]. The positive holes can either oxidize the pollutant directly or indirectly through the formation of $OH^{\cdot}$ radicals, whereas the electron in the conduction band reduces the adsorbed oxygen [94,98]. Recombination of electron – hole pairs is detrimental for the photocatalytic reaction and presence of electron scavengers such as oxygen is crucial to inhibit the recombination. Adsorbed oxygen molecules can scavenge the electron to form a superoxide radical ($O_2^{\cdot -}$). The superoxide radical can be protonated to form a hydroperoxyl radical ($HO_2^{\cdot}$) and finally hydrogen peroxide (H_2O_2).

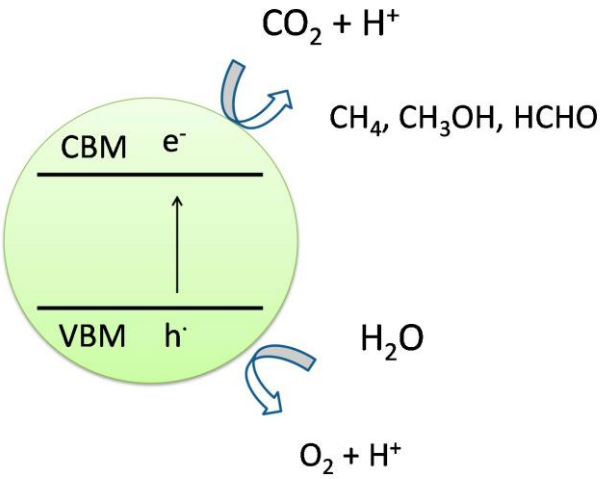

Figure 2.5: Basic principle of photocatalytic redox processes over a semiconductor photocatalyst given for degradation of organic compounds [7]. CBM and VBM refer to conduction and valence bands.

The catalytic setup for the reaction may constitute a particulate photocatalyst or a photoelectrochemical cell without any alteration in the basic principle. Particulate photocatalyst setups are deemed more promising for large-scale applications at the moment due to their simplicity, whereas sufficiently cost-effective and stable electrochemical setups are still not developed [97,99,100].

A suitable photocatalyst for such applications should ideally be visible-light active in order to utilize larger portion of solar spectrum [7]. The material should possess high chemical stability to withstand corrosion from the photogenerated oxidant species. High crystallinity can induce increased catalytic activity, which is usually ascribed to minimization of surface defects in the material that act as traps/recombination centers for the charge carriers [101].

Similarly, decreasing particle size impedes recombination as a result of smaller diffusion path-lengths for charged particles. High surface area usually leads to increased activity due to enhanced number of active sites for the reaction.

Since early 1970s, TiO_2 has been the most widely studied material for photocatalytic applications due to its abundance, high stability and tunable band gap [102]. Despite its considerable activity, this material suffers from some drawbacks. For instance, fast charge carrier recombination in TiO_2 can impede the efficiency of the photocatalytic reaction. Nonstoichiometric H_2/O_2 production can be encountered as a result of self-oxidation of TiO_2 [103,104]. Also, similar to most investigated photocatalysts, TiO_2 can absorb only ultraviolet portion of solar irradiation, which amounts to ~ 5% of total light that reaches earth [105].

Perovskite oxides show great promise in photocatalysis thanks to their flexibility of composition and electronic structure which enables easy band gap engineering. Significant photocatalytic performance was determined for titanate and tantalate based perovskite oxides [106–111]. $SrTiO_3$ based perovskite oxides are particularly promising under UV irradiation with excellent photocorrosion resistance and structural stability [112,113]. Although in its pristine state $SrTiO_3$ is only UV-active, doping with suitable ions at each cationic or anionic position can induce visible-light response and enhance activity in these photocatalysts by reducing the band gap [114–116]. Fig. 2.6 illustrates remarkable increase in generation of visible light-response by raising the top of the valence band via 0.5 mol.% B-site doping, particularly for the elements, Mn, Rh, Ru and Ir [117]. Reduction of band-gap was also demonstrated for $Sr_{0.66}Zn_{0.33}TiO_3$ due to creation of new Zn 2p energy states at the bottom of the conduction band [118]. Li et al. recently prepared Fe-doped $SrTiO_3$ nanoparticles with a solvothermal synthesis route [119]. Thanks to the band gap narrowing induced by Fe^{3+} substituents, 3 mol% Fe doped $SrTiO_3$ led to 14 times higher conversion than the undoped $SrTiO_3$ sample in the photocatalytic degradation of tetracycline under visible light irradiation. F-doping [120] and N-doping [121–123] on the anionic sites were shown to enhance the performance of the photocatalyst in the degradation reactions of organic pollutants as well, probably due to enhanced electron mobility as well as the formation of Ti^{3+} ions with high capability for visible light absorption [24].

Along with band-gap engineering and nanostructuring, increasing porosity of perovskite oxides is a very effective approach to enhance photocatalytic activity due to increased number of active sites, better utilization of incoming light as a result of multi-reflections within pores,

enhanced separation of electron – hole pairs and quick transport kinetics through the interfaces [124]. Higher activities were reported for nanoporous $SrTiO_3$ based oxides in comparison to nonporous counterparts and commerical TiO_2 (P25) in photocatalytic degradation [125,126] as well as water splitting [127,128].

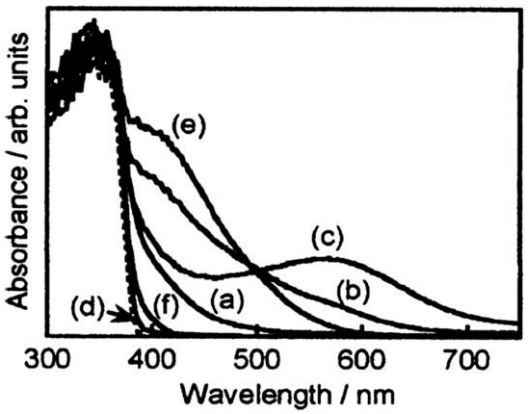

Figure 2.6: Diffuse reflactance UV/Vis spectra of $SrTiO_3$ substituted with 0.5% dopant cation (a) Mn (b) Ru (c) Rh, (d) Pd (e) Ir (f) Pt [117].

Dong et al. prepared porous $SrTiO_3$ nanospheres with 26 $m^2 g^{-1}$ via hydrothermal treatment with P25 surfactant. Porous spheres showed superior photocatalytic performance in the degradation of Rhodamine B dye under UV irradiation [129]. Fan et al. prepared mesoporous $SrTiO_3$ with surface areas up to 206 $m^2 g^{-1}$ using an excess of $SrCO_3$ precursor which was later removed from the final product by a mild acetic acid treatment [125]. The influence of porosity on the photocatalytic performance of the material was investigated by a 2-propanol to acetone conversion reaction. Mesoporous photocatalysts showed up to 30 times higher activity than bulk $SrTiO_3$ prepared with solid state reaction. Ouyang et al. prepared nanoporous $SrTiO_3$ with a template assisted sol− gel hydrothermal reaction [130]. Porosity of the material was enhanced with increasing template amount, whereas crystallinity of the perovskite phase decreased. 40 mol.% SiO_2 templated $SrTiO_3$ system showed optimum performance due to combined effect of porosity and crystallinity, leading to 8 times higher conversion than a commercially obtained nanoparticulate $SrTiO_3$ in the photocatalytic degradation of organic pollutant, isopropanol. Three dimensionally ordered macroporous (3DOM) semiconductor materials can be beneficial for photocatalytic applications due to the enhanced light-matter interaction through the periodic structure [14]. Recently, Yu et al. prepared 3DOM-$SrTiO_3$ photocatalysts with differing size of macropores and demonstrated

substantially superior photocatalytic performance of the 3DOM structure in comparison to the bulk counterpart prepared by solid state reaction [131].

2.3.2 Chemical catalysis – CO and CH_4 oxidation

Natural gas based power generation fulfills a significant portion of global energy consumption and is predicted to steadily increase its output in coming decades [132]. Conversion of natural gas to electricity is realized typically via steam generator or gas turbines, while electrochemical conversion with solid oxide fuel cells (SOFCs) can provide a potentially superior alternative with higher efficiency, better scalability as well as fuel flexibility [3,26,133,134]. Notwithstanding the mechanistic differences between utilized processes, catalyst performance and stability play a central role in deciding the overall efficiency of the fuel conversion system. In this respect, CO and CH_4 oxidation can be employed as model low and high temperature chemical reactions to investigate catalytic properties of potential perovskite oxide catalysts.

Independent of the type of the reaction, a heterogeneously catalyzed reaction over oxide catalysts goes through similar fundamental steps involving the adsorption of reactant species on the catalyst followed by a redox reaction between reactants and finally desorption of products. The suprafacial (surface) reaction involving the adsorption of both reactants on the catalyst surface at neighboring sites and their subsequent reaction is described by Langmuir-Hinshelwood, whereas Eley-Rideal proposed a reaction mechanism for only one of the reactant species adsorbing on the catalyst surface and reacting with the other molecule directly from the gas phase [5]. Accordingly, the individual steps that CO oxidation undergoes over metal oxide catalysts can be described through combination of both pathways as follows:

$$O_2(g) \rightleftharpoons 2O(ads) \tag{2.2a}$$

$$CO(g) \rightleftharpoons CO(ads) \tag{2.2b}$$

$$CO(ads) + O(ads) \rightleftharpoons CO_2(ads) \rightleftharpoons CO_2(g) \tag{2.2c}$$

$$CO(g) + O(ads) \rightleftharpoons CO_2(g) \tag{2.2d}$$

Zhang-Steenwinkel et al. experimentally confirmed the coexistence of Eley-Rideal and Langmuir-Hinshelwood mechanisms in CO oxidation reaction by kinetic studies and ^{18}O labeling over a $La_{0.8}Ce_{0.2}MnO_3$ catalyst [135]. The authors concluded that carbon monoxide is

easily adsorbed on the oxide surface in carbonate form and the reaction between adsorbed CO and O_2 species constitute the rate-determining step in the reaction. CO oxidation rates over oxide catalysts are usually first order with respect to CO, whereas the reaction order with respect to oxygen is usually between 0 – 0.5 and tends to approach zero in oxygen rich atmospheric conditions [5].

It is widely acknowledged that CO oxidation over unsupported metal catalysts proceeds mainly through Langmuir-Hinshelwood pathway [23]. Reaction orders over metal catalysts show different behavior than of oxides with the reaction orders with respect to CO and O_2 approach -1 and 1 respectively [136]. This disparity is due to strong adsorption affinity of carbon monoxide leading to preferential adsorption of this molecule over oxygen on metal surfaces [136,137]. Increasing CO partial pressure leads to more carbon monoxide adsorption on catalyst surface which inhibits the O_2 adsorption and impedes the reaction.

For oxidation of more stable molecules such as CH_4, the activation barrier is remarkably higher. The surface reactions involved in CH_4 oxidation over oxides can be shown through following pathways [15]:

$$M^nO_x + O_2(g) \rightleftharpoons [O][M^{n+1}O_m] \tag{2.3a}$$

$$H_3C - H + [O][M^{n+1}O_m] \rightleftharpoons CH_3^{\cdot} + [OH][M^{n+1}O_m] \tag{2.3b}$$

$$CH_3^{\cdot} + [OH][M^{n+1}O_m] \rightleftharpoons [OH][M^nO_{m-3}CO_2] + 2[OH_2] \tag{2.3c}$$

$$[M^nO_{m-3}CO_2] \rightleftharpoons M^nO_x + CO_2 \tag{2.3d}$$

These reactions take place at higher temperatures (usually above 500 °C) in which the bulk of the catalyst (i.e. lattice oxygen) may also actively take part in the reaction. As a result, consumed oxygen in the reaction is not only replenished by adsorption from the gaseous state like in low temperature catalysis, but also by diffusion of lattice oxygen from the catalyst towards the empty position. The partial participation of the catalyst in the reaction as a reagent by subsequent depletion and replenishment steps were first broadly acknowledged through the reports of Mars and van Krevelen and the pertaining reaction mechanism is commonly named Mars and van Krevelen (MvK) mechanism [138,139]. Auer and Thyrion investigated kinetics of CH_4 oxidation over a $La_{0.9}Ce_{0.1}CoO_3$ perovskite and concluded that the best fit was given by a MvK mechanism, whereas solely suprafacial reaction mechanisms failed to describe the empirical results [140]. The rate equation for such pathway can be

expressed with an additional term that is independent of oxygen partial pressure which describes the contribution of lattice oxygen to the oxidation reaction [10,141]:

$$r = k_s P_{CH_4} (K_{O_2} P_{O_2})^{1/2} + k_i P_{CH_4} \quad (2.4)$$

where K_{O_2} is the equilibrium constant for oxygen adsorption, k_s and k_i are rate constants for suprafacial (surface contribution) and intrafacial (lattice contribution) reactions respectively. The suprafacial reaction term is similar to given terms for CO oxidation, whereas the intrafacial reaction term ($k_i P_{CH_4}$) describes the contribution of lattice oxygen to the oxidation reaction and is independent of oxygen partial pressure.

Due to the substantial stability of CH_4 molecule, the dissociative adsorption of methane on catalyst surface is the rate determining step in the reaction. Experimentally determined reaction orders for CH_4 over oxide catalysts are usually ~ 1, whereas the reaction orders for oxygen are usually found to be between 0 – 0.5 [5,15]. Unlike CO oxidation, strong preferential adsorption of CH_4 over unsupported metal catalysts is usually not observed and the reaction over metal catalysts is first order with respect to methane and oxygen [142].

Fig. 2.7 gives an overview of the main surface reaction models over oxide catalysts. It should be noted that interaction of the catalyst with reactants is a complex and dynamic phenomenon that is unique for each individual catalyst and thus many conflicting pathways are proposed in literature for similar systems based on empirical findings [5,15,23,143,144].

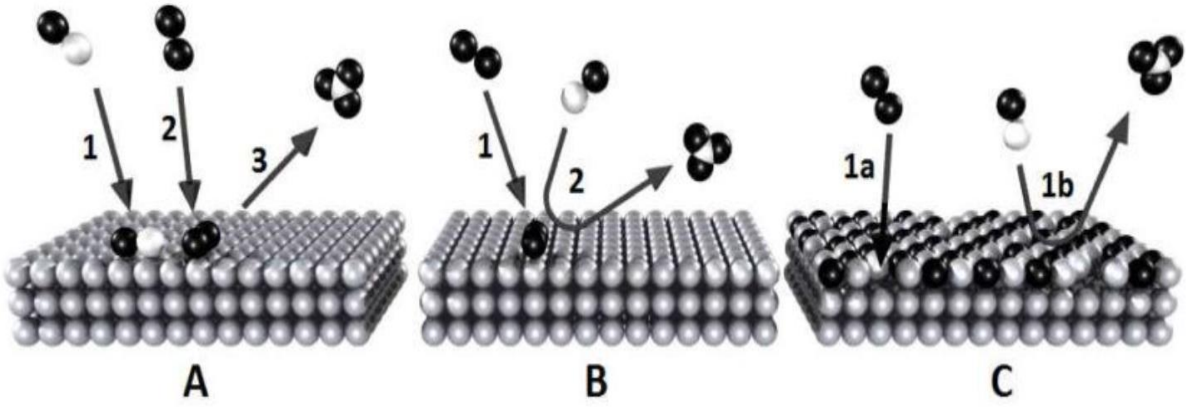

Figure 2.7: Schemes or (a) Langmuir – Hinshelwood (LH) mechanism (b) Eley – Rideal (ER) mechanism (c) Mars and van Krevelen (MvK) mechanism [145].

2.3 Environmental catalysis with $SrTiO_3$ based perovskites

Perovskite oxides constitute one of the most promising family of materials with the potential to replace metal catalysts in thermally initiated catalytic combustion of fuels and volatile organic compounds (VOCs) as well as pollution control systems such as automotive exhaust catalysis. Since the demonstration of their catalytic performance in early 1980s, lanthanum based perovskite oxides have remained the most widely investigated perovskite catalysts, probably as a result of accumulated knowledge in these systems considering the relatively minor influence of the A-site cations to the catalytic activity [25,146,147]. The activity of perovskite catalysts is usually correlated with the redox properties of the B-site cations in the structure. Most active B-site cations (Mn, Co, Ni, Fe) usually accommodate mixed oxidation states, which facilitate catalytic reaction by providing active adsorption sites for the reactants and enhancing oxygen mobility. Although catalytic performance depends on a wide variety of material properties, oxidation activity usually follows Mn > Co > Fe for the B-site cations, whereas inverse behavior is observed for thermal stability [148–151]. Moreover, partial substitution of B-site cations can be employed as a strategy to tailor material's stability and catalytic activity through modification of its defect structure and physicochemical properties [25].

Mixed oxidation states of B-site cations in the perovskite oxide catalyst strongly promote methane oxidation through facilitation of dissociative adsorption in the methane molecules [5]. Conversely, since the adsorption of CO on oxide surface does not have a high energy barrier, carbon monoxide oxidation is not affected strongly by mixed oxidation state of B-site cations in the perovskite [23]. Another key parameter for the activity is the oxygen mobility in the catalyst lattice. CO oxidation is predominantly promoted by surface oxygen mobility, whereas for high temperature CH_4 oxidation reaction, both bulk and surface oxygen mobility affects the catalytic activity [152]. It is also worth mentioning that oxygen mobility and nature of B-site cations in perovskite structure are closely related parameters.

There are very few reports in literature concerning the chemical oxidation performance of perovskite oxides with stoichiometry close to end group member $SrTiO_3$, as these compositions do not show appreciable catalytic activity towards the oxidation of CH_4, CO or other VOCs. Alkali or noble metal doped $SrTiO_3$ shows activity towards diesel soot combustion [153–156], whereas decent CO and CH_4 oxidation performance was reported for compositions such as $LaFeO_3$ [12,157], $La_{0.8}Sr_{0.2}FeO_3$ [157] and $La_{0.66}Sr_{0.34}Co_{0.2}Fe_{0.8}O_{3-\delta}$ [158] possessing surface areas below ~ 5 $m^2\ g^{-1}$. With regard to electrochemical oxidation of

CH_4 and H_2 fuels in SOFCs, La-substituted $SrTiO_3$ (LSTO) sintered under reducing atmospheres has attracted significant attention as potential anode material due to its significant n-type conductivity and phase stability [67,159–165]. Moreover, STF ($SrTi_{1-x}Fe_xO_{3-\delta}$) and LSTF ($La_ySr_{1-y}Ti_{1-x}Fe_xO_{3\pm\delta}$) compositions were investigated both as anode and cathode materials in literature [166–169]. Fagg et al. showed that under oxidizing conditions catalytic activity of strontium titanate based materials can be increased by substitution of Fe cations on the B-sites, whereas La substitution on the A-sites improves the phase stability of the material and impede thermal expansion [32].

Despite challenging preparation of these materials, significantly enhanced performance is possible by utilization of porous perovskite oxide catalysts. Several researchers prepared three dimensionally ordered macroporous (3DOM) perovskite oxides with colloid crystal template method using polymethlyl methacrylate (PMMA) or polystyrene (PS) microspheres. Enhanced CO, CH_4 and VOC oxidation performance over these 3DOM perovskite oxides was demonstrated for $LaFeO_3$ (surface area = 19 – 20 $m^2\ g^{-1}$) [170,171], $LaCo_{0.6}Fe_{0.4}O_3$ (surface area = 20 $m^2\ g^{-1}$) [170], $SrFeO_{3-\delta}$ (surface area = 34 – 61 $m^2\ g^{-1}$) [172], $La_{0.6}Sr_{0-4}MnO_3$ (surface area = 32 – 40 $m^2\ g^{-1}$) [141] and $LaCo_{0.5}Fe_{0.5}O_3$ [173]. Improved catalytic activity was assigned to increased surface area, enhanced oxygen mobility and better low temperature reducibility.

Nanocasting route involving infiltration of the pores of an ordered mesoporous template with reaction precursors is the main strategy for preparation of mesoporous perovskite oxides in literature, since high temperatures required for crystallization of perovskite phase are unsuitable for soft templating routes. Wang et al. prepared mesoporous $LaCoO_3$ with surface areas as high as ~ 97 $m^2\ g^{-1}$ through a nanocasting route using a silica template combined with citrate gel synthesis [174]. Mesoporous material showed substantially higher methane combustion activity in comparison to bulk counterpart. The surface area of perovskite catalyst decreased to ~ 70 $m^2\ g^{-1}$ after the first catalytic run, possibly due to restructuring of porous morphology. The authors found higher concentration of O_2^{2-} / O^- species in mesoporous $LaCoO_3$, which are strongly electrophilic reactants and likely contributed to the enhanced activity. Nair et al. prepared mesoporous $LaMO_3$ (M = Mn, Co, Fe) with surface areas 110 – 155 $m^2\ g^{-1}$ by nanocasting with ordered mesoporous KIT-6 silica template [175]. Mesoporous $LaMnO_3$ showed enhanced performance in methanol oxidation, despite XPS analysis showing

retainment of 10% residual Si in the sample after etching treatment to remove the silica template. Lima et al. prepared mesoporous $LaFe_{1-x}Co_xO_3$ (x = 0, 0.4) with surface areas 30 – 50 $m^2 g^{-1}$ by utilizing a micro-mesoporous carbon mold as template [176]. Complete oxidation of CO was achieved over nanocast $LaFeO_3$ sample (30 $m^2 g^{-1}$) at 400 °C, whereas bulk sample (6 $m^2 g^{-1}$) reached complete oxidation at 560 °C. Mesoporous $LaFe_{0.6}Co_{0.4}O_3$ on the other hand showed poorer performance, likely due to La_2O_3 impurity phase found in the sample inhibiting the reaction.

Despite the advances made in the development of perovskite oxide catalysts, reported catalytic performance for these materials in CH_4 and CO oxidation do not show comparable values to state of art supported metal noble catalysts, such as Pd/CeO_2-Al_2O_3 [177] and Au/CeO_2 [178]. In such systems, metal-support interactions lead to unique catalytic properties. Enhanced activity due to electronic and ionic transfer between metal and support [179–183], stabilization of the oxidation state of the active phase [182,184–187] and sintering resistance [188–191] are reported for numerous supported metal catalysts. Support materials utilized for such systems are typically chemically/thermally stable mesoporous materials with high surface area to to provide superior dispersion and reactivity of metal sites [192], enhanced contact area and easy access of reactants [193,194] and resistance to deactivation [190,195]. Recently mesoporous MIEC materials, such as CeO_2 found great interest as support materials due to their high oxygen supply capabilities to the active phase [6,196]. Considering superior stand-alone catalytic performance and tunable stability of perovskite oxides, utilizing such materials as active support can potentially offer a better alternative to current CeO_2 supported systems. However, very few works in literature reported perovskite oxide supported metal catalysts due to the difficulties in preparation of pure-phase multiternary perovskite oxides with high porosity. Recently, some works demonstrated enhanced CH_4 oxidation activity for 3DOM perovskite oxide supported metal nanoparticle catalysts with compositions, $Ag/La_{0.6}Sr_{0-4}MnO_3$ [197] and $Pd/LaMnO_3$ [198].

2.4 Design of $SrTiO_3$ based perovskites for environmental catalysis

Catalytic activity of perovskite oxides depend on a wide variety of material properties such as, mixed oxidation states of their B-site cations, the oxygen mobility in the structure as well as number and reactivity of active sites for the reaction [5,15,25]. Nanostructure and morphology of the material are as crucial as chemical composition in designating these parameters and

pertaining catalytic performance of the material. Moreover, commercial application of perovskite oxide catalysts is mainly limited by their poor textural and structural properties [5,14]. Nanostructured perovskite oxide catalysts with mesoporous morphology possess numerous advantages to bulk counterparts due to their high surface areas and short diffusion pathways for charge carriers which leads to increased number and reactivity of active sites, enhanced redox properties, superior oxygen mobility and charge carrier transport [5,14,15]. Hence, development of a multifaceted design approach is required to prepare high-performance perovskite oxide catalysts which combine mesoporosity, controlled cationic substitution as well as nanostructure and defect structure engineering [5]. In this section, relevant strategies regarding the design of nanoscale perovskite oxides for environmental catalysis applications will be briefly discussed.

2.4.1 Low and intermediate temperature synthesis strategies

Conventionally, perovskite oxides are prepared by solid state synthesis in which precursor salts or single metal oxides are mechanically mixed and sintered at high temperatures (> 1000 °C) to induce mass transport within solids. The process is energy-consuming as the high temperature treatment is carried out for 8 – 24 hours to enable satisfactory phase purity [199]. Moreover, the final product suffers from numerous drawbacks such as poor homogeneity, broad particle size distribution and poor textural properties [200]. Due to straight-forwardness of the approach, solid state synthesis routes are still widely employed in preparation of perovskite oxides. However, several alternative synthesis strategies were developed in order to lower the exceedingly high reaction temperatures and enable nanostructuring.

Common intermediate temperature synthesis routes for single metal oxides, such as co-precipitation and evaporation induced self-assembly (EISA), are usually not applicable for mixed metal oxides due to differing solubility and reactivity of the metal ions. However, some reports of perovskite oxides prepared by these routes can still be found in literature [201–203].

Among more suitable routes, autocombustion synthesis is widely employed due to its advantages of simplicity, high purity and fast reaction. The process is realized by mixing the cationic precursors with a solvent and fuel/oxidizer. After solvent evaporation, the gel is heated on a heating plate or muffle furnace until the highly exothermic autocombustion reaction is initiated to produce the desired perovskite. The fuel can be typically urea, glycin,

glycerol or alanine. Surface areas between 5 – 40 m^2 g^{-1} are commonly reported with this route [204–206]. Although, autocombustion synthesis is attractive for its simplicity and scalability, relatively high reaction temperature (typically ~ 800 °C) and limited control over calcination conditions prevent effective nanostructure engineering via this process [205,206]. Moreover, multicomponent oxides prepared by this route can contain impurities. Baharuddin et al. observed the growth of impurity phases, $Sr_3Fe_2O_{7-\delta}$ and TiO_2, independent of reaction conditions in $SrTi_{0.5}Fe_{0.5}O_3$ synthesis using glycine and metal nitrates as precursors [207].

2.4.1.1 Sol-Gel Process

Sol-gel processing is a widely employed wet-chemistry route for the fabrication of metal oxides as it enables intimate control of final product through control of reaction parameters. Fundamental formation mechanism of the oxide species in this route were thoroughly investigated using silica-based systems. The main principles of the process apply to preparation of other oxides as well, despite the differences in the chemistry of precursors [208].

In a typical sol-gel preparation of silica species, silicon alkoxide precursors go through hydrolysis and condensation reactions in an aqueous medium to form a colloidal solution called ‘sol’ that accommodates the growing silica network. As the rates of competing hydrolysis and condensation reactions are pH dependent, connectivity of the forming silica network is manipulated by addition of acid or base to the system [209]. The growth of the three dimensional complex network of silica leads to gradual increase of the viscosity and culminates in the gelation of the reaction mixture, where a diphasic system of the liquid solvent and the amorphous solid coexist. Heat treatment is then implemented on the gel to enable further polycondensation reactions of the silica network (aging) and remove remaining solvent from the structure (drying). Finally, the amorphous gel is calcined to obtain crystalline silica material. By intimate control of reaction parameters as well as use of structure directing agents, silica and other oxide materials with a wide range of morphology and nanostructures were prepared by this approach [210,211].

Preparation of single phase multicomponent oxide systems by the traditional sol-gel process is challenging due to the varying hydrolysis and condensation rates of different metal precursors. In such cases, the mobility and reactivity of the metal cations are commonly moderated by use of chelating agents. Citrate gel route is an example of such synthesis

approach, in which the metal precursors and citric acid are dissolved in an aqueous medium to form metal-citrate complexes. The gelation is then achieved by the evaporation of the solvent, followed by calcination to remove the organics and crystallize the perovskite oxide phase. Although, many perovskite oxide compositions are successfully obtained by citrate gel route [212,213], the crystallinity and phase purity of the final products in this approach are usually unsatisfactory for $SrTiO_3$ based perovskites due to the exceedingly high reactivities of the available titanium precursors for the synthesis [214,215]. Utilization of the polymer complex approach can be more advantageous for preparation of such materials.

2.4.1.2 Polymer Complex Route

An established synthesis route that is applicable for a wide range of perovskite oxide compositions at intermediate temperatures is the polymer complex approach introduced by Pechini in 1967 [215–217]. In this so called Pechini process, metal ions are dissolved and chelated within a polycarboxylic acid/polyol solution (commonly citric acid and ethylene glycol). Heating the reaction mixture over 100 °C results in a polyesterification reaction fixing the chelated metal cations in the polymer resin. The homogeneous distribution of the metal cations at atomic scale within the gel dramatically reduces the diffusion requirement during perovskite crystal phase formation and along with the exothermic burning reaction of the polyester gel, crystalline perovskite oxides can be obtained at intermediate temperatures ($T < 800$ °C). Commonly used citric acid can form very stable chelate complexes with a wide range of multivalent metal cations thanks to its one hydroxyl and three carboxylic acid groups. On top of that, fixing the metal cations in a polymer resin containing water resistant metal-citrate complexes is particularly advantageous when readily hydrolyzed metal precursors such as alkoxides are used in the synthesis. Thus, polymer complex route offers superior compositional and structural homogeneity in comparison to other solution-based techniques, especially in the synthesis of complex multicomponent oxides prepared with readily hydrolysable precursors, such as metal alkoxides [215].

Kakihana et al. analyzed the intermediate stages in the thermal decomposition of polyester gel chelated with Sr and Ti precursors in order to explain the greater homogeneity of the $SrTiO_3$ prepared by polymer complex route [217]. Fig. 2.8 shows the X-ray diffractograms and Raman spectra of $SrTiO_3$ intermediate phase and single metal intermediates calcined at 400 °C for 2 h under air. When single metal precursors were fixed in the polyester resin, TiO_2 and

$SrCO_3$ were formed after 400 °C heat treatment, whereas these isolated phases were not observed for the (Sr,Ti) polyester intermediates. In line with previous reports [218,219], the authors assigned the superior compositional homogeneity of the final $SrTiO_3$ product to the formation of a heterometallic (Sr,Ti) citrate complex which transforms to a mixed metal carbonate intermediate upon calcination of the polyester gel and then goes through a single step decomposition to form the crystalline perovskite oxide. Due to this superior homogeneity, numerous chemically complex perovskite oxide solid solutions such as, $La_{0.8}Sr_{0.2}FeO_3$ [220], $Ba_{1-x}Sr_xTiO_3$ [221], $(La_{0.75}Sr_{0.25})_{0.95}MnO_{3\pm\delta}$ [222] and $Ba_xSr_{1-x}Ti_{1-y}Fe_yO_{3-y/2+\delta}$ [223] were successfully prepared with polymer complex route.

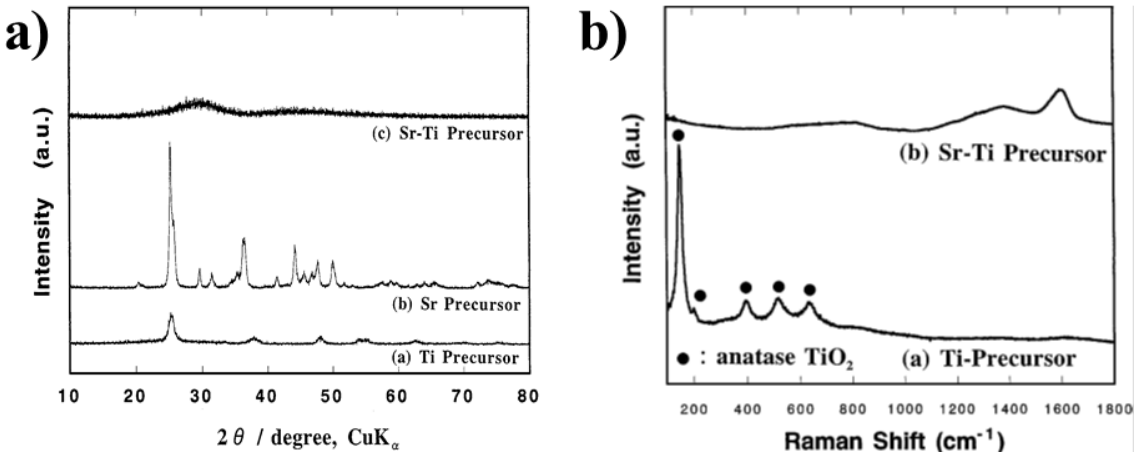

Figure 2.8: X-ray diffractograms (a) and Raman spectra (b) of the thermal decomposition products obtained at 400 °C for 2 h in static air atmosphere from standard polymer complex route with ethylene glycol, citric acid, Sr and Ti precursors. Adapted from [217].

Despite the improved material properties and performance achieved for the products prepared by the Pechini approach, small amounts of carbonate impurities are usually unavoidable due to the excessive amount of organics present in the initial polymer gel [215]. Surface areas around 15 – 20 $m^2\ g^{-1}$ are commonly retained with this route as opposed to 1 – 2 $m^2\ g^{-1}$ observed for perovskites prepared by solid state synthesis [213].

2.4.1.3 Solvothermal Synthesis

Solvothermal synthesis routes can be facilitated to prepare perovskite oxide nanoparticles with tailored particle size and shape. The method has several advantages; namely, low energy requirement (reaction temperature between 100 – 200 °C), simplicity, high purity as well as

effective control of nanostructure and morphology [224,225]. Solvothermal route is typically based on the simultaneous heat and heat induced pressure treatment of the precursors in a water (hydrothermal reaction) or solvent based medium. The reaction takes place in a sealed container, i.e. high-pressure autoclave. Perovskite oxide nanoparticles prepared by solvothermal route typically show higher catalytic activity than bulk perovskites as a result of their high surface to bulk ratio, good surface crystallinity and quantum size effects [124]. Moreover, the materials can be tailored by altering the reaction parameters to have the optimal particle shape and size that is favorable for the target catalytic application [226,227].

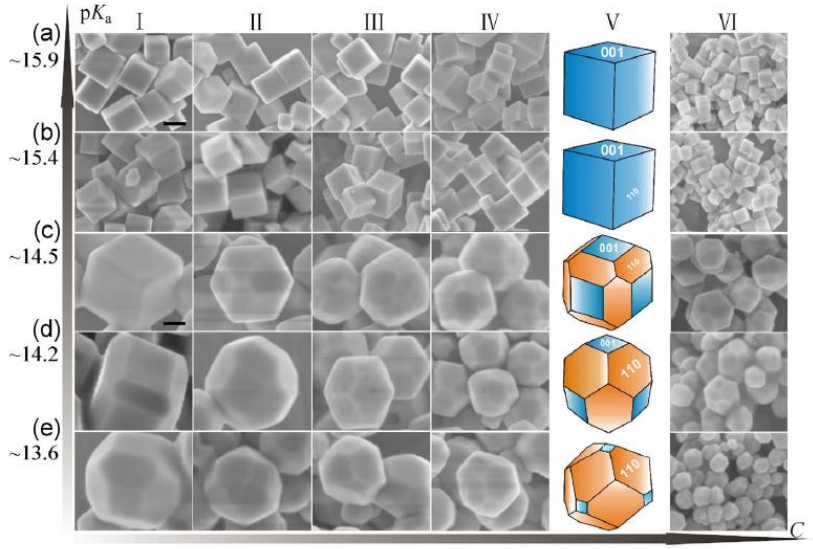

Figure 2.9: SEM images of $SrTiO_3$ nanocrystals prepared by solvothermal synthesis varying the nature and amount of used alcohol surfactants. (a) Ethanol (b) 1,4-Butanediol (c) 1,2-Propanediol (d) Ethylene glycol (e) Pentaerythritol. I – VI refers to increasing alcohol amount [228].

Solvothermal process is not suitable for the preparation of some perovskite compositions. For instance, there are only few reports for the successful synthesis of ferrites in solvothermal conditions where exceedingly high temperatures (> 250 °C) were needed compared to normal operation range of standard Teflon liners [229,230]. However, there are numerous reports in literature on the preparation of size and shape controlled $SrTiO_3$ nanomaterials, such as spheres [231], dendritic nanostructures [232], nanowires [233], nanofibers [234,235] and nanocuboids [236,237]. The reactions are all undergone under basic pH to stabilize formation of $SrTiO_3$ and avoid the growth of single metal oxide phases [227,238]. Since shape-tailored

synthesis is kinetically controlled, different surfactants can selectively interact and stabilize a particular crystal facet, leading to well defined morphologies [227]. Dong et al. investigated the systematic morphology evolution of $SrTiO_3$ nanocrystals by using a series of alcohols with different pK_a values (acidity) as surfactants [228]. Change in the nature and amount of the added alcohol led to $SrTiO_3$ with varying shape and size from nanocuboidal to dodecahedral morphology (Fig. 2.9).

Moreover, although one-step solvothermal routes are not feasible for the preparation of complex multicomponent oxides with several cations in their structure, small amounts (< 5 at.%) of Fe- [119], Rh- [107], Mn- [239] and Ba- [240,241] substitution in $SrTiO_3$ lattice were successfully achieved with this route.

2.4.2 Preparation of nanoporous perovskite oxides

In comparison to bulk and nanoparticulate perovskites, nanoporous counterparts demonstrate further improvements in catalytic performance as a result of their percolated structure enabling easy access for reactants as well as enhanced number of active sites for catalytic reaction and short diffusion path lengths for charge carriers [194]. The preparation strategies of nanoporous perovskite oxides are mainly based on utilizing soft or hard templating routes.

Soft templating approach mainly refers to the use of sacrificial templates that are structure directing agents (SDAs) in a wet chemistry route to form the porous oxide [242]. Template materials are commonly ionic or non-ionic surfactants which are amphiphilic polymers containing hydrophilic and hydrophobic components. These polymers self-organize into micelles through weak forces such as hydrogen bonding and van der Waals when their concentration surpasses CMC (critical micelle concentration) [243]. The geometric arrangement of the micelles is determined by the nature and concentration of the surfactant in the solution. Metal oxide precursors organize around the micelles via electrostatic interactions or hydrogen bonding based on the ionic or nonionic character of the surfactants respectively [244]. The templating process follows either a cooperative self-assembly or a true liquid crystal template mechanism depending on the concentration of the surfactant in the solution. In the former case the inorganic and organic species co-assemble simultaneously to form the geometric arrangement, whereas in the latter case the concentration of the surfactant is high enough to form a lyotropic liquid crystalline (LC) phase by itself and the inorganic precursors can be incorporated into the already organized structure (Fig. 2.10). After a stable inorganic-

organic hybrid composite is formed, the template is typically removed from the composite by calcination in air to achieve porosity. Adjustment of the reaction parameters enables effective tailoring of the final product morphology. However, exact determination of the desired parameters is challenging due to the complex interactions between the inorganic and organic species.

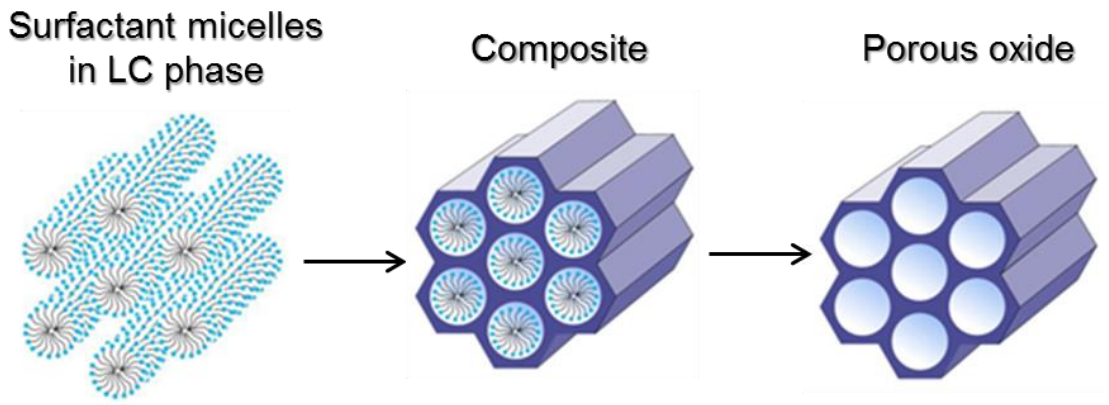

Figure 2.10: Schematic representation of liquid crystal template mechanism leading to porous oxide with hexagonal pore structure. Adapted from [245].

Ever since the first successful implementation of the soft templating approach by Mobil researchers in 1992, a wide range of materials with ordered or disordered mesoporosity were successfully prepared with this route, having tremendous practical implications in industrial heterogeneous catalysis [246,247]. On the other hand, only few reports are present in literature concerning successful preparation of mesoporous perovskite oxides by this approach due to the inadequacy of the wet synthesis routes associated with soft templating for preparation of multi-metal oxides as well as exceedingly high formation temperature of perovskite phase [173,248]. Liu et al. used a modified EISA route employing P123 block copolymer as surfactant to prepare $La_{0.5}Sr_{0.5}Co_{0.5}Fe_{0.5}O_3$ with surface areas up to 65 $m^2\ g^{-1}$ [249]. However, these surface areas determined for amorphous material dropped down to 0.25 $m^2\ g^{-1}$ after high temperature treatment to obtain crystalline phase. Lertpanyapornchai et al. used the same triblock copolymer in a combined citrate gel/combustion route to prepare $SrTiO_3$ with surface areas up to 41.5 $m^2\ g^{-1}$ [250]. Notwithstanding their decent porosity, $SrTiO_3$ materials obtained in this route contained $SrCO_3$ and $SrCl_2$ impurities. Suzuki et al. utilized a soft templated sol-gel route to prepare $SrTiO_3/BaTiO_3$ composite films with surface areas up to ~ 36 $m^2\ g^{-1}$ [251].

Hard templating approach refers to the use of templates with rigid framework that remain non-interactive with the reacting species, i.e. the initial inorganic precursor towards the final oxide structure. Whereas, soft templating is by definition an endotemplating route in which the template is added into the reaction mixture with the growing solid particle as an isolated precursor, hard templating can branched into endo- and exotemplating categories [252]. Exotemplating (commonly called as nanocasting) involves the use of a structure which provides a scaffold with voids. The precursor solution for the desired product is brought into the pores of this porous matrix [253]. The matrix is typically a mesoporous silica or carbon prepared by soft templating route, such as SBA-15 or MCM-48. The crystalline phase is formed inside the pores of the template upon heat treatment. Subsequently, the template matrix can be removed by either chemical etching in the case of silica or simply by calcination in air atmosphere for carbon. The resulting final product is ideally a precise negative replica of the template material (Fig. 2.11).

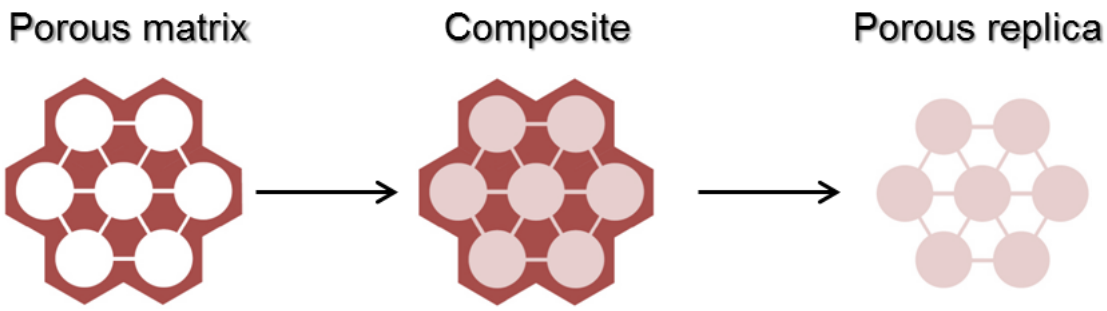

Figure 2.11: Schematic representation of typical nanocasting mechanism.

Nanocasting is a suitable route for the preparation of perovskite oxides, since the synthesis routes associated with this approach are not limited to cooperative assembly or co-precipitation processes and the template materials are thermally stable to withstand high temperatures required for perovskite phase formation. However, this route suffers from some drawbacks as well. Usually several optimized impregnation steps are required to attain a satisfactory pore filling while avoiding formation of the desired phase outside of the pores. Moreover, complete removal of the template material by etching is often difficult to achieve. Kleitz et al. prepared $LaMO_3$ (M = Co, Fe, Mn) through an exotemplating route using KIT-6 [175]. Very high surface areas up to 155 m^2 g^{-1} were observed for the final materials, along with substantial residual silica amounts as high as 10 at.%. Similarly, Zhang et al. showed that

$LaFeO_3$ nanocasted within a SBA-15 matrix led to 158 $m^2\ g^{-1}$ along with a residual Si amount of 5.4 at.% [254].

Inorganic endotemplating can provide a more facile alternative to the nanocasting route, as well as higher flexibility to the nanostructure and morphology of the final product. In this pathway, a non-interacting inorganic template goes through cooperative assembly with the precursor of the desired product. For instance, Liu et al. prepared carbon/silica nanocomposites by cooperative assembly of resol and tetraethoxy orthosilicate precursors [255]. Highly porous carbon was then obtained by removing SiO_2 phase by HF etching, whereas calcination in air led to porous silica product. The microstructure and porosity of the final materials could be tailored by adjusting the precursor amounts.

Colloidal crystal template approach can be classified as a hard templating route to prepare three dimensionally ordered macropored (3DOM) materials. In this method, silica or polymer spheres form a close-packed monodisperse structure with high periodicity in three dimensions. The void spaces of this close-packed structure are filled with precursor solution and the desired phase is formed upon calcination accompanied with the removal of template spheres. Relatively high calcination temperatures can be used with this route (~800 °C), since most template materials (polystyrene, poly(methyl methacrylate) (PMMA) spheres) are more heat resistant in comparison to surfactant based soft templates. Three dimensionally ordered macroporous $SrFeO_{3-\delta}$ [172], $La_{0.6}Sr_{0.4}MnO_3$ [141], $LaCo_xFe_{1-x}O_3$ [173] with surface areas between 30 – 60 $m^2\ g^{-1}$ were successfully prepared by PMMA templating.

2.4.3 Flash sintering of perovskite oxides

Nanostructured and nanoporous perovskite oxides often show significantly superior catalytic performance than their bulk counterparts. However, these materials commonly possess lower thermal and mechanical stability, which prevents them from retaining their initial structure and morphology when exposed to relatively higher temperatures (> 600 °C). Thus, a sintering process is usually necessary to enhance mechanical and thermal robustness of the ceramic material as well as to achieve sufficient overall connectivity of the particles.

Although some supplementary techniques such as hot isotactic pressing or microwave mediated heating were developed to improve the method, the main pathway of conventional ceramic sintering simply involves a high temperature treatment for several hours to consolidate and densify the material to a contiguous body. The processing temperature is set

around two thirds of the material's melting point in order to activate the mass transport through diffusion. Accordingly, $SrTiO_3$ based ceramics are typically sintered at temperatures between 1000 and 1700 °C in various atmospheres [80,162,169,256,257].

Ceramic flash sintering is a novel method first demonstrated by Cologna et al. in 2010, in which the material is heated in the presence of an electric field [258]. When a critical temperature is reached at a given electric field, a flash event characterized by a nonlinear increase in conductivity and power dissipation takes place and rapid consolidation of the material in a time frame of few seconds is observed [259]. The consolidation temperature in flash sintering is typically much lower than the temperatures required for conventional sintering [260], enabling a great reduction in energy and time costs of the process [261].

Although the consolidation phenomenon is initially explained solely by preferential Joule heating across the grain boundaries as a result of the sharp increase in the conductivity [262], the moderate temperatures comparable with conventional sintering were insufficient in explaining such rapid densification [263,264]. Some works suggested the connection of rapid consolidation with enhanced diffusion and atomic mobility as a result of temperature gradients formed between the grain boundary and grain core as well as partial reduction of the material upon the flash event [263,265]. Others pointed to the effect extremely high heating rates on the scale of 10^4 K min^{-1} which favors such rapid densification process [266,267]. It is plausible to consider that multiple processes are simultaneously responsible for observed densification effect, however further investigations are required to reach conclusive experimental confirmation for the proposed mechanisms.

The non-equilibrium nature of flash sintering technique can be utilized as an effective strategy to tailor the nanostructure and defect chemistry of ceramic materials. Several researchers reported consolidated perovskite oxide particles with nano-sized grains using flash sintering process (Fig. 2.12) [268,269]. Moreover, presence of electric field during heat treatment can promote formation of ionic defects, which in turn enhances atomic diffusion and densification rate of the particle [19,270,271]. Liu et al. recently showed that flash sintering engenders larger vacancy concentrations at the grain boundaries in comparison to conventionally sintered counterparts, leading to thinner grain boundary layers [272]. Karakuscu et al. determined formation of non-stoichiometric Ruddlesden-Popper phases in $SrTiO_3$ material induced by flash sintering treatment [273]. Shomrat et al. successfully consolidated Fe-doped $SrTiO_3$ particles by flash sintering and found that onset of flash event decreased with

increasing Fe substitution and oxygen partial pressure [274]. Rheinheimer et al. investigated the defect chemistry of undoped and acceptor doped $SrTiO_3$ samples [275]. The researchers reported a gradient of oxygen vacancy concentration between electrodes which led to a decreasing non-stoichiometry at the grain boundaries of the sintered material towards the negative electrode.

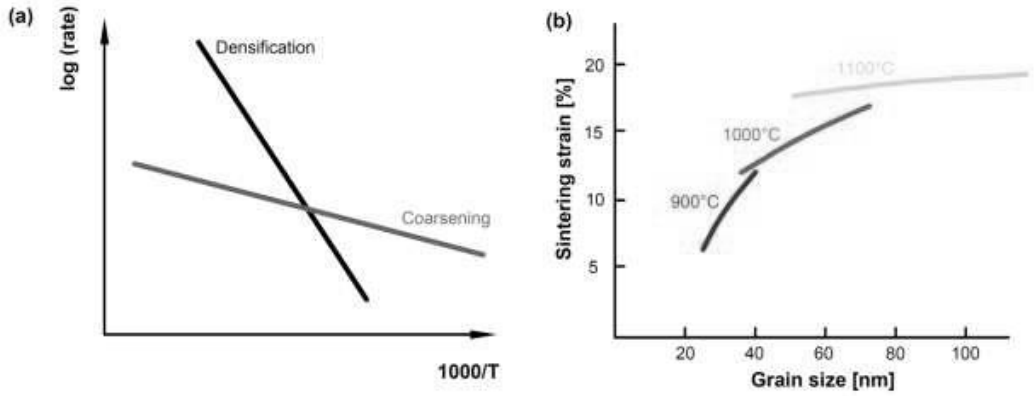

Figure 2.12: (a) Rate of coarsening and densification as a function of sample temperature (b) Shrinkage induced by sintering vs. evolution of grain size for flash sintering of samarium doped ceria nanoparticles at three different temperatures [19].

2.5 Defect chemistry of $SrTiO_3$ based perovskites

As major portion of beneficial properties of $SrTiO_3$-based systems can be described as a function of their MIEC nature, it is crucial to understand the mechanism of charge movement over $SrTiO_3$ lattice. A well-established model for the defect chemistry of $SrTiO_3$ based perovskite oxides is present in literature thanks to the extensive efforts both experimentally and theoretically [21,257]. In this section, a brief introduction for the defect chemistry of $SrTiO_3$ and related perovskites will be given.

2.5.1 Introduction to defects in crystalline solids

It has been established since the beginning of 20^{th} century that inorganic solids exhibit deviations from the ideal theoretical structure. These deviations can be observed as different types of defects in the crystal lattice. Defects are not only fundamental in the movement of charge carrier species in the lattice but also directly affect many physical and chemical properties of the material. The so-called zero-dimensional or point defects are formed when

the defect is limited only to a specific lattice site and its immediate vicinity (Fig. 2.13). The description of defect chemistry of $SrTiO_3$ based perovskites in this work will focus on these zero-dimensional defects. However, it should be noted that defects of higher dimensions such as dislocations (1D), grain boundaries (2D) and voids (3D) play a role in the material properties as well.

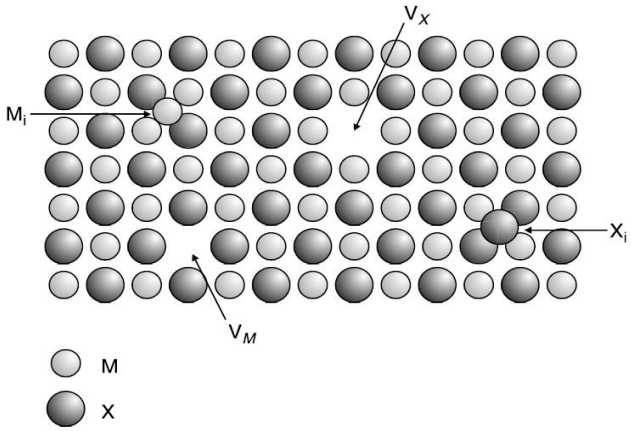

Figure 2.13: Possible point defects in a pure crystal, MX. V_M and V_X correspond to vacancy of metal and non-metal species, M_i and X_i are metal and non-metal interstitial sites [38].

Point defects are split into several different categories. The absence of a pair of ions in their expected lattice position leading to a vacancy on those sites is called a Schottky defect, whereas if an atom leaves its lattice position and moves to an interstitial site, a Frenkel defect is formed (Fig. 2.14). Other point defects include electrons and holes. Altogether, these deviations from the ideal solid can be classified as intrinsic point defects, since they are native to the crystal and cannot be eliminated.

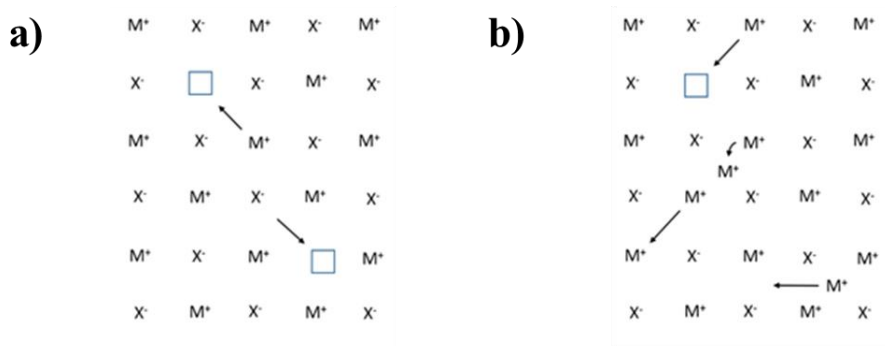

Figure 2.14: Schottky (a) and Frenkel (b) defects [276]

Introduction of foreign atoms to the lattice in small amounts can tailor material's physical and chemical properties due to size effects and rearrangement of defect species according to electroneutrality condition. The foreign atoms are called dopants and they constitute an example for extrinsic point defects.

Kröger – Vink notation is the most widely employed system to describe defect equilibria [277,278]. A list of the notable defect species present in $SrTiO_3$ system and the pertaining symbols according to Kröger – Vink notation are given in Table 2.1.

Table 2.1: Kröger-Vink notation of the species that take part in defect equilibria of $SrTiO_3$ and related perovskites [277].

Description	Kröger-Vink Notation
Fully ionized oxygen vacancy	$V_O^{\cdot\cdot}$
Fully ionized strontium vacancy	V_{Sr}''
Strontium partial Schottky	$V_{Sr}''+V_O^{\cdot\cdot}$
Schottky	$V_{Sr}''+V_{Ti}''''+3V_O^{\cdot\cdot}$
Lanthanum substituted in strontium sites	$La_{Sr}^{\cdot}$
Iron substituted in titanium sites	Fe_{Ti}'
Electrons	e'
Holes	$h^{\cdot}$
Neutral titanium on regular titanium sites	Ti_{Ti}^{x}
Neutral strontium on regular strontium sites	Sr_{Sr}^{x}
Neutral oxygen on regular oxygen sites	O_O^x

2.5.2 Defect chemistry of nominally undoped $SrTiO_3$

The defect chemistry of nominally undoped $SrTiO_3$ is governed by three temperature ranges which designate the mobility of charge carrier species, namely high temperature regime (T > 1000 °C), intermediate temperature regime (600 °C < T < 1000 °C) and low temperature regime (T < 400 °C). At temperatures above 1000 °C, the vacancy species in $SrTiO_3$ are all mobile and in equilibrium with the surrounding atmosphere [279]. Since ionic vacancies are energetically more favorable than interstitials in $SrTiO_3$ lattice and SrO partial Schottky is known to be the dominant intrinsic disorder, strontium and oxygen vacancies are the main ionic defects found in $SrTiO_3$-based systems [280,281]. The equilibrium for SrO partial Schottky disorder reaction is given as:

$$Sr_{Sr}^{x} + O_{O}^{x} \rightleftharpoons V_{Sr}'' + V_{O}^{\cdot\cdot} + SrO\ (s) \tag{2.5}$$

SrO in this equilibrium can originate from secondary Ruddlesden-Popper phases in the interior of the crystal (Fig. 2.3) or from grain terminations [282,283]. Equilibrium constant for the formation of Schottky defects, $K_{Sch}(T)$, is given by mass-action law:

$$K_{Sch}(T) = [V_{Sr}''][V_{O}^{\cdot\cdot}] = K_{Sch}^{\circ}\ exp\ [-\Delta H_{Sch}/k_B T] \tag{2.6}$$

where ΔH_{Sch} is the enthalpy of formation for SrO partial Schottky. ΔH_{Sch} values were given as ~ 3.48 eV by defect chemical modelling, whereas the experimentally determined values are reported as ~ 1.0 eV smaller [75,257]. The reason of this discrepancy is unknown. The solution of Eq. (2.6) by using the given enthalpy values predicts the respective oxygen and strontium vacancy concentrations to be around 10 ppm each at 1200 °C. Nominally undoped $SrTiO_3$ readily contains acceptor impurities from the earth's crust, such as Al, Fe and Mg. These impurities are typically of higher concentrations than of the intrinsic defects and are almost impossible to eliminate from the crystal, as the earth's crust is abundant with these cations with lower valence [284]. Thus, the defect chemistry of $SrTiO_3$ is generally dictated by acceptor-type dopants (Acc_{Ti}') rather than intrinsic defects, i.e. nominally undoped system practically acts as acceptor doped $SrTiO_3$.

Below 1000 °C (intermediate temperature regime), strontium vacancies don't show sufficient mobility and as a result Eq. (2.5) is not active at these conditions. $[V_{Sr}'']$ can then be considered as a fixed value and the frozen-in strontium vacancies act effectively as additional acceptor species. However, the equilibrium between the oxygen in the oxide and oxygen in the

surrounding atmosphere is still active above ~ 450 °C. The equilibrium reaction can be written in two forms:

$$½\ O_2(g) + V_O^{\cdot\cdot} \rightleftharpoons\ O_O^x +\ 2h^{\cdot} \tag{2.7a}$$

$$O_O^x \rightleftharpoons\ ½\ O_2(g) + V_O^{\cdot\cdot} + 2\mathrm{e}' \tag{2.7b}$$

respectively for the oxidation (2.7a) and reduction (2.7b) of the oxide. The equilibrium constant $K_{Red}(T)$ for the reduction of the oxide to form doubly ionized oxygen vacancies is given by,

$$K_{Red}(T)\ =\ [V_O^{\cdot\cdot}]\ [\mathrm{e}']^2 P_{O_2}^{½}\ =\ K_{Red}^{\circ}\ exp\ [-\Delta H_{Red}/k_B\ T] \tag{2.8}$$

where, P_{O_2} is the oxygen partial pressure. The reduction enthalpies, ΔH_{Red}, for the reaction were given in the range of 5-6 eV in literature [257,285]. The enthalpy of oxygen vacancy migration, $\Delta H_{mig}(V_O^{\cdot\cdot})$, was in turn reported between 0.62 and 0.67 eV [286,287].

Below ~ 400 °C (low temperature regime), the oxide is no longer in equilibrium with the surrounding atmosphere. The most important reaction that is still active at this temperature range is generation of electrons and electron holes by thermal excitation:

$$nil\ \rightleftharpoons\ \mathrm{e}' +\ h^{\cdot} \tag{2.9}$$

The equilibrium constant, $K_{eh}(T)$, for this reaction can be written in its simplified form as:

$$K_{eh}(T)\ =\ [\mathrm{e}'][h^{\cdot}]\ =\ K_{eh}^{\circ}\ exp\ [-\mathrm{E}_{BG}/k_B\ T] \tag{2.10}$$

where E_{BG} is the bandgap between the valence and conduction bands with a value ~ 3.2 eV (see Chapter 2.2).

Another important reaction at this temperature range is the ionization of acceptor dopants, which goes through following equilibrium:

$$Acc_{Ti}^x\ \rightleftharpoons\ Acc_{Ti}'\ +\ h^{\cdot} \tag{2.11}$$

The reverse reaction in this equilibrium corresponds to the trapping of electron holes by acceptor centers. The equilibrium constant for the reaction can be given as:

$$K_{Acc}(T)\ =\ \frac{[Acc_{Ti}'][h^{\cdot}]}{[Acc_{Ti}^x]}\ =\ K_{Acc}^{\circ}\ exp\ [-\Delta H_{Acc}/k_B\ T] \tag{2.12}$$

where enthalpy of ionization for the acceptor species, ΔH_{Acc}, is usually given as > 1 eV [288,289]. Acceptor dopant cations have deep levels above valence band in the bandgap. Accordingly, it shouldn't be overlooked that the acceptor centers can act as traps for electron holes at oxygen excess regime even at relatively high temperatures above 500 °C through the reverse reaction on Eq. (2.11), thereby hindering p-type conductivity dramatically [49,290].

In addition to the abovementioned defect species, several other point defects are present in $SrTiO_3$ lattice: singly charged strontium and oxygen vacancies, hydroxide ions, dopant-vacancy associates as well as neutral acceptor dopants, neutral oxygen and strontium vacancies. However, in certain conditions the contribution of these defects are negligible and the electroneutrality equation above 500 °C in dry conditions can then be written as:

$$[\mathrm{e}'] + [Acc'_{Ti}] + 2[V''_{Sr}] = [h^{\cdot}] + 2[V^{\cdot\cdot}_{O}] \qquad (2.13)$$

Each value on Eq. (2.13) can be determined precisely by proper design of conductivity experiments, since determined values from these experiments will be directly dependent on the concentration and mobility of the charge carriers at given conditions.

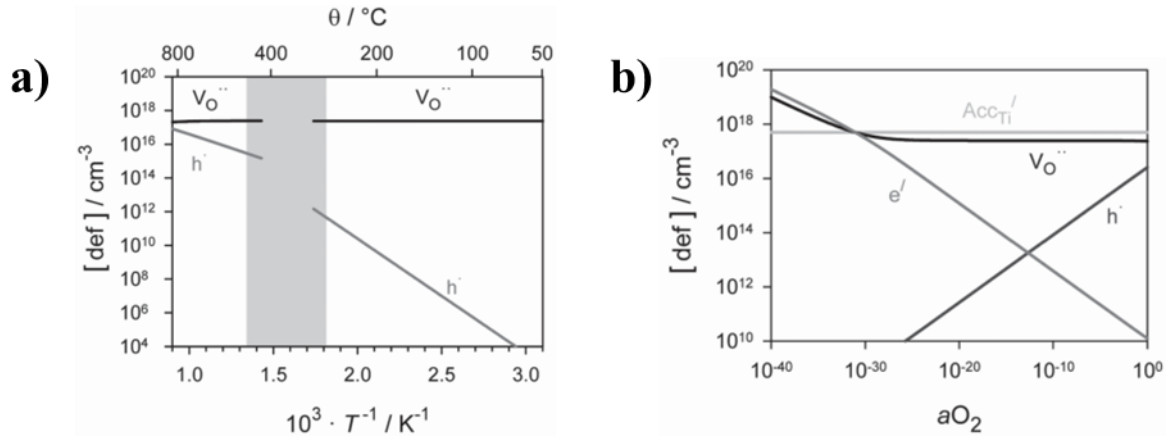

Figure 2.15: Kröger-Vink diagrams for change in mobile point defect concentrations with temperature in oxidizing conditions (a) point-defect concentrations at ~ 650 °C as a function of oxygen activity (b) in acceptor-doped $SrTiO_3$ predicted by defect modelling [21].

At temperatures above 500 °C, the conductivity is predominantly electronic, since electronic defects (electrons and holes) have orders of magnitude higher mobility than ionic vacancies [291]. Below 300 °C, acceptor dopants and strontium vacancies act as traps to suppress electron holes and as a result electronic contribution to the total conductivity is dramatically

reduced. For $SrTiO_3$, in oxidizing conditions major contribution to conductivity was determined as electron holes above 500 °C and doubly charged oxygen vacancies below 300 °C [21,286]. Using defect mobilities and defect concentrations predicted on Fig. 2.15a, the partial conductivities, σ, in the intermediate temperature regime between 500 < T < 1000 °C can be calculated with the following equation:

$$\sigma = u_{h^{\cdot}}[h^{\cdot}] + u_{V_O^{\cdot\cdot}}[V_O^{\cdot\cdot}] \tag{2.14}$$

where, $u_{h^{\cdot}}$ and $u_{V_O^{\cdot\cdot}}$ are mobilities of electron holes and oxygen vacancies respectively at given temperature.

As mentioned, strontium vacancies act as additional acceptor species below 1000 °C and the effective acceptor concentration $[Acc'_{eff}]$ is given as the total of acceptor species and strontium vacancies. By observing Fig. 2.15b and Eq. (2.13), one can discern that the defect chemistry at a wide pO_2 range is dictated by the acceptor species at intermediate temperature regime by following equation:

$$[Acc'_{Ti}] + 2\,[V''_{Sr}] = \left[Acc'_{eff}\right] = 2\,[V_O^{\cdot\cdot}] \tag{2.15}$$

Combining Eq. (2.15) and (2.8), the dependence of electronic conductivity in reducing conditions can be predicted:

$$[\mathrm{e}'] = \left(\frac{K_{Red}(T)\left[Acc'_{eff}\right]}{2}\right)^{-1/2} P_{O_2}^{-1/4} \tag{2.16}$$

Eq. (2.16) shows that the electronic conductivity has a $P_{O_2}^{-1/4}$ dependence at reducing conditions. By applying the same calculation for the hole concentration at oxidizing conditions, a $P_{O_2}^{1/4}$ dependence can be deduced. Under exceedingly reducing conditions, the products of reduction in Eq. (2.8) can surpass the acceptor concentration and the defect chemistry of $SrTiO_3$ is then dictated intrinsically by the formed oxygen vacancies:

$$[\mathrm{e}'] \approx 2\,[V_O^{\cdot\cdot}] \tag{2.17}$$

Combining Eq (2.17) and (2.8), one can deduce that in these conditions, electronic conductivity should show a $P_{O_2}^{-1/6}$ dependence. Indeed, the expected conductivity vs. pO_2 relationship was demonstrated in experimental works on nominally undoped $SrTiO_3$ [284].

Fig. 2.16 shows the changing trend in conductivity of nominally undoped $SrTiO_3$ with oxygen activity at three different temperatures. The V-shaped lines correspond to p-type conductivity at high oxygen activities and n-type conductivity at low oxygen activities. The flattening of the curve at ~ 680 °C (950 K) evidences the increasing ionic contribution to the total conductivity.

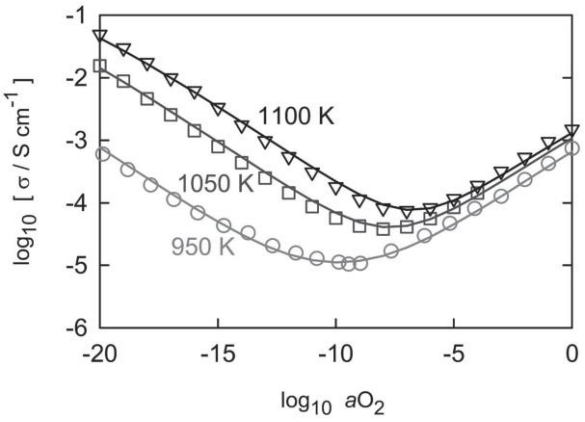

Figure 2.16: Evolution of conductivity in nominally undoped $SrTiO_3$ single crystal with changing oxygen activity [21,292].

2.5.3 Acceptor substitution: Defect chemistry of $SrTi_{1-x}Fe_xO_{3-\delta}$

While the end member $SrFeO_{3-\delta}$ lacks in structural stability, intermediate $SrTi_{1-x}Fe_xO_{3-\delta}$ (STF) compositions are stable MIECs with high ionic and electronic conductivity [52,293]. Considering most high-performance MIECs have chemically complex structures with several cations in framework, the additional complexity introduced to $SrTiO_3$ makes STF a suitable model system for further studies on charge movement. Although insertion of Fe into $SrTiO_3$ lattice accounts to acceptor-type substitution, the model presented in Chapter 2.5.2 is only valid for dilute solutions of acceptor dopant ($Acc'_{Ti} < 1\,mol\%$), where the interactions between defect centers and change in electronic states can be neglected. For higher amounts of Fe substitution, the simplified model can no longer predict the concentration of defect species accurately [294].

Substitution of trivalent Fe ions in the tetravalent Ti sites leads to generation of additional oxygen vacancies according to the equation:

$$Fe_2O_3 \xrightarrow{SrTiO_3} 2\,Fe'_{Ti} + V_O^{\cdot\cdot} \qquad (2.18)$$

Rotschild et al. suggested a defect model for STF which takes Fe as a native component in the structure and incorporates anionic-Frenkel disorder in the defect equilibria, given that in intermediate STF compositions, despite the absence of long range ordering of oxygen vacancies, Ti and Fe sites tend to be mostly 6-fold and 5-fold coordinated respectively [53,56,294]. It should be noted that interstitial oxygen sites are not favored in perovskite lattice, and thus, this model presents an approximation of the actual defect structure.

In this pseudo-brownmillerite estimation of STF system, anionic-Frenkel disorder reaction is formed through following defect equilibrium:

$$O_O^x + V_i^x \rightleftharpoons V_O^{\cdot\cdot} + O_i'' \tag{2.19}$$

And the corresponding equilibrium constant for anionic-Frenkel reaction, $K_{aF}(T)$ is:

$$K_{aF}(T) = [V_O^{\cdot\cdot}][O_i''] = K_{aF}^{\circ}\, exp\,[-\Delta H_{aF}/k_B\, T] \tag{2.20}$$

where K_{aF}° value varies with the iron incorporation into the lattice. ΔH_{aF} values were determined to be around ~ 0.4 eV [53].

The electroneutrality condition in this case becomes:

$$[\mathrm{e}'] + 2\,[O_i''] = [h^{\cdot}] + 2\,[V_O^{\cdot\cdot}] \tag{2.21}$$

The main premise of this model is the systematic change in enthalpy of formation values in defect equilibria as a function of varying iron substitution. Electronic structure of end members $SrTiO_3$ and $SrFeO_{3-\delta}$ differ significantly, with a change from a non-degenerate semiconductor to metallic conductor [61]. As Fe concentration increases, the electronic states derived from Fe starts to overlap and form admixtures with O 2p valence states [295]. The model's predictions for charge diffusion behavior over STF have been consistent with experimental data in literature, yet further investigations may be required to confirm its exact validity [53,60]. Moreover, the model's assumptions of non-interacting defect centers and two different types of oxygen defects in a single oxygen ion sublattice are disputable.

Fig. 2.17 shows the development of conductivity with changing composition of STF. Although there are magnitudes of improvement in the conductivity with increasing Fe amount, conductivity profiles follow similar V-form for each composition. Only at very low

concentrations of Fe, the defect model for nominally undoped $SrTiO_3$ holds, since iron centers are too dilute to interact with each other and form degenerate electronic states.

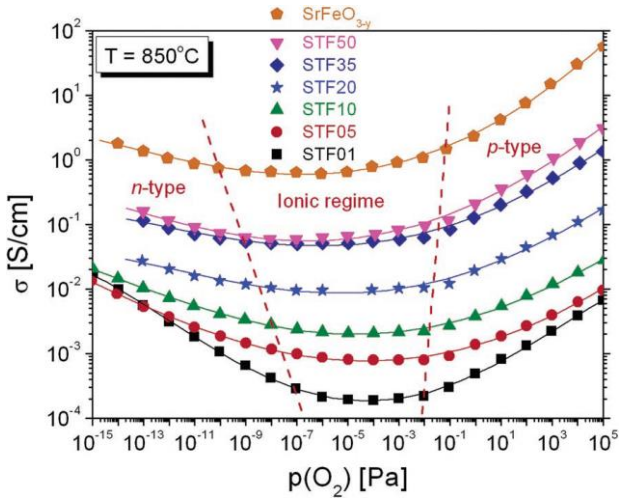

Figure 2.17: Electrical conductivities at T= 850 °C as a function of oxygen partial pressure, $p(O_2)$, given for of $SrTi_{1-x}Fe_xO_{3-\delta}$ with varying Fe substitution from 1 mol% (STF01) to 50 mol% (STF50) [53].

2.5.4 Donor substitution: Defect chemistry of $La_{1-y}Sr_yTiO_{3+\delta}$

As discussed on Chapter 2.2.2, donor substituted $SrTiO_3$ shows remarkable n-type conductivity upon thermal treatment in reducing conditions. This conductivity arises from the formation of additional free electrons as a result of titanium reduction. On the other hand, if the material is sintered under oxidizing conditions, then it does not undergo Ti reduction and hence shows insulating behavior. In this work, the focus is given on La-substituted strontium titanate (LSTO). However, disregarding some alterations due to size effects, same principles in defect mechanism upholds for substitution with other donors, such as Y and Nb [21,26].

Both for oxygen and cation stoichiometric LSTO, substitution of trivalent La ions in the divalent Sr sites leads to generation of additional strontium vacancies according to the equation:

$$La_2O_3 \xrightarrow{SrTiO_3} 2\,La_{Sr}^{\cdot} + V_{Sr}'' \qquad (2.22)$$

As mentioned in Chapter 2.5.2, interstitial oxygen is energetically unfavorable for this densely packed structure and therefore highly unlikely. Parallel to Eq. (2.13) given for nominally

undoped $SrTiO_3$, the simplified electroneutrality condition for La-substituted $SrTiO_3$ above 1000 °C can be written as:

$$[e'] + 2[V_{Sr}''] = [h^{\cdot}] + 2[V_O^{\cdot\cdot}] + [La_{Sr}^{\cdot}] \quad (2.23)$$

At highly reducing conditions oxygen vacancies exceed the amount of donors and the simplified electroneutrality condition becomes:

$$[e'] \cong 2[V_O^{\cdot\cdot}] \quad (2.24)$$

In agreement with the trend observed for nominally undoped $SrTiO_3$ at highly reducing conditions, the same $P_{O_2}^{-1/6}$ dependence of electronic conductivity is calculated for this regime by combining Eq. (2.8) and (2.24).

As the P_{O_2} increases oxygen vacancy concentration diminishes and the electronic conductivity becomes independent of oxygen partial pressure. For a given temperature, the electronic conductivity in this plateau region is solely dependent on donor concentration, given by:

$$[e'] \cong [La_{Sr}^{\cdot}] \quad (2.25)$$

Upon further pO_2 increase to mildly reducing or oxidizing conditions, the donor species are mainly counterbalanced by strontium vacancies (Fig. 2.18). Thus, the electroneutrality condition can be further simplified to:

$$2[V_{Sr}''] \cong [La_{Sr}^{\cdot}] \quad (2.26)$$

Combining Eq. (2.26) with (2.6) and (2.8), it can be deduced that the electronic conductivity shows a $P_{O_2}^{-1/4}$ dependence to the oxygen partial pressure at this pO_2 range. Fig. 2.18 depicts the n-type conductivity of donor substituted $SrTiO_3$ in the whole pO_2 range corresponding to metallic behavior in parallel with above calculations.

It should be noted that $P_{O_2}^{-1/4}$ dependence ascribed for relatively high pO_2 values does not uphold for A-site deficient LSTO, since in this case the excessive amount of strontium vacancies cannot be compensated by oxygen vacancies. The change in electronic conductivity then shows $\boldsymbol{\sigma} \propto P_{O_2}^{-1/6}$ behavior, in accordance with Eq. (2.8) [296]. Predicted enhancement of n-type conductivity with increasing donor substitution was confirmed experimentally by Marina et al. for the range $0.1 \leq x \leq 0.4$ in $La_ySr_{1-y}TiO_{3+\delta}$ lattice [80].

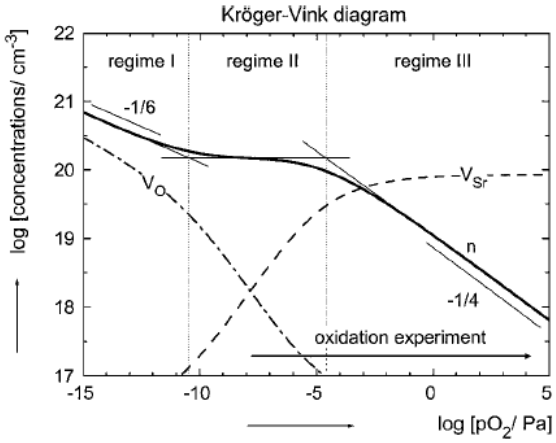

Figure 2.18: Calculated defect concentrations and evolution of conductivity as a function of pO_2 in 1.0 mol% donor substituted $SrTiO_3$ at 1400 °C [282].

At moderate temperatures (500 – 700 °C), strontium vacancies can be considered frozen-in and defect chemistry is mainly dictated by the effective donor concentration, $[D_{eff}^{\cdot}]$:

$$[D_{eff}^{\cdot}] = [La_{Sr}^{\cdot}] - 2[V_{Sr}^{''}] \tag{2.27}$$

In this case, only two different conductivity regimes are present in the whole pO_2 range. At reducing conditions, the electroneutrality condition given at Eq. (2.24) is preserved and the characteristic $\boldsymbol{\sigma} \propto P_{O_2}^{-1/6}$ behavior can be observed, whereas at highly oxidizing conditions a constant conductivity regime is predicted [282].

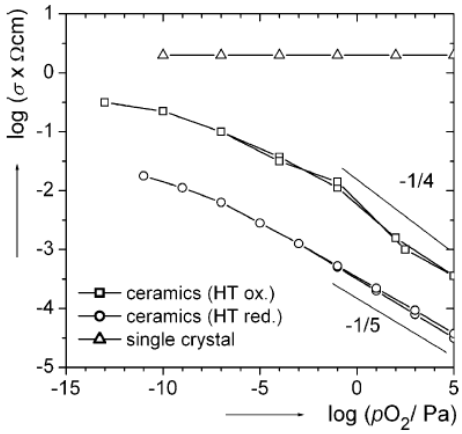

Figure 2.19: Evolution of conductivity as a function of pO_2 in 0.5 mol% La substituted $SrTiO_3$ at 850 °C [297]. HT ox and HT red refer to former high temperature treatment implemented under oxidizing and reducing conditions respectively.

Fig. 2.19 shows the moderate temperature conductivity profiles of donor doped $SrTiO_3$ samples which have undergone high temperature treatment at reducing and oxidizing conditions. Both materials show similar behavior, despite their differing absolute values of conductivity. This difference can be simply explained through the amounts of created strontium vacancies in the high temperature treatment and resulting effective donor concentration.

2.5.5 Donor/acceptor co-substitution: La/Fe- co-substituted $SrTiO_3$

Further complexity in the defect chemistry ensues with simultaneous co-substitution of non-dilute acceptor and donor species in $SrTiO_3$ lattice. Only few works attempted to identify the charge movement in such chemically complex systems.

Perry et al. investigated the defect model of STF with increasing donor substitution in oxidizing conditions [298]. Starting from the STF defect model of Rotschild et al. discussed in Chapter 2.5.3 [53], upon lanthanum substitution the electroneutrality condition expressed in Eq. (2.21) becomes:

$$[\mathrm{e}'] + 2\,[O_i''] + 2\,[V_{Sr}''] = [h^{\cdot}] + 2\,[V_O^{\cdot\cdot}] + [La_{Sr}^{\cdot}] \tag{2.28}$$

Fig. 2.20 shows the concentration of defect species for $(La,Sr)Ti_{0.65}Fe_{0.35}O_{3-\delta}$ at 600 °C in oxidizing conditions given as a function of La substitution predicted for two separate partial Schottky enthalpies, 2.5 eV and 1.5 eV respectively. For each case, the concentration where $[La_{Sr}^{\cdot}]$ surpasses Fe amount ($[La_{Sr}^{\cdot}] \geq [Fe]$), i.e. total oxygen interstitial sites, represents a transition in the concentration of defect species. For $\Delta H_{Sch} = 2.5\,eV$, a significant drop in hole concentration is expected, which in turn would induce a transition from p-type to n-type conductivity for the material. However, the conductivity measurements in the work of Perry et al. showed a better fit with a lower partial Schottky value, $\Delta H_{Sch} = 1.5\,eV$, as no n-type conductivity was determined experimentally even at high $[La_{Sr}^{\cdot}]$ values [298]. Increasing La substitution suppressed Fe^{4+} sites and p-type conductivity, but did not induce n-type behavior. They concluded that with increasing La-substitution, the donors were compensated with oxygen interstitial sites accompanied by a decrease in oxygen vacancy and hole concentration up to $[La_{Sr}^{\cdot}] \cong [Fe]$ and as the filling of oxygen interstitials approach saturation, more energetically costly cationic vacancies may be formed to compensate the additional charge. The authors however could not conclusively identify the origin of the defect behavior upon

changing donor concentration and speculated other factors rather than cationic vacancies, such as gradual change in reduction enthalpy may be playing a role in the retained p-type conductivity under oxidizing conditions. Moreover, considering the best fitting model in this work employed significantly lower ΔH_{Sch} than of experimentally determined enthalpies for partial Schottky formation, further studies are clearly necessary in order to better understand the defect behavior of chemically complex systems such as (La,Sr)(Ti,Fe)$O_{3\pm\delta}$ (LSTF) with non-dilute substitution. Fig. 2.21 roughly illustrates the trends in concentration of charge carrier species, stability and chemical expansion properties as a result of variation of La : Sr : Ti : Fe ratios in the perovskite lattice.

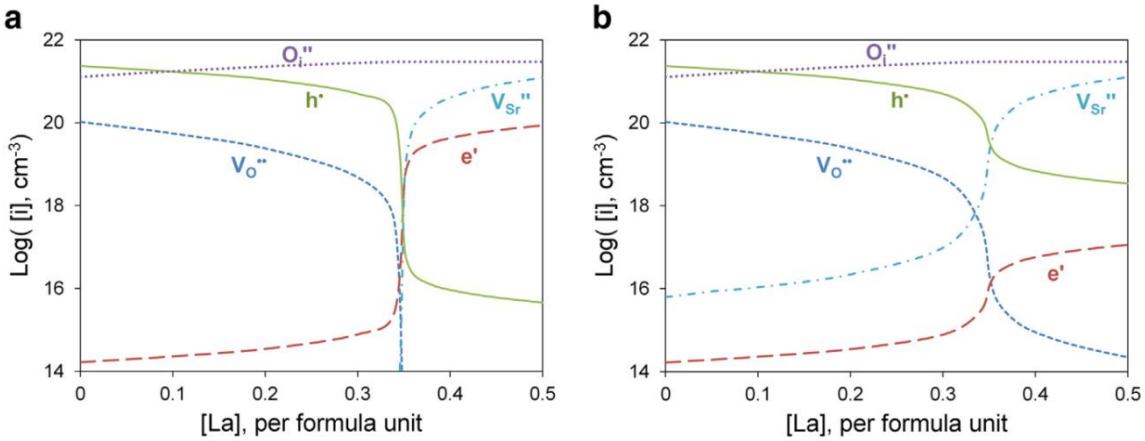

Figure 2.20: The concentration of defect species for (La,Sr)$Ti_{0.65}Fe_{0.35}O_{3-\delta}$ at 600 °C in oxidizing conditions given as a function of La substitution in lattice predicted for (a) $\Delta H_{Sch} = 2.5\ eV$ (b) $\Delta H_{Sch} = 1.5\ eV$ [298].

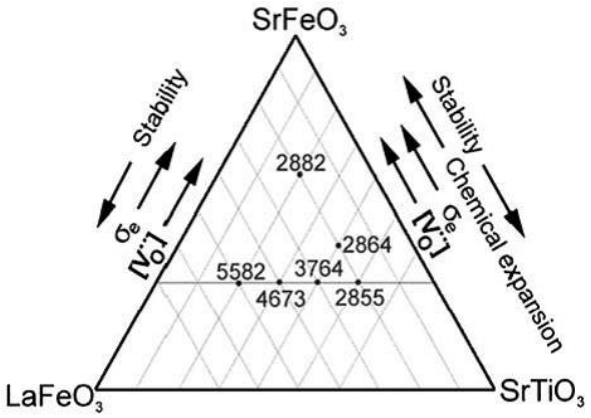

Figure 2.21: Pseudo ternary phase diagram showing evolution of stability and defect properties with variation of cations in LSTF lattice [83].

Chapter 3

Physical Methods

In this chapter, the fundamental principles of the analytical methods employed in characterization of perovskite oxides with regards to their applications in environmental catalysis are briefly summarized.

3.1 Gas physisorption

Gas physisorption is one of the most widespread used experimental methods for characterization of porous surfaces. It allows evaluation of porous features in a wide size range from micropores (below 2 nm) to mesopores (between 2 – 50 nm) and even macropores up to 100 nm [299,300]. Mesoporous oxides are most commonly characterized by nitrogen sorption analysis performed at the boiling point of nitrogen (77 K). Nitrogen is widely employed in physisorption analyses due to its suitable size, abundance and non-reactivity.

In a physisorption experiment, a known quantity of non-reactive gas (adsorptive) is admitted on the surface of the investigated solid (adsorbent). Due to weak dipole-dipole and van der Waals forces, physical adsorption on the solid surface takes place and the adsorptive is removed from the gas phase gradually. The fluid in the adsorbed state is then called the adsorbate.

By recording the gradual uptake (adsorption) and release (desorption) of gas in equilibrium conditions a physisorption isotherm can be constructed. The isotherms commonly illustrate the volume of adsorbed/desorbed gas as a function of relative pressure from vacuum conditions up to saturation vapor pressure of the adsorptive, i.e. atmospheric pressure when the experiment takes place at the boiling point of the adsorptive).

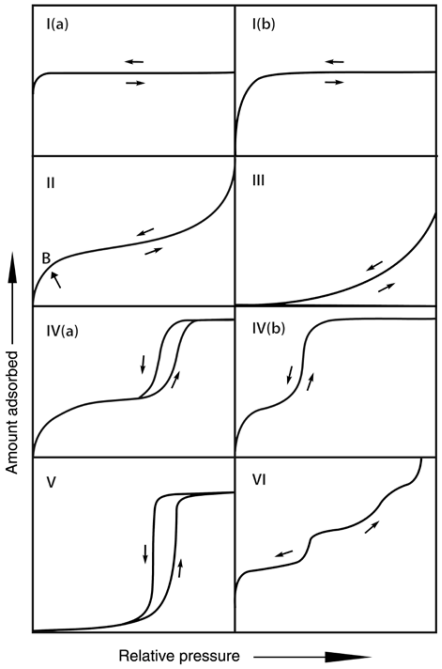

Figure 3.1: Classification of physisorption isotherms [299].

Porous features of the solid can be determined in detail by employing the well-established adsorption-desorption models on the obtained isotherm. Majority of physisorption isotherms can be classified in one of the six main types shown on Fig 3.1 according to IUPAC recommendations [299].

Type I (a) and type I (b) isotherms, which are characterized by adsorbate uptake at very low relative pressures, are characteristic of microporous solids with relatively small external surface (e.g. zeolites, metal-organic frameworks). The pore width is typically around ~ 1 nm in the case of type I(a), whereas type I(b) isotherms are associated with a broader pore size distribution with possible presence up to ~ 2.5 nm diameter pores. Type II isotherms, typical of macroporous or nonporous adsorbents, are described by unrestricted monolayer-multilayer adsorption. In this isotherm type, an initial sharper slope (up to point B in Fig. 3.1) would be due to complete monolayer coverage before multilayers are formed. Type III and type V isotherms indicate weakly interacting adsorbate-adsorbent species. The former curve is given for a macroporous/non-porous sample, whereas the latter is observed for microporous-mesoporous adsorbents. Such isotherm shape can be physically explained by the clustering of adsorbed molecules around the relatively more favorable sites on the adsorbent surface. Type VI isotherms describe a stepwise multilayer adsorption on a uniform non-porous adsorbent.

The isotherms of mesoporous solids in most cases are characterized as type IV. In this type, an initial monolayer-multilayer adsorption as observed for type II isotherms is followed by capillary condensation in mesopores usually accompanied by a hysteresis. Materials with very narrow mesopores may not lead to a hysteresis depending also on the adsorbate used as well as shape of the pores [301,302]. Shape of the hysteresis loops can give insights on the mesostructured (Fig. 3.2). Hysteresis loop H1 corresponds to a narrow size distribution of uniform mesopores, whereas H2 is usually given for less defined pore structures (e.g. ink-bottle pore shape). H3 and H4 hysteresis loops indicate slit-like pores observed in different material morphologies. H5 type loop is rarely observed and it is associated with a combination of open and partially blocked mesopores.

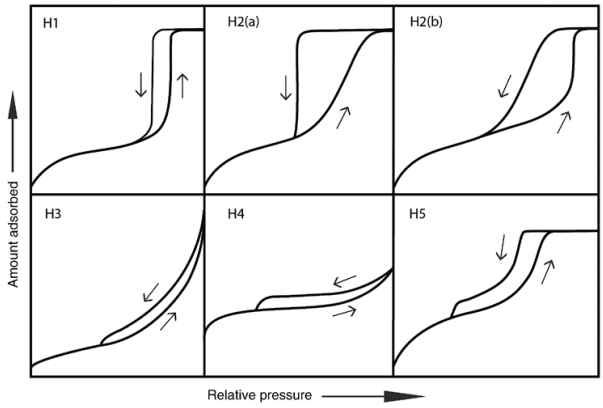

Figure 3.2: Different types of hysteresis loops [299].

Brunauer-Emmet-Teller (BET) method is commonly employed to determine the surface area of obtained physisorption isotherms [303]. Number of adsorbed gas molecules on the first monolayer is multiplied by the cross-sectional area of one gas molecule to estimate the BET surface area. For this purpose, the isotherm is transformed into a BET plot to solve following equation:

$$\frac{p/p^0}{n\,(1-p/p^0)} = \frac{1}{n_m\,C} + \frac{C-1}{n_m\,C}\,p/p^0 \qquad (3.1)$$

where p/p^0 is the relative pressure, n is the amount of adsorbed gas molecules, C is the BET constant dependent on adsorbent-adsorbate interactions and n_m is the specific monolayer capacity. Eq. (2.1) is solved in the linear range of the BET plot which is usually given within the p/p^0 values between 0.05 – 0.30 for mesoporous/macroporous materials. Pore filling may

be already taking place at these relative pressures for microporous solids and thus further considerations may be necessary before implementing the method to estimate surface area of microporous materials [304].

Once the specific monolayer capacity, n_m, is calculated, BET surface area, S_{BET} is given by the following equation:

$$S_{BET} = n_m \, a_m \, N_A \tag{3.2}$$

where, N_A is Avogadro constant and a_m is cross-sectional area of the gas molecule. For N_2 at 77 K, this value is given as 0.176 nm^2 [299].

The total pore volume, V_p, of mesoporous adsorbents can be estimated directly from the amount of adsorbed gas in plateau region at relative pressures close to unity [300,305]. If the mesoporous material also contains macropores, such horizontal region is not present and total pore volume cannot be evaluated directly.

Pore size distribution of mesoporous adsorbents are investigated by analyzing the capillary condensation at the mesopores, since surface tension of the condensed fluid and curvature of the liquid meniscus is strongly dependent on pore geometry. Several models were proposed based on the gas-liquid phase thermodynamics of the adsorbate species. Among them, NLDFT (Non-local DFT) model is widely used and gives decent estimations of pore size distribution for a wide range of mesostructures upon proper choice of surface structure and pore geometry parameters for the applied fit [302,306].

3.2 X-ray diffraction

The interference phenomenon of X-rays passing through a crystalline solid was first demonstrated by Max von Laue in 1912 at the Bavarian Academy of Science [307]. Shortly thereafter William Henry and William Lawrence Bragg, father and son, could identify the theoretical principles underlying the formation of a diffraction pattern by the – now well-known – Bragg condition [308]. The discovery led to a huge sensation earning Laue and the Braggs the Nobel Prize in Physics on 1914 and 1915 respectively. Today, X-ray diffraction (XRD) is one of the most fundamental tools in characterization of long-range ordered solids (about 95% of all solid materials), since each crystalline substance forms a unique diffraction pattern [309].

Crystalline materials are composed of periodically arranged atoms with an interatomic spacing similar to the wavelength of the X-rays (~ 1 Å) [310]. When an incident X-ray beam impinges on a crystalline solid a constructive or destructive interference occurs. The condition for constructive interference is given by the Bragg equation [311]:

$$n\,\lambda = 2d\,sin\theta \tag{3.3}$$

where λ is the wavelength and θ is the angle of the incident radiation, d is the interplanar spacing and n is an integer representing the order of reflection given for the different crystal planes. The X-rays impinging on the crystal in a way that fulfills the Bragg condition is illustrated in Fig. 3.3. When the condition is not met, the interference of the scattering beams leads to zero overall intensity. By scanning the crystalline specimen over a range of specular angles, the diffraction pattern specific of the material can be constructed.

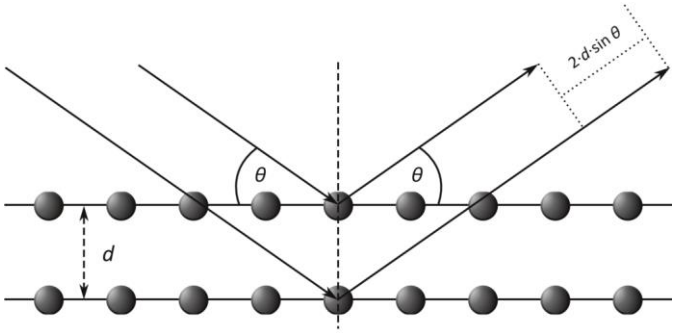

Figure 3.3: Schematic representation of X-rays diffracting on crystal planes to create constructive interference [312].

If the acquisition is done at 2θ < 5°, the technique is called small angle X-ray scattering (SAXS), which can provide information on particle shape, size and porosity. Wide angle X-ray scattering (WAXS) is collected usually within angles 5° > 2θ > 80°. Analysis of peak positions in WAXS reveals the unit cell geometry and symmetry group of the crystalline material. Moreover, crystallite size of the specimen can be calculated by using the Scherrer equation [313,314]:

$$D_{hkl} = \frac{k\,\lambda}{\beta_{hkl}\,\cos\theta} \tag{3.4}$$

where, D_{hkl} is the crystallite size, k is the so-called shape factor which is generally approximated to 0.9, λ is the wavelength of the X-ray radiation impinging over the crystal,

β_{hkl} is the diffraction broadening obtained by acquiring the full-width at half maximum (FWHM) value of the investigated XRD signal with Miller indices hkl given in radians, and finally θ is the Bragg angle given for the peak position. Miller indices describe the different planes of atomic order in the lattice.

For solid solutions that involve multiple constituents, Vegard's law is commonly followed with regard to lattice parameter determined from XRD analysis. This empirical rule postulates that lattice parameters vary linearly with composition in a continuous substitutional solid solution with following equation [315]:

$$a_{A_{(1-x)}B_x} = (1-x)a_A + xa_B \tag{3.5}$$

where, a is the lattice parameter of constituents A and B as well as substitutional solid solution $A_{(1-x)}B_x$. Positive and negative deviations from Vegard's law is common, and this rule should be considered as an approximation which holds for ideal solid solutions with less than 5% difference in the lattice parameters of its pure constituents A and B [316].

3.3 Electron Microscopy

Conventional light microscopes are limited in their resolution by the wavelength of the probing visible radiation. Electron microscopes are analogous to light microscopes in their working principle while achieving sub-Ångstrom level resolutions by probing the specimen with high-energy electrons.

The wave-like characteristics of electrons were first proposed by de Broglie in 1924 with an equation that relates the particle momentum to its wavelength:

$$\lambda = \frac{h}{mv} \tag{3.6}$$

where, λ is the so-called de Broglie wavelength, h is Planck's constant, m is the mass and v is the speed of the particle. This equation shows that electrons can possess wavelengths well smaller than of the size of atoms within the specimen if they are sufficiently fast. For example, an electron source employing a 300 kV accelerating voltage is capable of producing electrons with ~ 2 pm wavelength [317]. Achievable accelerating voltages are in the range of 100 – 300 kV for most modern TEM instruments [318].

A V-shaped filament with a tungsten tip is commonly employed to produce the electron beam. Electrons are accelerated by applying a potential between the cathode filament and the anode plate while heating the tungsten tip, so that a stream of electrons from the cathode towards the anode plate is generated. The shape and the trajectory of the electron beam are then controlled through a series of electromagnetic and electrostatic lens system controlled by lens currents. Finally, different type and position of detectors can be employed to analyze generated signals shown in Fig. 3.4 that are characteristic of the material.

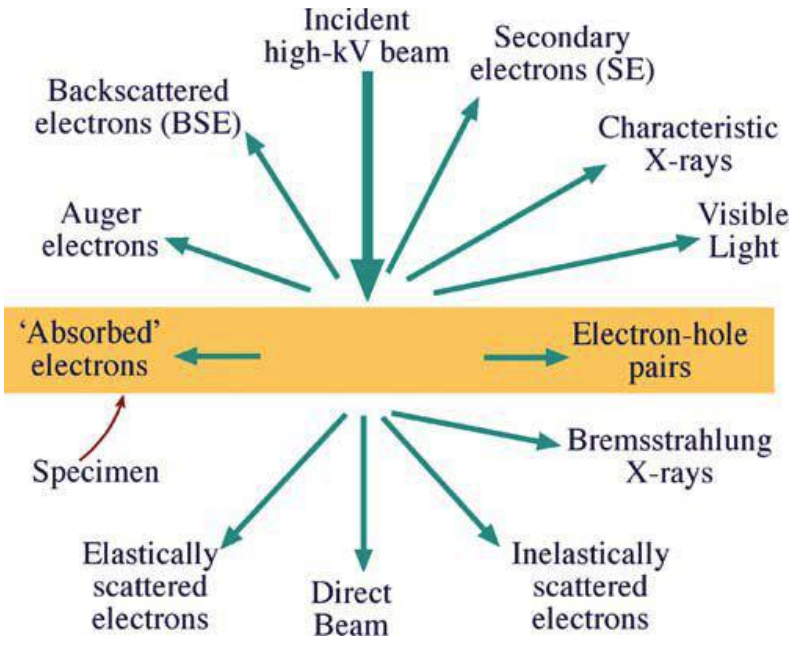

Figure 3.4: Signals generated by the interaction of a high-energy electron beam with the specimen [317].

3.3.1 Transmission Electron Microscopy

Transmission electron microscopy (TEM) makes use of transmitted electrons through a very thin specimen to form the image. The transmitted beam is further magnified by a series of electromagnetic lenses and projected on a screen often in real time using a CCD (charge-coupled device) camera. The amount of transmitted electrons is inversely proportional with the sample thickness. Thus, thicker portions in the specimen would appear darker in the 2D projected image. The contrast of the final image is also influenced by coherent diffraction and the phase contrast as a result of interference between diffracted electrons.

The image contrast can be better controlled by employing the instrument in STEM (scanning transmission electron microscopy) mode. In this mode, a highly focused electron beam (< 0.2 nm) is scanned over the sample in a raster form. By appropriate positioning of the high-angle annular dark field (HAADF) detector, inelastically scattered electrons can be analyzed to form an image with enhanced mass contrast dependent on atomic number of analyzed species [318].

The TEM image simultaneously contains information on the elastically scattered electrons by the specimen. Thus, the electromagnetic lens system can be easily manipulated to project the image in reciprocal space and produce a diffraction pattern. This so called diffraction mode is an invaluable tool to obtain information on the crystal phase from a localized area in the specimen, e.g. a single crystallite [317].

Although TEM is a very powerful tool for characterization of nanoporous materials, its working principles contain inherent limitations. Firstly, since the information is obtained from a spatial area of only few nanometers, interpretation of overall material properties should be only made with supplementation of other bulk characterization tools. Moreover, since specimen thickness should not surpass few hundred nanometers, sample preparation can be a complex procedure [319]. Finally, the benefits of using the technique should be justified considering the tradeoff from the extensive operation costs due to high-vacuum and high-energy source requirements of the instrument.

3.3.2 Scanning Electron Microscopy

In contrast to TEM, scanning electron microscopy (SEM) analyzes the electrons emitted from the specimen to construct the image. Similar to STEM, a focused electron beam is scanned line by line over a rectangular raster pattern of the specimen surface in SEM. The secondary electrons emitted by the excited atoms as a result of primary electron illumination are identified by detectors and digitally converted to an image illustrating surface topography. Since the secondary electrons are low in energy, only electrons emitted from first few nanometers over the sample surface are detected.

Alternatively, elastically scattered electrons out of the sample surface can be analyzed to construct an image sensitive to chemical composition. The enhanced mass contrast in this case is due to heavier elements back-scattering more strongly than light elements, leading to brighter spots in the final image. The image resolution in SEM is dependent on the size of the

incident electron beam. SEM electron source commonly operates with an accelerating voltage between 1 – 30 kV and the maximum achievable spatial resolution is ~ 1 nm [317]. Despite its relatively low resolution, SEM images can be acquired from large areas enabling better sampling compared to TEM. Moreover, since SEM does not operate in transmission mode, the analyzed samples don't have any thickness requirement, though they should be sufficiently conductive.

3.3.3 Energy Dispersive X-ray Spectroscopy

Spectroscopic methods commonly accompany electron microscopy through analyzing different signals that arise from the electron illumination of the specimen. Energy dispersive X-ray (EDX) spectroscopy can be employed in this respect to obtain information on the elemental composition of the sample. When a focused electron beam impinges at the specimen, the atoms within the sample may be excited to emit an electron from their inner electron shells. In such case, an electron from the outer shell with higher energy fills the inner shell and its excess energy is released in the form of X-rays with an energy that is characteristic to the element.

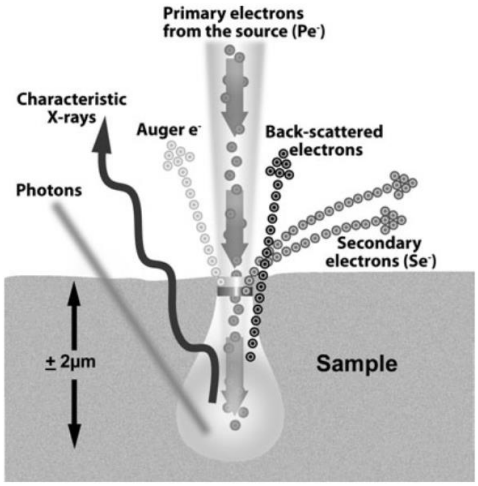

Figure 3.5: The interaction volume and signals generated from different regions in an SEM experiment [320].

X-ray detectors based on silicon semiconductors are typically employed to convert the photon energy to voltage signal. The accuracy of the technique and the spatial resolution depends on a variety of parameters; such as nature of the specimen, incident beam energy and detector

sensitivity. In practice, all major elements having atomic numbers 4 to 92 can be successfully quantified with typically less than 2% error [310]. The penetration depth of which the elemental composition is investigated commonly varies between a few hundred nanometers to few microns (Fig. 3.5). Better spatial resolution can be obtained when EDX spectroscopy is coupled with TEM on a thin specimen, but in this case beam damage by the high energy electrons should be also considered. Elemental mapping of the investigated samples are acquired by employing EDX spectroscopy in combination with SEM or STEM [321].

3.4 X-ray Photoelectron Spectroscopy

X-ray photoelectron spectroscopy is a close relative to the EDX spectroscopy, employed to investigate the elemental composition and chemical character of the sample surface [318,322]. In contrast to EDX spectroscopy, the signal in XPS is due to the release of electrons from the material as a result of x-ray photons impinging at the sample. Since the energy of incident photons from a monochromatic source are known, the binding energy of electrons, E_b, reaching the detector can be determined based on the equation:

$$E_b = hv - (E_k + \Phi) \tag{3.7}$$

where hv is the photon energy, E_k is the kinetic energy of the electrons reaching the detector and Φ is the work function required to bring the electron from the material's Fermi level to the vacuum. The kinetic energy distribution of emitted electrons is measured by an energy analyzer to calculate the binding energies given in the spectrum. As the binding energy is specific to the element as well as its local chemical environment; information on the type of elements, their oxidation number and the bonding hybridization with the nearest neighbor atoms can be obtained by XPS. The technique is very surface sensitive with an information depth of 1 – 10 nm, since only the electrons from the top few atomic layers have enough energy to escape the material.

3.5 Ultraviolet and Visible Spectroscopy

Ultraviolet-visible (UV-Vis) spectroscopic analysis is based on absorption or reflection of electromagnetic radiation through a specimen from ultraviolet to visible spectral range [323,324].

Energy of a photon, E_P, is directly proportional to its wavelength, λ (frequency, $v\ \alpha\ \frac{1}{\lambda}$):

$$E_P = hv = \frac{hc}{\lambda} \tag{3.8}$$

where, c is the velocity of light ($2.998\,x\,10^8$ m s^{-1}). A small wavelength range of approximately 400 – 800 nm constitutes the spectra visible to human eye, whereas higher energy photons with wavelength between 10 – 400 nm (Fig. 3.6) make up the ultraviolet radiation range. Absorption of UV-Vis photons can promote electronic transitions in the atoms and molecules from lower to higher energy levels (Fig. 3.7). Since the energy levels of the atomic and molecular orbitals are quantized, only a precise amount of photonic energy will be absorbed to induce an electronic transition.

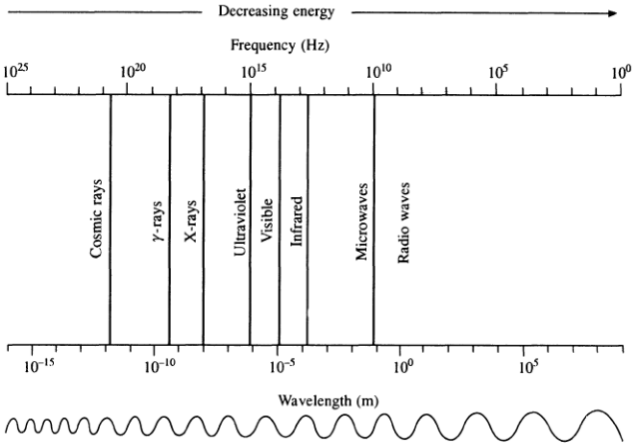

Figure 3.6: The electromagnetic radiation spectrum [324].

UV-Vis spectroscopy measures the fraction of absorbed photons passing through a sample as a function of their wavelength, usually in the form of transmittance, T:

$$T = \frac{I}{I_0} \tag{3.9}$$

where, I_0 and I are the intensity of incident and transmitted radiation respectively. The transmittance amount is inversely proportional to the concentration of the substance in the solution as well as optical path length. Beer-Lambert law describes this relation by employing absorbance, A [325]:

$$A = -\log T \; = \; \varepsilon \, c \, I \tag{3.10}$$

where, ε is molar extinction (absorptivity) characteristic of the material (in M^{-1} cm^{-1}), c is concentration in solution (in M) and I is the optical path length (in cm).

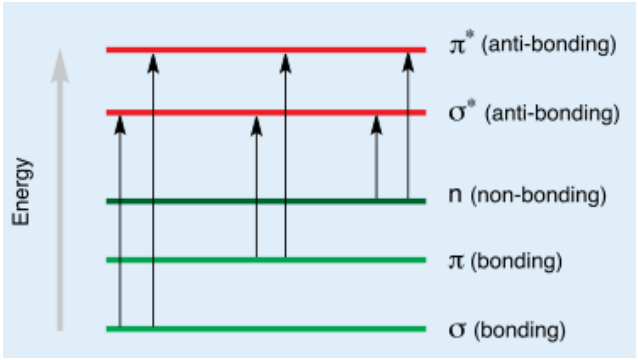

Figure 3.7: Possible electronic transitions induced by UV-Vis radiation [323].

UV-Vis spectroscopy can provide insights on the chemical composition as well as presence of functional groups and conjugation within the analyzed sample. Moreover, precise quantitative analysis of UV-Vis active molecules can be employed following Beer-Lambert law.

When UV-Vis radiation impinges on powdered solids, a significant portion of the light is scattered in different directions due to surface roughness (diffuse reflectance) [326]. In this case, the absorbance cannot be accurately assessed. In order to overcome this limitation, UV-Vis spectrometer can be operated in diffuse reflectance mode where the diffuse reflected beams are simultaneously detected and the reflectance of the sample with respect to a non-absorbing reference is scanned. Subsequent to data acquisition, the optical properties of the powdered sample are commonly determined by employing the Kubelka-Munk model [327–329]. This model assumes infinitely thick sample with particle size smaller or equal to the wavelength of the incident radiation. The Kubelka-Munk function, F(R) is then given as:

$$F\,(R) = \frac{(1-R)^2}{2R} \tag{3.11}$$

where, R is the measured reflectance. Once the reflectance values are converted to $F\,(R)$, the band gap – absorption strength relation given for a direct allowed electronic transition proposed by Tauc et. al can be exploited to calculate the band gap of the material [330,331]:

$$\alpha h\nu = A_1\,(h\nu - E_{BG})^{0.5} \tag{3.12}$$

where, $h\nu$ is the photon energy, α is the absorption coefficient of the material, E_{BG} is the band gap and A_1 is a proportionality constant. Since absorption coefficient, α, is proportional to the Kubelka-Munk function, $F\,(R)$, Eq. (3.11) can be rewritten as:

$$|F(R)\,h\nu|^2 = A_2\,(h\nu - E_{BG}) \tag{3.13}$$

where A_2 is a proportionality constant. The linear region of the curve is extrapolated in the so-called Tauc plot which depicts the change of $|F(R)\ h\nu|^2$ against photon energy ($h\nu = \frac{1239.7}{\lambda}$ eV). The band gap value, E_{BG}, is then given for the solution of the linear fit curve where y-axis approaches zero. This value is a crucial characterization parameter for semiconductor photocatalysts, since it determines the energy of photons required to activate the photocatalytic reaction.

3.6 Infrared Spectroscopy

Infrared (IR) spectroscopy investigates the interaction of the matter with electromagnetic radiation in the infrared spectral region covering the wavelengths between 800 nm to 1000 μm (Fig. 3.6) [332–334]. Infrared photons are not energetic enough to induce electronic transitions, but they are capable of causing changes in the quantized vibrational and rotational energy levels of the molecule. These vibrational and rotational modes correspond to different movement of the molecule, such as bending, stretching, scissoring, rocking and twisting. They are characteristic to the functional groups present in the sample and thus IR spectroscopy provides fingerprint information to identify the chemical composition of the material. Fig. 3.8 depicts the common IR modes arising from the characteristic functional groups.

All molecules that are capable of producing a change in their dipole moment when they vibrate are IR active. The number of vibrational modes in a molecule with n atoms are given as 3n-6, since the molecule have 3n degrees of freedom in total of which three degrees of freedom describe the translation and another three describe the rotation of the molecule itself. For linear molecules the number of vibrational modes is 3n-5 considering in this case only two degrees of freedom describe the rotation of the molecule.

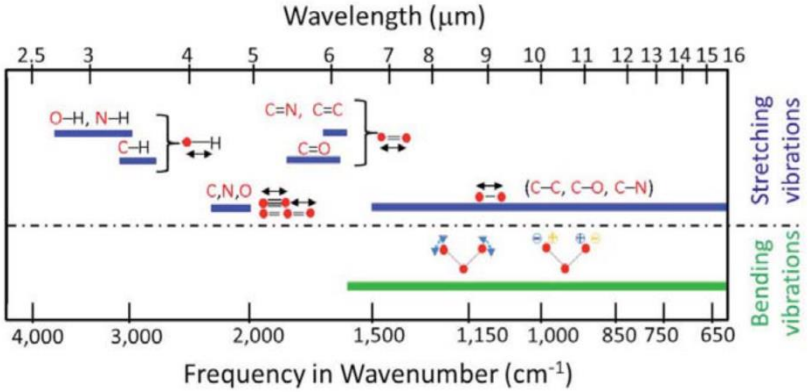

Figure 3.8. Common characteristic IR modes and their position in cm^{-1} [335].

3.7 Electrochemical Impedance Spectroscopy

Electrochemical impedance spectroscopy (EIS) is a powerful experimental method to analyze dynamics of electrochemical processes as well as electronic properties of the material that measures the system response to a perturbation as a function of frequency [336]. The measurements can be carried out in different atmospheres and temperatures to enable understanding of complex electrochemical phenomena that are atmosphere and temperature dependent. Although, the fundamental principles of EIS is known since Nernst's experimental work in 1894, complex data processing and analysis requirements prevented its widespread implementation as a common research tool until early 1990s when computer controlled digital systems became available [337,338].

In a typical potentiostatic EIS experiment, a small amplitude AC voltage is applied on the system under study and the induced current is measured as a function of frequency. Alternatively same experiment can be performed with galvanostatic EIS, in which the voltage response of the system due to the induced current is measured. Usually AC voltage is applied on top of a constant DC bias. The response of the electrochemical systems to applied voltage is intrinsically nonlinear, however by employing small amplitudes of AC voltage, pseudo-linear response can be obtained. The applied voltage, $V(\omega, t)$, and induced current $I(\omega, t)$ as a function of time and angular frequency, can be described by following equations:

$$V(\omega, t) = \bar{V} + \hat{V} \sin(\omega t) \tag{3.14}$$

$$I(\omega, t) = \bar{I} + \hat{I} \sin(\omega t - \phi) \tag{3.15}$$

where, $\bar{V}$ and $\bar{I}$ are DC voltage and current values, $\hat{V}$ and $\hat{I}$ are amplitudes of applied AC voltage and current, ω is the angular frequency ($\omega = 2\pi f$ where f is the variable frequency expressed in Hz units), and ϕ is the phase difference between voltage and current. The phase difference can be expressed as shown in Fig. 3.9. In the pseudo-linear system, applied potential induces a current response of the same frequency with shifted phase given by angle ϕ [339].

The impedance, Z, can be described as the frequency dependent resistance of the system and given by Ohm's law which is commonly used in DC circuits:

$$Z(\omega, t) = \frac{V(\omega,t)}{I(\omega,t)} \tag{3.16}$$

By making use of complex number notations, the AC terms in Eq. (3.14) and (3.15) can be rewritten as:

$$V\ (\omega, t) = \ \hat{V} e^{i\omega t} \tag{3.17}$$

$$I\ (\omega, t) = \ \hat{I} e^{i(\omega t - \phi)} \tag{3.18}$$

where, i is the imaginary unit. Considering these expressions of current and voltage, Eq. (3.16) can be rewritten in the form:

$$Z\ (\omega, t) = \frac{V\ (\omega,t)}{I\ (\omega,t)} = \ \frac{\hat{V}}{\hat{I}}\ e^{i\phi} = \ |Z|\ e^{i\phi} \tag{3.19a}$$

where, $|Z|$ is the so-called impedance modulus. This equation can be further reformulated using Euler's relation :

$$Z\ (\omega, t) = \ |Z|\ e^{i\phi} = \ |Z|\ (\cos\phi + i \sin\phi) = Z'(\omega) + \ iZ^{"}(\omega) \tag{3.19b}$$

where Z' and $Z^{"}$ are respectively the real and imaginary parts of the measured impedance.

In an EIS experiment, obtained impedance data is represented either as a Nyquist or Bode plot. Nyquist representation plots Z' as a function of $Z^{"}$, whereas in Bode representation frequency dependence is clearly shown by plotting $\log|Z|$ and ϕ as a function of $\log f$ [336].

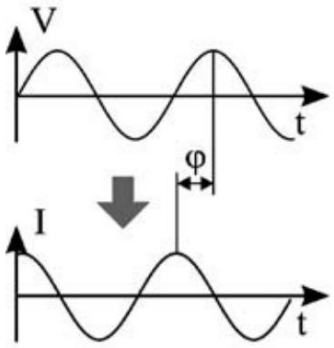

Figure 3.9: Current response to applied sinusoidal voltage in a linear system [340].

EIS experiments can be conducted with varying electrode configurations, the simplest being the two-electrode configuration with a working electrode and a counter electrode. In this case, the measured impedance would include contributions from both electrode-sample interface sites. It can be useful to add a third electrode as reference to eliminate contribution from the

counter electrode. The addition of further electrodes can in general improve the precision of the measurement at the cost of added complexity. Therefore, experimental setup should be carefully chosen based on the desired material properties to be analyzed.

In addition to providing linear response to perturbation, measured system should fulfill causality, stability and finiteness conditions: The response of the system should be only dependent on applied perturbation, should be constant with time and finite in the whole frequency range with regard to both real and imaginary parts. The fulfillment of these conditions can be tested by Kramer-Kronig relations, which enable obtaining real or imaginary component of the impedance as a function of the other component [341,342].

Interpretation of the data is realized by fitting the obtained spectra to a model circuit with proper choice of electrical elements that describe the electrochemical phenomena taking place at the measurement conditions. In order to make a physically meaningful assignment, some knowledge of sample properties as well as the nature of possible electrochemical processes would be required.

Most common circuital elements are resistors, capacitors and inductors. Resistor, R, describes current response in phase with sinusoidal voltage ($\phi = 0$), so that Eq. (3.19) becomes:

$$Z_R\,(\omega, t) = \frac{V\,(\omega,t)}{I\,(\omega,t)} = \frac{\hat{V}}{\hat{I}} = R \tag{3.20}$$

In the case of a capacitor with capacitance C, current response is out of phase with respect to sinusoidal voltage ($\phi = -\pi/2$), leading to the relation:

$$Z_C\,(\omega, t) = \frac{1}{i\omega C} \tag{3.21}$$

The capacitor behaves as a pure imaginary component with a phase angle $-\pi/2$, whereas the inductor with inductance L, is a purely imaginary component with phase angle $\pi/2$:

$$Z_L\,(\omega, t) = i\omega L \tag{3.22}$$

Other less common circuital elements can be further introduced to the system in order to describe particular electrochemical phenomena. Once the model is determined, the total impedance is given by each individual contribution of electrical elements depending on their combination. In Fig. 3.10, a simple two resistor setup connected in series and in parallel is

depicted. In the case of serial connection, the total impedance is given by addition of each element, whereas in parallel connection, inverse of the individual impedance values (i.e. admittance) is additive for the total.

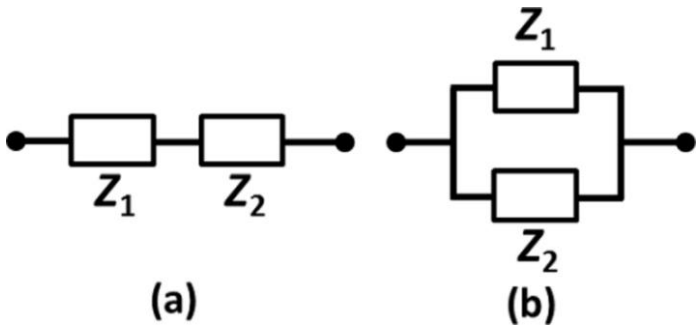

Figure 3.10: Electrical circuit formed by combination of resistors (a) in series (b) in parallel [339].

3.8 Nuclear Magnetic Resonance Spectroscopy

Nuclear magnetic resonance (NMR) spectroscopy is a technique that exploits the characteristic spin interactions of the nuclei in the analyzed material to give information on the material's unique structure and chemical environment [343–345].

Atomic nuclei are spinning charged particles with their own magnetic moments. The spins are in random directions in the absence of an external magnetic field. If the number of neutrons and protons in the elemental isotope are both even numbers, there is no net spin and thus these isotopes are NMR-inactive (e.g. ^{12}C, ^{16}O).

When a magnetic field is applied the nuclei energy states split and align either in same or opposite direction to the field with an energy difference that increases with increasing strength of the external magnetic field. The energy difference between spin states are typically in the energy range of radio frequency electromagnetic radiation (Fig. 3.6).

In an NMR experiment, an electromagnetic radiation pulse in radio frequency range is sent to the investigated nuclei within a strong homogeneous external magnetic field. When the frequency of the radiation matches the energy difference between the lower and higher energy spin states, a resonance condition occurs where the proton from lower energy spin state absorbs the radiation and flips to the higher energy spin state. Upon relaxation, the nuclei return to their original state, thereby emitting electromagnetic signals which are detected to

record a free-induction decay (FID) plot. Finally, the NMR spectrum showing intensity of the signals as a function of chemical shift is obtained by converting the FID signal to frequency domain. The chemical shift value is expressed as the difference in resonance frequency of the investigated nuclei from a reference standard, usually tetramethylsilane (TMS).

The position and shape of the peaks are dependent on the electron density surrounding the nuclei as well as the orientation and bonding of the neighboring nuclei. Since electrons also align in opposite direction to the external magnetic field, they induce a shielding effect on the nucleus requiring increasing field strength (or decreasing radio wave frequency) to achieve resonance condition with increasing electron density. Thus nuclei in highly shielding environment are positioned on the higher field (right) side of the spectrum. The orientation of the neighboring nuclei on the other hand can cause splitting of the NMR signal as a result of J-coupling.

In contrast to solution NMR spectra where anisotropic interactions do not affect the spectra due to rapid random tumbling, in solid state NMR, anisotropic and orientation dependent interactions can dominate the spectrum. In order to minimize the influence of these interactions on the resulting NMR spectra several methods were developed.

Magic angle spinning (MAS-NMR) is such a method which is commonly implemented to analyze solids [345,346]. In this method, the sample is spinned at a high rate (20 – 50 kHz) at a specific (magic) angle $\theta_{MAS} = 54.74$ with respect to the external magnetic field direction. In these conditions, the contribution to the NMR signals from the anisotropic nuclear magnetic interactions can be greatly reduced. Further enhancement of the signal can be achieved by implementing cross-polarization (CP-MAS NMR Spectroscopy) between different nuclei in the pulse sequence.

3.9 ^{57}Fe Mössbauer Spectroscopy

Mössbauer Spectroscopy is a versatile method which can provide precise information on the local chemical environment as well as magnetic properties of the analyzed system [322,347]. The technique is similar to NMR spectroscopy in that the minuscule shifts in the energy levels of the atomic nuclei in response to excitation are analyzed.

Similar to a gun firing bullets, a free nucleus recoils when it emits or absorbs gamma rays and nuclear resonance cannot be observed. When the nuclei in a solid matrix absorbs or emits

gamma rays, the recoil energy is released in the form of phonons. Rudolf Mössbauer discovered that a portion of the emission and absorption events can go through without any loss of momentum when the gamma ray energy is too small to form a phonon. Such recoil-free event is called the Mössbauer effect, which is the basic principle of Mossbauer spectroscopy.

In a Mössbauer spectroscopy experiment, the atomic isotope to be analyzed is impinged with gamma rays from a source of the same isotope. The source is accelerated in a range of velocities to induce shifts in the incoming gamma ray energy due to relativistic Doppler effect and the intensity of transmitted gamma rays as a function of source velocity is plotted. Since the sample and the source are in different chemical environments, their resonant absorption energies differ slightly. By finding the velocities in which a dip in the intensity of the gamma rays takes place, the resonant absorption energies for the analyzed nuclei can be determined.

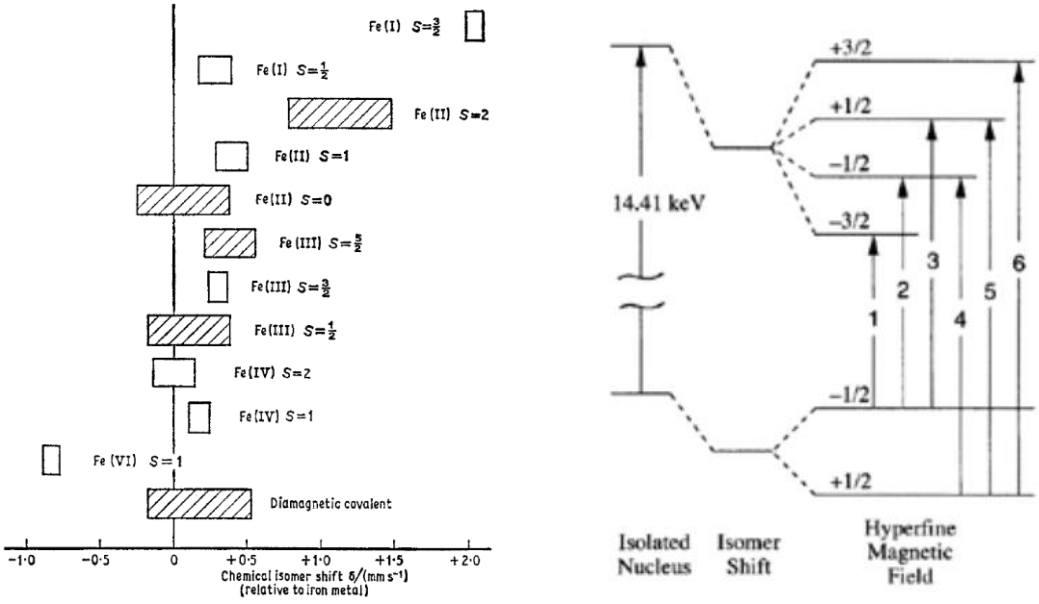

Figure 3.12: Isomer shift ranges for given oxidation and spin states of Fe and energy level diagrams of ^{57}Fe showing the nuclear interactions [348,349]

The position and shape of the peaks in the Mossbauer spectrum depends on three main types of nuclear interactions. First is the isomer shift (chemical shift) which is related with the electron charge density in the s orbitals of the nuclei. This value gives information on the oxidation state of the atoms as well as valence states and electron shielding.

Second interaction is the quadrupole splitting which arise from the non-spherical charge distribution of the nuclei with a spin state larger than +1/2. The nuclear energy levels are split due to the presence of asymmetric charge distribution or ligand arrangements which induces an asymmetric electric field. Quadrupole interactions also provide information on the oxidation and spin states of the nuclei as well as local symmetry and chemical environment.

Third type of interaction is the magnetic hyperfine splitting (Zeeman splitting), which arises from the interaction between the nucleus and the surrounding magnetic fields. In the presence of these fields, each nuclear energy level I, splits into 2l+1 sub-levels. Magnetic properties of the material can be studied by analyzing the magnetic hyperfine splitting. Fig. 3.12 shows the typical isomer shift ranges for ^{57}Fe at different oxidation and spin states. and the energy level diagrams for different nuclear interactions.

While many nuclei are Mössbauer active, suitable gamma ray sources are limited which in turn limits the application of Mössbauer spectroscopy. ^{57}Fe is the most common element that is analyzed by this technique, since the decay of ^{57}Co source by electron capture provides an ideal gamma ray source for analysis. ^{119}Sn and ^{121}Sb are other commonly investigated elements.

3.10 Electron Spin Resonance Spectroscopy

Electron spin resonance (ESR – or electron paramagnetic resonance, EPR) spectroscopy is another analogous technique to NMR, in which the energy transitions of unpaired electrons instead of nuclei in a sample exposed to an external magnetic field is detected. Like protons, electrons are spinning charged particles with a self-induced magnetic moment. Under an external magnetic field, the paramagnetic (unpaired) electrons align with or against the the field due to Zeeman effect [46,324,350]. The electrons aligning parallel to the magnetic field are at a lower energy state with respect to the electrons with opposite alignment. Upon microwave irradiation these lower energy electrons can be flipped to the higher energy level. Electron spin resonance spectroscopy investigates the resonant energy levels of the paramagnetic electrons by scanning the sample response at a constant frequency microwave radiation (typically ~ 100 kHz) with varying magnetic field strength, G. Alternatively, the magnetic field strength can be kept constant while varying the frequency of microwave radiation as well; however this type of application of the technique is not as common.

The magnetic moment of an electron exposed to a given external magnetic field is dependent on the electron environment described with a g-factor. The g value for a free electron is 2.00232 [351]. When the electrons are confined in a molecular orbital or within an energy band in the crystal lattice, the confinement condition induces a change in the g-factor similar to the chemical shift observed in NMR spectroscopy. Other important factor which affects the spectrum features are the hyperfine interactions as discussed in Chapter 3.9. These interactions are described as J-coupling for NMR spectroscopy. ESR spectroscopy is an extremely sensitive method which can provide extensive information on the oxidation states and defect structures as well as chemical environment and orientation of atoms near the unpaired electron. Moreover, the change of line shapes in the spectrum can be analyzed to interpret dynamic processes, such as rate of chemical reactions.

3.11 Thermogravimetric analysis

Thermal analysis methods refer to any technique that studies the physicochemical properties of materials as a function of temperature [352]. Thermogravimetric analysis (TGA) is a subset of thermal analysis methods in which the weight change of the sample is measured as a function of temperature and time. Information on kinetic processes over the sample, such as decomposition, evaporation, oxidation – reduction and adsorption – desorption can be obtained by employing this method. The experiment can be performed with different gas composition and flow rate to extract thermal stability and reactivity information in different atmospheres. TGA instruments can determine precise sample mass changes through a thermally isolated sensitive balance which can detect changes as low as 0.1 μm.

Differential scanning calorimetry (DSC) is often also measured within the appropriately equipped TGA setup to determine rate of energy change with temperature. In DSC, the difference between the heat flow of the sample and a reference is simultaneously detected at a given temperature ramp. DSC can provide additional information about the processes taking place in the sample environment, such as phase changes and thermally activated reactions.

The TGA setup can be coupled with other instruments for a more comprehensive analysis. For instance, coupling the setup with a mass spectrometer can give information on the composition of evolving gas due to physical or chemical processes taking place in the sample environment.

3.12 Temperature Programmed Desorption of Oxygen

Temperature programmed methods are sensitive techniques based on probing the material surface as a function of temperature in a controlled atmosphere [353]. Temperature programmed desorption (TPD) is particularly relevant for study of catalyst materials, since it can provide insights on the active sites on catalyst surface as well as mechanism of catalytic processes. Temperature programmed desorption of oxygen (TPD-O_2) is commonly employed to assess the oxygen mobility in oxide catalysts, which is an important parameter for catalytic performance.

In a typical TPD-O_2 run, the catalyst is placed in a reactor, heated in O_2 atmosphere to saturate the oxygen vacancy sites and subsequently cooled down. An inert gas such as N_2 or Ar is then flown through the sample chamber to establish an inert atmosphere. The reactor temperature is increased with a linear heating rate and the desorption of oxygen from the sample is monitored. The evolution of desorbed gas with increasing temperature is quantitatively detected by a thermal conductivity detector (TCD) or a mass spectrometer [5].

3.13 Temperature Programmed Reduction by Hydrogen

Temperature programmed reduction by H_2 (TPR-H_2) can provide quantitative information on the reducibility of different components on an oxide catalyst [354]. The analysis method is analogous to TPD-O_2 with the difference that instead of performing the experiment under inert atmosphere, a reducing gas with typically 3 to 15% H_2 content diluted in Ar or N_2 is flown through the sample chamber as the temperature is increased at a linear heating rate. The change in the gas stream is monitored by a TCD or mass spectrometer. H_2 is consumed when a reduction takes place in the sample environment. The amounts of consumed H_2 with increasing temperature provide a measure of reducibility of the catalyst. Careful evaluation of the experimental parameters is crucial for interpreting the data, since the heating rate, H_2 concentration and flow rate of the gas influences the TPR results.

Chapter 4

Results & Discussion

4.1 Porosity variation: $SrTiO_3$

Attainment of mesoporous nanoarchitectures with superior surface areas stands as an essential goal for the preparation of high performance perovskite oxide catalysts. One of the major shortcomings of perovskite materials preventing their widespread utilization in environmental catalysis is their sub-optimal morphology and nanostructure [5,14]. Established porous oxide preparation strategies such as direct co-condensation with soft templates, are usually not applicable for multi-metal oxides due to differing solubility and reactivity of the metal ions in the structure as well as high temperatures required for the crystallization of perovskite phase [14,201]. Thus, synthesis of porous perovskites are mainly achieved by nanocasting routes in literature, in which perovskite oxide precursors are impregnated into the pores of a host material, usually an ordered mesoporous silica matrix. However, this approach requires several optimized impregnation steps to ensure a satisfactory loading of precursor solution in the pores of the host material while avoiding possible formation of perovskite particles outside of the pores [355]. Moreover, the confinement of the growing multi-metal oxide phase in template pores leads to severe impediment of the crystal growth [175]. Thus, simpler and more flexible routes are needed for the preparation of multi-metal oxides with high porosity.

In this work, an innovative facile method based on a cooperative assembly modification of polymer complex synthesis was utilized to prepare mesoporous $SrTiO_3$. A pre-hydrolyzed alkoxysilane solution is added to the initial reaction mixture as inorganic endotemplate. The intermixing of organic and inorganic constituents at molecular level leads to a well

interwoven network of the polyester and SiO_2 upon polymerization reactions. As a result, after calcination step, in situ formed silica template could be removed from the matrix by NaOH etching, leading to phase-pure $SrTiO_3$ with extremely high surface areas.

Highly porous structure of materials prepared with this route can be explained not only through the templating process, but also through the choice of glycerol as polyol precursor in the reaction instead of commonly used ethylene glycol. Glycerol likely promotes crosslinking in the initial polyesterification reaction by its additional hydroxide groups, which leads to a more porous structure upon removal of the entangled polymer gel by calcination. Indeed, when ethylene glycol was used in $SrTiO_3$ synthesis while keeping other conditions unchanged, the product showed only 20 m^2 g^{-1} as opposed to 60 m^2 g^{-1} surface area determined for the sample synthesized with glycerol (Fig. 4.1). Moreover, perovskites prepared with glycerol show high phase purity even in the presence of water in the initial reaction mixture from the template solution.

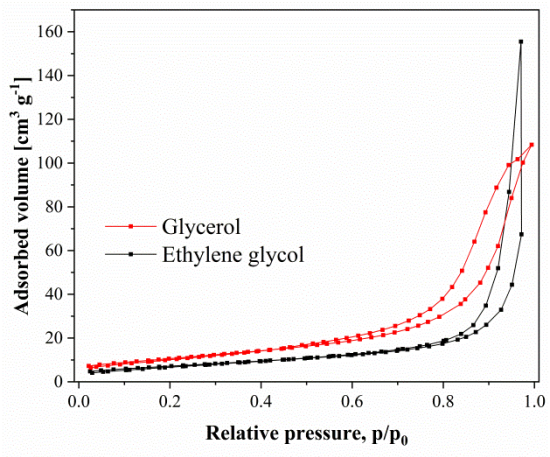

Figure 4.1: N_2 physisorption isotherms of $SrTiO_3$ showing the porosity enhancement due to glycerol use instead of ethylene glycol in its template free polymer complex preparation.

The tuning of porosity and nanostructure is investigated in this sub-chapter by variation of template load in the preparation process. The influence of these characteristics on the catalytic performance of the material is studied through a photocatalytic methylene blue dye degradation test, relevant for wastewater treatment applications. Molar ratios of $SrTiO_3$: SiO_2 were varied between 10 : 1 and 1 : 1 corresponding to a template load between 6 vol.% and 40 vol.% respectively. $SrTiO_3$ samples were labeled as STO_##, where ## refers to vol.%

template load from STO_06 (6 vol.% template) to STO_40 (40 vol.% template), whereas template free material was labeled as STO (Table 6.1). Physicochemical properties and photocatalytic performance of the materials prepared in this work were benchmarked against a commercially obtained $SrTiO_3$ powder with nanoparticulate morphology. This nanoparticulate $SrTiO_3$ reference sample was labeled as STO_NP.

4.1.1 Structural Characterization

Thermogravimetric analysis was employed on the polymer gels to determine the optimal final temperature for the calcination process as well as to study the kinetics of the high temperature treatment (Fig. 4.2). All gels show similar reaction kinetics with an initial sharp mass loss around 200 °C followed by a plateau around 350 – 450 °C. Finally, above ~ 560 °C no further mass loss is detected. Based on these findings, two constant temperature steps of 2 h were implemented in the heating ramp at the intermediate temperature 350 °C and final temperature 600 °C.

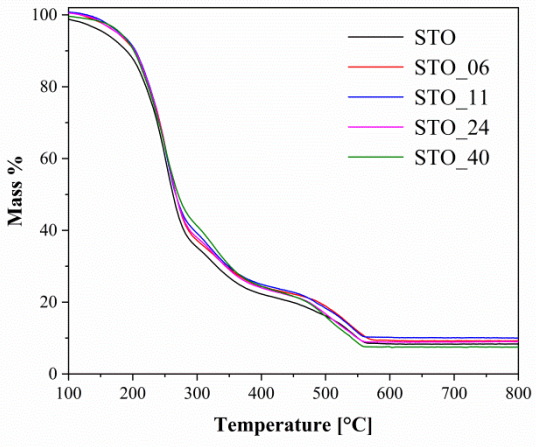

Figure 4.2: Thermograms of nanoporous $SrTiO_3$ powders with 0 – 40 vol.% template loading.

Following the calcination process, resulting $SrTiO_3$: SiO_2 nanocomposites were characterized by X-ray diffractometry as depicted on Fig 4.3a. All nanocomposites show well-crystalline cubic perovskite oxide phase, whereas additional weak reflections were detected in as-prepared samples at high template loads. These weak reflections were assigned to amorphous siliceous species ($2\theta \approx 30°$) and a $SrCO_3$ impurity phase. After acetic acid (HOAc) and NaOH

etching treatment to remove carbonates and template respectively, pure-phase cubic perovskite oxide was observed for all analyzed samples (Fig. 4.3b).

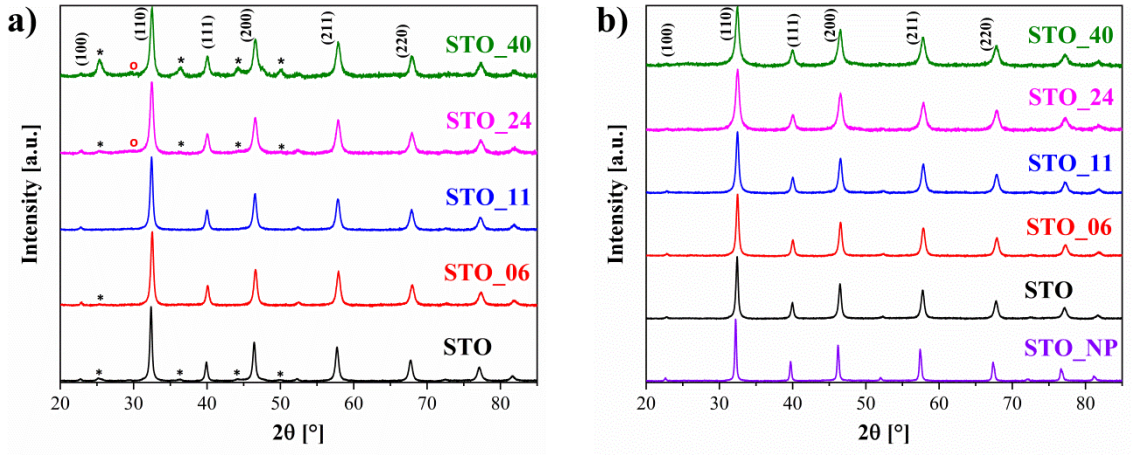

Figure 4.3: X-ray diffractograms of investigated STO systems (a) as-prepared nanocomposites. Asterisks refer to $SrCO_3$ phase, red circles mark the presence of amorphous siliceous species. (b) pure-phase mesoporous STO oxides after acetic acid and sodium hydroxide treatment along with commercially obtained nanoparticulate reference $SrTiO_3$ sample (STO_NP).

Crystallite sizes of the $SrTiO_3$ oxides were calculated by applying Scherrer equation (3.4) on the [110] reflection. Grain sizes decrease progressively with increasing template load from 31 nm for template free STO down to 17 nm for STO_40 (Table 4.1). The decline in crystallite sizes can be explained by the rising diffusion barrier to mass transport of the perovskite phase due to the addition of siliceous species.

The effective removal of the carbonates and silica template was characterized by the disappearance of $–CO_3$ mode at ~ 1460 cm^{-1} and Si-O modes around 800 – 1200 cm^{-1} in the IR spectra subsequent to the acetic acid and sodium hydroxide etching steps respectively [324] (Fig 4.4a). In agreement with XRD findings, infrared spectra of the STO samples show a single broad band around 560 cm^{-1} characteristic of the perovskite phase [356] (Fig 4.4b).

Considering that infrared spectroscopy cannot provide definitive evidence to complete removal of siliceous species from the system, surface composition of $SrTiO_3$ samples were further investigated by X-ray photoelectron spectroscopy. Peak positions on the XPS spectra align well with the expected oxidation states of each element (Fig 4.5).

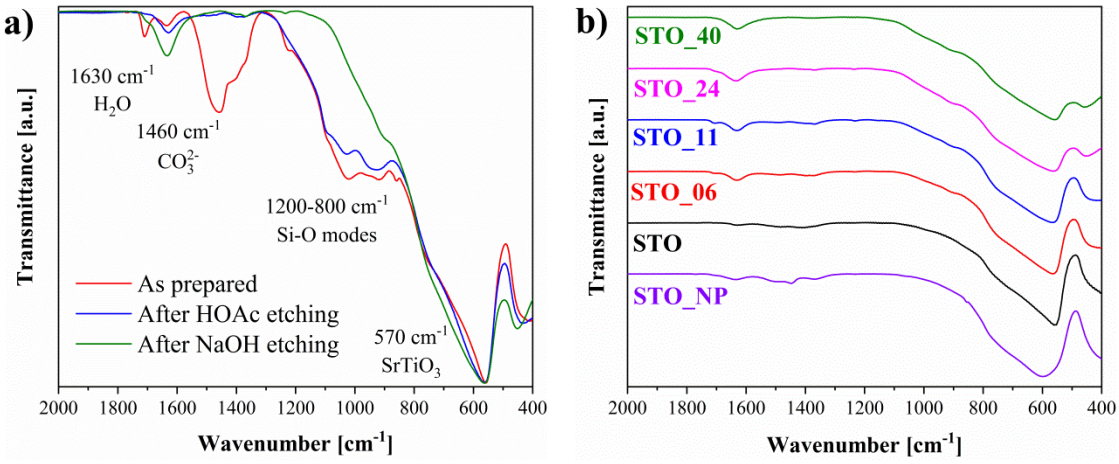

Figure 4.4: Infrared spectra of investigated STO systems (a) STO-24 sample chosen as representative system at different treatment steps. (b) Pure-phase mesoporous STO oxides after acetic acid and sodium hydroxide treatment along with reference STO_NP.

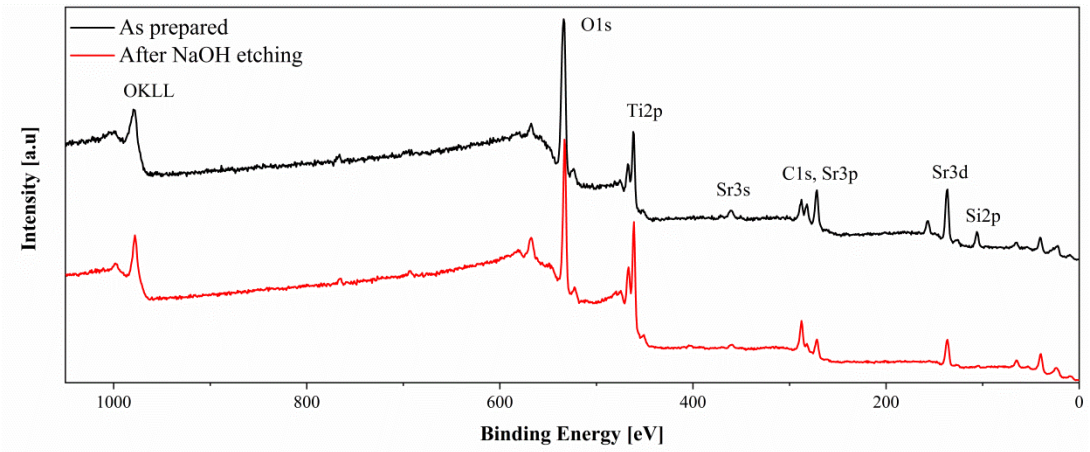

Figure 4.5: XPS survey spectrum of STO_40 before and after sodium hydroxide treatment.

Peaks observed at the binding energy range between 60 – 10 eV can be attributed to the different p and s states of Sr (4s, 4p), Ti (3s, 3p) and O (1s) [357]. Calculated elemental compositions on the surface of as-prepared $SrTiO_3$ samples and the Si amount before and after etching treatment are summarized on Table 4.1. Determined elemental compositions are in good agreement with the nominal $SrTiO_3$ stoichiometry for each sample apart from the slight Sr deficiency detected at high template loads (STO_24, STO_40). The deviations in Sr/Ti ratio can be partially explained by increased $SrCO_3$ formation at higher template amounts. Silica enrichment in the matrix may also play a role in the deviations affecting the distribution of metal atoms on material's surface [358]. Investigated samples in XPS possess

relatively high amounts of carbon impurities, which is likely due to surface contamination from the atmosphere, although carbonate formation during the preparation of the samples may also have an influence. Efficacy of the silica removal is evidenced by the low residual Si amounts (Si_e) determined subsequent to NaOH etching (Table 4.1).

Table 4.1: Structural and morphological features of investigated STO samples. Specific surface area (S_{BET}) and pore volume (V_P) determined by nitrogen physisorption; Crystallite size (Φ) obtained by XRD; atomic composition of the as-prepared samples along with the residual amount of silicon after etching procedure (Si_e) in at.% units.

Sample	S_{BET} [$m^2\ g^{-1}$]	V_P [$cm^3\ g^{-1}$]	Φ [nm]	C	O	Ti	Sr	Si	Si_e
STO	60	0.22	31	15.5	55.3	14.9	14.2	-	-
STO_06	79	0.23	26	9.8	58.4	15	13.8	3.16	1.1
STO_11	114	0.29	23	15.2	54.8	13.8	12.1	4.1	2.2
STO_24	216	0.36	17	8.2	61.8	13.6	9.5	6.7	1.7
STO_40	239	0.39	15	12.3	59.3	9.9	7.2	11.2	3
STO_NP	38	-	48	-	-	-	-	-	-

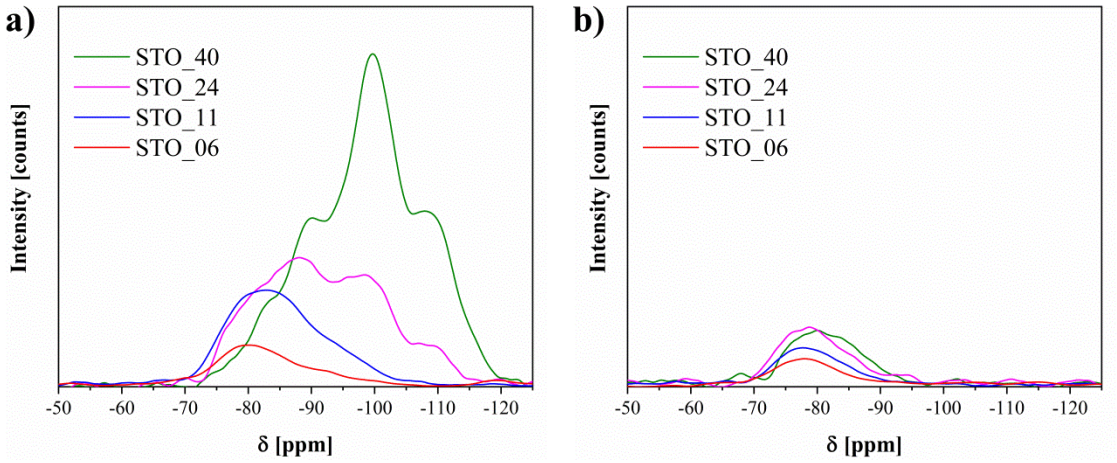

Figure 4.6: ^{29}Si CP-MAS NMR spectra of investigated STO systems (a) before NaOH etching (b) after NaOH etching. Approximate signal positions : Q0 at –78 ppm, Q1 at –85 ppm, Q2 at –90 ppm, Q3 at –100 ppm and Q4 at –110 ppm.

The structure of siliceous species in the nanocomposite and their removal process were further investigated by ^{29}Si CP-MAS NMR spectroscopy (Fig. 4.6). By analyzing the NMR spectra, it was determined that the networking of siliceous species in the nanocomposite vary with the initial prehydrolyzed alkoxysilane amount added to the reaction mixture. For low amounts of template loading (STO_06, STO_11) only Q0, Q1 and Q2 sites are present, which correspond to monomeric, dimeric and oligomeric units respectively. At higher template loads between 24 – 40 vol.% (STO_24, STO_40), Q3 and Q4 signals, which can be assigned to pure SiO_2, dominate the spectra.

Evolution of Si amounts was investigated via a semi-quantitative analysis by keeping acquisition time and sample mass constant in each NMR survey. Subsequent to NaOH etching, Q3 and Q4 sites were completely removed from each matrix, whereas small residual amounts of Q0 and Q1 sites remained for all samples. However, the absolute amounts of the residual Si didn't differ significantly for varying template loading. These results indicate that a minor portion of siliceous species independent of the template amount incorporate into the matrix in the form of silicates and cannot be removed from the structure. Accordingly, X-ray diffractograms and IR spectra of as-prepared nanocomposites of STO_24 calcined at higher temperatures confirm the presence of a growing $Sr_2TiSi_2O_8$ silicate phase (Fig. 4.7). It can be also mentioned that relative amount of carbonates in the nanocomposites decrease significantly with higher temperature calcination (Fig. 4.7b).

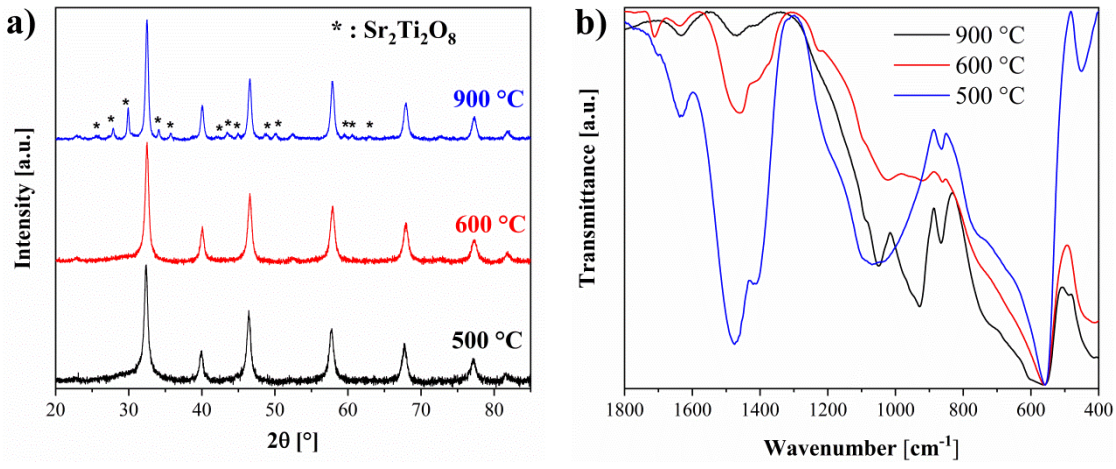

Figure 4.7: X-ray diffractograms (a) and infrared spectra (b) of as prepared STO-24 nanocomposites calcined at different temperatures.

4.1.2 Evaluation of textural properties

Porous features of the $SrTiO_3$ oxides were investigated by nitrogen physisorption analysis. The physisorption isotherms depicted in Fig. 4.8a can all be categorized as type IV(a) with broad hysteresis independent of the template loading [299]. The steep increase of the adsorbed volume near the saturation pressure of nitrogen can be assigned to interparticle porosity. Specific surfaces areas calculated from BET model (S_{BET}) and pore volumes (V_P) increased progressively with increasing template load (Table 4.1) [359]. Template free STO already showed a surface area of 60 m^2 g^{-1}, whereas an extremely high surface area of ~ 240 m^2 g^{-1} was determined for STO_40.

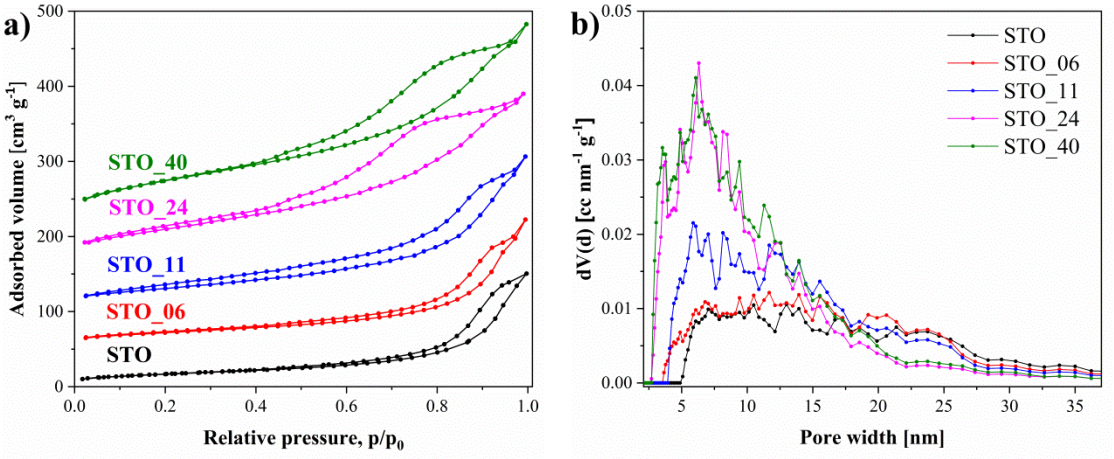

Figure 4.8: Nitrogen physisorption isotherms (a) and pore size distribution (b) of investigated STO systems. The isotherms were shifted upwards by 50 cm^3 g^{-1} relative to each other for clarity.

A broad distribution of pore diameters between 5 to 30 nm were identified for template free STO as well samples with low template loading (Fig. 4.8b). Above 24 vol.% template load, smaller pores down to 3 nm are formed and a progressive pore size narrowing around 6 nm is observed. The changes in pore size distribution can be described through the findings in ^{29}Si NMR spectroscopy. At low template loads, only oligomeric siliceous species are formed which contribute poorly to the templating process. Thus, pore size distribution does not change significantly in comparison to template free STO. At higher template amounts, three dimensional networks of SiO_2 evolve around the perovskite lattice and effectively form the pore space. It should be noted that no significant difference was observed between STO_24

and STO_40 in terms of pore size distribution and BET surface area. Thus, we can argue that the additional silica in the STO_40 nanocomposite does not substantially contribute to the templating action but rather tend to form phase separated SiO_2 domains.

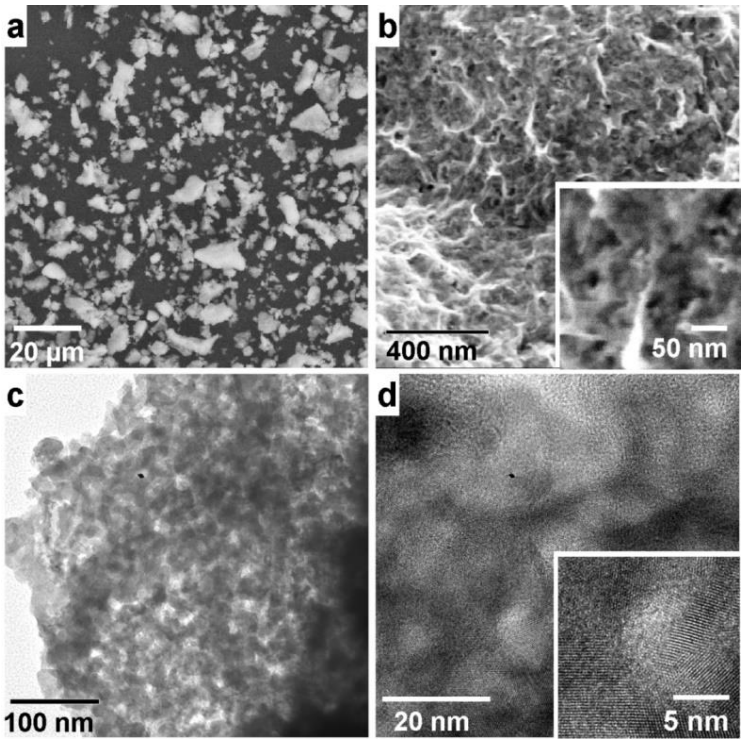

Figure 4.9: SEM (a,b) TEM (c) and HRTEM (d) micrographs of STO_24 sample chosen as representive system. The insets are enlarged viewings of the corresponding micrographs.

Further characterization of the materials' textural properties was carried out via electron microscopy. According to the TEM images, all samples display polycrystalline aggregates of several micrometers with a disordered distribution of well interconnected pores with diameter between 10 – 20 nm (Fig. 4.9) in agreement with the N_2 physisorption findings. HR-TEM investigations revealed crystalline pore walls in accordance with XRD findings (Fig 4.9d).

4.1.3 Influence on catalytic performance: Photocatalyzed dye degradation

The relation of the textural and structural features with material's photocatalytic properties were investigated subsequent to the thorough characterization of nanoporous $SrTiO_3$ oxides. The samples show identical crystalline phase and chemical composition except for minor Sr deficiencies observed at higher template loads.

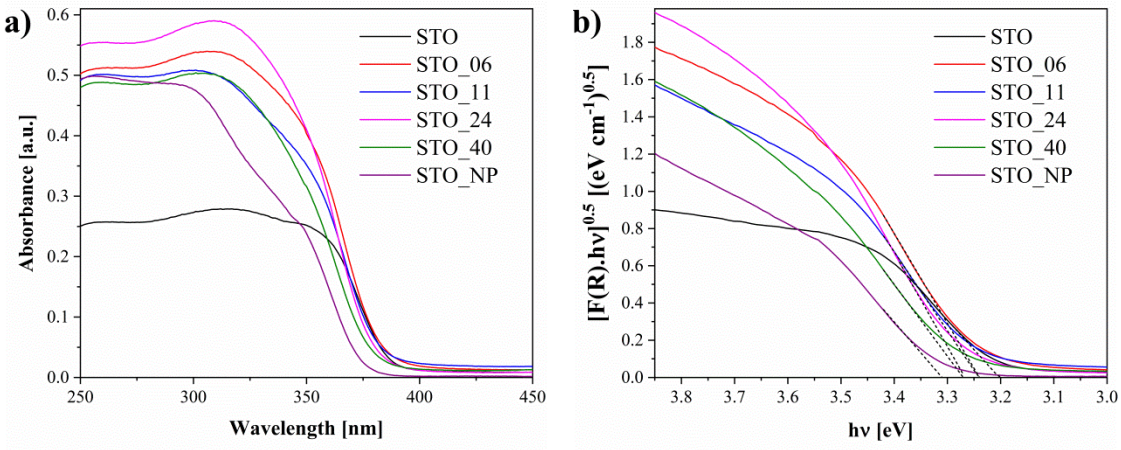

Figure 4.10: Diffuse reflectance UV spectra (a) and pertaining Tauc plots (b) of investigated STO systems as well as commercially obtained nanoparticulated reference STO_NP.

Since the efficiency of a photocatalyst is strongly dependent on its light absorption properties, the band gap energies (E_{BG}) of the investigated samples were initially determined by diffuse reflectance UV (DR-UV) spectroscopy. The band gap energies were calculated from the linear fit of the modified Kubelka-Munk function in the Tauc plots on Fig 4.10a. The fitting parameters were given in Table 6.2. E_{BG} of the samples were all found to be around ~3.24 eV in line with the literature values. Band gap energies increased slightly with increasing template amount up to 3.27 eV (Fig 4.10b, Table 4.2). This increase can be associated to higher porosity [360,361] as well as lower crystallite size which may lead to enhanced quantum size effects and induce band gap widening [17,362].

The catalytic performance of the perovskite oxide samples were studied via a photocatalyzed methylene blue (MB) dye degradation reaction relevant for wastewater treatment. The extent of dye degradation was determined by acquiring UV-spectra of the dye solution over each catalyst at given time increments within 2 h of total irradiation time.

Prior to the irradiation of the dye solutions treated with $SrTiO_3$ photocatalysts, they were subjected to 1 h dark stirring to reach complete dye adsorption. The saturation of dye adsorption was ensured by collecting the UV spectra of the solutions after 1 h and 3 h of dark stirring, which remained identical for all samples (Fig. 4.11a).

Additionally, bare MB solution was irradiated in the absence of photocatalysts for 2 h. Resulting spectrum after irradiation remained identical with the initial one, confirming that the degradation in the experiment is a purely catalytic process (Fig. 4.11b).

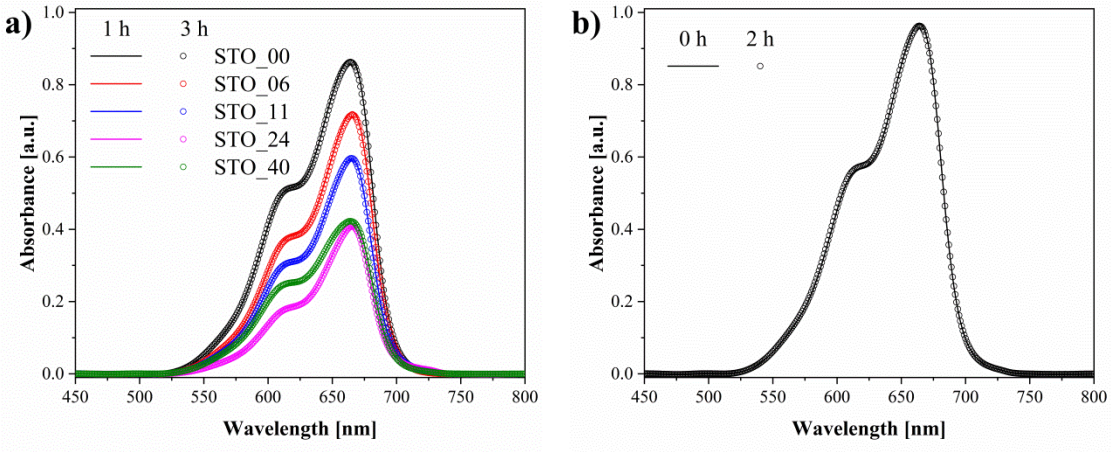

Figure 4.11: Dark stirring plots of the dye solution with investigated STO catalysts at 1 h and 3 h (a) spectra of MB dye solution without catalyst before and after 2 h UV irradiation (b).

MB degradation over template free STO sample was already 15% higher than of the commercially obtained STO_NP showing the enhanced catalytic properties of mesoporous $SrTiO_3$ aggregates in comparison to nanoparticulated system (Fig. 4.12a). MB dye degradation increased progressively with increasing template amount of the $SrTiO_3$ photocatalyst, leading to a maximum of ~ 75% degradation for STO_40.

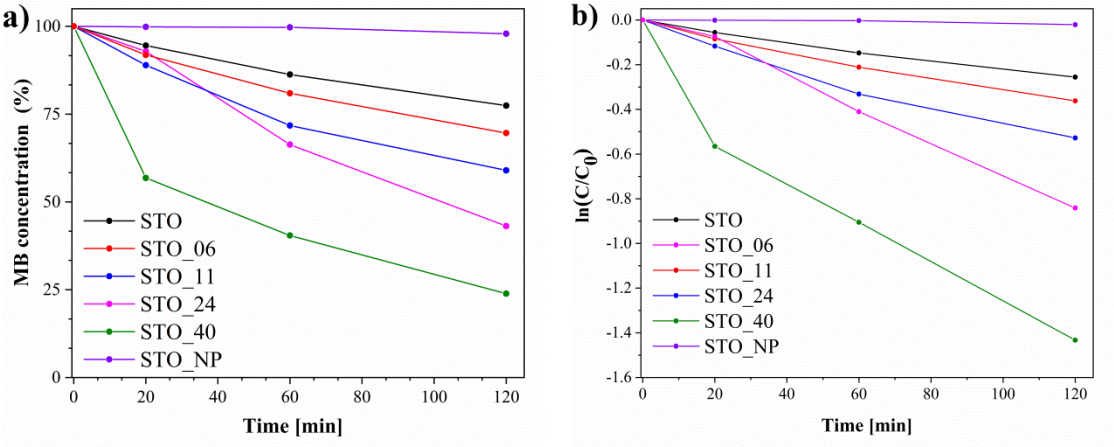

Figure 4.12: Extent of photocatalyzed dye degradation (a) and plots of $\ln(C/C_0)$ calculated from the dye concentration vs. time plots (b).

Kinetics of the dye degradation reaction over STO samples were studied by plotting $\ln(C/C_0)$ against reaction time (Fig 4.12b). Apparent rate constants of the reaction, $k_{app,}$ were extracted from the slope of the curves (Table 4.2). Near-straight line observed for each curve points to a

first order reaction kinetics for each sample. The apparent rate constant values were normalized by surface area ($K_{norm} = k_{app}/S_{BET}$) to pinpoint the influence of porosity on the photocatalytic performance. No significant differences between the normalized rate constant values, K_{norm}, of the samples indicate a directly proportional relation between catalytic performance and porosity of the materials. Minor increase of the K_{norm} value given for STO_40 can be likely assigned to increased contribution of decreasing grain size to the photocatalytic performance, which can enable quantum effects [363].

Origin of photocatalytic performance was further investigated by determining the dye adsorption amounts over templated $SrTiO_3$ samples. The stock solution was stirred with each $SrTiO_3$ sample to reach saturation of dye adsorption. Subsequently, total dye adsorption values for each sample were assessed by UV spectroscopy (Table 4.2).

Table 4.2: Photocatalytic properties of investigated STO samples: surface areas ($\mathbf{S_{BET}}$) determined from N_2 physisorption, Bang-gap energy ($\mathbf{E_{BG}}$) calculated from the Kubelka-Munk plots of the materials' UV spectra; MB adsorption determined from UV spectroscopy, apparent ($\boldsymbol{k_{app}}$) and normalized ($\boldsymbol{K_{norm}}$) reaction rate constants for the degradation of MB.

Sample	S_{BET} [$m^2\ g^{-1}$]	E_{BG} [eV]	MB adsorption [%]	k_{app} [min^{-1}]	K_{norm} [$g\ m^{-2}\ min^{-1}$]
STO	60	3.20	10	$2.1x10^{-3}$	$3.5x10^{-5}$
STO_06	79	3.24	26	$3.0\ x10^{-3}$	$3.8x10^{-5}$
STO_11	114	3.24	39	$4.4\ x10^{-3}$	$3.9x10^{-5}$
STO_24	216	3.27	61	$7.2\ x10^{-3}$	$3.3x10^{-5}$
STO_40	239	3.27	58	$1.1\ x10^{-2}$	$4.6x10^{-5}$
STO_NP	38	3.31	3	$2.0\ x10^{-4}$	$5.3x10^{-6}$

The adsorption increased progressively with increasing template load up to ~ 6 times with respect to template free STO. Indeed, introducing a 6 vol.% template load already had an effect of 1.5 times adsorption enhancement despite the minor increase in the surface area. The dramatic rise in dye adsorption in this case may be related with surface alkalization as a

result of NaOH treatment of the templated $SrTiO_3$ samples which can lead to stronger adsorption sites for the dye [361].

Dye adsorption capacities of STO_40 and STO_24 samples remain comparable despite the differing surface areas of two samples. The higher photocatalytic performance of STO_40 in this case can be plausibly attributed to the quantum size effects in accordance with the smaller crystallite size of the STO_40 aggregates, which can lead to superior separation of electron – hole pairs and enhance the efficiency of the photocatalytic process [364,365]. Thus, enhanced activity of the templated $SrTiO_3$ photocatalysts prepared by the novel cooperative assembly approach can be explained by the mutual variation of porosity and microstructure of the perovskite oxides.

4.1.4 Sub-chapter summary

A facile synthesis route was developed by combining in-situ silica templating with modified polymer complex synthesis to prepare mesoporous perovskite oxides with nano-sized grains. Due to well intermixing of the growing silica network and the polyester containing metal chelate complexes at a molecular level, pure-phase mesoporous $SrTiO_3$ with nano-sized grains, highly interconnected pores and substantial surface areas could be obtained after calcination and silica template removal via sodium hydroxide etching.

The influence of different template loads on the structure and morphology of the final oxides were investigated by varying the template amount between 6 – 40 vol.%. CP-MAS NMR studies on the $SiO_2/SrTiO_3$ nanocomposites showed that for low template loads (6 – 11 vol.%) only siliceous species with dimeric and oligomeric domains were observed, whereas condensed domains which can be assigned to pure SiO_2 signifying successful templating action were mainly formed at high template loads (24 – 40 vol.%). Siliceous species were successfully removed from the matrix by NaOH etching, notwithstanding low amounts of residual Si remaining in the samples (< 3 at.%) in silicate form.

The porosity of the $SrTiO_3$ samples was successfully tuned by varying the template load. Template free sample already showed mesoporous morphology with 60 $m^2\ g^{-1}$ due to the choice of glycerol as polyol precursor in the initial synthesis, which leads to more porous product upon calcination. Porosity increased with template load, leading to extremely high surface areas up to 239 $m^2\ g^{-1}$ for $SrTiO_3$ templated with 40 vol.% SiO_2. Grain sizes on the other hand decreased from 31 nm to 15 nm due to the increasing amount of SiO_2 template

which acts as a diffusion barrier to mass transport. Moreover, all $SrTiO_3$ samples showed excellent crystallinity and phase-purity with only minor Sr deficiency observed at higher template loads.

The enhancement of perovskite catalysts' functional properties by nanostructure and porosity tuning was investigated through photocatalytic methylene blue dye degradation tests. Dye conversion progressively increased with increasing porosity & decreasing crystallite size, showing almost no change in the surface area normalized rate constant. $SrTiO_3$ samples prepared with the facile route developed in this work showed ~ 7 times higher surface area normalized dye degradation activity than commercially obtained nanoparticulate $SrTiO_3$ reference.

4.2 Composition variation: $La_{0.3}Sr_{0.7}Ti_{1-x}Fe_xO_{3\pm\delta}$

Substitution in the native sites of perovskite oxides with foreign cations is an established strategy to enhance and optimize the catalytic performance of these materials. Achieving co-substitution of perovskite structures with mesoporous morphology, in particular stands as an essential design strategy for high performance perovskite catalysts. However, such materials are challenging to prepare due to the chemical complexity of the system.

In this sub-chapter, the evolution of material properties as a result of co-substitution in a mesoporous $SrTiO_3$ lattice is investigated by varying the iron substitution in $La_{0.3}Sr_{0.7}Ti_{1-x}Fe_xO_{3\pm\delta}$ (LSTF) between $0 < x < 0.5$. Fe is chosen as B-site substituent due to its high abundance, complete solubility in $SrTiO_3$ lattice and excellent reactivity it provides to the perovskite oxide system in thermally activated catalytic reactions [28,29]. Lanthanum, on the other hand, was chosen due to its stabilizing effect on the perovskite solid solution without altering the catalytic performance [30–32]. Mesoporous solid solutions were prepared by the template free modification of established polymer complex route (Chapter 6.1), where glycerol is used a instead of the commonly utilized ethylene glycol as polyol precursor (Fig. 4.1).

The evolution of material's structural and functional properties upon varying Fe substitution was thoroughly characterized. The catalytic performance improvement of the samples with regard to CH_4 and CO oxidation was correlated to the mutual influence of composition and morphology. Prepared LSTF samples were labeled as LST.##F, where ## refers to mol.% iron substitution in the $La_{0.3}Sr_{0.7}Ti_{1-x}Fe_xO_{3\pm\delta}$ composition from LST.00F ($La_{0.3}Sr_{0.7}TiO_{3+\delta}$) to LST.50F ($La_{0.3}Sr_{0.7}Ti_{0.5}Fe_{0.5}O_{3-\delta}$).

4.2.1 Structural and textural characterization

Assessment of textural properties by N_2 physisorption indicates similar type IV (a) isotherms for each system corresponding to surface areas of ~ 65 $m^2\ g^{-1}$ and pore volumes of ~ 0.2 $cm^3\ g^{-1}$ (Fig. 4.13a, Table 4.3). These findings are in line with the textural parameters determined for template free $SrTiO_3$ (STO) (Table 4.1), whereas pore size analysis indicates a narrower distribution of mesopores between 7 – 17 nm diameter for LSTF solid solutions along with a small amount of larger mesopores up to 30 nm (Fig 4.13b).

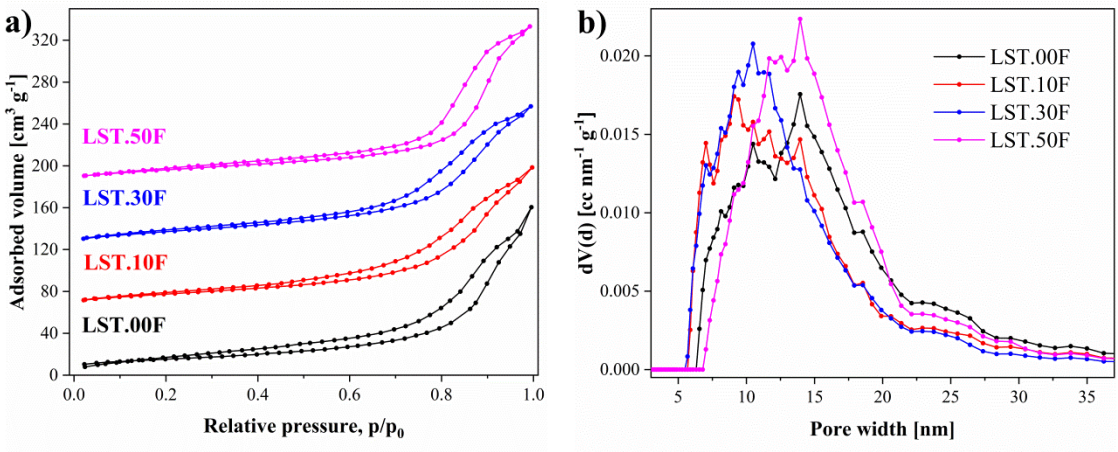

Figure 4.13: N_2 physisorption isotherms (a) and pore size distribution (b) of investigated $La_{0.3}Sr_{0.7}Ti_{1-x}Fe_xO_{3\pm\delta}$ systems. The isotherms were shifted upwards by 50 cm^3 g^{-1} relative to each other for clarity.

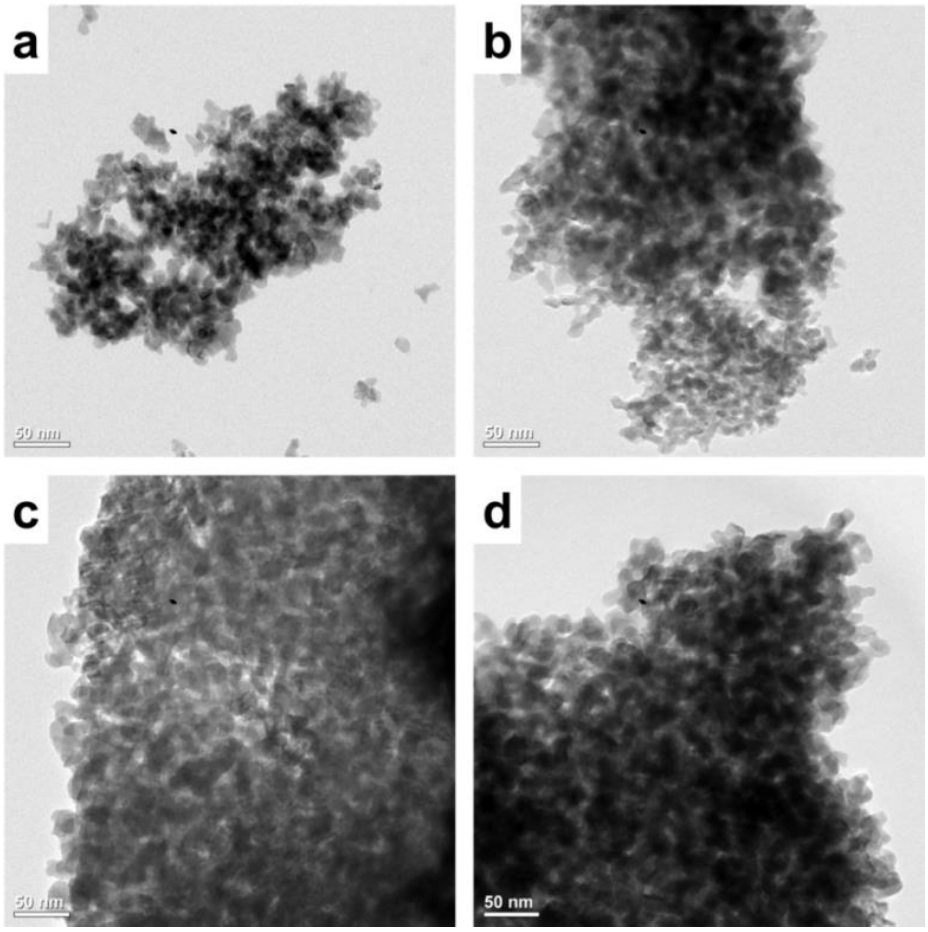

Figure 4.14: Representative TEM images of investigated $La_{0.3}Sr_{0.7}Ti_{1-x}Fe_xO_{3\pm\delta}$ solid solutions (a) LST.00F (b) LST.10F (c) LST.30F (d) LST.50F.

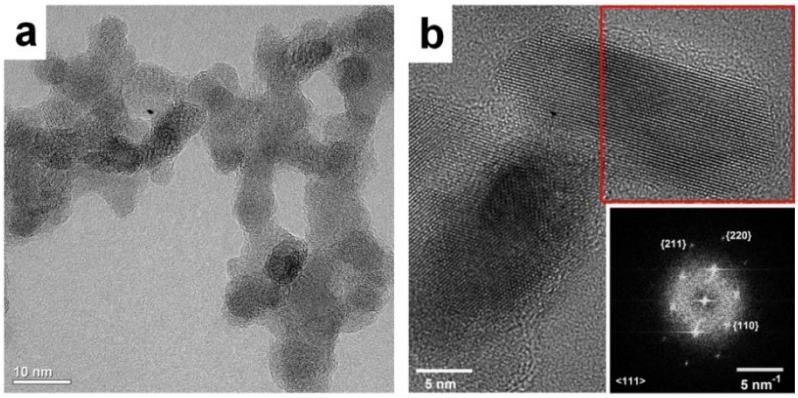

Figure 4.15: HR-TEM images of LST.50F chosen as representative system, showing (a) clear presence of pores with ~ 15 nm diameter (b) phase purity of a single crystallite via FFT representation given as inset for the area marked with the red square.

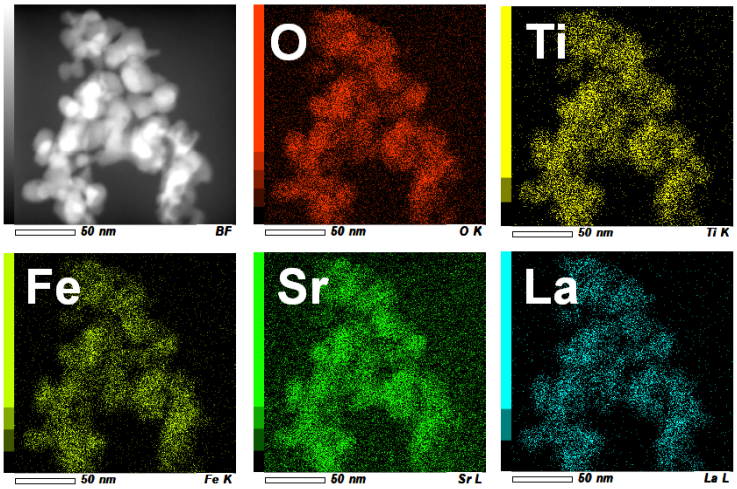

Figure 4.16: Elemental distribution over a LST.50F particle chosen as representative system retrieved by EDX mapping.

Gas sorption findings are confirmed by transmission electron microscopy imaging which shows for each sample a disordered distribution of ~ 15 nm pores on polycrystalline particle aggregates of up to several diameters (Fig 4.14 – 4.15). FFT representations of single crystallites of about 25 nm diameter show a phase-pure crystalline structure (Fig. 4.15b). Elemental compositions of the solid solutions were analyzed via EDX spectroscopy coupled with TEM. The atomic ratios were determined to be in good agreement with the corresponding nominal stoichiometries of each LSTF sample (Table 4.3). Moreover, high magnification EDX mapping on LSTF perovskites shows a well homogeneous structure over the particles with no local deficiency or enrichment of a specific element (Fig. 4.16).

Table 4.3: Crystallite sizes (**Φ**) retrieved from XRD, specific surface area ($\mathbf{S_{BET}}$) and pore volume ($\mathbf{V_P}$) determined by N_2 physisorption, average atomic composition of elements determined by EDX (at. % values normalized by total nominal cation amount in $La_{0.3}Sr_{0.7}Ti_{1-x}Fe_xO_{3\pm\delta}$ molecular formula), and composition of different Fe sites (Fe^{3+} site 1, Fe^{3+} site 2 and Fe^{4+}) retrieved by Mössbauer spectroscopy for investigated $La_{0.3}Sr_{0.7}Ti_{1-x}Fe_xO_{3\pm\delta}$ solid solutions from 0 (LST.00F) to 50 (LST.50F) mol.% Fe substitution on B-site.

Sample	Φ [nm]	S_{BET} [$m^2\ g^{-1}$]	V_P [$cm^3\ g^{-1}$]	La	Sr	Ti	Fe	Fe^{3+} 1 [%]	Fe^{3+} 2 [%]	Fe^{4+} [%]
LST.00F	22	54	0.21	0.29	0.72	1.00	-	-	-	-
LST.10F	27	63	0.19	0.29	0.74	0.84	0.13	59	41	-
LST.30F	25	65	0.20	0.34	0.65	0.67	0.34	60	36	4
LST.50F	22	59	0.23	0.29	0.70	0.55	0.53	60	30	10

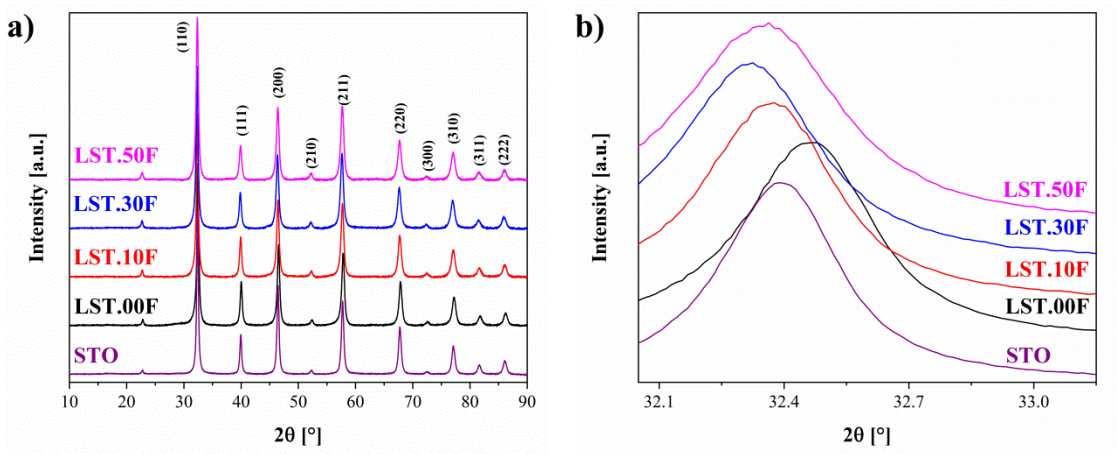

Figure 4.17: X-ray diffractograms of investigated $La_{0.3}Sr_{0.7}Ti_{1-x}Fe_xO_{3\pm\delta}$ systems with $0 \leq x \leq 0.5$ (a) Magnification of [110] reflection illustrating the contraction and expansion of the lattice (b). Template free $SrTiO_3$ labeled as STO is included for comparison.

X-ray diffractograms on Fig 4.17a points to a pure-phase cubic perovskite structure with Pm-3m space group for all samples in accordance with microscopy findings. Crystallite sizes extracted by applying Scherrer equation (3.4) on the [110] reflection were calculated to have similar values between 22 – 27 nm (Table 4.3). The influence of substitution on the unit cell

parameter of the perovskite oxides were analyzed by evaluating the shift of the [110] reflection (Fig. 4.17b). When La^{3+} (r = 1.36 Å) is substituted on the Sr sites (r = 1.44 Å), the unit cell shrinks which is characterized by the shift of the reflection towards higher 2θ angles. Upon iron substitution on Ti^{4+} sites (r = 0.605 Å), the reflection initially shifts towards lower 2θ and then back to higher 2θ angles with increasing iron amount. The pertaining expansion and contraction of the unit cell were explained by incorporation of Fe^{3+} (r = 0.645 Å) and Fe^{4+} (r = 0.585 Å) ions to the lattice respectively. It is well established for intermediate STF compositions that at low amounts of iron substitution, only Fe^{3+} species are present in the lattice due to higher stability of this oxidation state, whereas Fe^{4+} ions start to form at higher iron amounts (≥ 30 mol%) [60,366].

Mössbauer spectroscopic analysis was performed to precisely investigate the oxidation state and local chemical environment of the iron species in the perovskite lattice. The spectra show a similar central absorption for each sample which is typically assigned to paramagnetic iron nuclei (Fig. 4.18). The type and relative amount of different Fe species were summarized on Table 4.3, whereas the Mössbauer parameters were given on Table 6.3.

The best fit for LST.10F was given with two octahedral ferric sites separated by their differing symmetrical environments. The presence of separate symmetrical environments can be justified by double substitution of Sr and La species on the A-site [366,367]. When the iron substitution was increased to 30 mol.% (LST.30F), formation of Fe^{4+} sites at the expense of the octahedral Fe^{3+} species (Fe^{3+} site 2) was identified. Relative amounts of Fe^{4+} species increased from 4 to 10 % when the iron substitution increased from 30 to 50 mol.% confirming the lattice contraction determined by XRD (Fig. 4.17b).

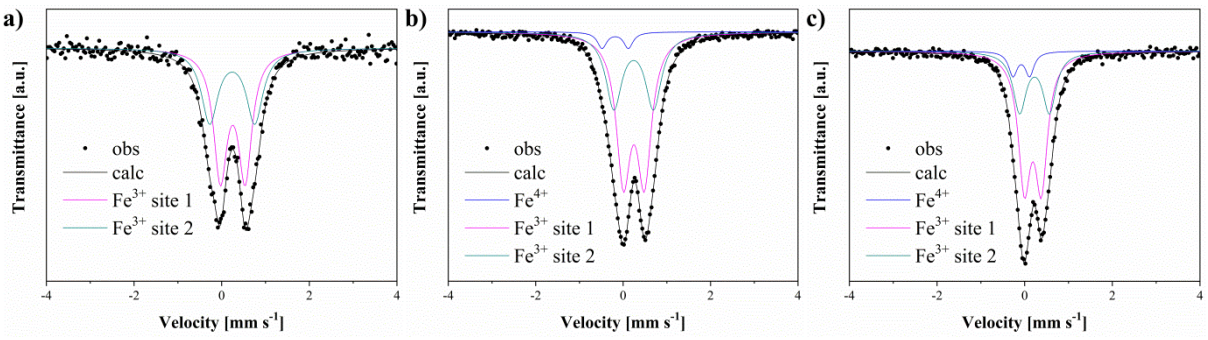

Figure 4.18: Mössbauer spectra and fitting of Fe sites in investigated $La_{0.3}Sr_{0.7}Ti_{1-x}Fe_xO_{3\pm\delta}$ solid solutions (a) LST.10F (b) LST.30F (c) LST.50F.

Electrical properties of the LSTF solid solutions with varying Fe amount were assessed by electrochemical impedance spectroscopy (EIS). The analysis was performed at 600 °C under 4% oxygen atmosphere in order to preserve materials' structural parameters. The Arrhenius plots extracted from EIS on Fig. 4.19 show that the conductivity of the systems increases as expected with increasing iron amount. A substantial drop in the activation energy of charge transport was determined when the x value in $La_{0.3}Sr_{0.7}Ti_{1-x}Fe_xO_{3\pm\delta}$ increased from 0.1 to 0.3, whereas further increase in the iron substitution to 50 mol.% did not engender a further alteration in E_a^{EIS} (Table 4.3). The latter case indicates an unchanged transport mechanism for $x \geq 0.3$, where the increasing charge carrier concentration (holes and oxygen vacancies) accounts for the rising conductivity. The changes in the transport regime between 10 to 30 mol.% Fe substitution can be described by the defect model of LSTF under oxidizing conditions presented by Perry et al. (See Fig. 2.20) [298]. In the condition where [La] > [Fe], oxygen vacancy and hole formation are suppressed resulting in the slowed down charge transport. When [Fe] ≥ [La] condition is fulfilled, further charge carriers are formed creating the substantial enhancement in the charge transport mobility.

X-ray photoelectron spectroscopy was employed to determine the changes in the chemical nature of elements on the surface of LSTF solid solutions with varying Fe substitution. All elements in LSTF lattice were identified on the surface in agreement with the ratios determined from EDX spectroscopy (Fig. 4.20a). Peaks observed at the binding energy range between 60 – 10 eV can be attributed to the different p and s states of Sr (4s, 4p), Ti (3s, 3p), La (5p, 5s) and O (1s) [357].

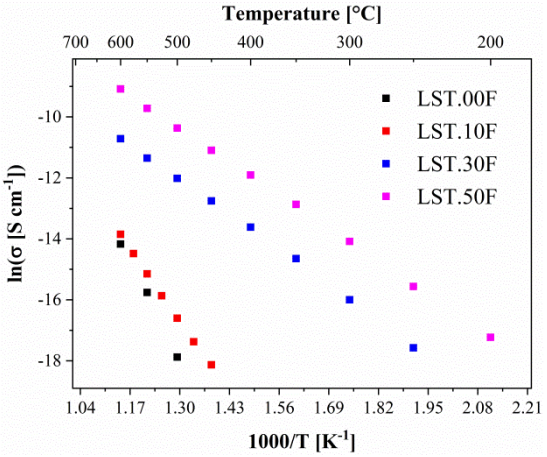

Figure 4.19: Arrhenius plots of conductivity retrieved by EIS for investigated $La_{0.3}Sr_{0.7}Ti_{1-x}Fe_xO_{3\pm\delta}$ solid solutions.

Close inspection of oxygen 1s peaks showed that the amount of chemisorbed oxygen which can be assigned to surface oxygen vacancy sites increased progressively with increasing Fe amount (Fig. 4.20b). In-depth analysis of different Fe species on the LSTF surface could not be achieved due to the presence of satellite peaks and close proximity of Fe^{3+} and Fe^{4+} binding energies preventing the deconvolution as well as the poor signal to noise ratio.

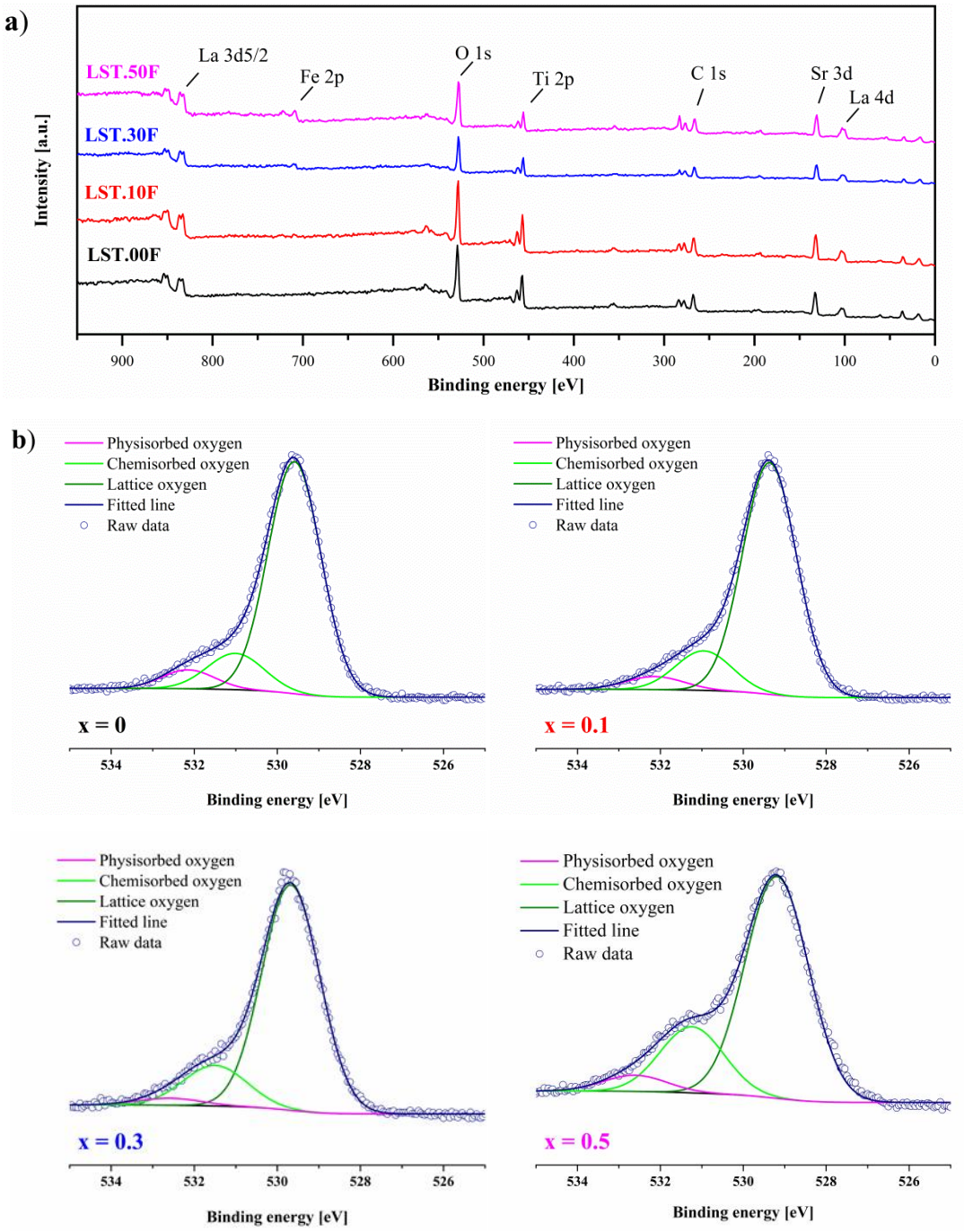

Figure 4.20: XPS survey of the surface for investigated $La_{0.3}Sr_{0.7}Ti_{1-x}Fe_xO_{3\pm\delta}$ solid solutions with $0 \leq x \leq 0.5$ (a) O 1s region of each spectrum (b).

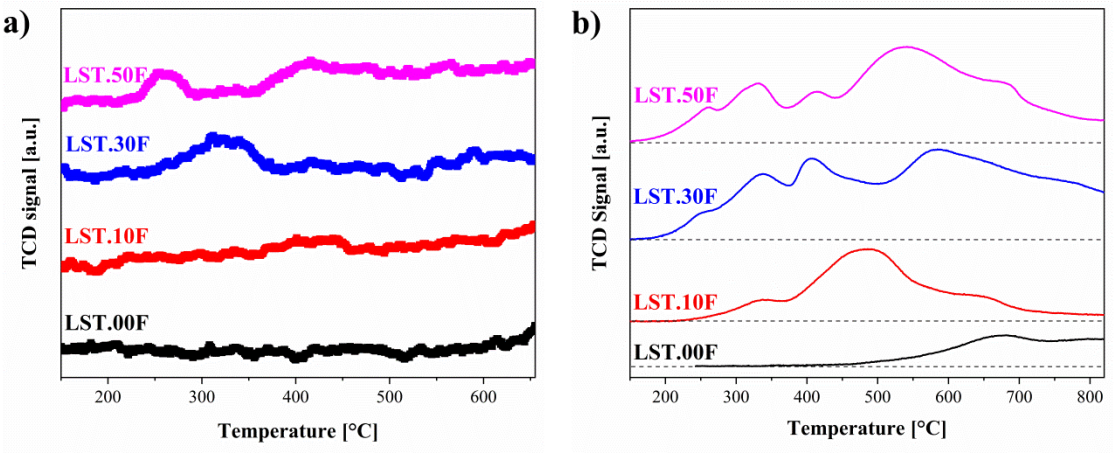

Figure 4.21: (a) Temperature programmed desorption (TPD-O_2) and (b) Temperature programmed reduction (TPR-H_2) profiles of $La_{0.3}Sr_{0.7}Ti_{1-x}Fe_xO_{3\pm\delta}$ with $0 \leq x \leq 0.5$. Curves are shifted by offsets for clarity, dashed lines correspond to the baselines of each curve.

The oxygen mobility and reducibility of the LSTF samples were investigated via temperature programmed experiments concerning desorption of oxygen (O_2-TPD) and reduction by hydrogen (H_2-TPR). TPD-O_2 and TPR-H_2 profiles are plotted in Fig 4.21, whereas the amounts of O_2 desorption and H_2 consumption for each sample are given on Table 4.3.

Two separate peaks are commonly found in the TPD-O_2 profiles of perovskite oxide materials. The first peak originate from the so-called alpha oxygen (α-oxygen) which is associated to the desorption of weakly adsorbed oxygen species from the surface at relatively low temperatures (T < 500 °C). The peak observed above 500 °C is typically associated to the desorption of tightly bound lattice oxygen, i.e. beta oxygen (β-oxygen) [368,369].

TPD-O_2 profile of LST.00F ($La_{0.3}Sr_{0.7}TiO_{3+\delta}$) shows an oxygen release only above 600 °C, which can be attributed to release of β-oxygen (Fig 4.21a). As x in $La_{0.3}Sr_{0.7}Ti_{1-x}Fe_xO_{3\pm\delta}$ increase from 0.1 to 0.5, the onset of β-oxygen evolution shifts towards lower temperatures down to 400 °C and the intensity of this continuous signal in the investigated temperature range increases. Moreover, an additional low temperature peak associated with α-oxygen is present in Fe-substituted samples. The onset temperature for α-oxygen release was reduced from ~ 400 °C for LST.10F to as low as ~ 250 °C for LST.50F. Interestingly, it was observed that largest α-oxygen peak was given for LST.30F rather than LST.50F, which will be further discussed in the evaluation of catalytic performance in LSTF systems. The quantitative determination of separate contributions of alpha and beta oxygen was not possible due to the

continuous release of oxygen at each temperature. However, total amounts of oxygen release per unit mass increases progressively with increasing Fe-substitution. This trend is further confirmed by XPS, which shows increasing amount of chemically adsorbed oxygen species at higher Fe amounts (Table 4.4).

The redox features of LSTF perovskites were characterized by H_2-TPR (Fig. 4.21b). The H_2-TPR profile of LST.00F ($La_{0.3}Sr_{0.7}TiO_{3+\delta}$) is characterized by a broad single peak appearing above 650 °C, which can be attributed to reduction of Ti^{4+} to Ti^{3+}. In contrast to $La_{0.3}Sr_{0.7}TiO_{3+\delta}$, Fe-substituted LSTF samples show several reduction steps. The initial peak observed both for LST.30F and LST.50F around ~260 °C can be assigned to reduction of Fe^{4+} to Fe^{3+} [172,370]. In confirmation to the findings of Mössbauer spectroscopy, this signal was not observed for LST.10F (10 mol.% Fe), indicating the absence of Fe^{4+} sites at this substitution amount. The three signals observed between 300 °C and 650 °C were attributed to the gradual reduction of Fe^{3+} to Fe^{2+} [172,371]. The final peak appearing after 650 °C may be attributed to Ti^{4+} reduction following $La_{0.3}Sr_{0.7}TiO_{3+\delta}$, however reduction of Fe^{2+} to metallic iron is also possible at this temperature range [172,371].

4.2.2 Influence on catalytic performance: Catalytic CH_4 and CO oxidation

Percolated pore structure with high surface area, highly crystalline pure phase structure, presence of mixed oxidation states on the B-site, high reducibility and oxygen mobility determined for LSTF samples deem these materials promising candidates for oxidation catalysis [53,370,372]. The performance of LSTF oxides with varying Fe substitution was investigated via CO and CH_4 oxidation tests. Since CO and CH_4 oxidation are respectively low and high-temperature reactions, their combined study enables a comprehensive understanding of the catalytic properties of $La_{0.3}Sr_{0.7}Ti_{1-x}Fe_xO_{3\pm\delta}$ in oxidative catalysis.

Oxidation of methane over reference $SrTiO_3$ and $La_{0.3}Sr_{0.7}TiO_{3+\delta}$ perovskites prepared in same conditions leads to a similar conversion values of about 10 % at 600 °C, whereas carbon monoxide conversion over these catalysts leads to similar conversion of ~ 5% at 300 °C (Fig. 4.22). These results are in agreement with reports in literature that postulate A-site substitution does not have a significant influence on the catalytic activity [5]. The slight performance loss observed for the lanthanum containing sample can be explained through minor suppression of charge carriers, holes and oxygen vacancies, due to donor substitution in the system (Fig. 2.20).

Table 4.4: Activity parameters of LSTF catalysts towards oxidation catalysis. **H_2-TPR**: Hydrogen consumption obtained from temperature programmed reduction experiments. **O_2-TPD**: Oxygen desorption obtained from temperature programmed desorption experiments. E_a^{EIS} : Activation energy for charge migration obtained by electrochemical impedance spectroscopy. $E_a^{CO\ ox.}$, $E_a^{CH_4\ ox.}$: Activation energy for CH_4 and CO oxidation reactions over LSTF catalysts obtained below 10% conversion. *m*, *n*: Empirically calculated reaction orders ***m*** with respect to CH_4 and ***n*** with respect to O_2 obtained below 10% CH_4 conversion (reaction rate = $kP_{CH_4}{}^{m}P_{O_2}{}^{n}$), **SRR**: *Suprafacial* reaction rate dependent on the contribution of α-oxygen. IRR: *Intrafacial* reaction rate dependent on the contribution of β-oxygen. **IRR** and **SRR** were obtained at 510 °C with $pCH_4 = 0.002$, $pO_2 = 0.03$ atm. **TRR**: Total reaction rate.

Sample	H_2-TPR [mmol g^{-1}]	O_2-TPD [µmol g^{-1}]	E_a^{EIS} [kJ mol^{-1}]	$E_a^{CO\ ox.}$ [kJ mol^{-1}]	$E_a^{CH4\ ox.}$ [kJ mol^{-1}]	*m*	*n*	SRR [x 10^{-8}]	IRR [x 10^{-8}]	TRR [x 10^{-8}]
LST.00F	0.43	1.5	-	92	134	0.71	0.39	0.806	0.266	1.07
LST.10F	0.72	9.4	150	64	109	0.73	0.26	4.06	3.30	7.36
LST.30F	1.26	38.3	74	56	92	0.68	0.14	11.2	43.9	55.1
LST.50F	1.31	108.6	70	66	90	0.76	0.02	4.73	73.2	77.9

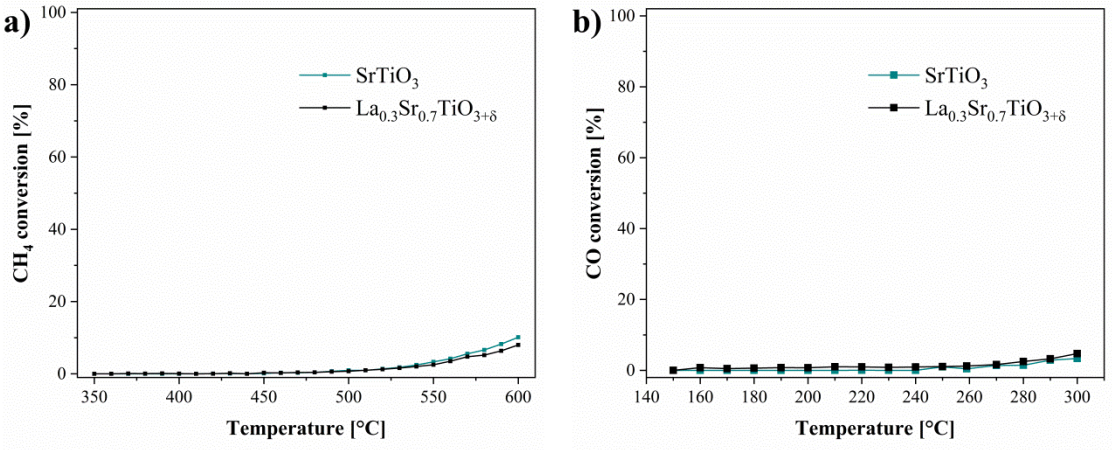

Figure 4.22: Steady state conversions obtained for CH_4 oxidation (a) CO oxidation (b) over $SrTiO_3$ (STO) and $La_{0.3}Sr_{0.7}TiO_{3+\delta}$ (LST.00F).

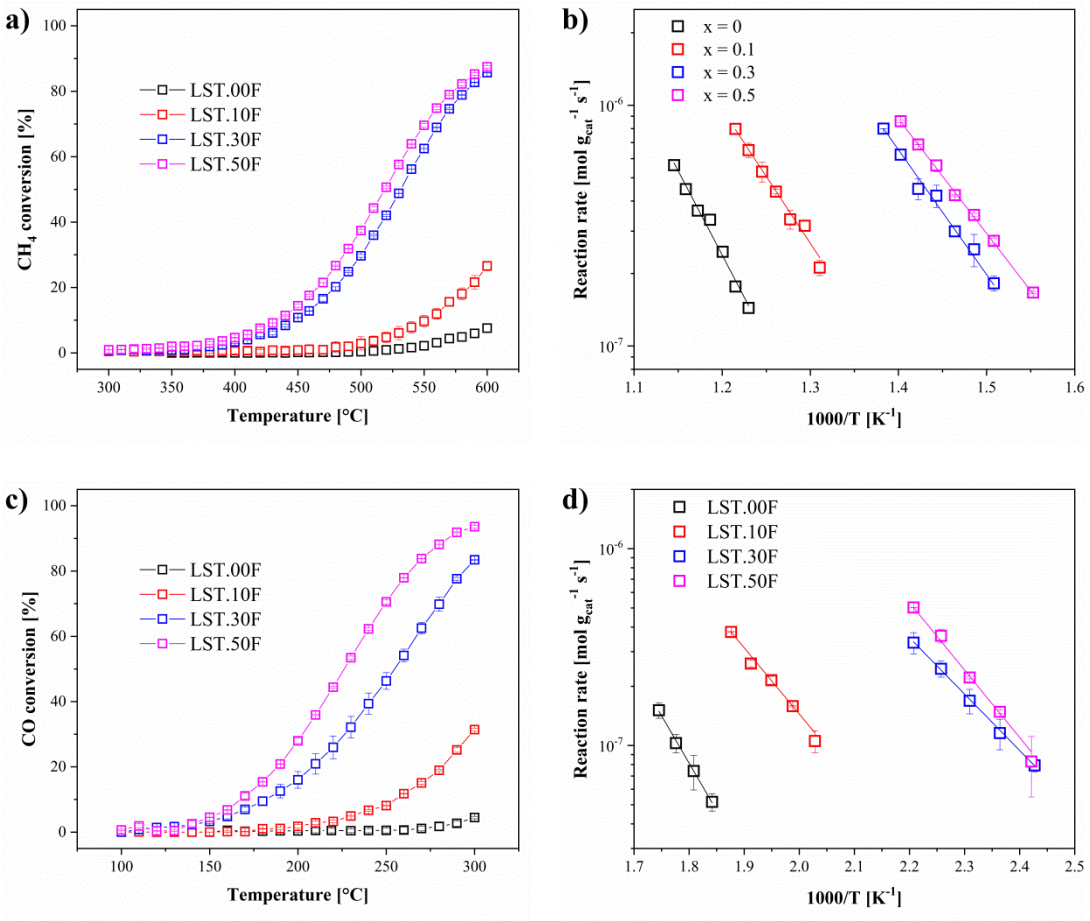

Figure 4.23: Steady state conversions obtained for the oxidation reaction of CH_4 (a) and oxidation reaction of CO (c) over $La_{0.3}Sr_{0.7}Ti_{1-x}Fe_xO_{3\pm\delta}$ catalysts with $0 \leq x \leq 0.5$ and pertaining Arrhenius plots respectively for CH_4 oxidation (b) and CO oxidation (d).

Steady state CH_4 conversion plots obtained for $La_{0.3}Sr_{0.7}Ti_{1-x}Fe_xO_{3\pm\delta}$ catalysts are illustrated on Fig 4.23a. Products of CH_4 oxidation over LSTF catalysts were solely CO_2 and H_2O in each test, pointing to a complete oxidation of methane. The conversion increases with increasing iron substitution in the $La_{0.3}Sr_{0.7}Ti_{1-x}Fe_xO_{3\pm\delta}$ catalyst lattice leading to almost complete oxidation (~90%) at 600 °C for both x = 0.3 and x = 0.5. In contrast, reaction over LST.10F leads to only 27% conversion at the same temperature, which further decreases to 8% for iron-free LST.00F. The substantial activity difference induced by increasing Fe substitution from 10 to 30 mol.% may be explained through the defect chemistry of the LSTF solid solution as evidenced by electrochemical impedance spectroscopy (Fig. 4.19).

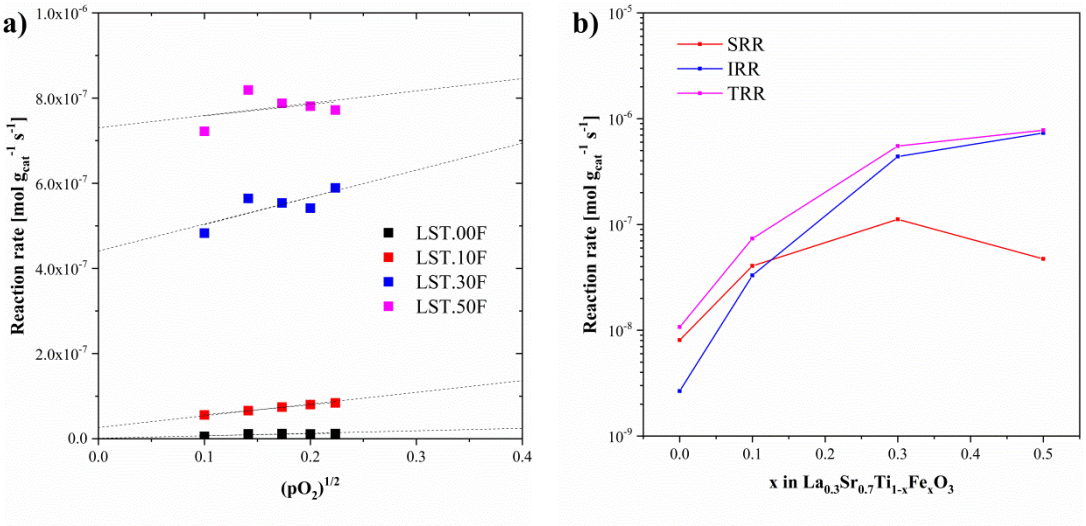

Figure 4.24: (a) Plots of methane oxidation rate, *r*, over $La_{0.3}Sr_{0.7}Ti_{1-x}Fe_xO_{3\pm\delta}$ catalysts with $0 \leq x \leq 0.5$ vs oxygen partial pressure. Data acquired at 510 °C, total pressure is 1 atm. (b) Change in *suprafacial* reaction rate (SRR) governed by α-oxygen and *intrafacial* reaction rate (IRR) governed by β-oxygen with variations in Fe substitution. TRR corresponds to the total reaction rate.

The catalytic properties of the LSTF oxides in a low temperature reaction were investigated by CO oxidation tests. Similar trend with CH_4 oxidation was observed for the conversion ratios as well as the activation energy values calculated from pertaining Arrhenius plots (Fig. 4.23c-d). Iron-free catalyst has a large activation barrier of 92 kJ mol^{-1}, whereas iron substituted samples show similar E_a values between 56 – 66 kJ mol^{-1} (Table 4.4). Thus, in this case the differing catalytic performance of the $La_{0.3}Sr_{0.7}Ti_{1-x}Fe_xO_{3\pm\delta}$ perovskites with varying x values can be explained by a compensatory effect [372], which postulates that increasing

conversion ratios at higher Fe substitution are due to the higher number of active sites on catalyst surface rather than an enhanced reactivity of individual sites.

In light of the catalytic performance studies combined with the structural characterization of the $La_{0.3}Sr_{0.7}Ti_{1-x}Fe_xO_{3\pm\delta}$ catalysts, it can be concluded that the Fe species directly provide the active sites for the oxidation reaction. The dependence of the reaction on the reacting oxygen and methane species were determined via kinetic studies (Table 4.4). The empirical rate equation for methane oxidation can be expressed as:

$$r = k\, P_{CH_4}^{m} P_{O_2}^{n} \tag{4.1}$$

where r is the reaction rate, k is the rate constant, $P_{CH_4}^{m}$ and $P_{O_2}^{n}$ are partial pressure of the gases methane and oxygen with reaction orders of m and n respectively. The value, m, was determined as ~ 0.7 for all LSTF oxides independent of Fe substitution. Methane oxidation over oxide catalysts typically leads to first order rate with respect to CH_4 indicating an insufficient methane supply for the surface reaction. This can be associated to the high energy barrier regarding dissociative adsorption of methane on catalyst surface. On the other hand, the reaction order, n, determined for oxygen decreases from 0.46 to ~ 0 with increasing Fe-substitution. The independence of the reaction from oxygen partial pressure at higher Fe-loading indicates that Fe-sites promote the oxygen activity on the catalyst surface. As discussed in Chapter 2.3.2, a previously developed kinetic model based on Mars and von Krevelen (MvK) mechanism which identifies two simultaneously occurring processes can be employed to describe the change in kinetics of CH_4 oxidation over LSTF oxides [10,141]:

$$r = k_s P_{CH_4} (K_{O_2} P_{O_2})^{1/2} + k_i P_{CH_4} \tag{4.2}$$

where k_s and k_i are rate constants for suprafacial and intrafacial reactions respectively, whereas K_{O_2} is the equilibrium constant for oxygen adsorption. The term describing the suprafacial reaction; $(k_s P_{CH_4} (K_{O_2} P_{O_2})^{1/2})$ is an equilibrium process which is dependent on oxygen partial pressure and therefore loosely bound α-oxygen is mainly associated to this term. As methane oxidation is a high-temperature catalytic reaction, bulk of the catalyst can also actively take part in the reaction. The intrafacial reaction term $(k_i P_{CH_4})$ describes the bulk contribution from the tightly bound lattice oxygen (β-oxygen) to the reaction and is independent of oxygen partial pressure. In this case, the oxygen from oxide lattice is

consumed and subsequently replenished in the reaction process [138,139]. The variation in the reaction order, n, of LSTF catalysts with respect to oxygen can therefore be explained by the simultaneous contributions of suprafacial and intrafacial processes [10,373] .

Separate contributions of alpha and beta oxygen species were successfully identified using the kinetic model expressed in Eq. (4.2). Measured reaction rates are in very good agreement with the kinetic model. Fig 4.24a plots the reaction rate of LSTF catalysts against $(P_{O_2})^{1/2}$. Contribution of intrafacial mechanism is given as the intercept of the dotted lines. By subtracting this value from the total reaction rate, the contributions of suprafacial mechanism which are dependent on β-oxygen were determined. Fig 4.24b illustrates the evolution of suprafacial (SRR) and intrafacial reaction rate (IRR) as well as the total reaction rate as a function of Fe-substitution in LSTF catalysts. The participation of β-oxygen to the reaction increases progressively with increasing Fe-loading of the LSTF catalyst, exceeding the intrafacial contribution at Fe-substitution higher than 30 mol.%. Contrarily, the intrafacial reaction rate (IRR) increases up to 30 mol.% Fe-substitution followed by a slight decrease at higher Fe-loading. This phenomenon, also characterized by the α-oxygen amounts in TPD-O_2 profiles of the catalysts (Fig. 4.21a), may be explained by a dilution effect. The intrafacial reaction can be promoted by the dilution of Fe sites on the surface, since the reactivity of the individual sites with oxygen bound to isolated Fe atoms are enhanced in comparison to sites with oxygen bound to several Fe atoms [12]. The existence of dilution effect is also supported by the activation energy lowering observed for CO oxidation over the catalyst with 30 mol.% Fe substitution.

The kinetic studies show that the catalyst performance can be increased progressively with increasing Fe-load particularly due to the enhanced contributions of β-oxygen species. However, the structural instability of the perovskite oxide engendered by increasing Fe-substitution should not be overlooked (Fig 2.21). Thus, LST.30F composition may be regarded to provide an optimal compromise between performance and stability by maximizing the dilution effect.

Although, state-of-art Pd-based catalysts for methane oxidation show at least about a magnitude higher performance than oxides, they suffer from deactivation in the presence of water vapor [177,374]. The influence of water vapor on the catalytic activity of LSTF catalysts was investigated by flowing 1.2 vol.% H_2O in the feed gas for 1 h at temperatures

between 450 and 550 °C. Figure 4.25 shows that regardless of Fe substitution, all catalysts showed a minor reduction in their reaction rate which becomes more pronounced at lower temperatures. The effect was fully reversible and reaction rates went back to their former values when flow of water vapor was stopped. These results are in line with previous works and indicate that inhibition of reaction rate is due to competitive adsorption of O_2 and H_2O on the catalyst surface [10,141].

Thermal stability of the LSTF materials was studied by exposing the samples to heat treatment under oxidizing and reducing atmospheres. All samples retained their crystalline phase, microstructure and textural features as shown by XRD (Fig. 4.26) and nitrogen physisorption analysis (Fig. 4.27) subsequent to the heat treatment. Retained crystallite size and surface areas of the samples after heat treatment under reducing atmosphere are reported on Table 4.5.

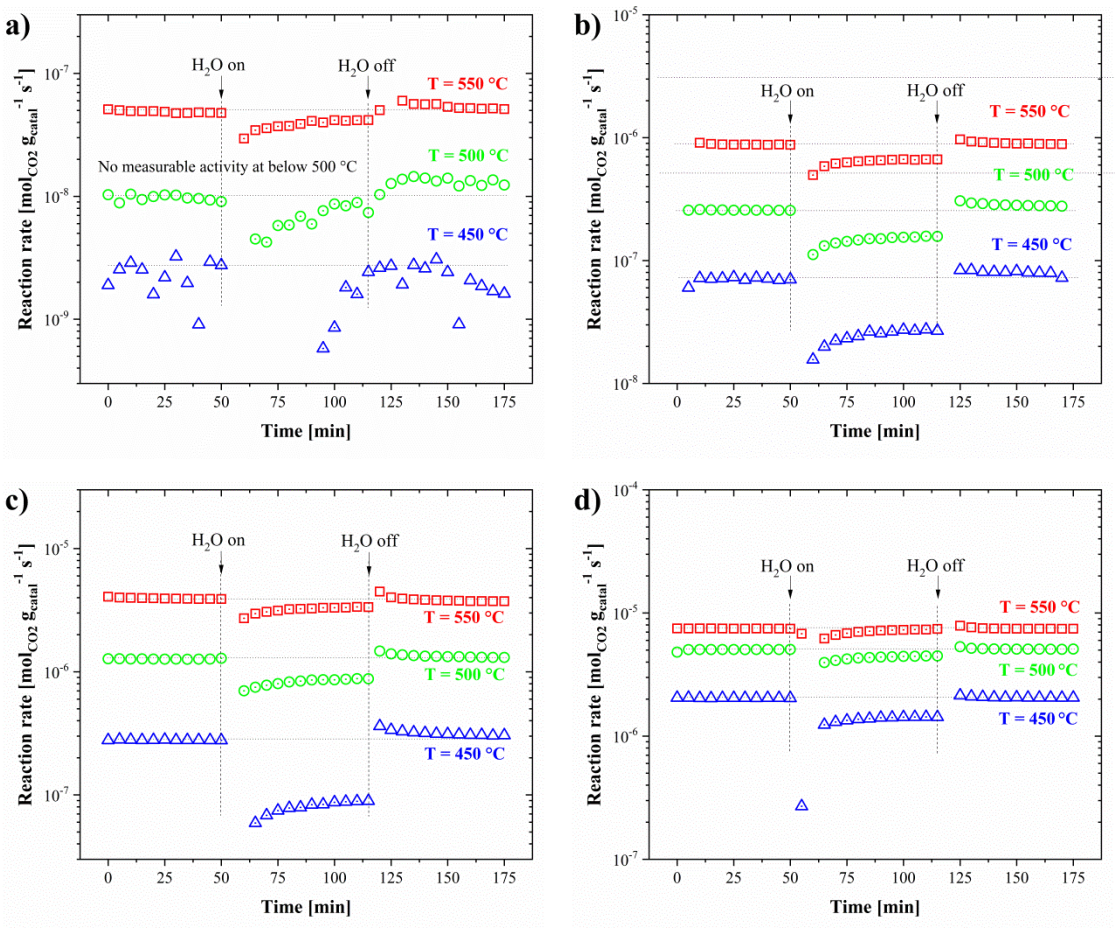

Figure 4.25: Influence of H_2O vapor (1.2 vol.%) on CH_4 oxidation over $La_{0.3}Sr_{0.7}Ti_{1-x}Fe_xO_{3\pm\delta}$ catalysts (a) LST.00F (b) LST.10F (c) LST.30F (d) LST.50F.

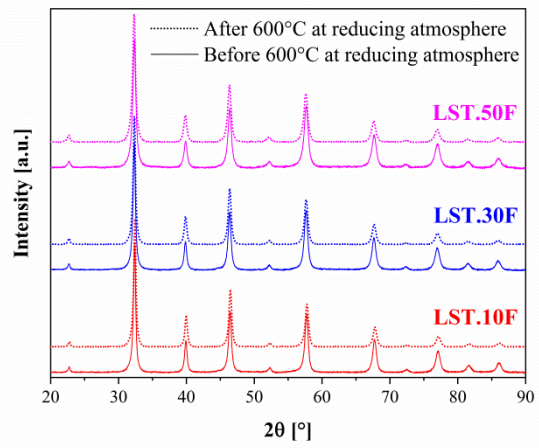

Figure 4.26: X-ray diffractograms of LSTF catalysts before and after heat treatment at 600 °C under reducing atmosphere.

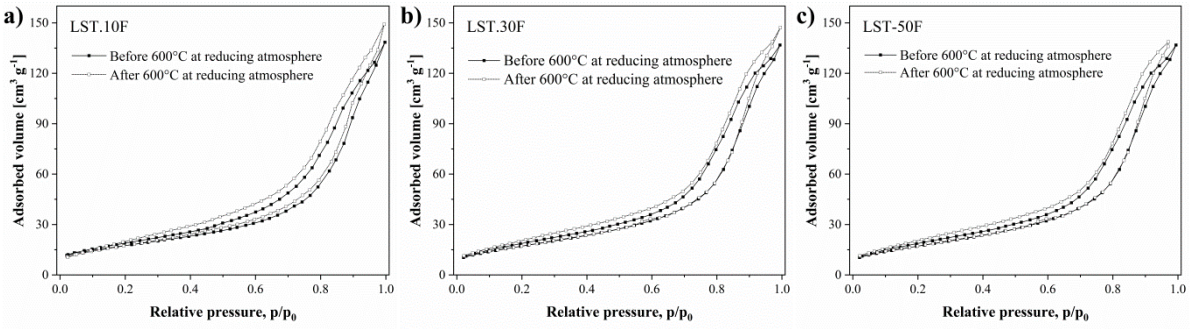

Figure 4.27: Nitrogen physisorption isotherms of (a) LST.10F (b) LST.30F and (c) LST.50F before and after heat treatment at 600 °C under reducing atmosphere.

Table 4.5: Crystallite sizes (Φ) retrieved from XRD, specific surface area (S_{BET}) determined by N_2 physisorption before (Φ^i, S_{BET}^i) and after (Φ^f, S_{BET}^f) heat treatment of LSTF systems at 600 °C under reducing atmosphere.

Sample	Φ^i [nm]	Φ^f [nm]	S_{BET}^i [$m^2\ g^{-1}$]	S_{BET}^f [$m^2\ g^{-1}$]
LST.10F	27	27	63	66
LST.30F	25	25	65	65
LST.50F	20	20	59	56

The catalytic performance of highly performing LST.30F and LST.50F oxides were compared with bulk and porous ferrite-based perovskite catalysts reported in literature. In order to account for different reaction conditions and catalysts employed in each work, a turnover frequency (TOF) value was calculated for each catalyst with following equation:

$$\mathrm{TOF}(s^{-1}) = \frac{(converted\ CH_4\ amount)}{(time)\times(Amount\ of\ Fe\ active\ sites\ in\ catalyst)} \tag{4.3}$$

Molar amount of Fe species in each sample was calculated using the catalyst stoichiometry and total mass of catalyst used in the test. The conversion ratios were extracted at 560 °C and 300 °C for CH_4 and CO oxidation respectively. In the case of TOF calculation for $LaCo_{0.6}Fe_{0.4}O_3$ [170], $La_{0.66}Sr_{0.34}Ni_{0.2}Fe_{0.8}O_{3-\delta}$ [158], $La_{0.66}Sr_{0.34}Co_{0.2}Fe_{0.8}O_{3-\delta}$ [158], Ni and Co species in the B-site of perovskite were included to the active site calculation. The resulting TOF values for each ferrite-based perovskite catalyst were summarized on Fig. 4.28.

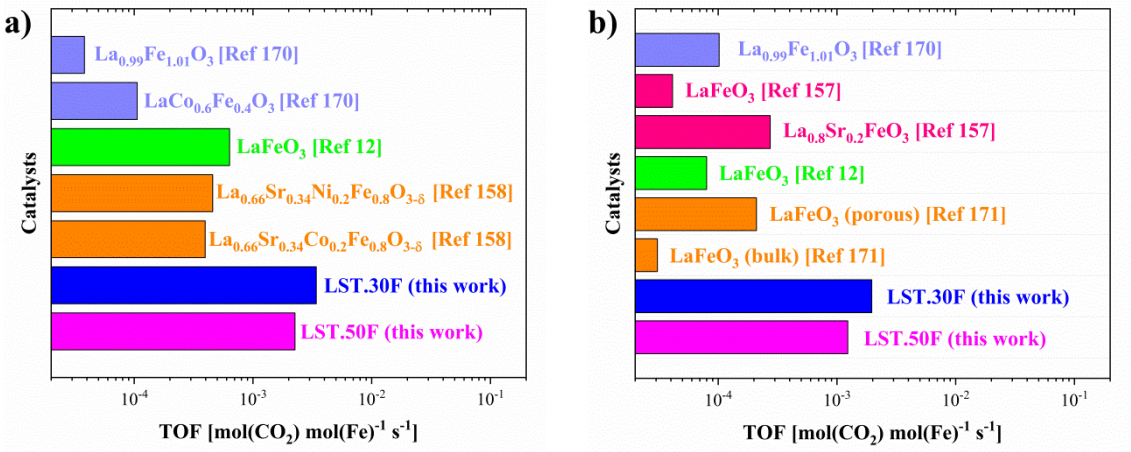

Figure 4.28: Turnover frequencies (See Eq. 4.3) of LST.30F and LST.50F compared with reported values for Fe-based perovskite catalysts in literature [12,157,158,170,171] (a) CH_4 oxidation at T = 560 °C (b) CO oxidation at T = 300 °C.

The results indicate that LST.30F and LST.50F catalysts attain significantly higher activity in CO and CH_4 oxidation with up to 90 times performance improvement in comparison to the catalyts reported in literature. The substantial catalytic performance of the LSTF samples prepared in this work can be explained by the unique textural and structural properties of our materials. The percolated mesoporous structure embedded on catalyst particles of up to micrometer scale guarantees effective solid-gas contact and short diffusion pathways for the

mobile oxygen species. Moreover, high porosity of the LSTF materials in this work is reinforced by excellent crystallinity, phase-purity and stability, which can further promote the catalytic activity and is rarely achieved for complex multi-metal oxides reported in literature.

4.2.3 Sub-chapter summary

Mesoporous solid solutions with $La_{0.3}Sr_{0.7}Ti_{1-x}Fe_xO_{3\pm\delta}$ ($0 \leq x \leq 0.5$) were successfully prepared by a simple variation of the polymer complex synthesis. The evolution of catalytic properties of the materials upon changing amount of co-substitution was investigated through CO and CH_4 oxidation tests.

LSTF samples showed excellent crystallinity and phase purity as well as precise agreement to their respective nominal stoichiometries. Mesoporous morphology with a specific surface area of ~ 65 $m^2\ g^{-1}$ was determined for each solid solution, despite the differing Fe substitution amounts. Increasing iron amounts in the LSTF solid solutions led to gradual enhancement of charge carrier activity due to the creation of electron holes and oxygen vacancies in the lattice. In accordance with the change in charge transport properties, low temperature reducibility and oxygen release of the samples were greatly enhanced at higher Fe substitution.

Carbon monoxide and methane oxidation tests indicated excellent catalytic activity for LSTF samples with increasing iron content, leading to a maximum of over 90% conversion of CH_4 and CO at 600 and 300 °C respectively for 50% Fe substituted sample, LST.50F. Through kinetic studies of CH_4 oxidation over LSTF catalysts, suprafacial and intrafacial contributions to the total reaction rate were successfully identified. The findings indicate that suprafacial reaction rate over LST.30F is maximized, since the number of highly reactive isolated iron sites is highest at 30% Fe substitution. As a result, LST.30F shows optimal catalytic properties with minimal compromise between performance and stability. Co-substituted mesoporous LSTF samples in this work showed substantially higher performance (up to 90 times) than similar Fe-containing perovskite catalysts reported in literature.

The superior catalytic properties stem from the combined effects of morphology and composition. Fe-substitution triggers the reactivity of the catalyst by providing active reaction sites, enhanced redox properties and increased number of ionic and electronic charge carriers. Nanoporous morphology of the material with well interconnected pores, on the other hand, enables short diffusion pathways for ionic and electronic charge carriers, enhanced contact of reactants and higher number and reactivity of active sites for the reaction [14].

4.3 Design of highly porous (La,Sr)(Ti,Fe)$O_{3-\delta}$ perovskites as active support for oxidation catalysis

The attractive catalytic properties of (La,Sr)(Ti,Fe)$O_{3-\delta}$ (LSTF) solid solutions discussed on Chapter 4.2 indicate great application potential in catalysis upon further optimization of material characteristics.

Development of highly porous perovskite oxide systems with high chemical and textural complexity is not only desirable for their stand-alone catalytic performance, but also for their potential application as active supports for industry-standard supported noble metal catalysts. Recently, mesoporous MIEC oxides like CeO_2 are being widely employed as support material, thanks to their excellent oxygen supply to the active phase as well as high chemical stability and excellent dispersion of metal nanoparticles due to the highly porous structure [6,16,183,196]. Highly porous LSTF perovskites can provide a promising alternative to CeO_2 supported noble metal catalysts due to the greater relative abundance of its constituent elements and excellent stand-alone catalytic performance.

With this motivation, the influence of systematic porosity enhancement on the catalytic properties of the co-substituted LSTF oxide with nominal composition $La_{0.3}Sr_{0.7}Ti_{0.5}Fe_{0.5}O_{3-\delta}$ (LST.50F) is investigated in this sub-chapter, which showed highest absolute performance in oxidation catalysis.

LSTF samples were prepared by the cooperative assembly synthesis route that was previously implemented to prepare highly porous $SrTiO_3$ aggregates. The influence of templating process and etching treatment on the catalytic performance of the LSTF materials was investigated by methane oxidation tests. Finally, the application potential of LSTF oxides with $La_{0.3}Sr_{0.7}Ti_{0.5}Fe_{0.5}O_{3-\delta}$ nominal stoichiometry as active support was studied by depositing Pt nanoparticles on the highly porous LST.50F_40, followed by CO and CH_4 oxidation tests over LST.50F_40 supported Pt.

Porosity was varied by setting perovskite product to template molar ratio LSTF : SiO_2 between 5 : 1 (11 vol.%) to 1 : 1 (40 vol.%), similar to the range followed for $SrTiO_3$ in Chapter 4.1. Samples with $La_{0.3}Sr_{0.7}Ti_{0.5}Fe_{0.5}O_{3-\delta}$ nominal stoichiometry were labeled as LST.50F_##, where ## refers to vol.% template load from LST.50F_11 (11 vol.%) to LST.50F_40 (40 vol.%). Identical to Chapter 4.2, template free $La_{0.3}Sr_{0.7}Ti_{0.5}Fe_{0.5}O_{3-\delta}$ is named LST.50F.

4.3.1 Characterization of (La,Sr)(Ti,Fe)$O_{3-\delta}$ with tailored porosity

XRD investigations indicated that a cubic perovskite oxide single phase with space group Pm-3m was retained for all LSTF samples with varying template amounts (Fig. 4.29). Average crystallite sizes calculated with Scherrer equation (3.4) from the [110] reflection remained essentially unchanged with a slight decrease from 22 nm to 18 nm with increasing template amount (Table 4.6). The decrease in grain sizes can be related with the diffusion barrier to mass transport induced by the introduction of siliceous template.

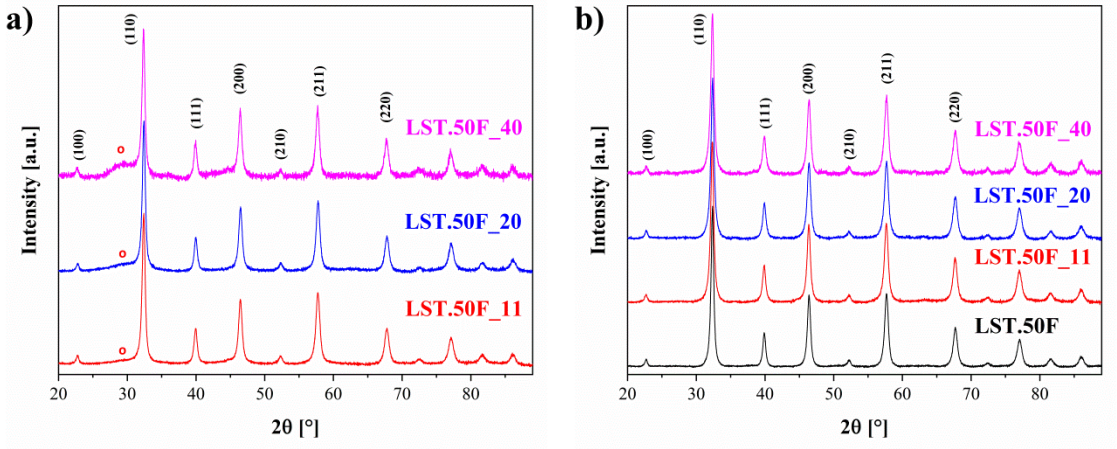

Figure 4.29: X-ray diffractograms of investigated LST.50F samples (a) as-prepared nanocomposites. Red circles indicate amorphous siliceous species. (b) pure-phase mesoporous LSTF oxides after acetic acid and sodium hydroxide treatment.

Effectivity of etching process of the siliceous template from the nanocomposite was analyzed by IR spectroscopy. Fig 4.30a shows that the carbonate impurities and siliceous species were almost completely removed from the system as a result of acetic acid and sodium hydroxide etching treatment, in line with the results for STO (Fig 4.4 – 4.6). EDX spectroscopy was employed to further analyze the elemental composition and homogeneity of the LSTF samples at local level subsequent to the etching treatment. Clear quantification of residual Si amounts could not be achieved due to the overlap of Si and Sr peaks. However, the samples showed progressively increased deviations from the nominal composition $La_{0.3}Sr_{0.7}Ti_{0.5}Fe_{0.5}O_{3-\delta}$ with increasing template loads.

The relative amounts of cations in the LSTF lattice for each sample show an increasing deficiency in Fe and Sr with higher template loads (Table 4.7). Observed deficiencies may be

a result of siliceous species bonding near Fe and Sr sites preferentially and being jointly removed as a result of etching treatment. Considering that the X-ray diffractograms display a crystalline pure cubic phase for all samples and the material has highly porous aggregate morphology, majority of the deficiency may be likely arising from the surface etching of the oxide materials. However, overall deviation from nominal stoichiometry in the bulk of the material is apparent as well in the EDX findings. High resolution TEM/EDX mapping over LSTF samples also show highly homogeneous distribution of elements over the particles with no phase-segregation (Fig. 4.31).

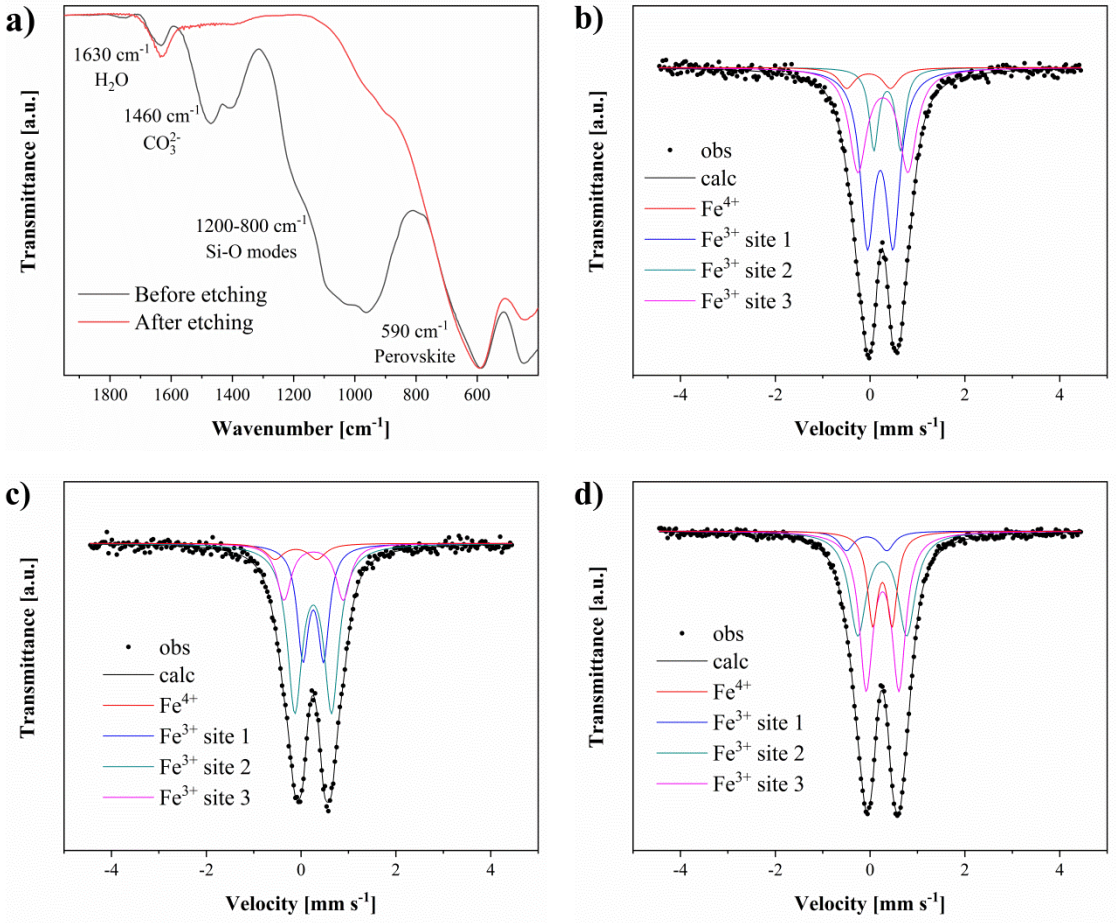

Figure 4.30: (a) Infrared spectra of LST.50F_40 chosen as representative system acquired before and after etching treatment. (b – d) Mössbauer spectra of the templated LST.50F samples (b) LST.50F_11 (c) LST.50F_20 (d) LST.50F_40.

Mössbauer spectra of the templated LST.50F samples all show similar characteristics (Fig. 4.30b – d). The best fitting is achieved by using a 4 component model: one doublet is assigned to Fe^{4+} and the other three to Fe^{3+} sites (Table 4.7, Table 6.4). The increasing of the SiO_2

template load do not modify the amount of Fe^{4+}. With regard to the three Fe^{3+} sites, site 1 and 2 can be assigned to octahedral Fe^{3+} differing in their symmetrical environments due to double substitution of Sr and La species, in accordance with the spectrum of template free LST.50F (Table 4.3) [366,367]. The third Fe^{3+} site, which is only present for templated samples, can be assigned to octahedral ferric cations that are within a symmetrical environment associated with silicates in structure. The relative concentration of these sites increases substantially with increasing template load from 16 to 38 % at the expense of Fe^{3+} site 1.

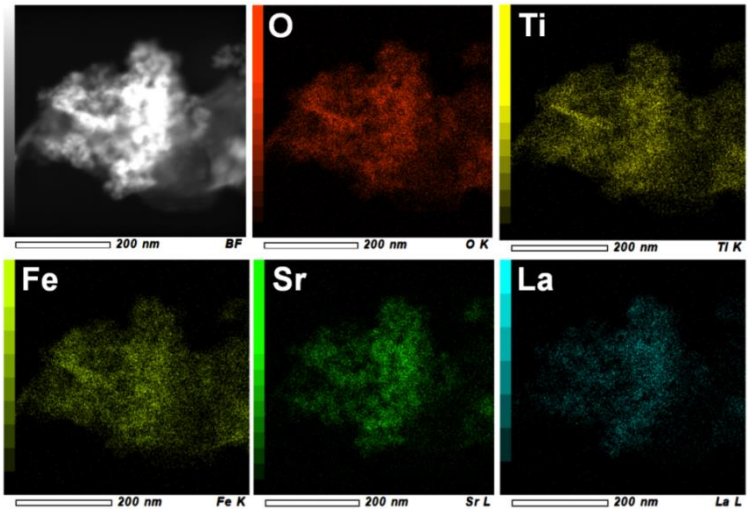

Figure 4.31: HR-TEM/EDX mapping over a LST.50F_40 particle chosen as representative system.

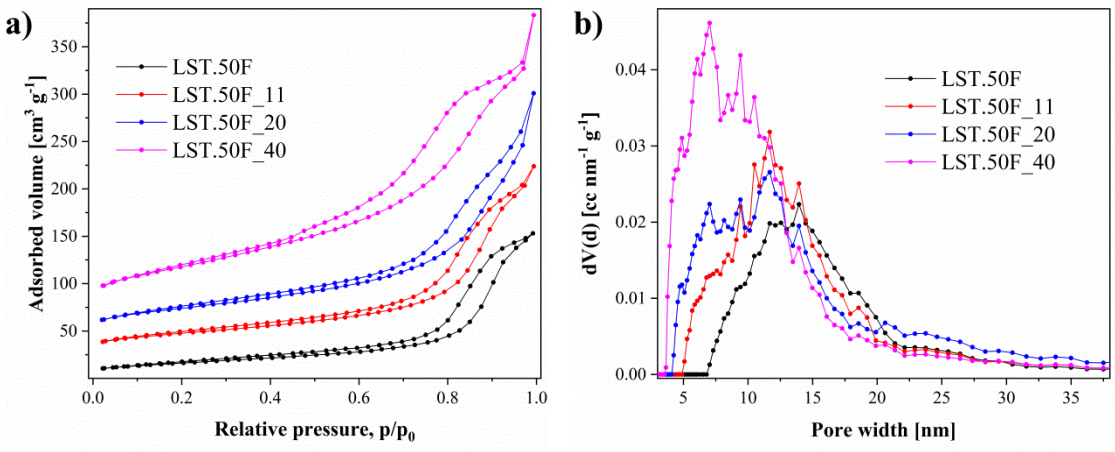

Figure 4.32: Nitrogen physisorption isotherms (a) and pore size distribution plots (b) of investigated LST.50F samples. The isotherms were shifted by 20 cm^3 g^{-1} offset for clarity.

Table 4.6: Initial crystallite sizes (Φ^i) retrieved from XRD, specific surface areas (S_{BET}^i) and pore volumes (V_P^i) determined by N_2 physisorption, as well as final crystallite size (Φ^f) and specific surface areas (S_{BET}^f) and pore volumes (V_P^f) after heat treatment at 600 °C under reducing atmosphere for investigated LST.50F samples.

Sample	Φ^i [nm]	S_{BET}^i [$m^2\ g^{-1}$]	V_P^i [$cm^3\ g^{-1}$]	Φ^f [nm]	S_{BET}^f [$m^2\ g^{-1}$]	V_P^f [$cm^3\ g^{-1}$]
LST.50F	22	60	0.24	-	-	-
LST.50F_11	20	98	0.29	20	98	0.31
LST.50F_20	19	125	0.34	-	-	-
LST.50F_40	18	201	0.41	18	168	0.41

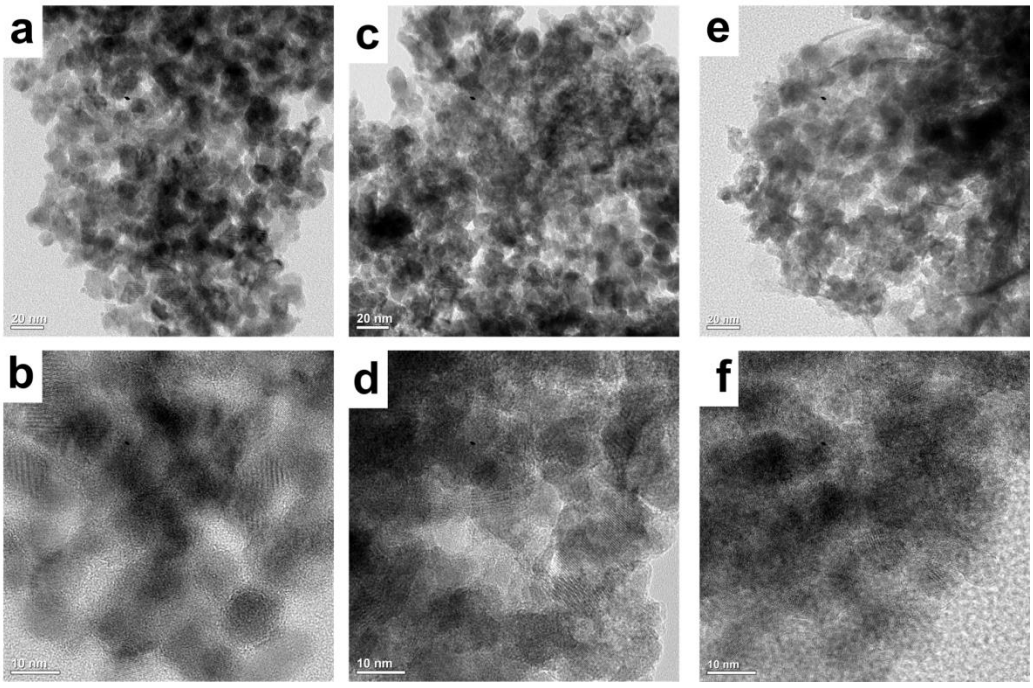

Figure 4.33: HR-TEM images of (a, b) LST.50F_11 (c, d) LST.50F_20 (e, f) LST.50F_40.

The porous features were investigated by nitrogen physisorption analysis. All were identified as Type IV(a) with increasing surface area and pore volume up to ~ 200 $m^2\ g^{-1}$ and 0.411 $cm^3\ g^{-1}$ respectively (Fig. 4.32a) [299]. The specific surface area and pore volumes of the

investigated samples were summarized on Table 4.6. Contrary to STO aggregates characterized in Chapter 4.1, no significant pore size narrowing was observed for LST.50F samples with increasing template amount, but additional contributions from smaller mesopores appeared with smallest pore diameter shifting from 7 nm for template free sample to ~ 4 nm for the sample with 40 vol.% template load (Fig. 4.32b). Transmission electron microscopy investigations were in agreement with rest of the characterization methods, illustrating for each sample polycrystalline particle aggregates of several micrometers with crystalline pore walls (Fig. 4.33). All samples have a disordered distribution of pores of about 10 nm diameter over the particles.

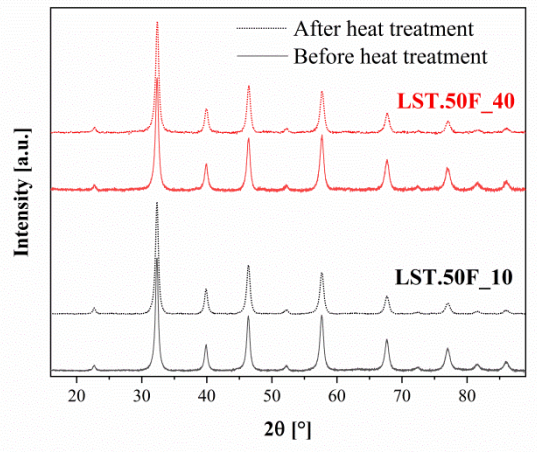

Figure 4.34: X-ray diffractograms of porous LST.50F samples before and after heat treatment at 600 °C under reducing atmosphere.

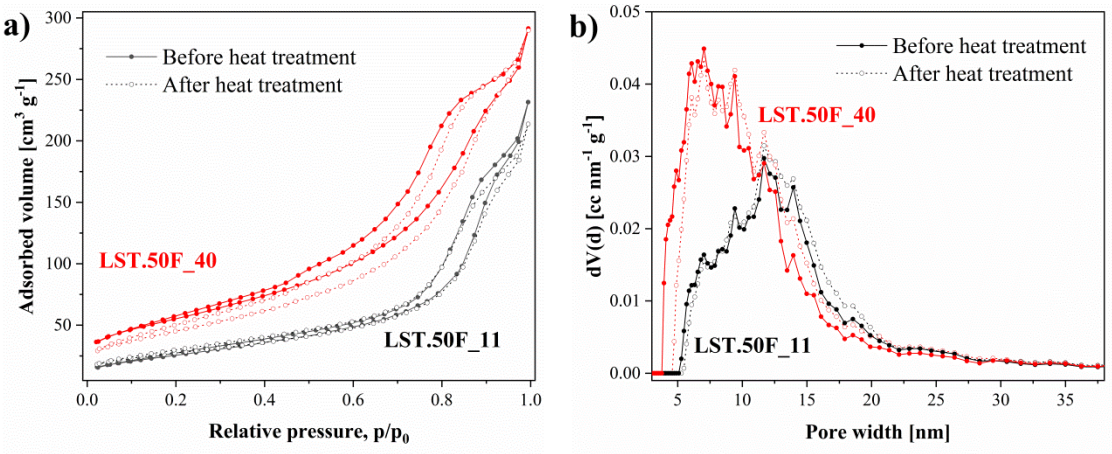

Figure 4.35: Nitrogen physisorption isotherms (a) and pore size distribution (b) of porous LST.50F samples before and after heat treatment at 600 °C under reducing atmosphere.

Table 4.7: Average atomic composition of elements determined by EDX (at. % values normalized by total nominal cation amount in $La_{0.3}Sr_{0.7}Ti_{0.5}Fe_{0.5}O_{3-\delta}$ molecular formula) and relative amounts of different Fe sites retrieved by Mössbauer spectroscopy for investigated LST.50F samples.

Sample	La	Sr	Ti	Fe	Fe^{3+} (1) [%]	Fe^{3+} (2) [%]	Fe^{3+} (3) [%]	Fe^{4+} [%]
LST.50F	0.27	0.64	0.50	0.48	60	30	-	10
LST.50F_11	0.24	0.51	0.50	0.45	33	41	19	7
LST.50F_20	0.17	0.38	0.50	0.34	33	46	16	5
LST.50F_40	0.16	0.25	0.50	0.29	23	32	38	7

Highly porous LST.50F samples were exposed to 1 h heat treatment under oxidizing and reducing atmospheres in order to assess the thermal stability of the material. XRD analyses after heat treatments showed no change in phase purity or microstructure of the material (Fig. 4.34). Porosity was largely retained as well except for some minor loss (~ 15%) for the highly porous sample LST.50F_40 treated under reducing conditions, which can be likely assigned to relatively lower crystallinity of the sample leading to reduced thermal stability (Fig. 4.35, Table 4.6). Pore volume of LST.50F_40 after heat treatment was retained, which points to minor rearrangement of pore structure at the expense of small pores (Fig. 4.35b).

4.3.2 Influence of templating approach to the catalytic performance

The catalytic performance of LST.50F samples was examined via methane oxidation tests as shown on Fig. 4.36. Templated samples showed poorer performance than the template free LST.50F catalyst. The loss of performance observed for LST.50F_11 despite its higher surface areas and retained composition can be ascribed to NaOH treatment which causes surface deactivation on the sample. Indeed, when the template free sample LST.50F is exposed to sodium hydroxide treatment, its initial 90% methane conversion at 600 °C drops to 67%, in accordance to the activity of LST.50F_11 catalyst with 11 vol.% template load. The comparable amounts of methane conversion of the samples despite differing porosity may

indicate a limit to activity enhancement by increasing surface area as reported in previous works [375,376]. When the template load was increased to 40 vol.% (LST.50F_40) a further drop in the conversion rate was observed. Since Fe species form the active sites for the catalysis of methane oxidation, this impediment of performance may be attributed to the increase in Fe deficiency on the LST.50F_40 surface as shown by EDX analysis (Table 4.7).

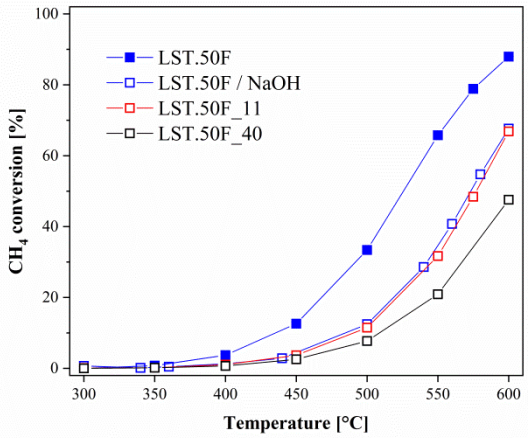

Figure 4.36: Steady state conversions obtained for CH_4 oxidation over investigated LST.50F systems evidencing the effect of surface modification on catalytic performance.

4.3.3 Performance of (La,Sr)(Ti,Fe)$O_{3-\delta}$ as active support in oxidation catalysis

Despite the reduction in catalytic performance in highly porous LST.50F_40 due to sodium hydroxide treatment, such modifications on surface structure can induce interesting functional properties. A high number of defect species on surface which can provide ideal sites for reactant adsorption as well as bonding sites for Pt nanoparticles (NPs) were reported for non-stoichiometric support systems, such as CeO_2, leading to attractive catalytic performance [185,188,377–379]. In parallel to these observations, LST.50F_40 perovskite's high crystallinity along with superior textural properties deems it an intriguing system for potential application as active support in oxidation catalysis.

In order to investigate the material's performance in this application, 1 wt.% Pt nanoparticles of ~ 8 nm diameter size were deposited on the oxide through a simple reduction route. The successful dispersion of the Pt nanoparticles is evidenced by transmission electron microscopy and EDX mapping (Fig. 4.37). Determination of surface coverage was unfortunately not possible due to presence of some local inhomogeneities in the size distribution of Pt NPs (Fig. 4.37c-d).

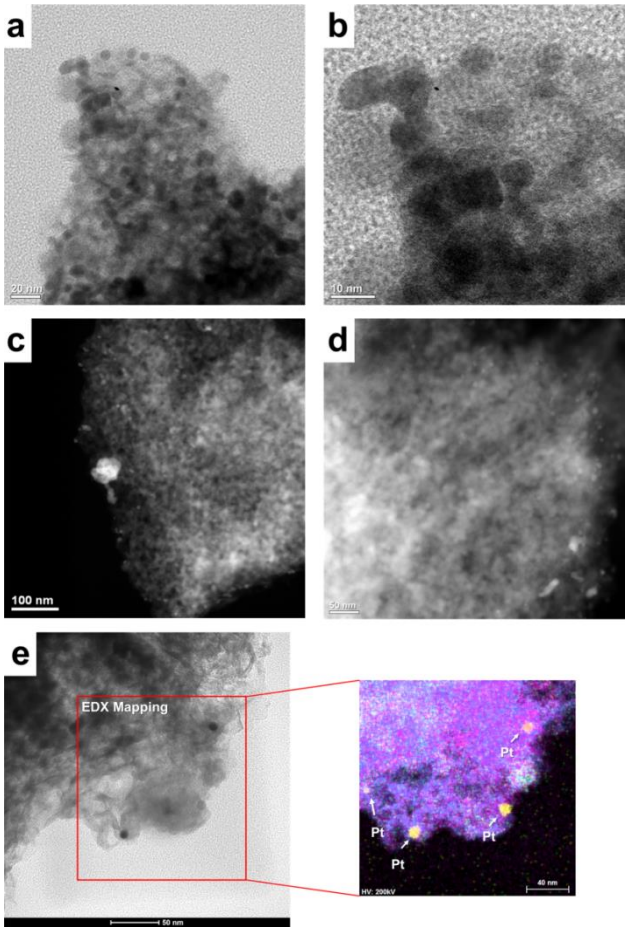

Figure 4.37: HR-TEM (a, b) and HAADF-STEM (c, d) HR-TEM/EDX-mapping (e) images of Pt nanoparticles deposited on LST.50F_40 oxide.

The feasibility of LSTF as active support was studied via proof-of-concept CH_4 and CO oxidation tests over the Pt/LST.50F_40 supported metal system and compared with catalytic performance of bare oxide catalysts, template free LST.50F and highly porous templated LST.50F_40. Products of CH_4 oxidation over Pt/LST.50F_40 were solely CO_2 and H_2O, pointing to a complete oxidation of methane. Fig. 4.38a shows that the reaction over Pt/LST.50F_40 catalyst is significantly enhanced in comparison to bare LST.50F_40, leading to complete conversion of methane at ~ 565 °C with a $T_{50\%}$ value of ~ 510 °C. Activation barrier for methane oxidation reaction over different catalysts ($E_a^{CH_4\ ox.}$) goes through a gradual decrease from 108 to 84 kJ mol^{-1} in the order LST.50F_40 > LST.50F > Pt/LST.50F_40 (Fig. 4.38b, Table 4.8). Since the presence of reducible cations like Fe promotes the methane oxidation reaction, higher activation barrier given for LST.50F_40 relative to template free LST.50F may be due to the iron deficiency of this material (Table

4.8) [380]. On the other hand, the drop in the apparent activation energy for Pt/LST.50F_40 may be explained through the roles of oxide and metal constituents in the system. Pt nanoparticles, in this case, facilitate the adsorption of methane and oxygen species, whereas LST.50F_40 acts as an oxygen supplier for the reaction and provides additional active sites for CH_4 adsorption. The reaction orders determined via kinetic studies on the Pt/LST.50F_40 system were given as 0.34 with respect to methane and ~ 0 with respect to oxygen (See Eq. 4.1 for rate equation, Table 4.8). Reaction over Pt supported with inert oxides such as Al_2O_3 leads to a reaction order close to unity with respect to methane [381]. Compared to this reference system, lowering of the reaction dependence to methane may indicate the active participation of LSTF sites (metal-support interface as well as oxide surface) to catalysis. Zero reaction order with respect to oxygen points to excellent oxygen supply from the LSTF support for the reaction.

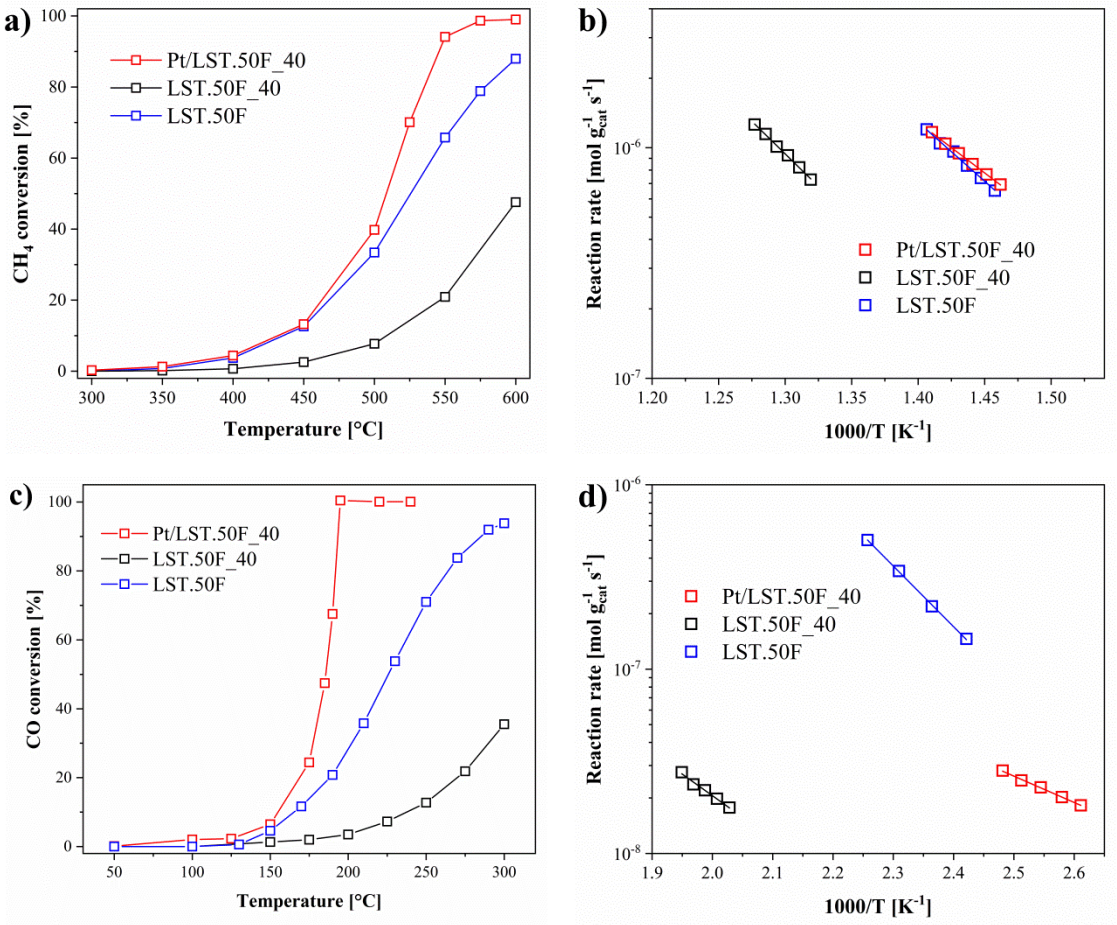

Figure 4.38: Steady state conversions obtained for the oxidation reaction of CH_4 (a) and oxidation reaction of CO (c) over investigated samples and pertaining Arrhenius plots respectively for CH_4 oxidation (b) and CO oxidation (d).

For the low temperature carbon monoxide oxidation reaction, the trend of catalytic activity remains similar (Fig 4.38c). Pt/LST.50F_40 shows remarkably high catalytic performance. The reaction is already initiated at 55 °C over Pt/LST.50F_40 catalyst and complete conversion (~99%) of carbon monoxide is attained at ~ 175 °C. The superior performance of the Pt/LST.50F_40 system can be related to the excellent oxygen supply to the Pt phase from the support. Moreover, partial confinement of the metal nanoparticles in the mesopores of the porous LSTF oxide may be playing a role in superior activity, which was demonstrated in literature to engender enhanced oxygen mobility and reactivity of the support material near the metal sites [16].

The activation barrier for CO oxidation ($E_a^{CO\ ox.}$) was given between from 65 to 91 kJ mol^{-1} with the order Pt/LST.50F_40 > LST.50F ≈ LST.50F_40 (Table 4.8, Fig 4.38d). In contrast to the trend for methane oxidation, the relatively unchanged $E_a^{CO\ ox.}$ value observed for highly porous LST.50F_40 with respect to LST.50F indicates that similar CO oxidation mechanism is followed for the bare LSTF samples with differing porosity. Superior overall carbon monoxide conversion over template free LST.50F compared to LST.50F_40 notwithstanding equal $E_a^{CO\ ox.}$ values can be explained through the higher number of active sites the catalyst possesses as a result of its precise stoichiometry (Table 4.7). Determined $E_a^{CO\ ox.}$ increased to 91 kJ mol^{-1} over Pt/LST.50F_40 sample. This value is in the same range with activation energies reported for CeO_2 supported Pt catalysts in literature [136]. In such systems, reaction mechanism is mainly governed by metal and metal/support interface sites in the CO oxidation over Pt/LST.50F_40, whereas oxide surface does not provide active sites for reaction. The inactivity of bare LST.50F_40 catalyst below 200 °C confirms this interpretation (Fig. 4.38c).

The dependence of the reaction on the reacting oxygen and carbon monoxide species were determined via kinetic studies (Table 4.8). The empirical rate equation for carbon monoxide oxidation can be expressed as:

$$rate = k\, P_{C0}^{q} P_{O_2}^{r} \tag{4.4}$$

where k is the rate constant, P_{C0}^{q} and $P_{O_2}^{r}$ are partial pressure of the gases carbon monoxide and oxygen with reaction orders of q and r respectively. The reaction over Pt/LST.50F_40 yielded a slightly negative order with respect to carbon monoxide ($q = -0.35$), whereas the rate was independent of oxygen ($r \sim 0$). Reaction order being zero with respect to oxygen

indicates the condition in which oxygen is supplied sufficiently from the MIEC material to the reaction sites. Negative reaction order for LST.50F_40 supported system indicates that CO oxidation takes place on Pt surface. Noble metals deposited on inert supports such as SiO_2 are typically deactivated by increase of CO partial pressure in atmosphere ($q = -1$), since carbon monoxide preferentially adsorbs on metal surface preventing oxygen adsorption necessary for the reaction to take place [136,137]. Since the reaction over Pt/LST.50F_40 is less dependent on CO species, it can be concluded that carbon monoxide oxidation also occurs actively at oxide – metal interface sites [187].

Despite the decent methane oxidation activity observed for Pt/LST.50F_40 ($T_{50\%}$ = 510 °C), performance of this system does not significantly surpass common alumina supported catalysts (Pt/Al_2O_3) reported under similar conditions ($S_{BET}^{Al_2O_3} = 200\ m^2 g^{-1}$, $T_{50\%} = 520$ °C) [382,383]. This result can be explained through the Fe deficiency of LST.50F_40 support due to synthesis conditions, as well as surface deactivation of the oxide due to etching treatment. Hence, further optimization of the synthesis route is required in order to benefit from the excellent application potential of the material as active support for CH_4 oxidation.

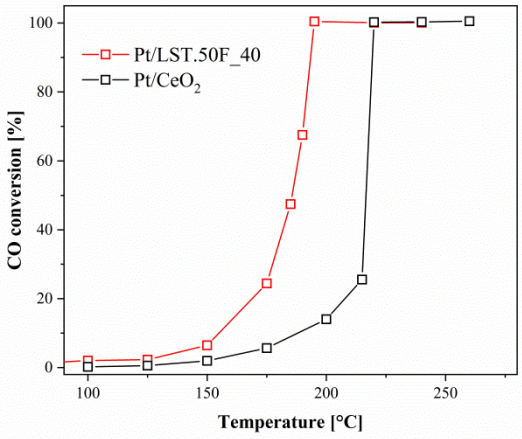

Figure 4.39: Steady state conversions obtained for the CO oxidation over LST.50F_40 and CeO_2 supported Pt nanoparticles.

On the other hand, a substantial improvement in the CO oxidation performance could be observed over Pt/LST.50F_40, since the role of the support is less dependent on the presence of Fe sites in this reaction. Hence, the CO oxidation performance of Pt/LST.50F_40 catalyst was compared with a commonly employed Pt/CeO_2 system (S_{BET} (CeO_2) = ~ 75 m^2 g^{-1}).

Complete conversion of carbon monoxide over Pt/CeO_2 was attained at 220 °C, pointing to the superior performance of Pt/LST.50F_40 which reached complete oxidation at 195 °C (Fig. 4.39).

Table 4.8: Activity parameters of investigated catalysts. $E_a^{CH_4\ ox.}$, $E_a^{CO\ ox.}$: Activation energy for CO and CH_4 oxidation reactions over investigated catalysts obtained below 10% conversion. q, r: Empirically calculated reaction orders q with respect to CO and r with respect to O_2 obtained below 10% conversion for CO oxidation ($rate = k\ P_{CO}^{q} P_{O_2}^{r}$).

Sample	$E_a^{CH_4\ ox.}$ [kJ mol^{-1}]	$E_a^{CO\ ox.}$ [kJ mol^{-1}]	q	r
LST.50F	90	66	+ 0.80	0
LST.50F_40	108	65	+ 0.98	0
Pt / LST.50F_40	84	91	– 0.37	0

4.3.4 Sub-chapter summary

Cooperative assembly route, which was developed to prepare highly porous $SrTiO_3$ powders, was expanded to enhance the porosity of chemically complex $(La,Sr)(Ti,Fe)O_{3+\delta}$ solid solutions. Phase pure LSTF solid solutions with $La_{0.3}Sr_{0.7}Ti_{0.5}Fe_{0.5}O_{3-\delta}$ nominal stoichiometry and substantial surface areas were successfully prepared. Porosity of the samples was tailored by varying the template amount between 11 – 40 vol.%. With increasing template load average pore diameter decreased from 15 to 8 nm, whereas surface areas increased from 60 to 201 $m^2\ g^{-1}$. Along with the enhancement of textural characteristics, significant Fe and Sr deficiency was observed on the solid solutions prepared with high template loads.

Stand-alone catalytic performance of highly porous LSTF oxides was assessed by CH_4 oxidation tests. The samples all showed reduced catalytic activity in comparison to template free LST.50F sample. For moderate template loads (11. vol%, LST.50F_11) activity loss was mainly attributed to the surface deactivation due to sodium hydroxide etching treatment. Further performance loss observed at high template loads (40 vol.%, LST.50F_40) was

attributed to the deficiency of Fe species on the catalyst, which provides the active sites for the oxidation reaction.

The feasibility of highly porous LSTF oxides as active support in oxidation catalysis was assessed by depositing Pt nanoparticles on the perovskite surface and studying the catalytic properties of Pt/LST.50F_40 supported metal systems via proof-of-concept CH_4 and CO oxidation tests. LST.50F_40 supported catalysts yielded complete conversion of CH_4 at ~565 °C and CO at 195 °C. Although, significant enhancement of activity from bare LSTF oxide catalysts was observed with respect to both reactions, CH_4 oxidation activity did not substantially surpass the values reported for Al_2O_3 supported Pt catalysts in literature. This result was explained by the notable Fe deficiency of the LST.50F_40 oxide, which leads to considerable performance impediment, since presence of Fe active sites are crucial for the methane oxidation reaction.

Contrarily, since oxidation of carbon monoxide is less dependent on the presence of Fe sites on the support surface, substantial CO oxidation over LST.50F_40 supported catalyst could be achieved, leading to superior performance than commonly employed Pt/CeO_2 catalysts. Remarkable performance of the Pt/LST.50F_40 was assigned to the excellent oxygen supply capability of the LSTF oxides to the active phase, as well as to possible partial nanoconfinement effects which can increase the reactivity on the metal/support interface sites. Moreover, highly porous LSTF oxides show very good thermal stability, with only minor loss of porosity (~15%) after heat treatment at 600 °C under reducing conditions.

Notwithstanding the failure in attaining the nominal stoichiometry; excellent porosity and stability of LST.50F_40 along with its outstanding performance as support in CO and CH_4 oxidation catalysis point to a strong application potential of the material upon further optimization of these parameters.

4.4 Modification of defect structure: $La_{0.1}Sr_{0.9}TiO_{3+\delta}$

Cationic substitution on the A-sites does not typically affect the catalytic properties of perovskite oxides [5] and hence donor substituted $SrTiO_3$ show insulating characteristics and poor activity towards thermally activated oxidation reactions [384]. However, pre-treatment of perovskite oxides can engender significant alterations of material's functional properties. For instance, defect structure and resulting charge transport properties of donor substituted $SrTiO_3$ systems are significantly modified depending on the atmospheric conditions of the heat treatment they undergo [26]. Flash sintering is a novel technique that is extensively investigated in recent years to enhance the thermal stability of ceramics at lower energy and time costs while retaining material's nano-sized grains [19]. Although, the mechanism of this technology is not yet fully understood, simultaneous heat treatment and electric field exposure employed in this process can lead to altered charge transport properties as a result of modification of the material's defect structure [271]. Application of this technique as a means to trigger the reactivity of initially inactive perovskite oxide catalyst by modification of material's functional properties is investigated in this sub-chapter.

As prepared $La_{0.1}SrTiO_{3+\delta}$ (LSTO) nanoparticles prepared by a modified solvothermal synthesis route were subjected to heat treatment under air atmosphere at two different electric field strengths; 300 and 600 V cm^{-1}. The alterations in material properties due to flash sintering process were investigated with reference to a conventionally sintered counterpart. The catalytic performance of each sample was assessed by CH_4 oxidation tests and observed activities were correlated with the morphology and charge transport properties of the materials.

Samples were labeled based on the treatment that they have gone through. As prepared LSTO nanoparticles were labeled as AP. Conventionally sintered sample was named CS, whereas flash sintered samples were labeled as FS-300 and FS-600 for electric field exposure respectively at 300 V cm^{-1} and 600 V cm^{-1}.

4.4.1 Structural characterization of as prepared nanoparticles

X-ray diffractograms of the as-prepared (AP) $La_{0.1}Sr_{0.9}TiO_{3+\delta}$ and $SrTiO_3$ nanoparticles point to a highly pure and crystalline cubic perovskite phase with Pm-3m space group (Fig 4.40a). The contraction of the unit cell characterized by the shift of [110] reflection towards higher 2θ

upon La substitution implies successful incorporation of smaller La^{3+} cations (r = 1.36 Å) on Sr^{2+} sites (r = 1.44 Å) in the perovskite lattice. Crystallite sizes calculated from [110] reflection with the Scherrer equation determined a grain diameter of 40 nm (Table 4.9). Electron microscopy investigations concur with the XRD results, showing nanocuboids of approximately 40 nm size with decent homogeneity regarding particle shape and size (Fig. 4.40b). The compliance of the elemental composition to the nominal stoichiometry of $La_{0.1}Sr_{0.9}TiO_{3+\delta}$ as well as the local elemental homogeneity was analyzed by EDX spectroscopy (Fig. 4.40c). The average elemental ratio between cations **La** : **Sr** : **Ti** was identified as **0.10** : **0.93** : **0.97**. The elemental ratios on several survey points were found to be between 0.07 to 0.15 for La and between 0.85 to 1.05 for Sr respectively, confirming the nominal La doping of 10 mol.% (Table 4.10). Nitrogen physisorption analysis of as prepared (AP) LSTO particles determined a specific surface area of 24 m^2 g^{-1} (Fig 4.42a, Table 4.9).

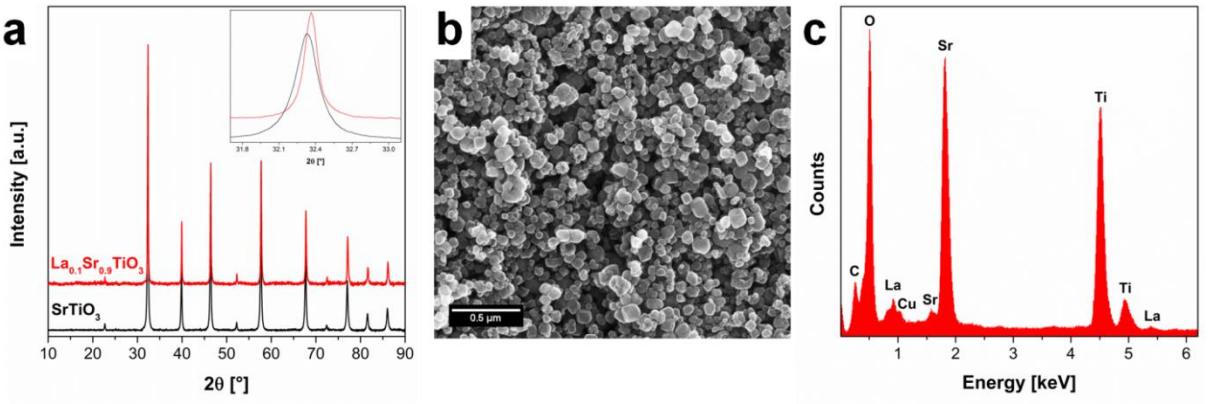

Figure 4.40: (a) X-ray diffraction patterns of as-prepared (AP) $SrTiO_3$ and $La_{0.1}Sr_{0.9}TiO_3$ (LSTO) nanoparticles. The shift of [110] reflection due to La-substitution is presented in the inset. (b) SEM micrograph of AP LSTO (c) EDX spectrum of AP LSTO (Position 1 on Table 8.1). Cu peak on Fig. 4.40c is due to the copper grid on the experimental setup.

4.4.2 Variation of sintering conditions

Conventional sintering was implemented with the firing program depicted on Fig. 4.41a employing a maximum temperature of 1150 °C. The initial contraction and expansion observed in the ceramic body below 200 °C is due to processes involving the removal of the binder material.

Flash sintering of LSTO pellets was achieved via simultaneous heating and electric field exposure with field strength 300 (FS-300) and 600 V cm^{-1} (FS-600) at an implemented current limit of 2.5 mA mm^{-2}. The flash event, characterized by the spontaneous electrical power dissipation within the ceramic material was observed at 1190 °C for 300 V cm^{-1} and 980 °C for 600 V cm^{-1} field (Fig. 4.41b). FS-300 sample showed a power dissipation of 75 mW mm^{-3}, which increased two-fold to ~ 150 mW mm^{-3} when the electric field strength was 600 V cm^{-1}. The flash event accompanies sudden consolidation of material in a matter of few seconds with characteristics correlating to the observed power dissipation [385,386]. The power peaks reported in literature that accompanies total densification of sintered bodies is typically about one order magnitude higher than the values observed in this work [385,387].

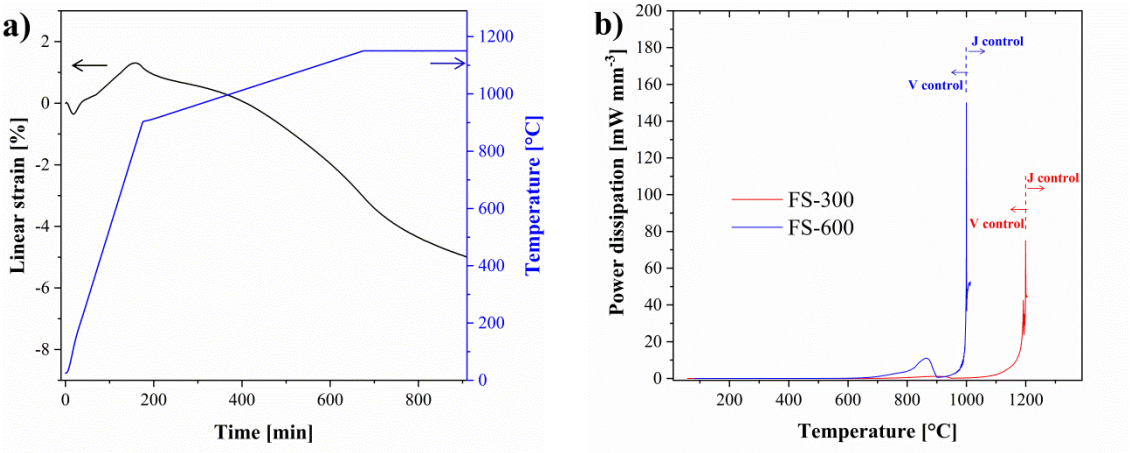

Figure 4.41: (a) Temperature program and relative shrinkage of LSTO by conventional sintering (b) power dissipation plots for flash sintering of LSTO.

4.4.3 Characterization of sintered materials

All samples showed about 55% relative density subsequent to the sinter processing at different conditions (Table 4.9, See Chapter 6.4 for density calculation). Such values are representative of initial stages of sintering in which interparticle necks are formed, but total densification of the material is not yet achieved [388]. Accordingly, only a moderate decrease in material's surface area was determined subsequent to the sintering process. Flash sintered materials both display a 9 m^2 g^{-1} S_{BET}, whereas conventional sintering led to a 5 m^2 g^{-1} specific surface area (Fig. 4.42a, Table 4.9).

Table 4.9: Physical and catalytic parameters for $La_{0.1}Sr_{0.9}TiO_{3+\delta}$ (LSTO) systems. Relative density (**ρ**), crystallite size (**Φ**) and lattice parameters (***a***), specific surface areas ($\mathbf{S_{BET}}$), TEM/EDX derived average atomic compositions of investigated LSTO systems acquired at several survey positions normalized to nominal stoichiometric amounts in $La_{0.1}Sr_{0.9}TiO_{3+\delta}$ formula (**La**, **Sr**, **Ti**), activation energies for the migration of charge carriers ($\boldsymbol{E_a^{EIS}}$) under air, surface area normalized activation energies ($E_a^{CH_4\ ox.}$) and the temperature for 50% of CH_4 conversion ($T_{50\%}$).

Sample	ρ [%]	Φ [nm]	*a* [Å]	S_{BET} [$m^2\,g^{-1}$]	La	Sr	Ti	E_a^{EIS} [eV]	$E_a^{CH_4\ ox.}$ [kJ mol^{-1}]	$T_{50\%}$ [°C]
AP	-	39	3.902	24	0.10	0.93	0.97	-	-	-
CS	56	57	3.908	5	0.12	0.94	0.94	1.079 (± 0.007)	124.1 (± 2.8)	787
FS-300	51	56	3.907	9	0.11	1.03	0.86	0.942 (± 0.008)	101.3 (± 3.4)	674
FS-600	55	53	3.911	9	0.12	0.96	0.92	0.971 (± 0.004)	103.9 (± 2.4)	664

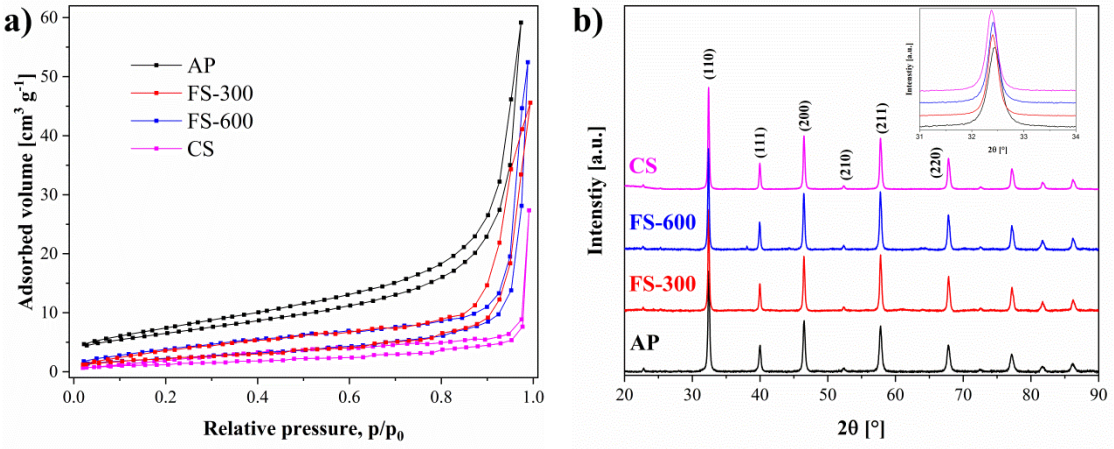

Figure 4.42: N_2 physisorption isotherms (a) and X-ray diffractograms (inset showing the shift of [110] reflex) (b) of investigated LSTO systems.

XRD analysis over investigated systems shows that cubic phase is retained with a modest grain growth of almost equal extent for each sample (Fig 4.42b, Table 4.9). This phenomenon is commonly observed on donor substituted $SrTiO_3$ and is ascribed to the formation of SrO rich phases which inhibits the grain growth [26]. SrO formation in the sintering process of donor doped $SrTiO_3$ accompanied by inhibition of grain growth was reported by several works in literature [282,389–391]. Furthermore, the shift of reflections to higher 2θ angles upon material pre-treatment indicates that sintering promotes expansion of the lattice unit cell. The shift is more pronounced in flash sintered samples, likely due to the enhancement in concentration of intrinsic point defects induced by the field assisted treatment [392].

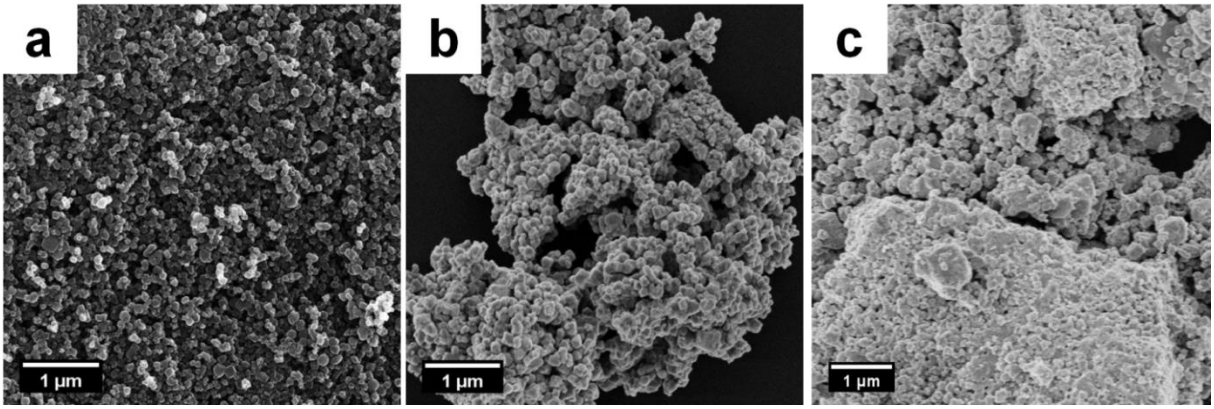

Figure 4.43: SEM micrographs of LSTO systems (a) AP (b) FS-600 (c) CS.

Formation of cuboidal agglomerates with smoothened edges was observed in scanning electron microscopy analysis, in accordance with the predicted morphology for the calculated relative density values (Fig 4.43). HR-TEM investigations revealed the presence of local high contrast phases on the grain surface which gets more conspicuous for flash sintered samples (Fig 4.44). These local phases were ascribed to SrO. Sintering of $SrTiO_3$ under oxidizing conditions promotes formation of partial Schottky pairs, V_{Sr}'' and $V_O^{\cdot\cdot}$, in accordance to (Eq. 2.5). Segregated strontium cations are then accommodated mainly on strontium-rich sites at grain terminations or as local Ruddlesden-Popper phases in the lattice (Fig. 2.3) [282,283].
SrO segregation is enhanced in donor substituted $SrTiO_3$ due to a further SrO formation mechanism (Eq. 2.22) [390]. Additional charge introduced by donor cations in these systems is mainly compensated by formation of free electrons. Oxygen from atmosphere can get reduced by these additional free electrons during heat treatment under oxidizing conditions. Reduced oxygen can then react further with strontium sites on the surface to form SrO phase.

As a result, higher number of strontium vacancies are generated in the system in comparison to oxygen vacancies [257,279].

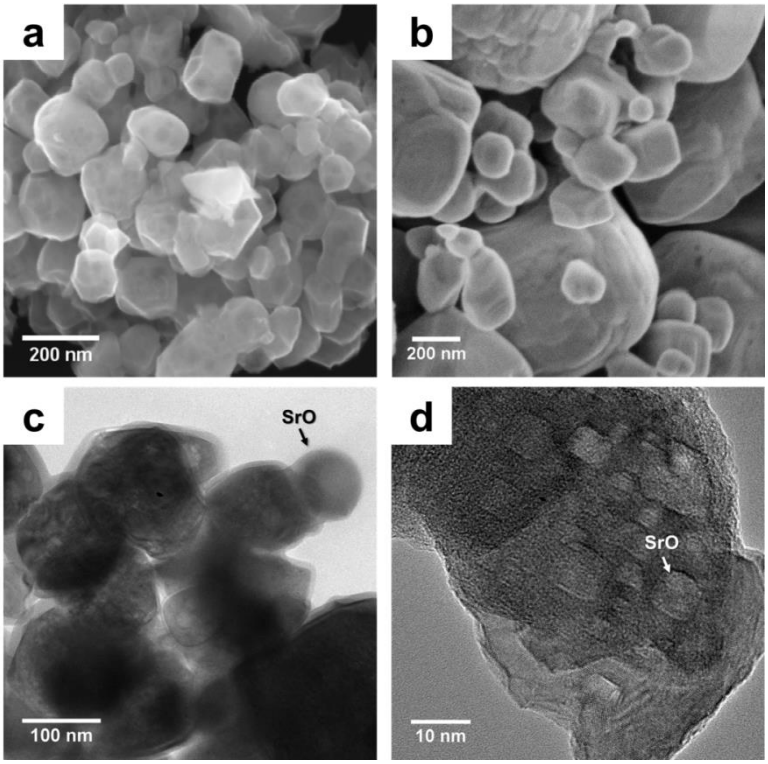

Figure 4.44: SEM and TEM micrographs of **(a-c)** FS-600 **(b-d)** CS LSTO systems.

The increase in the thickness of SrO rich layers observed for flash sintered samples can be explained by presence of higher number of strontium vacancies in accordance to the lattice relaxation observed in XRD (Fig. 4.42b inset). The composition of observed higher contrast surface layer of FS-600 was confirmed to be solely SrO by EDX analysis, whereas only moderate Sr enrichment could be identified for the conventionally sintered counterpart (Fig. 4.45). Further enhancement of SrO layer and strontium vacancy concentration in flash sintering is likely due to the supply of additional electrons to the system induced by the applied current, which in turn leads to enhanced oxygen reduction from the atmosphere.

ESR spectroscopy was performed on CS and FS-600 samples in order to investigate the effect of sintering treatment on the state of charge of the ionic species in the materials. Both systems displayed a complex spectrum with a broad anisotropic signal at g = 2.003 superimposed of different O^- centers (Fig. 4.46). This signal is of higher intensity for FS-600 and its deconvolution by simulation studies yielded five components with different g values (Table 4.11). The decrease in $g_\perp$ value of different O^- centers corresponds to the strengthening of

metal-oxygen interactions. In light of this correlation, the major signal component given for $g_{\perp} = 2.055$ ($O^{-}_{[I]}$) was assigned to oxygen centers adsorbed on SrO [153,393]. The remaining components ($O^{-}_{[II]}$, $O^{-}_{[III]}$ and $O^{-}_{[IV]}$) likely arise from oxygen centers adsorbed on Ti^{4+} sites with differing chemical environments. Finally, almost isotropic peaks centered around g = 1.979 can be assigned to Ti^{3+} centers. Other minor features were also identified on the complex ESR spectra, which may be assigned to Mn^{2+} impurities. These signals denoted with asterisks are slightly more conspicuous for conventionally sintered sample, CS. Such acceptor impurities can be readily observed for nominally undoped $SrTiO_3$ and are almost impossible to eliminate due to relative abundance of cations of lower valence in earth's crust [284]. The larger concentration and stability of O^{-} centers in FS-600 can be explained by the increased amount of strontium vacancies in this system [394]. Strontium vacancies which modify the state of charge are mainly located at surface and sub-surface region where they become available to react at the interface sites upon temperature activation. These paramagnetic defects may be arising from the current exposure in flash sintering or due to charge compensation mechanisms related with cationic vacancies. However, clear discernment of the specific contribution of these mechanisms was unfortunately not possible.

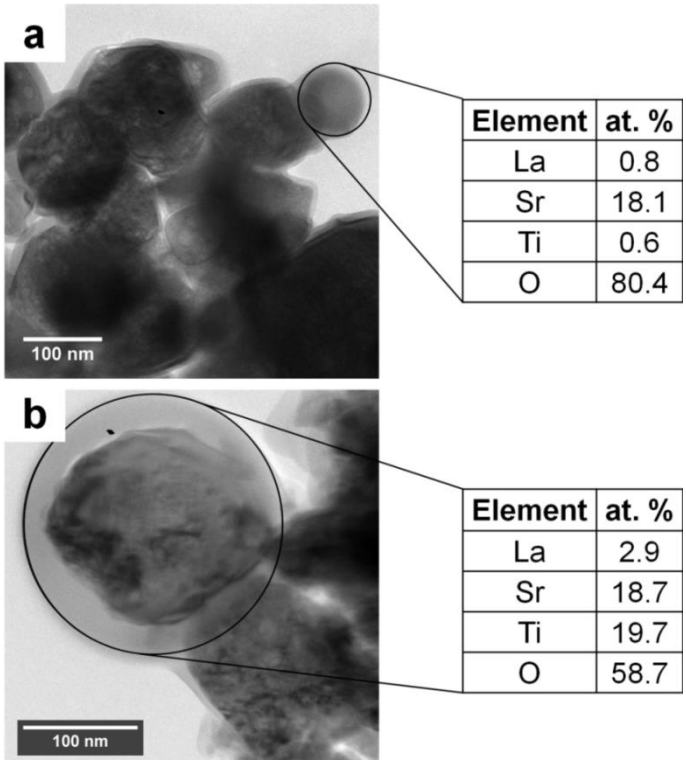

Figure 4.45: Atomic compositions acquired from TEM/EDX over the circular area of investigated LSTO samples (a) FS-600 (b) CS.

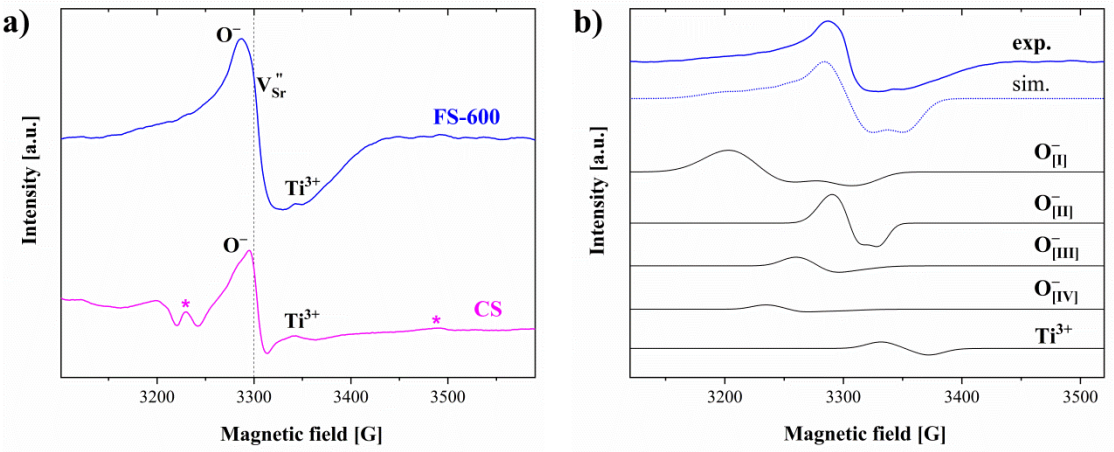

Figure 4.46: (a) ESR spectra of differently processed LSTO samples at 130 K in vacuum with the asterisks denoting the Mn^{2+} defects. (b) Magnification and simulation of the resonance occurring in FS-600: experimental (exp.) and simulated (sim.) spectra; deconvolution of ESR signal into different paramagnetic species.

Table 4.10: *g* tensor values of the paramagnetic defects detected over FS-600 sample, determined by simulation of the ESR features. The relative contributions of the O^- and Ti^{3+} species (calculated as % of the total signal intensity) are also reported.

Species	*g*-values	Contribution [%]
$O^-_{[I]}$	$g_\perp = 2.0550$, $g_\parallel = 1.9950$	45
$O^-_{[II]}$	$g_\perp = 2.0030$, $g_\parallel = 1.9990$	22
$O^-_{[III]}$	$g_\perp = 2.0190$, $g_\parallel = 1.9970$	12
$O^-_{[IV]}$	$g_\perp = 2.0350$, $g_\parallel = 2.0030$	6
Ti^{3+}	g =1.979	15

The oxygen mobility and reactivity were investigated further by TPD-O_2 studies (Fig. 4.47). All LSTO samples showed similarly negligible desorption, in accordance with the established defect chemistry relations that estimate very low oxygen vacancy concentrations for LSTO samples sintered at oxidizing conditions [384,390].

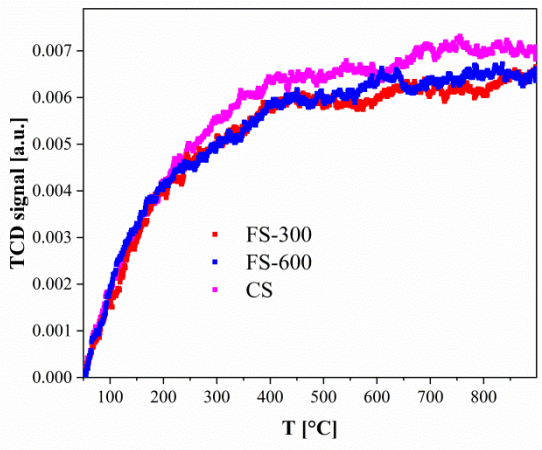

Figure 4.47: Temperature programmed desorption (TPD-O_2) profiles of LSTO systems sintered at different conditions.

As discussed in Chapter 2.5.4, preparation route and pretreatment of the material have a strong influence to the defect chemistry of donor substituted strontium titanate. Considering the concentration of electrons are always substantially larger than holes ($[e'] \gg [h^{\cdot}]$) in donor substituted $SrTiO_3$ at the whole pO_2 range [390], the electroneutrality condition above 1000 °C given on Eq. (2.23) with the Kröger-Vink notation [278] can be written as:

$$2[V_O^{\cdot\cdot}] + [La_{Sr}^{\cdot}] = 2[V_{Sr}^{''}] + [e'] \tag{4.5}$$

where $V_O^{\cdot\cdot}$ and $V_{Sr}^{''}$ are doubly charged oxygen and strontium vacancies respectively, $La_{Sr}^{\cdot}$ is lanthanum donor species substituted on strontium sites, and e′ are the electrons [390].

LSTO materials show substantially high n-type conductivity upon sintering in reducing atmospheres through formation of oxygen vacancies which are compensated by free electrons in the system [65,257,395]. In oxidizing conditions, the concentration of oxygen vacancies decreases and as the partial pressure of oxygen increases the donor species get mainly counterbalanced by electrons and strontium vacancies respectively according to equations (2.25) and (2.26). At this regime, the ceramic material then shows insulating behavior. The concentration of strontium vacancies is mainly governed by material's synthesis and sintering conditions [390]. At intermediate temperature range (below 1000 °C), the strontium vacancies can be considered as fixed in since they are not mobile enough to equilibrate with atmosphere.

Fig. 4.48a shows the conductivity of materials sintered at different conditions as a function of oxygen partial pressure at the intermediate temperature range up to 700 °C determined by

electrochemical impedance spectroscopy. In accordance with the abovementioned defect chemistry behavior and reports in literature (Fig. 2.19) [282,297], the materials all showed constant conductivity independent of oxygen partial pressure at this intermediate pO_2 regime. It should be noted that the low relative densities of the materials might have led to decreased grain contact which can affect the outcome of conductivity measurements. For instance, a slight p-type conductivity could be assigned to FS-600 sample on Fig. 4.48a (slope = + 0.04), which is confirmed by the relatively high hole concentration of the material as evidenced by ESR analysis.

Lower conductivity of the flash sintered samples in comparison to their CS counterpart can be ascribed to the higher concentration of strontium vacancies, which are fixed in to the lattice in the intermediate temperature regime (700 °C). The effective donor dopant concentration is determined by these fixed in species, which in turn governs the concentration of the mobile charge carriers.

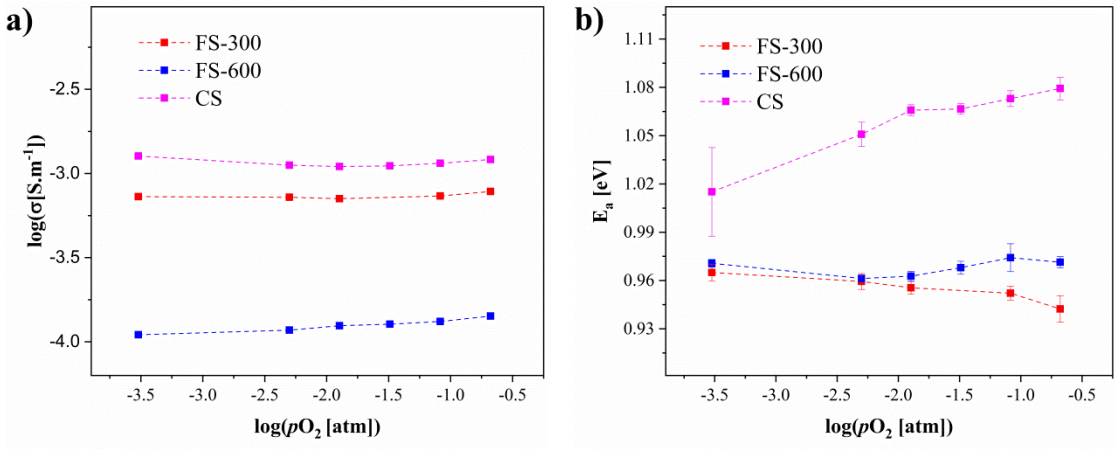

Figure 4.48: (a) Specific conductivity of LSTO systems sintered at different conditions as a function of oxygen partial pressure at 700 °C determined by electrochemical impedance spectroscopy (b) Calculated activation energies for charge migration from the Arrhenius-type conductivity plots of EIS.

The influence of flash sintering on the charge transport properties are also evident in the evolution observed in activation energies of charge migration, E_a^{EIS} (Fig 4.48b, Table 4.9). Conventionally sintered LSTO, shows an E_a^{EIS} value of 1.08 eV under air atmosphere and the activation barrier is lowered when oxygen partial pressure is decreased. The decrease in E_a^{EIS}

in this case may be due to additional contributions from newly formed charge carriers such as oxygen vacancies. However, the activation energy lowering does not accompany an evident increase in the conductivity, probably due to minuscule oxygen vacancy amounts as shown by TPD-O_2 measurements, lacking grain contact or a combination of both effects.

Flash sintered samples on the other hand, show unchanging activation energy for charge migration at the investigated pO_2 range. FS-300 and FS-600 samples both show similar E_a with a magnitude about 0.1 eV lower than CS counterpart, due to the higher $[V_{Sr}'']$ in their lattice. The charge carrier mobility can be promoted by A-site deficiency in LSTO, since the excess strontium vacancies push the equilibrium Eq. (2.7b), which describes reduction of the oxide, to the direction of products and facilitate formation of free electrons [396–398].

Mesoscopic size effects may also be playing a role in the enhanced charge transport of flash sintered LSTO ceramics. These effects refer to the condition in which grains and space charge zones induced by the grain boundaries are of similar dimensions, so that unperturbed bulk behavior is not observed within the particles [399,400]. In such cases, overlap of Schottky barriers at grain boundaries lead to substantial decrease in space charge potentials and significantly alter the material's electrical properties [401–403]. Although the grains of conventional and flash sintered materials are of similar dimensions, FS samples may possess a much larger space charge region due to the significantly higher number of strontium vacancies engendered by the electric field exposure, which can in turn lead to grain depletion effects and facilitate charge transport. Unfortunately, determination of space charge widths at the grain boundaries via electrochemical impedance analysis was not possible due to insufficient densification of LSTO samples.

4.4.4 Influence of sintering on catalytic properties

The influence of the modified defect configuration to catalytic properties of the LSTO systems upon high temperature treatment under electric field exposure were investigated via activity tests of model high temperature catalytic reaction, CH_4 oxidation. Reaction products have been carbon dioxide and water over each catalyst, pointing to full oxidation of methane. The steady state conversions over LSTO catalysts in Fig. 4.49a show that the catalytic performances of flash sintered samples are significantly higher in comparison to conventionally sintered counterpart. Methane oxidation over FS catalysts is already initiated at 500 °C and almost complete oxidation is observed at 800 °C. CS sample on the other hand

only attains 58% conversion at this temperature. Accordingly, $T_{50\%}$ values given for FS samples are about 100 °C lower than of CS (Table 4.9).

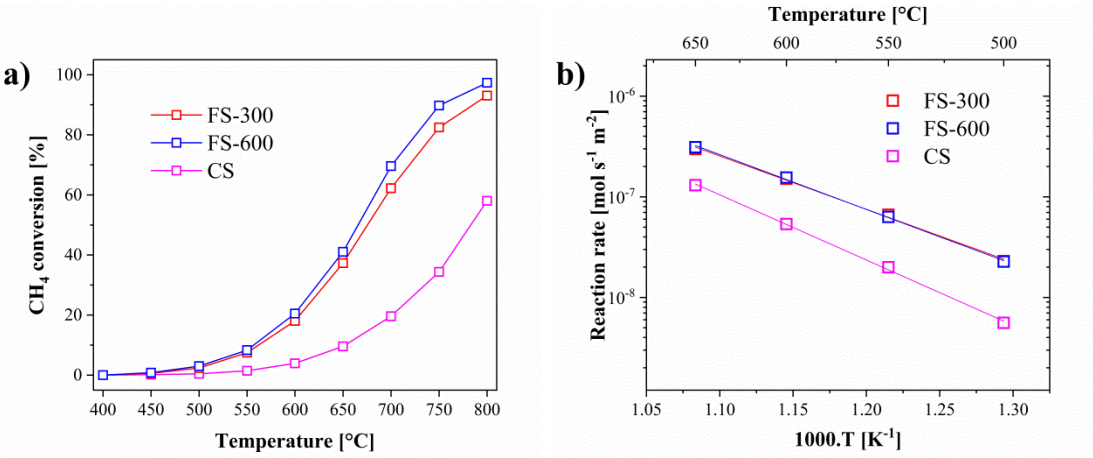

Figure 4.49: (a) Steady state conversions obtained for CH_4 oxidation over LSTO systems sintered at different conditions. (b) Pertaining Arrhenius-type plots. Reaction rates are normalized by surface area of each sample.

Arrhenius plots determined from the kinetic investigations also indicate a higher activation barrier for methane oxidation for conventionally sintered LSTO in comparison to flash sintered counterparts (Fig. 4.49b, Table 4.9). The $E_a^{CH_4\ ox.}$ values for methane oxidation are in good agreement with the trend observed for the activation barrier determined of charge carrier migration by electrochemical impedance spectroscopy. These findings indicate a correlation between improved catalytic activity and enhanced concentration of charge carrier species in FS samples. Furthermore, similar $E_a^{CH_4\ ox.}$ values determined for flash sintered samples with varying applied potential during electric field treatment indicate that methane oxidation over these samples involves similar reaction mechanism.

The large disparity between the catalytic performance of conventional and flash sintered LSTO is intriguing, in particular considering the identical chemical environment and microstructure. The phenomenon can be partially explained by the higher surface area of FS samples (Table 4.9), but cannot account for it completely since surface area normalized reaction rates still indicate a superior catalytic activity for FS samples (Table 4.11).

Considering the defect structure analysis and reports in literature, the enhancement of catalytic activity in flash sintered LSTO is mainly ascribed to the larger concentration of O^{-}

centers in these systems [153,404]. Typical oxide catalysts for chemical oxidation of methane as well as LSTO sintered in reducing atmospheres accommodate a sizable amount of oxygen vacancies, which can provide sites for oxygen to react with the dissociatively adsorbed methane molecules [370,373,405,406]. Considering the insignificant amount of oxygen vacancies present in LSTO sintered in oxidizing conditions (Fig. 4.47), we can plausibly argue that the active O^- species that react with methane on these oxides are the ones stabilized around cationic centers. Although oxygen species near Ti^{4+} centers are considered as the main active sites in these systems [153], recently Staykov et al, demonstrated that O^- sites stabilized around Sr^{2+} cations of surface SrO can also promote the oxidation reaction [407]. The significant enrichment of O─ sites near Ti^{4+} and Sr^{2+} for flash sintered samples as determined in ESR measurements (Fig. 4.46a) can therefore account for the catalytic performance improvement. Enhanced charge carrier mobility as a result of increased A-site deficiency in the flash sintered systems may also be considered as a further contributor for the superior performance [396,397].

Table 4.11: Comparison of reaction rates over LSTO systems presented in this work and reported values in literature for similar $Sr_{0.9}Gd_{0.1}TiO_3$ system treated in oxidizing conditions [408] along with MIEC perovskites, such as $LaFeO_3$[12], $La_{0.66}Sr_{0.34}Co_{0.2}Fe_{0.8}O_3$[158] and $LaCo_{0.6}Fe_{0.4}O_3$[170]. All values were retrieved at T = 600 °C and normalized by surface area.

Material	Reaction rate [10^{-7} mol s^{-1} m^{-2}]
$La_{0.1}Sr_{0.9}TiO_{3+\delta}$ / CS [this work]	0.54
$La_{0.1}Sr_{0.9}TiO_3$ / FS-300 [this work]	1.51
$La_{0.1}Sr_{0.9}TiO_3$ / FS-600 [this work]	1.55
$Sr_{0.9}Gd_{0.1}TiO_3$ [408]	0.24
$LaFeO_3$ [12]	4.51
$La_{0.66}Sr_{0.34}Co_{0.2}Fe_{0.8}O_3$ [158]	6.5
$LaCo_{0.6}Fe_{0.4}O_3$ [170]	0.27

The reaction rates over investigated LSTO catalysts in this work were compared to other donor substituted $SrTiO_3$ insulators sintered in oxidizing conditions as well as MIEC perovskites with known methane oxidation activity (Table 4.11). The surface area normalized reaction rates indicate that flash sintered LSTO shows over 6 times higher activity in comparison to donor substituted $Sr_{0.9}Gd_{0.1}TiO_3$ system [408], demonstrating the significant performance improvement achieved by the defect structure modification. Although, determined rates are of same order of magnitude with the values reported for MIEC perovskites such as $La_{0.66}Sr_{0.34}Co_{0.2}Fe_{0.8}O_3$ [158] and $LaFeO_3$ [12] in literature; comparable performance could not be attained by the defect structure modification of $La_{0.1}Sr_{0.9}TiO_{3+\delta}$ oxides via flash sintering treatment. This result is not unexpected considering the substantially superior oxygen mobility and redox characteristics of MIEC systems, which promotes the oxidation reaction.

4.4.5 Sub-chapter summary

Catalytic property improvement through defect structure modification of $La_{0.1}Sr_{0.9}TiO_{3+\delta}$ (LSTO) insulator system was investigated via flash sintering approach, which is a novel technique mainly employed to enhance thermal stability of ceramics at lowered energy and time costs. Flash sintering of LSTO nanoparticles under oxidizing conditions engendered larger concentration of strontium vacancies in comparison to conventionally sintered counterpart. On the other hand, alteration of electric field strength did not induce significant difference in material characteristics. The difference likely stems from the additional electrons introduced to the system by the induced current, which can reduce the oxygen from atmosphere and lead to the reaction of reduced oxygen species with strontium sites on the surface. HR-TEM/EDX investigations confirmed the enhancement of strontium segregation on the surface of flash sintered (FS) samples in the form of SrO sites. In accordance with enhanced concentration of V_{Sr}'' sites, activation energies for charge migration determined by EIS were determined to be 0.1 eV lower for FS samples compared to CS counterpart. Moreover, ESR studies showed significant enrichment of O^- centers near Ti^{4+} and Sr^{2+} for FS samples. Enhancement of catalytic properties by modified defect structure was demonstrated by model high temperature reaction, CH_4 oxidation. Flash sintered samples showed significantly improved methane oxidation performance than conventionally sintered counterpart as well as similar donor substituted $SrTiO_3$ oxides reported in literature, thanks to their altered functional properties.

Chapter 5

Conclusions & Outlook

In this work, a comprehensive design approach towards high performance perovskite oxide catalysts was presented. Variation of porosity, composition and defect structure were investigated over a $SrTiO_3$ based perovskite system and the structure – function relationships were identified via catalytic tests of model reactions relevant for environmental catalysis.

A facile route was developed to prepare perovskite oxides with tailored mesoporous nanostructure. In this novel process, polycondensation of metal chelate complexes and alkoxysilanes leads to an interpenetrating network through cooperative assembly of inorganic and organic constituents. Close intertwinement of networks enables effective removal of in situ formed silica template from the perovskite/silica nanocomposite obtained through calcination. Porosity enhancement of $SrTiO_3$ basis composition was investigated by varying the template load between 6 – 40 vol.% in this cooperative assembly route.

The chemical nature of the siliceous species in as-prepared nanocomposites was assessed by ^{29}Si NMR spectroscopic analysis, which showed only monomeric, dimeric and oligomeric units at low template loads, whereas above 11 vol.% condensed silica species dominated, indicating successful templating action. Excluding a minor fraction of residual silicate species that incorporated into perovskite lattice, siliceous species were completely removed from each sample by sodium hydroxide etching. Subsequent to the etching treatment, pure-phase polycrystalline $SrTiO_3$ powders with highly interconnected mesopores and were obtained. Increasing template load led to gradually increasing specific surface areas between 60 – 240 $m^2\ g^{-1}$ accompanied by decreasing grain sizes from 31 to 15 nm. Shrinkage of grains was ascribed to the rising diffusion barrier to mass transport with increasing template load.

Although, minor Sr deficiency was present in highly porous samples, band gap energies remained relatively unaffected since these sites do not participate in the electronic band structure of $SrTiO_3$.

The activity enhancement of the highly porous materials was demonstrated via photocatalyzed methylene blue degradation tests that have practical relevance for wastewater treatment applications. Mesoporous $SrTiO_3$ photocatalysts yielded significantly enhanced dye conversion in comparison to the reference nanoparticulate $SrTiO_3$, showing ~ 7 times higher degradation rate after surface area normalization. The superior photocatalytic properties of the mesoporous $SrTiO_3$ samples can be explained through their excellent crystallinity within a three-dimensional mesoporous network with well interconnected pores which leads to enhanced utilization of incoming light as a result of multi-reflections within pores and quick charge transport kinetics due to short diffusion path lengths and lower amount of recombination centers for electronic charge carriers on the solid [124]. Moreover, dye degradation activity was enhanced almost linearly with growing porosity and decreasing crystallite size of the mesoporous $SrTiO_3$ catalysts. Increasing surface area leads to additional active sites accessible to the reactants, whereas down-sizing of grains can enable quantum effects that leads to enhanced charge transport, thereby improving catalytic activity [363].

Favorable photocatalytic activity of $SrTiO_3$ under UV irradiation stems largely from the electronic band structure and photocorrosion resistance of the material [409]. On the other hand, thermally activated catalytic reactions depend strongly on the dynamic chemical interaction between the catalyst and reactants. Highly performing catalysts in these reactions are by definition chemically instable materials and thus cannot remain effective for long periods of time without deactivation, whereas chemically stable materials such as $SrTiO_3$, do not show appreciable activity. The design principle for an optimum perovskite catalyst for these reactions, thus, requires a carefully tailored compromise between activity and stability. Adjustment of this compromise was investigated by modification of $SrTiO_3$ composition through La- and Fe- co-substitution. Mesoporous $La_{0.3}Sr_{0.7}Ti_{1-x}Fe_xO_{3\pm\delta}$ (LSTF) solid solutions with varying Fe-substitution between $0 \leq x \leq 0.5$ were prepared by a simple variation of the template-free polymer complex route. Highly crystalline pure-phase cubic perovskite oxides with ~ 65 $m^2\ g^{-1}$ specific surface area were obtained. The materials all showed excellent phase and thermal stability up to 600 °C under oxidizing and reducing conditions. This result can be ascribed to excellent crystallinity and phase purity of the prepared solid solutions as well as to

the presence of stabilizing La cations on the A-sites as previously reported for similar systems [30–32]. Charge transport properties, oxygen mobility and reducibility of the materials enhanced with increasing Fe substitution up to 50 mol.%. Catalytic activity towards model reactions, CO and CH_4 oxidation, followed similar trend leading to increasing conversion with higher Fe-substitution of the LSTF catalyst. Moreover, a drastic shift in catalytic characteristics was observed when the iron substitution in LSTF catalysts was increased from 10 to 30 mol.%. This shift was ascribed to the change in charge transport mechanism of the material from insulator characteristics with n-type conductivity ([Fe] < [La]) towards a p-type conductor with enhanced charge carrier mobility ([Fe] ≥ [La]). Moreover, easily reducible Fe^{4+} species that promote catalysis started being formed above 10 mol.% Fe substitution.

Yielding almost complete conversion of CO and CH_4 at 300 and 600 °C respectively, 30 and 50 mol.% Fe substituted samples showed similarly excellent oxidation performance, superior than of reported Fe-based perovskite catalysts in literature with up to 90 times higher activity. The superior performance was ascribed to the incorporation of chemically complex LSTF composition in a mesoporous bulk system with nano-sized grains, which enabled further enhancement of material's functional properties such as oxygen mobility and reducibility. Two separate reaction mechanisms for CH_4 oxidation were identified by kinetic studies over LSTF samples. These coexisting reaction mechanisms were ascribed to suprafacial and intrafacial processes and the contribution of each mechanism to total reaction rate was determined. At 50 mol.% Fe substitution, intrafacial reaction mechanism becomes prominent, whereas suprafacial mechanism is maximized at 30 mol.% Fe substitution. Considering the enhanced stability provided by the additional Ti sites on the $La_{0.3}Sr_{0.7}Ti_{0.7}Fe_{0.3}O_3$ system, 30 mol.% Fe substitution can be deemed to provide the optimum performance/stability compromise for stand-alone oxidation catalysis.

Simultaneous incorporation of chemical and textural complexity to the catalyst system design was investigated by employing cooperative assembly synthesis route to prepare highly porous LSTF solid solutions with $La_{0.3}Sr_{0.7}Ti_{0.5}Fe_{0.5}O_{3-\delta}$ nominal stoichiometry. Influence of siliceous template to the porosity and other material properties was investigated by setting the template load between 11 – 40 vol.%. Pure-phase highly crystalline mesoporous aggregates with specific surface areas up to 201 $m^2\ g^{-1}$ were successfully obtained. Moreover, highly porous LSTF showed decent thermal stability with only minor porosity loss (~15%) after heat treatment at 600 °C under reducing conditions. However, despite their higher surface areas,

porous LSTF oxides showed inferior catalytic performance in CH_4 oxidation. This contradictory finding can be explained by the stoichiometry deviation observed on the templated materials. Fe deficiency which becomes more prominent at higher template loads, likely plays a central role in performance loss, since iron centers provide the active sites for the methane oxidation in LSTF system. Another contribution to the performance loss was identified as the surface deactivation of the material due to sodium hydroxide etching treatment for template removal. Despite their sub-optimal functional properties, highly porous LSTF oxides showed promise as support material in oxidation catalysis. Pt nanoparticles supported by highly porous LSTF oxides attained higher performance than commonly employed CeO_2 supported Pt catalysts in CO oxidation. This result can be explained by the excellent oxygen supply capability of LSTF oxides to the Pt active phase, as well as possible nanoconfinement effects and interactions between metal and perovskite that enhance the reactivity at metal – oxide interface sites.

A-site substitution in perovskite oxides usually does not incur significant changes in catalytic performance [5]. In fact, donor substitution in $SrTiO_3$ based system can lead to minor performance losses due to suppression of charge carriers, as discussed for the $La_{0.3}Sr_{0.7}Ti_{0.9}Fe_{0.1}O_{3\pm\delta}$ system. However, complexity of the charge transport mechanism in substituted perovskite oxides can be potentially exploited through tailoring the concentration of ionic and electronic charge carriers and thereby the catalytic activity of the material. The application of this strategy was investigated by implementing the novel flash sintering technology on $La_{0.1}Sr_{0.9}TiO_{3+\delta}$ (LSTO) nanoparticles, which is mainly investigated in literature as a time and energy effective consolidation technique to obtain ceramics with high thermal stability. Simultaneous heat treatment and electric field exposure in flash sintering of LSTO samples led to enhanced concentration of Sr vacancies and O^{-} sites along with markedly lower activation energy for charge migration in comparison to the conventionally sintered counterpart. Moreover, flash sintered samples retained two-fold higher surface area. Combination of these improved properties enabled flash sintered LSTO to show significantly superior catalytic performance than similar donor substituted $SrTiO_3$ systems in literature.

Complexity and flexibility of perovskite oxide systems present many opportunities and challenges towards development of high performance functional systems in environmental catalysis. Variation of perovskite oxide composition, either by doping with small amount of foreign atoms or by devising single phase substitutional solid solutions with several

constituents is an effective strategy to precisely tailor the material for the desired functional properties. On top of that, design of mesoporous nanoarchitectures which are readily accessible to reactant molecules is crucial to maximize the number of active sites on catalyst surface as well as to attain unique surface properties and catalyst – reactant interactions that are enabled by the nanostructuring of the material. As demonstrated in this work through mesoporous $SrTiO_3$ and $La_{0.3}Sr_{0.7}Ti_{1-x}Fe_xO_{3\pm\delta}$ systems, such designs indeed induce significant enhancement of catalytic activity.

Thus, preparation of highly porous perovskite nanostructures within a chemically complex composition stands as a crucial design goal towards high performance perovskite catalysts. For instance, band gap engineering of highly porous $SrTiO_3$ nanostructures through ionic doping to enable visible radiation absorption can be a promising strategy towards superior photocatalysts in wastewater treatment and solar water splitting [117].

On the other hand, attaining highly porous structure and precise stoichiometry simultaneously is a challenging task as demonstrated through LSTF solid solutions prepared by the cooperative assembly route. Better optimization of synthesis and template removal parameters in this route to prepare LSTF solid solutions with precise stoichiometry may enable desired activity enhancement. Moreover, heat treatment of the material in different conditions can be utilized in attempt to re-activate the catalyst surface.

During last two decades significant efforts have been made to prepare nanoporous perovskite oxides by implementing the synthetic protocols developed in the broader nanotechnology field. However, perovskite oxides prepared by these routes are in most cases still fairly limited to non-substituted systems with mediocre surface areas (~50 $m^2\ g^{-1}$) [14]. Moreover, prepared materials commonly show sub-optimal structural and functional properties. Thus, further development of these routes is crucial in order to attain highly porous complex perovskite nanostructures with well-defined functional characteristics that can have commercial utilization.

A potentially fruitful application of these systems that has not yet found sufficient attention in perovskite catalysis research is their utilization as active support in combination with noble metal catalysts. Perovskite oxides with optimized textural properties can plausibly provide a superior alternative to currently used supports by benefiting from the unique interactions between the oxide and metal, as well as by providing additional active sites for the reaction and improving the life span of the catalyst system [410,411]. This application can be utilized,

not only in thermally activated reactions, but also in photocatalyzed processes such as photocatalytic water-gas shift reaction over supported noble metal catalysts [412,413]. Once porous perovskite nanostructures with decent stand-alone catalytic activity are obtained, research in this area should focus on improving the weak resistance of perovskite oxides towards poisons such as sulfur dioxide and exploiting the metal – perovskite interactions [5].

Furthermore, recently there is growing interest in in-situ exsolution of metal nanoparticles from the perovskite lattice through reductive heat treatment [414]. Retainment of the porous structure during the harsh conditions of the high temperature process should be further investigated to achieve active bifunctional systems through exsolution process [14].

Despite the large body of work that is accumulated over years which identifies the structure – function relationships in perovskite oxide catalysts and provides models to describe the mechanisms of catalytic reactions, a physical theory of the catalytic processes with knowledge of their atomic details is far from being achieved [144]. A major challenge in understanding these interactions stems from the fact that catalysts are often characterized in their static state, whereas electronic and geometric structure are modified in every catalytic cycle dependent on the dynamic interactions between the catalyst and reactants. Hence, in-situ analytical methods to characterize the active sites during reaction conditions should be extensively utilized and further developed if necessary for rational design of catalyst materials [143,415]. Moreover, quantum mechanics calculations can be implemented to determine the favorable conditions for the catalytic sites of particular processes [416] .

Notwithstanding the great achievements in perovskite catalyst research in recent decades, significant progress in material development is still required for commercial utilization of perovskite oxides in catalysis. In this respect, effective incorporation of the nanotechnology derived strategies to prepare chemically complex mesoporous perovskite oxide nanostructures can be deemed as the most immediate design challenge. The present work provides insights towards the preparation of such complex systems through precise tuning of composition, nanoarchitecture and defect structure.

Chapter 6

Experimental

6.1 Material preparation

In this section, the preparation procedures of $SrTiO_3$ and related perovskites investigated in this work are described. The precise amounts of precursor materials used in the syntheses are reported on Table 6.1.

Template-free preparation of $SrTiO_3$ and $La_{0.3}Sr_{0.7}Ti_{1-x}Fe_xO_{3\pm\delta}$ mesoporous powders

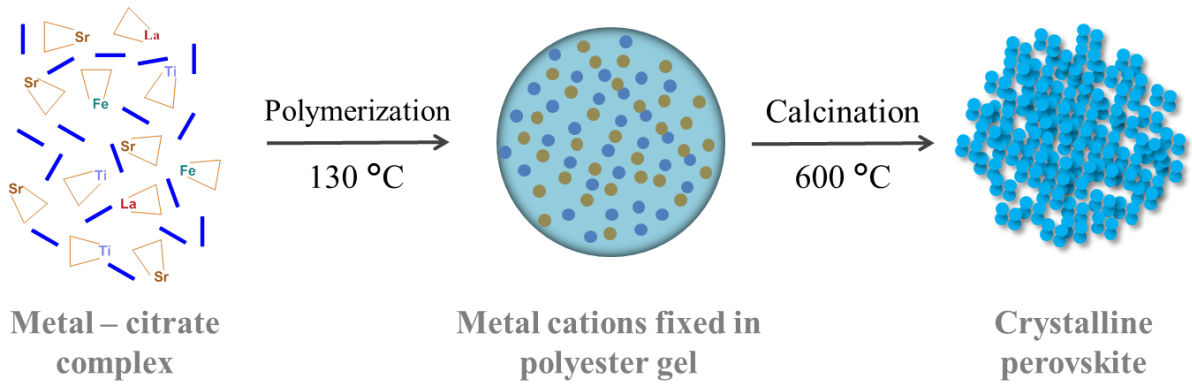

Figure 6.1: Synthesis scheme for template free polymer complex route.

An optimized polymer complex route was employed for the template free preparation of $SrTiO_3$ (STO) and $La_{0.3}Sr_{0.7}Ti_{1-x}Fe_xO_{3\pm\delta}$ (LSTF). In a typical synthesis, titanium (IV) isopropoxide ($Ti[OCH(CH_3)_2]_4$, TTIP) was initially introduced to 11.9 mL glycerol (15.0 g,

0.162 mol) and stirred for 30 min at room temperature. Then, 40.7 mmol citric acid (CA, 7.82 g) were added and the solution was heated to 60 °C. After further 30 min stirring, stoichiometric amounts of $Sr(NO_3)_2$, $La(NO_3)_3{\cdot}6H_2O$ and $Fe(NO_3)_3{\cdot}9H_2O$ were added one after another at 30 min intervals (See Table 6.1). When the addition of precursors were completed, the solution was stirred vigorously further for 2 h and then heated to 130 °C. The polycondensation reaction between the glycerol and citric acid at this temperature resulted in a polymer gel, which was then calcined in air to obtain desired perovskite oxides (Fig. 6.1). A 2 °C min^{-1} heating ramp was used in the calcination process with 2 h temperature hold steps at an intermediate temperature and the final temperature of 600 °C. The intermediate temperature was set at 350 °C for $SrTiO_3$ and 400 °C for $La_{0.3}Sr_{0.7}Ti_{1-x}Fe_xO_{3\pm\delta}$ compositions. Obtained perovskite powders (~700 mg) were treated with 100 mL acetic acid (1.0 M) for 1 h to remove carbonate impurities [125] and subsequently washed with deionized water thoroughly to attain pH neutrality.

Preparation of Prehydrolyzed Alkoxysilane Solution

61 ml ethanol and 61 ml TEOS were mixed and 6.9 ml HCl (0.02 M) was added dropwise on this solution. The mixture was stirred at 60 °C for 1.5 h and stored at 4 °C [417]. Prehydrolyzed TEOS solution is labeled p_TEOS on Table 6.1.

Cooperative assembly synthesis of mesoporous perovskites with enhanced porosity

A facile cooperative assembly route based on polymer complex process was developed for the preparation of highly porous perovskite powders with nominal stoichiometries of $SrTiO_3$ and $La_{0.3}Sr_{0.7}Ti_{0.5}Fe_{0.5}O_{3-\delta}$ (Fig. 6.2). In this modified route, subsequent to addition of cationic precursors and 1 h stirring, the prehydrolyzed alkoxysilane solution (p_TEOS) was added in varying amounts to the reaction mixture as an inorganic endotemplate. After 2 h further stirring the temperature was raised to 130 °C leading intimately growing polyester and silica chains to form into a well interwoven network. The resulting gel was then calcined under air to obtain an interpenetrating perovskite – silica nanocomposite. Obtained powders were initially subjected to the same acetic acid treatment described for template free samples. Subsequently, the nanocomposites (in 350 mg portions) were treated with 25 mL NaOH (2.0 M) at 90 °C for 24 h to remove the silica template. Finally, the acetic acid treatment was

repeated. After each step, the powders were washed thoroughly with deionized water to ensure pH neutrality.

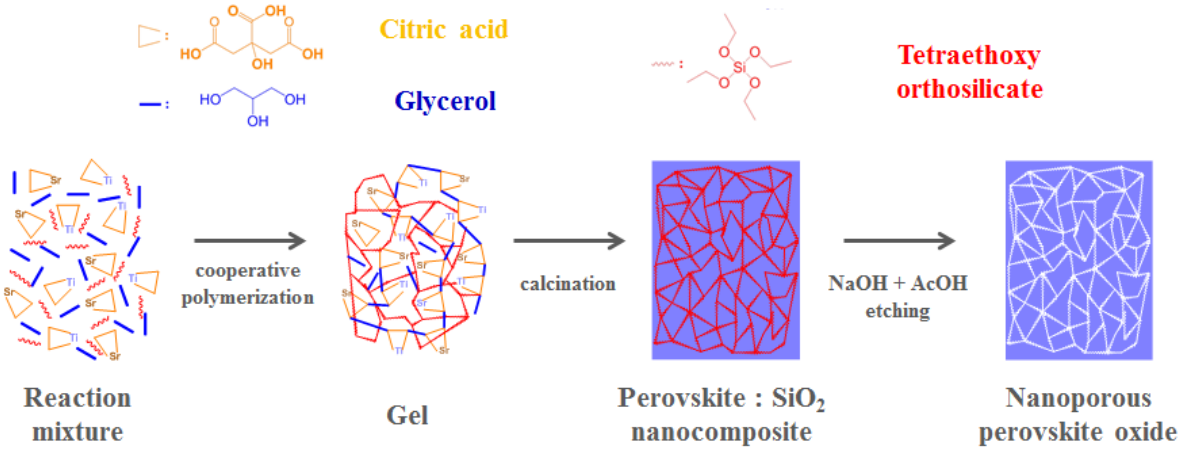

Figure 6.2: Synthesis scheme for cooperative assembly synthesis of perovskite oxides with tunable porosity. Red chains on the scheme represent formation of SiO_2 network..

Synthesis and deposition of Pt nanoparticles on highly porous LSTF

Synthesis and deposition of Pt nanoparticles were performed by Siwon Lee as part of collaboration with the research group of Prof. WooChul Jung at KAIST.

An aqueous solution was prepared by dissolving 12.5 mL alkyltrimethylammonium bromide, C_{18}TAB, (0.4 M) and 5 mL potassium tetrachloroplatinate(II), K_2PtCl_4, (0.01 M) in 29.5 mL deionized water under continuous stirring. Temperature was raised to 55 °C and the solution was further stirred for 25 min. Subsequently, 3 mL of an ice-cooled aqueous sodium borohydride ($NaBH_4$) solution (0.5 M) was added as reducing agent. Evolving hydrogen gas were released from the flask through a needle for 20 min. Reaction mixture under continuous stirring was maintained at 55 °C for 15 h. 10 mL ethanol was added to the resulting brown sol and the mixture was centrifuged at 12,000 rpm for 1 h. The supernatant solution was removed and then the centrifugation was repeated. Final precipitate comprised of Pt nanoparticles (NPs) was collected and redispersed in 5 mL deionized water.

The deposition of as prepared Pt NPs on the highly porous LSTF (LST.50F_40) was initiated by dispersing the oxide powder in a mildly basic (pH ~ 8) aqueous solution to induce negative surface charge. The colloidal Pt solution with positively charged Pt NPs was then added in a

suitable amount to give 1 wt.% of the total catalyst weight. The mixture was stirred for 10 min and the resulting suspension was centrifuged at 8000 rpm for 10 min. The precipitate was then collected, dried in an oven and annealed at 350 °C for 5 h under air.

Solvothermal Synthesis of $La_{0.1}Sr_{0.9}TiO_{3+\delta}$

The initial as-prepared $La_{0.1}Sr_{0.9}TiO_3$ (AP LSTO) particles with high purity and well-defined morphology in Chapter 4.4 were prepared by a modification of the solvothermal synthesis route described by Ouyang et al. (Fig. 6.3) [130].

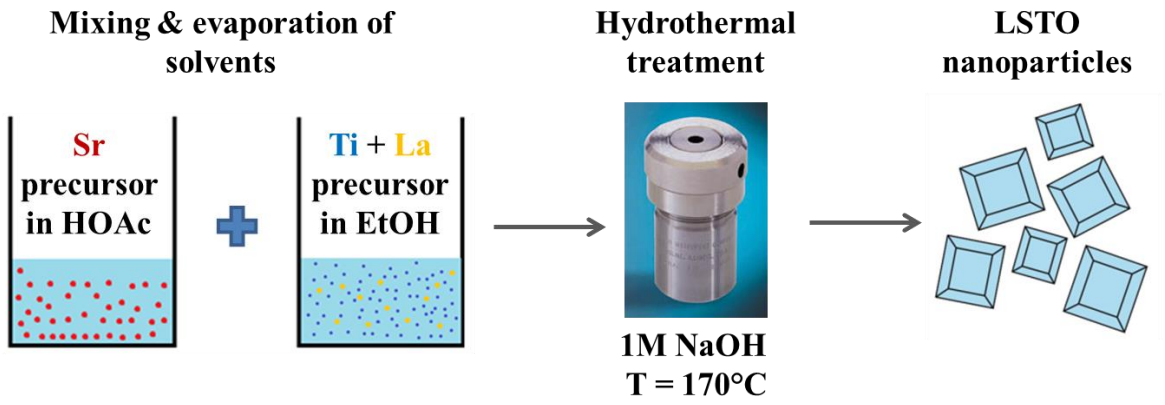

Figure 6.3: Synthesis scheme for solvothermal synthesis of $La_{0.1}Sr_{0.9}TiO_{3+\delta}$ nanoparticles.

In this approach, 5.0 mmol titanium (IV) isopropoxide (TTIP, 1.47 g) and 0.5 mmol lanthanum nitrate hexahydrate ($LaNO_3 \cdot 6H_2O$, 0.217 g) were respectively dissolved in 30 mL ethanol. A second solution was prepared by dissolving 4.5 mmol strontium acetate hemihydrate ($Sr(OOCCH_3)_2 \cdot 0.5H_2O$, 0.99 g) in 20 mL glacial acetic acid. This second solution was added dropwise on the ethanol based solution. Resulting mixture was stirred for 1 h at room temperature to ensure acetic acid chelation and then heated to 75 °C under continuous stirring until complete solvent evaporation (~ 48 h). Subsequently obtained gelatin was ground to a white powder and further dried at ~ 80 °C overnight. 700 mg of this powder was placed in a 10 mL Teflon liner, which was then filled to 80% of its total volume with a 1 M NaOH solution. The Teflon liner was sealed in a stainless steel autoclave and solvothermally treated in an oven under autogeneous pressure at 170 °C for 24 h. After cooling down, the precipitate was extracted from the Teflon liner and washed thoroughly with deionized water to ensure pH neutrality. Finally, the filter cake comprised of $La_{0.1}Sr_{0.9}TiO_3$ nanocuboids was dried at 80 °C overnight.

Table 6.1: Overview of STO and LSTF mesoporous aggregates prepared in this work along with template and cationic precursor amounts. Glycerol and citric acid (CA) were kept constant to give molar ratio **60 : 15 : 4** between **Glycerol : CA : Perovskite**.

Sample Code	Nominal stoichiometry	Perovskite : SiO_2 Molar ratio	p_TEOS [g]	$Sr(NO_3)_2$ [g]	$La(NO_3)_3 \cdot 6H_2O$ [g]	$Fe(NO_3)_3 \cdot 9H_2O$ [g]	TTIP [g]
STO	$SrTiO_3$	X	X	1.15	X	X	1.54
STO_06	$SrTiO_3$	10 : 1	0.22	1.15	X	X	1.54
STO_11	$SrTiO_3$	5 : 1	0.44	1.15	X	X	1.54
STO_24	$SrTiO_3$	2 : 1	1.11	1.15	X	X	1.54
STO_40	$SrTiO_3$	1 : 1	2.22	1.15	X	X	1.54
LST.00F	$La_{0.3}Sr_{0.7}TiO_{3+\delta}$	X	X	0.80	0.71	X	1.54
LST.10F	$La_{0.3}Sr_{0.7}Ti_{0.9}Fe_{0.1}O_{3+\delta}$	X	X	0.80	0.71	0.22	1.35
LST.30F	$La_{0.3}Sr_{0.7}Ti_{0.7}Fe_{0.3}O_{3\pm\delta}$	X	X	0.80	0.71	0.66	1.05
LST.50F	$La_{0.3}Sr_{0.7}Ti_{0.5}Fe_{0.5}O_{3-\delta}$	X	X	0.80	0.71	1.10	0.75
LST.50F_11	$La_{0.3}Sr_{0.7}Ti_{0.5}Fe_{0.5}O_{3\pm\delta}$	5 : 1	0.44	0.80	0.71	1.10	0.75
LST.50F_20	$La_{0.3}Sr_{0.7}Ti_{0.5}Fe_{0.5}O_{3\pm\delta}$	2.5 : 1	0.88	0.80	0.71	1.10	0.75
LST.50F_40	$La_{0.3}Sr_{0.7}Ti_{0.5}Fe_{0.5}O_{3\pm\delta}$	1 : 1	2.22	0.80	0.71	1.10	0.75

6.2 Instrumental characterization

N_2 physisorption The nitrogen sorption isotherms were obtained at 77 K using a Quadrasorb SI-MP by Quantachrome. Outgassing was performed with a Masterprep Degasser (Quantachrome Corp.) at 120 °C for 12 h. Specific surface areas were determined with the Brunauer–Emmett−Teller (BET) method [418] at $p/p_0 = 0.07 – 0.3$. Pore size distribution was determined with the NLDFT method [306] applying the model for cylindrical pores on the adsorption branch by using the Quantachrome ASiQWin software.

X-ray diffraction XRD analyses were carried out with an X'Pert Pro diffractometer (PANalytical Corp.) with 1.5406 Å Ni-filtered Cu-Kα radiation, operating at 45 kV and 40 mA. The mean crystallite sizes were calculated from the full width at half maximum (FWHM) of the most intense reflection (110) using the Scherrer equation (3.4).

Electron microscopy Transmission electron microscopy measurements were carried out on a JEOL JEM 2200 FS operating at 200 kV equipped with two CEOS Cs correctors (CETCOR, CESCOR), a JEOL JED-2300 Si(Li) EDX (energy dispersive X-ray spectroscopy) detector, a Gatan 4K UltraScan 1000 camera and a HAADF (high angle annular dark field) detector. The sample was grinded into a fine powder, which was suspended in toluene by sonication and dropped on a carbon coated 400 mesh TEM grid. The excess of solvent was removed with a filter paper and by drying the grid under air.

Energy dispersive X-ray spectra and mapping were acquired using 256x256 pixels (pixel size of 0.7 nm) and a dwell time of 0.5 ms $pixel^{-1}$ (corrected for dead time) with 30 cycles. Additionally, EDX measurements were repeated at least on three positions for each sample and less than 1.0 at. % disparity was observed for surveyed cations at each point.

Scanning electron microscopy images were obtained on a LEO1550 with a spatial resolution of ≈ 1 nm. The powder was fixed on a standard carbon conductive tab and was investigated without further conductive coating.

X-ray photoelectron spectroscopy XPS spectra of mesoporous $SrTiO_3$ aggregates (Chapter 4.1) were acquired by using a Perkin-Elmer 5600ci spectrometer using standard Al radiation (1486.6 eV) working at 250 W. The working pressure in the analysis chamber was <

$5 \cdot 10^{-8}$ Pa. The spectrometer was calibrated by assuming the binding energy (BE) of the $Au4f_{7/2}$ line at 83.9 eV with respect to the Fermi level. The standard deviation for the BE values was 0.15 eV. The reported BE were corrected for the charging effects, assigning to the C1s line of adventitious carbon the BE value of 284.6 eV [357,419].

Survey scans (187.85 pass energy, 1 eV/step, 25 ms per step) were obtained in the 0-1350 eV range. Detailed scans (29.35 eV pass energy, 0.1 eV/step, 100-150 ms per step) were recorded for the C1s, O1s, Ti2p, Sr3d, Si2p, TiLMM regions. The atomic composition of the powders, after a Shirley type background subtraction [420] was evaluated using sensitivity factors supplied by Perkin-Elmer[357]. The assignments of the peaks was carried out by using the values reported in the reference handbook [357].

XPS spectra of $La_{0.3}Sr_{0.7}Ti_{1-x}Fe_xO_{3\pm\delta}$ (Chapter 4.2) were acquired using a Sigma probe (Thermo Scientific, USA) under ultrahigh vacuum environment with a 400 μm-diameter beam of monochromatic X-ray source, Al Kα ($h\nu$ = 1486.6 eV) radiation.

Ultraviolet and visible spectroscopy UV/Vis spectra of the methylene blue solutions and of the porous $SrTiO_3$ samples (Chapter 4.1) were recorded with a Cary 5000 UV/Vis-NIR spectrophotometer of Varian. The powder measurements were implemented with the help of Praying Mantis Diffuse Reflection Accessory by Harrick. Obtained reflectance spectra were converted to absorbance mode with Cary WinUV software. The linearization parameters of the Tauc plots on Fig. 4.10 are reported on Table 6.2.

Infrared spectroscopy Infrared spectra were obtained in the region 400 – 4000 cm^{-1} in transmission mode with a Bruker Vertex 70 FTIR spectrophotometer.

Electrochemical impedance spectroscopy Impedance measurements were performed using a Novocontrol Alpha A impedance analyzer connected to a NorECs Probostat® sample chamber. A Novocontrol-HT controller connected to a type S thermocouple mounted next to the sample was employed for temperature control. A colloidal silver paste (Pelco®) was applied on both sides of the analyzed pellets to ensure contact to the Pt net electrodes. Frequencies in the range of 10^{-2} Hz to 10^{7} Hz were employed with an amplitude of 100 mV_{rms} for all measurements.

Novocontrol WinFIT was used for data evaluation and equivalent circuit fitting. An equivalent circuit consisting of three RQ elements usually ascribed to grain boundary, bulk and electrode interface contributions was employed to fit the experimental data. The oxygen partial pressure was set by mixing Ar 5.0 with air using MKS MF-1 mass flow controllers. Partial pressures were monitored using a NorECs miniature oxygen sensor electrode with a sealed internal metal/metal oxide reference and a Rigol DM-3058 multimeter.

A constant gas flow of 19 sccm was employed for all measurements in Chapter 4.4 with the gas supply tube ending in close proximity to the sample. All samples were equilibrated for 13 hours at the desired partial pressure. Each temperature was held for 3 hours before a measurement was performed. Temperature was varied between 700 – 400 °C with whereas pO_2 was varied between 0.21 – 10^{-4} bar by adjusting the air/Ar atmosphere.

$La_{0.3}Sr_{0.7}Ti_{1-x}Fe_xO_{3\pm\delta}$ powders in Chapter 4.2 were uniaxially pressed into disks with 13 mm in diameter and 1 mm thickness at 222 MPa. The samples were subsequently heated to 600 °C for 2 h, resulting in stable disks. Frequencies between 10^{-2} Hz and 10^{7} Hz were employed with an amplitude of 10 mV_{rms} for all measurements. Novocontrol WinFIT was used for data evaluation and equivalent circuit fitting. The sample resistance was obtained from the (RQ) elements not corresponding to the electrode response. Due to the porous structure of the samples no further analysis regarding grain boundary and bulk contributions was carried out. The oxygen partial pressure (4% oxygen atmosphere) was set by mixing Ar 5.0 with synthetic air using MKS MF-1 mass flow controllers. The oxygen partial pressure was verified using a NorECs miniature oxygen sensor electrode with a sealed internal metal/metal oxide reference and a Rigol DM-3058 multimeter. All samples were first equilibrated overnight at 500 °C at the desired partial pressure. Each temperature was held for 2 h before a measurement was performed. Each temperature was held for 2 h before a measurement was performed.

Nuclear magnetic resonance spectroscopy ^{29}Si cross polarization magic angle spinning nuclear magnetic resonance (CP/MAS NMR) experiments were performed at an operating frequency of 79.52 MHz on a Bruker AvanceII 400 spectrometer equipped with a 4 mm double resonance probe. ^{1}H 90°pulse length of 4.4 µs, contact time of 2 ms, and recycle delay of 5 s were used. All measurements were performed at room temperature and with the MAS frequency of 5 kHz. Continuous wave decoupling was used during the acquisition.

16000 transients were acquired for all the samples and the spectra were plotted in a calibrated intensity scale, taking into account the analyzed sample mass.

^{57}Fe Mössbauer Spectroscopy Room Temperature Mössbauer spectroscopy was performed on a conventional constant acceleration spectrometer mounting a Rh matrix ^{57}Co source, nominal strength 1850 MBq. The hyperfine parameters are compiled on Table 6.3 and 6.4. The spectra were fitted to Lorentzian line shapes with the minimum number of components. δ is quoted relative to standard α-Fe foil.

Electron Spin Resonance Spectroscopy The Electron Spin Resonance (ESR) investigations were performed by using a Bruker EMX spectrometer operating at the X-band frequency and equipped with an Oxford cryostat working in the temperature range of 4-298 K. The samples were inserted in quartz glass tubes connected to a high-vacuum pumping system. Spectra were recorded under in vacuo conditions ($p < 10^{-5}$ mbar) at 130 K. The g values were calculated by standardization with α,α′-diphenyl-β-picryl hydrazyl (DPPH). Care was taken to always keep the most sensitive part of the ESR cavity (1 cm length) filled. Spectra simulations and fits were performed using the SIM 32 program [421].

Thermogravimetric analysis Thermal characterization was carried out using a NETZSCH STA 449F3 coupled with Äeolos QMS403C (TG - MS) with 10 °C/min heating rate in an Ar/O_2 stream (volume ratio 78/22).

Temperature Programmed Desorption of Oxygen Temperature-programmed desorption of oxygen (O_2-TPD) profiles were retrieved by a Micromeritics AutoChem 2920 analyzer. Before TPD, each sample (~250 mg) was pretreated under 5% O_2 balanced in He (50 mL min^{-1}) at 550 °C for 2 h. After cooling to 50 °C, the TPD operation was carried out under a He carrier gas (30 mL min^{-1}) from 50 °C to 900 °C at a heating rate of 10 °C min^{-1}. The amount of oxygen desorbed was monitored by a thermal conductivity detector (TCD).

Temperature Programmed Reduction by Hydrogen Temperature-programmed reduction measurements under a H_2 environment (H_2-TPR) were performed with a

Micromeritics AutoChem 2920 analyzer. The catalyst (~100 mg) was pretreated under 5% O_2 stream balanced in He (50 mL min^{-1}) at 550 °C for 2h. After the sample cooled to 150 °C, a flow of 5% H_2 in He gas (50 mL min^{-1}) was introduced into the samples at a flow rate of 50 mL min^{-1}, and the temperature was increased to 650 °C at a ramping rate of 10 °C min^{-1}. The amount of consumed H_2 was measured using a thermal conductivity detector (TCD).

Table 6.2: Linearization parameters of the fits in the Tauc plots.

Sample	Adj. R-Square	Pearson's r	Intercept	Slope	E_{BG}
STO	0.9995	0.9998	-10.140	3.166	3.20
STO_06	0.9997	0.9998	-15.648	4.830	3.24
STO_11	0.9997	0.9999	-13.751	4.243	3.24
STO_24	0.9999	0.9995	-16.413	5.024	3.27
STO_40	0.9999	0.9999	-12.604	3.854	3.27
STO_NP	0.9994	0.9997	-10.966	3.313	3.31

Table 6.3: Room temperature Mössbauer parameters of template free prepared LSTF perovskites (Chapter 4.2).

Sample	δ [mm s^{-1}]	Δ [mm s^{-1}]	Γ [mm s^{-1}]	A [%]	χ^2	Attribution
LST.50F	0.03±0.01	0.38±0.03	0.24±0.05	10±3	1.08	Fe^{4+}
	0.30±0.01	0.39±0.01	0.34±0.02	60±3		Fe^{3+}site 1
	0.34±0.01	0.68±0.01	0.36±0.03	30±3		Fe^{3+}site 2
LST.30F	0.07±0.01	0.60±0.02	0.25±0.04	4±3	1.25	Fe^{4+}
	0.35±0.01	0.48±0.01	0.39±0.02	60±3		Fe^{3+}site 1
	0.35±0.01	0.91±0.03	0.44±0.02	36±3		Fe^{3+}site 2
LST.10F	0.36±0.01	0.56±0.04	0.37±0.05	59±3	1.09	Fe^{3+}site 1
	0.35±0.01	1.03±0.01	0.46±0.03	41±3		Fe^{3+}site 2

Table 6.4: Room temperature Mössbauer parameters of highly porous LSTF perovskites prepared by cooperative assembly (Chapter 4.3).

Sample	δ [mm s^{-1}]	Δ [mm s^{-1}]	Γ [mm s^{-1}]	A [%]	χ^2	Attribution
LST.50F_40	0.05±0.04	0.88±0.01	0.39±0.06	7±3	1.16	Fe^{4+}
	0.38±0.01	0.47±0.03	0.31±0.03	23±3		Fe^{3+}site 1
	0.37±0.01	0.79±0.02	0.34±0.09	32±3		Fe^{3+}site 2
	0.37±0.01	1.17±0.07	0.38±0.05	38±3		Fe^{3+}site 3
LST.50F_20	0.02±0.06	0.88±0.04	0.36±0.08	5±3	0.7	Fe^{4+}
	0.37±0.01	0.46±0.03	0.30±0.04	33±3		Fe^{3+}site 1
	0.37±0.01	0.81±0.03	0.36±0.09	46±3		Fe^{3+}site 2
	0.37±0.01	1.27±0.05	0.35±0.07	16±3		Fe^{3+}site 3
LST.50F_11	0.04±0.01	0.77±0.02	0.39±0.05	7±3	0.95	Fe^{4+}
	0.37±0.03	0.38±0.04	0.27±0.05	33±3		Fe^{3+}site 1
	0.38±0.01	0.68±0.04	0.32±0.09	41±3		Fe^{3+}site 2
	0.37±0.01	1.03±0.08	0.47±0.03	19±3		Fe^{3+}site 3

The hyperfine parameters isomer shift (δ), quadrupole splitting (Δ), full linewidth at half maximum (Γ) were expressed in mm s^{-1}, while internal relative areas (A) in % were obtained by means of standard least-squares minimization techniques.

6.3 Catalytic Tests

Photocatalytic dye degradation

Photocatalytic performances of nanoporous $SrTiO_3$ powders (Chapter 4.1) were assessed via a photocatalytic methylene blue decomposition reaction. A house-made photoreactor equipped with a 125 W high-pressure mercury vapor lamp (Philips HPK-125W) as UV-radiation source was employed for the catalytic tests. The UV-source was encased in a quartz glass water circulation apparatus for effective cooling. The irradiation spectrum of the high-pressure mercury lamp was given on Fig. 6.4.

The lamp provides maximum energy at 365 nm, with substantial radiation also at 435, 313, 253 and 404 nm. In addition, there is a continuum from 200 to 600 nm, peaking at 260 nm with approximately 20 % of the maximum energy measured in the line spectrum 50 ml of 50 mg l^{-1} methylene-blue solution treated with 50 mg $SrTiO_3$ powder was placed directly below the light source with a source to reactor distance of 10 cm. Based on the irradiance intensities given for source-to-reactor distance of 30 cm in Fig. 6.4, an effective irradiance of 29.25 W m^{-2} nm^{-1} at the reactor surface was calculated taking 365 nm as the highest lamp emission wavelength as reference and considering the source-to-reactor distance of 10 cm.

Saturation of dye adsorption was reached after 1 h of dark stirring. Methylene blue samples were investigated via UV-Vis spectroscopy after 0 min, 20 min, 60 min and 120 min of irradiation. Each sample (1 mL) was diluted with H_2O to 10 mL and centrifuged at 10000 rpm for 30 min to eliminate possibly suspended $SrTiO_3$ particles.

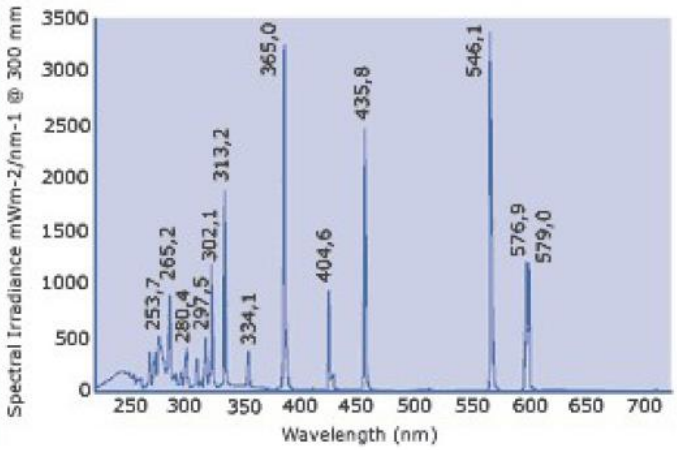

Figure 6.4: Spectral irradiance of the UV-source employed in the photocatalytic tests (msscientific Chromatographie-Handel Gmbh).

CH_4 and CO oxidation

The catalytic activities for CH_4 and CO oxidation were measured in a fixed-bed quartz flow micro-reactor with an internal diameter of 4 mm. For all the measurement, we used 100 mg catalyst mixed with 100 mg quartz sand and loaded in-between two plugs of quartz wool for preventing displacement of the catalyst. The feed of methane oxidation (composed of 2 vol% CH_4, 4 vol% O_2 in Ar) and carbon monoxide oxidation (composed of 1 vol% CO, 4 vol% O_2 in Ar) was flowed into the reactor. To investigate water vapor effect on methane oxidation activity, we flowed 2 vol% of CH_4, 1.2 vol% H_2O, 4 vol% O_2 balanced in Ar. The total flow rate was adjusted for both oxidation reactions to 50 mL min^{-1}. The gas hourly space velocity (GHSV) was 12,000 h^{-1} and the weight hourly space velocity (WHSV) was 30,000 mL g^{-1} h^{-1} in this experiment. The reactant and product gases were monitored in real time with a quadrupole mass spectrometer (PFEIFFER Vacuum GSD320) connected to the reactor outlet. The light-off curve was measured with a ramping rate at 3 °C min^{-1}, after activating the catalysts in the reaction atmosphere up to 600 °C for methane oxidation and 300 °C for CO oxidation. The CH_4 and CO conversion ratio (%) were defined as $100 \times (\text{mol}_{CH4,\,in} - \text{mol}_{CH4,\,out})/\text{mol}_{CH4,\,in}$. and $100 \times (\text{mol}_{CO,\,in} - \text{mol}_{CO,\,out})/\text{mol}_{CO,\,in}$, respectively. In order to determine the reaction order for CH_4 and O_2, we investigated the reaction rate by varying the partial pressure of methane (from 2×10^{-3} to 6×10^{-3} atm) while keeping the partial pressure of oxygen constant (5×10^{-2} atm). In the same way, we observed the reaction rate according to the partial pressure change of oxygen (from 1×10^{-2} to 5×10^{-2} atm) while keeping the partial pressure of methane (2×10^{-3} atm) the same. The signal of CH_4 was detected by the m/z = 15 peak instead of the 16 peak (the major peak of methane) to avoid the contribution caused by the cracking fragment of carbon monoxide (0.9%), water (1.1%), carbon dioxide (8.5%), and oxygen (11%). The signal of CO was corrected for the contribution from the cracking fragment of CO_2 (11.4%) with mass concentration determination mode.

6.4 Flash sintering

Cylindrical pellets (diameter = 8 mm, thickness ~ 3 mm) were shaped by uniaxial pressing at 350 MPa. The two flat surfaces of the green components were painted using a carbon-based conductive cement (Plano GmbH) and then subjected to flash sintering. The process was carried out into a modified dilatometer (Linseis L75) using a heating rate of 20 °C min^{-1}. The samples were placed between two platinum disks (diameter = 9 mm, thickness ~ 3 mm), which were connected to a DC power supply (Glassman EW 5 kV, 120 mA) and to a multimeter (Keithley 2100). The electrical parameters (current and voltage), the furnace temperature and the displacement of the dilatometric piston were recorded at 1 Hz. The flash sintering experiments were carried out using electric fields of 300 (FS-300) and 600 V cm^{-1} (FS-600) and a current limit of 2.5 mA mm^{-2}; once the current limit was reached upon flash experiments, the current was let flow through the ceramic components for 30 s, and then the power supply and the dilatometer furnace were switched off. Conventionally sintered (CS) bodies were manufactured with the following firing program: from room temperature to 900 °C with a 5 °C min^{-1} ramp, from 900 °C to 1150 °C with a 0.5 °C min^{-1} ramp, holding at 1150 °C for 4 h and free cooling in the furnace.

The bulk densities of the samples were measured as the ration between the weight and the volume (determined by a digital caliper). The relative density (ρ) was calculated in % using a value of 5.26 g cm^{-3} for fully dense $La_{0.1}Sr_{0.9}TiO_3$.

Chapter 7

Bibliography

[1] L. Capuano, International Energy Outlook 2018 (IEO2018), 2018. www.eia.gov.

[2] BP, BP Statistical Review of World Energy 2018, 2018.

[3] T.M. Gür, Comprehensive review of methane conversion in solid oxide fuel cells : Prospects for efficient electricity generation from natural gas, Prog. Energy Combust. Sci. 54 (2016) 1–64. doi:10.1016/j.pecs.2015.10.004.

[4] BP, 2018 BP Energy Outlook, 2018. doi:10.1088/1757-899X/342/1/012091.

[5] S. Royer, D. Duprez, F. Can, X. Courtois, C. Batiot-dupeyrat, S. Laassiri, H. Alamdari, Perovskites as substitutes of noble metals for heterogeneous catalysis: Dream or reality, Chem. Rev. 114 (2014) 10292–10368. doi:10.1021/cr500032a.

[6] X. Zhu, K. Li, L.M. Neal, F. Li, Perovskites as geo-inspired oxygen storage materials for chemical looping and three-way catalysis - A perspective, ACS Catal. 8 (2018) 8213–8236. doi:10.1021/acscatal.8b01973.

[7] P. Kanhere, Z. Chen, A review on visible light active perovskite-based photocatalysts, Molecules. 19 (2014) 19995–20022. doi:10.3390/molecules191219995.

[8] J. Shi, L. Guo, ABO_3 -based photocatalysts for water splitting, Prog. Nat. Sci. Mater. Int. 22 (2012) 592–615. doi:10.1016/j.pnsc.2012.12.002.

[9] S.P. Jiang, S.H. Chan, A review of anode materials development in solid oxide fuel cells, J. Mater. Sci. 39 (2004) 4405–4439. doi:10.1023/B:JMSC.0000034135.52164.6b.

[10] C.H. Wang, C.L. Chen, H.S. Weng, Surface properties and catalytic performance of $La_{1-x}Sr_xFeO_3$ perovskite-type oxides for methane combustion, Chemosphere. 57 (2004) 1131–1138. doi:10.1016/j.chemosphere.2004.08.031.

[11] S. Cimino, L. Lisi, S. De Rossi, M. Faticanti, P. Porta, Methane combustion and CO oxidation on $LaAl_{1-x}Mn_xO_3$ perovskite-type oxide solid solutions, Appl. Catal. B Environ. 43 (2003) 397–406. doi:10.1016/S0926-3373(03)00023-7.

[12] P. Ciambelli, S. Cimino, G. Lasorella, L. Lisi, S. De Rossi, M. Faticanti, G. Minelli, P. Porta, S. De Rossi, M. Faticanti, G. Minelli, P. Porta, CO oxidation and methane combustion on $LaAl_{1-x}Fe_xO_3$ perovskite solid solutions, Appl. Catal. B Environ. 37 (2002) 231–241. doi:10.1016/S0926-3373(02)00004-8.

[13] C. Aliotta, L.F.F. Liotta, F. Deganello, V. La Parola, A. Martorana, V. La Parola, A. Martorana, Direct methane oxidation on $La_{1-x}Sr_xCr_{1-y}Fe_yO_{3-\delta}$ perovskite-type oxides as potential anode for intermediate temperature solid oxide fuel cells, Appl. Catal. B Environ. 180 (2016) 424–433. doi:10.1016/j.apcatb.2015.06.012.

[14] X. Huang, G. Zhao, G. Wang, J.T.S.S. Irvine, Synthesis and applications of nanoporous perovskite metal oxides, Chem. Sci. 9 (2018) 3623–3637. doi:10.1039/c7sc03920d.

[15] J. Zhu, H. Li, L. Zhong, P. Xiao, X. Xu, X. Yang, Z. Zhao, J. Li, Perovskite oxides: Preparation, characterizations, and applications in heterogeneous catalysis, ACS Catal. 4 (2014) 2917–2940. doi:10.1021/cs500606g.

[16] M. Mao, H. Lv, Y. Li, Y. Yang, M. Zeng, N. Li, X. Zhao, Metal Support Interaction in Pt Nanoparticles Partially Confined in the Mesopores of Microsized Mesoporous CeO_2 for Highly Efficient Purification of Volatile Organic Compounds, ACS Catal. 6 (2016) 418–427. doi:10.1021/acscatal.5b02371.

[17] N. Satoh, T. Nakashima, K. Kamikura, K. Yamamoto, Quantum size effect in TiO_2 nanoparticles prepared by finely controlled metal assembly on dendrimer templates, Nat. Nanotechnol. 3 (2008) 106–111. doi:10.1038/nnano.2008.2.

[18] J. Zhang, J.H. Bang, C. Tang, P. V. Kamat, Tailored TiO_2 - $SrTiO_3$ heterostructure nanotube arrays for improved photoelectrochemical performance, ACS Nano. 4 (2010) 387–395. doi:10.1021/nn901087c.

[19] M. Biesuz, V.M. Sglavo, Flash sintering of ceramics, J. Eur. Ceram. Soc. 39 (2019) 115–143. doi:10.1016/j.jeurceramsoc.2018.08.048.

[20] S. Saraf, I. Riess, A. Rothschild, Parallel Band and Hopping Electron Transport in $SrTiO_3$, Adv. Electron. Mater. 2 (2016) 1–22. doi:10.1002/aelm.201500368.

[21] R.A. De Souza, Oxygen Diffusion in $SrTiO_3$ and Related Perovskite Oxides, Adv. Funct. Mater. 25 (2015) 6326–6342. doi:10.1002/adfm.201500827.

[22] J.W. Liu, G. Chen, Z.H. Li, Z.G. Zhang, Electronic structure and visible light photocatalysis water splitting property of chromium-doped $SrTiO_3$, J. Solid State Chem. 179 (2006) 3704–3708. doi:10.1016/j.jssc.2006.08.014.

[23] S. Royer, D. Duprez, Catalytic Oxidation of Carbon Monoxide over Transition Metal Oxides, ChemCatChem. 3 (2011) 24–65. doi:10.1002/cctc.201000378.

[24] E. Grabowska, Selected perovskite oxides: Characterization, preparation and photocatalytic properties-A review, Appl. Catal. B Environ. 186 (2016) 97–126. doi:10.1016/j.apcatb.2015.12.035.

[25] H. Zhu, P. Zhang, S. Dai, Recent Advances of Lanthanum-Based Perovskite Oxides for Catalysis, ACS Catal. 5 (2015) 6370–6385. doi:10.1021/acscatal.5b01667.

[26] M.C. Verbraeken, T. Ramos, K. Agersted, Q. Ma, C.D. Savaniu, B.R. Sudireddy, J.T.S. Irvine, P. Holtappels, F. Tietz, Modified strontium titanates: From defect chemistry to SOFC anodes, RSC Adv. 5 (2015) 1168–1180. doi:10.1039/c4ra09751c.

[27] J. Xu, X. Zhou, X. Dong, L. Pan, K. Sun, Catalytic activity of infiltrated $La_{0.3}Sr_{0.7}Ti_{0.3}Fe_{0.7}O_{3-\delta}$–$CeO_2$ as a composite SOFC anode material for H_2 and CO oxidation, Int. J. Hydrogen Energy. 42 (2017) 15632–15640. doi:10.1016/J.IJHYDENE.2017.05.016.

[28] T. Menke, R. Dittmann, P. Meuffels, K. Szot, R. Waser, Impact of the electroforming process on the device stability of epitaxial Fe-doped $SrTiO_3$ resistive switching cells, J. Appl. Phys. 106 (2009). doi:10.1063/1.3267485.

[29] C. Lenser, Z. Connell, A. Kovács, R. Dunin-Borkowski, A. Köhl, R. Waser, R. Dittmann, Identification of screw dislocations as fast-forming sites in Fe-doped $SrTiO_3$, Appl. Phys. Lett. 102 (2013) 183504. doi:10.1063/1.4804364.

[30] C.Y. Park, A.J. Jacobson, Thermal and chemical expansion properties of $La_{0.2}Sr_{0.8}Fe_{0.55}Ti_{0.45}O_{3-x}$, Solid State Ionics. 176 (2005) 2671–2676. doi:10.1016/j.ssi.2005.08.003.

[31] C.Y. Park, A.J. Jacobson, Electrical Conductivity and Oxygen Nonstoichiometry of $La_{0.2}Sr_{0.8}Fe_{0.55}Ti_{0.45}O_{3-\delta}$, J. Electrochem. Soc. 152 (2005) J65. doi:10.1149/1.1931307.

[32] D.P. Fagg, V. V Kharton, J.R. Frade, A.A.L. Ferreira, Stability and mixed ionic – electronic conductivity of $(Sr,La)(Ti,Fe)O_{3-\delta}$ perovskites, Solid State Ionics. 156 (2003) 45–57. doi:http://dx.doi.org/10.1016/S0167-2738(02)00257-6.

[33] M.R. Levy, Chapter 3: Perovskite Perfect Lattice, in: Cryst. Struct. Defect Prop. Predict. Ceram. Mater., 2005: pp. 79–114.

[34] V.M. Goldschmidt, Die Gesetze der Krystallochemie, Naturwissenschaften. 14 (1926) 477–485. doi:10.1007/BF01507527.

[35] M. Johnsson, P. Lemmens, Crystallography and Chemistry of Perovskites, Handb. Magn. Adv. Magn. Mater. (2007) 1–11. doi:10.1002/9780470022184.hmm411.

[36] J. Garcia-Munoz, J. Rodriguez Carvalhal, P. Lacorre, J. Torrance, Neutron-diffraction study of $RNiO_3$ (R=La,Pr,Nd,Sm): Electronically induced structural changes across the metal-insulator transition, Phys. Rev. B - Condens. Matter Mater. Phys. 46 (1992) 4414.

[37] T. Zhang, K. Zhao, J. Yu, J. Jin, Y. Qi, H. Li, X. Hou, G. Liu, Photocatalytic water splitting for hydrogen generation on cubic, orthorhombic, and tetragonal $KNbO_3$ microcubes, Nanoscale. 5 (2013) 8375–8383. doi:10.1039/c3nr02356g.

[38] R.J.D. Tilley, Defects in Solids, 2008. doi:10.1002/9780470380758.

[39] A. C. Marques, Advanced Si pad detector development and $SrTiO_3$ studies by emission channeling and hyperfine interaction experiments, Universidade de Lisboa, 2009.

[40] Y.I. Vorob'yev, A.A. Konev, Y. V. Malyshonok, G.F. Afonina, A.N. Sapozhnikov, Tausonite, $SrTiO_3$, A New Mineral of the Perovskite Group, Int. Geol. Rev. 26 (1984) 462–465. doi:10.1080/00206818409466573.

[41] S.N. Ruddlesden, P. Popper, New compounds of the K_2NIF_4 type, Acta Crystallogr. 10 (1957) 538–539. doi:10.1107/S0365110X57001929.

[42] S.N. Ruddlesden, P. Popper, The compound $Sr_3Ti_2O_7$ and its structure, Acta Crystallogr. 11 (1958) 54–55. doi:10.1107/S0365110X58000128.

[43] S.A. Hayward, E.K.H. Salje, Cubic-tetragonal phase transition in $SrTiO_3$ revisited: Landau theory and transition mechanism, Phase Transitions. 68 (1999) 501–522. doi:10.1080/01411599908224530.

[44] F.W. Lytle, X-ray diffractometry of low-temperature phase transformations in strontium titanate, J. Appl. Phys. 35 (1964) 2212–2215. doi:10.1063/1.1702820.

[45] P. Revie, Dielectric Properties of $SrTiO_3$ at Low Temperature, 26 (1971) 851–853.

[46] M.D. Drahus, An Electron Paramagnetic Resonance Investigation Of The Defect Chemistry Of The $(Sr_{1-y}La_y)(Ti_{1-x}Fe_x)O_{3-\delta}$ System, Albert-Ludwigs-Universität Freiburg im Breisgau, 2014.

[47] J.H. Haeni, C.D. Theis, D.G. Schlom, W. Tian, X.Q. Pan, H. Chang, I. Takeuchi, X.

Xiang, Epitaxial growth of the first five members of the $Sr_{n+1}Ti_nO_{3n+1}$ Ruddlesden – Popper homologous series, Appl. Phys. Lett. 78 (2001) 3292. doi:10.1063/1.1371788.

[48] B.E. Kayaalp, Y.J. Lee, A. Kornowski, S. Gross, M. D'Arienzo, S. Mascotto, Cooperative assembly synthesis of mesoporous $SrTiO_3$ with enhanced photocatalytic properties, RSC Adv. 6 (2016) 90401–90409. doi:10.1039/C6RA13800D.

[49] R. Merkle, J. Maier, How Is Oxygen Incorporated into Oxides? A Comprehensive Kinetic Study of a Simple Solid-State Reaction with $SrTiO_3$ as a Model Material, Angew. Chemie Int. Ed. 47 (2008) 3874–3894. doi:10.1002/anie.200700987.

[50] L.H. Brixner, Preparation and properties of the $SrTi_{1-x}Fe_xO_{3-x/2}$ system, Mater. Res. Bull. 3 (1968) 299.

[51] Y. Takeda, K. Kanno, T. Takada, O. Yamamoto, M. Takano, N. Nakayama, Y. Bando, Phase relation in the oxygen nonstoichiometric system, SrFeOx (2.5 < x <3.0), J. Solid State Chem. 63 (1986) 237–249. doi:10.1016/0022-4596(86)90174-X.

[52] J. Mizusaki, M. Okayasu, S. Yamauchi, K. Fuekio, Nonstoichiometry and Phase Relationship System at High Temperature of the $SrFeO_{2.5}$ - $SrFeO_3$, J. Solid State Chem. 99 (1992) 166.

[53] A. Rothschild, W. Menesklou, H.L.H.L. Tuller, E. Ivers-Tiffée, Electronic Structure, Defect Chemistry, and Transport Properties of $SrTi_{1-x}Fe_xO_{3-y}$ Solid Solutions, Chem. Mater. 18 (2006) 3651–3659. doi:10.1021/cm052803x.

[54] S. Inoue, M. Kawai, Y. Shimakawa, M. Mizumaki, N. Kawamura, T. Watanabe, Y. Tsujimoto, H. Kageyama, K. Yoshimura, S. Inoue, M. Kawai, Y. Shimakawa, M. Mizumaki, Single-crystal epitaxial thin films of $SrFeO_2$ with FeO_2 " infinite layers ," Appl. Phys. Lett. 92 (2008) 161911. doi:10.1063/1.2913164.

[55] S. Diodati, L. Nodari, M.M. Natile, U. Russo, E. Tondello, L. Lutterotti, S. Gross, Highly crystalline strontium ferrites $SrFeO_{3-\delta}$: an easy and effective wet-chemistry synthesis, Dalt. Trans. 41 (2012) 5517. doi:10.1039/c2dt11916a.

[56] P. Adler, S. Eriksson, Structural Properties, Mössbauer Spectra, and Magnetism of Perovskite-Type Oxides $SrFe_{1-x}Ti_xO_{3-y}$, Zeitschrift Für Anorg. Und Allg. Chemie. 626 (2000) 118–124. doi:10.1002/(SICI)1521-3749(200001)626:1<118::AID-ZAAC118>3.0.CO;2-K.

[57] A. Sendilkumar, P.D. Babu, M. Manivel Raja, V.R. Reddy, A. Gupta, S. Srinath, Structural and Mössbauer investigation of nanocrystalline $SrFe_{1-x}Ti_xO_{3-\delta}$, J. Am. Ceram. Soc. 96 (2013) 2973–2978. doi:10.1111/jace.12392.

[58] Z. Li, R. Laskowski, T. Iitaka, T. Tohyama, First-principles calculation of helical spin order in iron perovskite $SrFeO_3$ and $BaFeO_3$, Phys. Rev. B - Condens. Matter Mater. Phys. 85 (2012) 2–6. doi:10.1103/PhysRevB.85.134419.

[59] H. Yamada, M. Kawasaki, Y. Tokura, Epitaxial growth and valence control of strained perovskite $SrFeO_3$ films, Appl. Phys. Lett. 80 (2002) 622–624. doi:10.1063/1.1445805.

[60] V. Metlenko, W. Jung, S.R. Bishop, H.L. Tuller, R.A. De Souza, Oxygen diffusion and surface exchange in the mixed conducting oxides $SrTi_{1-y}Fe_yO_{3-\delta}$, Phys. Chem. Chem. Phys. 18 (2016) 29495–29505. doi:10.1039/C6CP05756J.

[61] A.E. Bocquet, A. Fujimori, T. Mizokawa, T. Saitoh, H. Namatame, S. Suga, N. Kimizuka, Y. Takeda, M. Takano, Electronic structure of $SrFe^{4+}O_3$ and related Fe perovskite oxides, Phys. Rev. B. 45 (1992) 1561–1570. doi:10.1103/PhysRevB.45.1561.

[62] J.C. Boivin, G. Mairesse, Recent Material Developments in Fast Oxide Ion Conductors, Chem. Mater. 10 (1998) 2870–2888. doi:10.1021/cm980236q.

[63] H.L. Tuller, Semiconduction and mixed ionic-electronic conduction in nonstoichiometric oxides : impact and control, Solid State Ionics. 94 (1997) 63–74.

[64] S.J. Litzelman, A. Rothschild, H.L. Tuller, The electrical properties and stability of $SrTi_{0.65}Fe_{0.35}O_{3-\delta}$ thin films for automotive oxygen sensor applications, Sensors Actuators, B Chem. 108 (2005) 231–237. doi:10.1016/j.snb.2004.10.040.

[65] R. Moos, K.H. Härdtl, Electronic transport properties of $Sr_{1-x}La_xTiO_3$ ceramics, J. Appl. Phys. 80 (1996) 393–400. doi:10.1063/1.362796.

[66] S. Hui, A. Petric, Evaluation of yttrium-doped $SrTiO_3$ as an anode for solid oxide fuel cells, J. Eur. Ceram. Soc. 22 (2002) 1673–1681. doi:10.1016/S0955-2219(01)00485-X.

[67] S. Hashimoto, L. Kindermann, P.H. Larsen, F.W. Poulsen, M. Mogensen, Conductivity and expansion at high temperature in $Sr_{0.7}La_{0.3}TiO_{3-\alpha}$ prepared under reducing atmosphere, J. Electroceramics. 16 (2006) 103–107. doi:10.1007/s10832-006-3490-1.

[68] A. Yaqub, C. Savaniu, N.K. Janjua, J.T.S. Irvine, Preparation via a solution method of $La_{0.2}Sr_{0.25}Ca_{0.45}TiO_3$ and its characterization for anode supported solid oxide fuel cells, J. Mater. Chem. A. 1 (2013) 14189–14197. doi:10.1039/c3ta12860a.

[69] M.C. Verbraeken, B. Iwanschitz, A. Mai, J.T.S. Irvine, Evaluation of Ca Doped $La_{0.2}Sr_{0.7}TiO_3$ as an Alternative Material for Use in SOFC Anodes, J. Electrochem. Soc. 159 (2012) F757–F762. doi:10.1149/2.001212jes.

[70] C.E. Bamberger, Homogeneity Ranges of Phases $Sr_{4-x}Ln_{2x/3}Ti_4O_{12}$ (Ln = Sm to Lu)

and $Sr_{1-y}Eu_yTiO_3$, J. Am. Ceram. Soc. 80 (1997) 1024–1026. doi:10.1111/j.1151-2916.1997.tb02939.x.

[71] Y. Jiang-Ni, Z. Zhi-Yong, Y. Jun-Feng, Z. Wu, Electronic Structure and Optical Properties of La-Doped $SrTiO_3$ and Sr_2TiO_4 by Density Function Theory, Chinese Phys. Lett. 26 (2009) 017107. doi:10.1088/0256-307X/26/1/017107.

[72] N.H. Park, F. Dang, C. Wan, W.S. Seo, K. Koumoto, Self-originating two-step synthesis of core-shell structured La-doped $SrTiO_3$ nanocubes, J. Asian Ceram. Soc. 1 (2013) 35–40. doi:10.1016/j.jascer.2013.02.004.

[73] J. Ravichandran, W. Siemons, H. Heijmerikx, M. Huijben, A. Majumdar, R. Ramesh, An epitaxial transparent conducting perovskite oxide: Double-doped $SrTiO_3$, Chem. Mater. 22 (2010) 3983–3987. doi:10.1021/cm1005604.

[74] B.F. Flandermeyer, A.K. Agarwal, H.U. Anderson, M.M. Nasrallah, Oxidation-reduction behaviour of La-doped $SrTiO_3$, J. Mater. Sci. 19 (1984) 2593–2598. doi:10.1007/BF00550814.

[75] A.H.H. Ramadan, N.L. Allan, R.A. De Souza, Simulation studies of the phase stability of the $Sr_{n+1}Ti_nO_{3n+1}$ Ruddlesden-Popper phases, J. Am. Ceram. Soc. 96 (2013) 2316–2321. doi:10.1111/jace.12300.

[76] J.C. Ruiz-Morales, J. Canales-Vázquez, C. Savaniu, D. Marrero-López, W. Zhou, J.T.S. Irvine, Disruption of extended defects in solid oxide fuel cell anodes for methane oxidation, Nature. 439 (2006) 568–571. doi:10.1038/nature04438.

[77] D. Neagu, J.T.S. Irvine, Structure and Properties of $La_{0.4}Sr_{0.4}TiO_3$ Ceramics for Use as Anode Materials in Solid Oxide Fuel Cells, Chem. Mater. 22 (2010) 5042–5053. doi:10.1021/cm101508w.

[78] P. Blennow, K.K. Hansen, L. Reine Wallenberg, M. Mogensen, Effects of Sr/Ti-ratio in $SrTiO_3$-based SOFC anodes investigated by the use of cone-shaped electrodes, Electrochim. Acta. 52 (2006) 1651–1661. doi:10.1016/j.electacta.2006.03.096.

[79] S. Hashimoto, F.W. Poulsen, M. Mogensen, Conductivity of $SrTiO_3$ based oxides in the reducing atmosphere at high temperature, J. Alloys Compd. 439 (2007) 232–236. doi:10.1016/j.jallcom.2006.05.138.

[80] O.A. Marina, N.L. Canfield, J.W. Stevenson, Thermal, electrical, and electrocatalytical properties of lanthanum-doped strontium titanate, Solid State Ionics. 149 (2002) 21–28. doi:10.1016/S0167-2738(02)00140-6.

[81] Y. Jiang-Ni, Z. Zhi-Yong, Y. Jun-Feng, D. Zhou-Hu, First-principles study of La and

Sb-doping effects on electronic structure and optical properties of $SrTiO_3$, Chinese Phys. B. 19 (2010) 017101–8. doi:10.1088/1674-1056/19/1/017101.

[82] Y.W. Song, Y. Ma, H. Xiong, Y.Q. Jia, M.L. Liu, M.Z. Jin, Synthesis, crystal structure, Mössbauer spectra and dielectric property of $La_{1-x}Sr_xFe_{1-x}Ti_xO_3$ (x = 0, 0.1, 0.3, 0.5, 0.7, 1), 78 (2002) 660–665. doi:10.1100/2012/149670.

[83] I. Kaus, K. Wiik, K. Kleveland, B. Krogh, S. Aasland, Oxygen transport properties in $La_{1-x}Sr_xFe_{1-y}M_yO_{3-\delta}$ (M = Cr, Ti), Solid State Ionics. 178 (2007) 817–826. doi:10.1016/j.ssi.2007.02.028.

[84] E. Bartonickova, K. Wiik, K. Maca, H.L. Lein, E.A. Rudberg, Synthesis and oxygen transport properties of $La_{0.2}Sr_{0.8}Fe_{1-x}Ti_xO_{3-\delta}$ (x = 0.2, 0.4) intended for syn-gas production, J. Eur. Ceram. Soc. 30 (2010) 605–611. doi:10.1016/j.jeurceramsoc.2009.06.037.

[85] J.N. Armor, A history of industrial catalysis, Catal. Today. 163 (2011) 3–9. doi:10.1016/j.cattod.2009.11.019.

[86] U.S. Energy Information Administration, International Energy Outlook 2017, 2017. https://www.eia.gov/outlooks/ieo/pdf/0484(2017).pdf.

[87] E. Kabir, P. Kumar, S. Kumar, A.A. Adelodun, K.H. Kim, Solar energy: Potential and future prospects, Renew. Sustain. Energy Rev. 82 (2018) 894–900. doi:10.1016/j.rser.2017.09.094.

[88] S. Zeng, P. Kar, U.K. Thakur, K. Shankar, A review on photocatalytic CO_2 reduction using perovskite oxide nanomaterials, Nanotechnology. 29 (2018). doi:10.1088/1361-6528/aa9fb1.

[89] L. Schlapbach, A. Züttel, Hydrogen-storage materials for Mobile Applications, Nature. 414 (2002) 353–358. doi:10.1038/35104634.

[90] H. Zollinger, Color Chemistry: Synthesis, Properties, and Applications of Organic Dyes and Pigments, 3rd revised edition, John Wiley & Sons, Ltd., 2003. http://doi.wiley.com/10.1002/col.20132.

[91] Z. Ye, H. Weinberg, Occurrence of antibiotics in drinking water, Disrupting Chem. Water. (2004) 138–142. http://info.ngwa.org/GWOL/pdf/042379983.pdf.

[92] D.G.J. Larsson, Antibiotics in the environment, Ups. J. Med. Sci. 119 (2014) 108–112. doi:10.3109/03009734.2014.896438.

[93] E. Forgacs, T. Cserháti, G. Oros, Removal of synthetic dyes from wastewaters: A review, Environ. Int. 30 (2004) 953–971. doi:10.1016/j.envint.2004.02.001.

[94] A. Houas, H. Lachheb, M. Ksibi, E. Elaloui, C. Guillard, J.-M. Herrmann, Photocatalytic degradation pathway of methylene blue in water, Appl. Catal. B Environ. 31 (2001) 145–157. doi:10.1016/S0926-3373(00)00276-9.

[95] D.S. Bhatkhande, V.G. Pangarkar, A.A.C.M. Beenackers, Photocatalytic degradation for environmental applications - A review, J. Chem. Technol. Biotechnol. 77 (2002) 102–116. doi:10.1002/jctb.532.

[96] K. Maeda, Photocatalytic water splitting using semiconductor particles: History and recent developments, J. Photochem. Photobiol. C Photochem. Rev. 12 (2011) 237–268. doi:10.1016/j.jphotochemrev.2011.07.001.

[97] W. Wang, M.O. Tadé, Z. Shao, Research progress of perovskite materials in photocatalysis- and photovoltaics-related energy conversion and environmental treatment, Chem. Soc. Rev. 44 (2015) 5371–5408. doi:10.1039/C5CS00113G.

[98] M.N. Chong, B. Jin, C.W.K. Chow, C. Saint, Recent developments in photocatalytic water treatment technology: A review, Water Res. 44 (2010) 2997–3027. doi:10.1016/j.watres.2010.02.039.

[99] O. Khaselev, J.A. Turner, A Monolithic Photovoltaic-Photoelectrochemical Device for Hydrogen Production via Water Splitting, Science (80-.). 280 (1998) 425–427. doi:10.1126/science.280.5362.425.

[100] S. Fang, Y.H. Hu, Recent progress in photocatalysts for overall water splitting, Int. J. Energy Res. Energy Res. (2018) 1–17. doi:10.1002/er.4259.

[101] A. Kudo, Y. Miseki, Heterogeneous photocatalyst materials for water splitting, Chem. Soc. Rev. 38 (2009) 253–278. doi:10.1039/B800489G.

[102] T. Jafari, E. Moharreri, A.S. Amin, R. Miao, W. Song, S.L. Suib, Photocatalytic water splitting - The untamed dream: A review of recent advances, Molecules. 21 (2016). doi:10.3390/molecules21070900.

[103] M. Ni, M.K.H. Leung, D.Y.C. Leung, K. Sumathy, A review and recent developments in photocatalytic water-splitting using TiO_2 for hydrogen production, Renew. Sustain. Energy Rev. 11 (2007) 401–425. doi:10.1016/j.rser.2005.01.009.

[104] K. Maeda, N. Murakami, T. Ohno, Dependence of activity of rutile titanium(IV) oxide powder for photocatalytic overall water splitting on structural properties, J. Phys. Chem. C. 118 (2014) 9093–9100. doi:10.1021/jp502949q.

[105] E.P. Melián, O.G. Díaz, A.O. Méndez, C.R. López, M.N. Suárez, J.M.D. Rodríguez, J.A. Navío, D.F. Hevia, J.P. Peña, Efficient and affordable hydrogen production by

water photo-splitting using TiO_2-based photocatalysts, Int. J. Hydrogen Energy. 38 (2013) 2144–2155. doi:10.1016/j.ijhydene.2012.12.005.

[106] Y. Ham, T. Hisatomi, Y. Goto, Y. Moriya, Y. Sakata, A. Yamakata, J. Kubota, K. Domen, Flux-mediated doping of $SrTiO_3$ photocatalysts for efficient overall water splitting, J. Mater. Chem. A. 4 (2016) 3027–3033. doi:10.1039/c5ta04843e.

[107] R. Niishiro, S. Tanaka, A. Kudo, Hydrothermal-synthesized $SrTiO_3$ photocatalyst codoped with rhodium and antimony with visible-light response for sacrificial $H_2$and O_2 evolution and application to overall water splitting, Appl. Catal. B Environ. 150–151 (2014) 187–196. doi:10.1016/j.apcatb.2013.12.015.

[108] L. Mu, Y. Zhao, A. Li, S. Wang, Z. Wang, J. Yang, Y. Wang, T. Liu, R. Chen, J. Zhu, F. Fan, R. Li, C. Li, Enhancing charge separation on high symmetry $SrTiO_3$ exposed with anisotropic facets for photocatalytic water splitting, Energy Environ. Sci. 9 (2016) 2463–2469. doi:10.1039/c6ee00526h.

[109] H. Tüysüz, C.K. Chan, Preparation of amorphous and nanocrystalline sodium tantalum oxide photocatalysts with porous matrix structure for overall water splitting, Nano Energy. 2 (2013) 116–123. doi:10.1016/j.nanoen.2012.08.003.

[110] B. Modak, S.K. Ghosh, Improvement of photocatalytic activity of $NaTaO_3$ under visible light by N and F doping, Chem. Phys. Lett. 613 (2014) 54–58. doi:10.1016/j.cplett.2014.08.054.

[111] A.K. Wahab, T. Odedairo, J. Labis, M. Hedhili, A. Delavar, H. Idriss, Comparing $Pt/SrTiO_3$ to $Rh/SrTiO_3$ for hydrogen photocatalytic production from ethanol, (2013) 83–89. doi:10.1007/s13203-013-0033-y.

[112] K. Domen, A. Kudo, T. Onishi, N. Kosugi, H. Kuroda, Photocatalytic decomposition of water into hydrogen and oxygen over nickel(II) oxide-strontium titanate ($SrTiO_3$) powder. 1. Structure of the catalysts, J. Phys. Chem. 90 (1986) 292–295. doi:10.1021/j100274a018.

[113] T. Alammar, I. Hamm, M. Wark, A.V. Mudring, Low-temperature route to metal titanate perovskite nanoparticles for photocatalytic applications, Appl. Catal. B Environ. 178 (2015) 20–28. doi:10.1016/j.apcatb.2014.11.010.

[114] Q. Wang, T. Hisatomi, Q. Jia, H. Tokudome, M. Zhong, C. Wang, Z. Pan, T. Takata, M. Nakabayashi, N. Shibata, Y. Li, I.D. Sharp, A. Kudo, T. Yamada, K. Domen, Scalable water splitting on particulate photocatalyst sheets with a solar-to-hydrogen energy conversion efficiency exceeding 1%, Nat. Mater. 15 (2016) 611–615.

doi:10.1038/nmat4589.

[115] Q. Wang, T. Hisatomi, S.S.K. Ma, Y. Li, K. Domen, Core/Shell Structured La- and Rh-Codoped $SrTiO_3$ as a Hydrogen Evolution Photocatalyst in Z-Scheme Overall Water Splitting under Visible Light Irradiation, Chem. Mater. 26 (2014) 4144–4150. doi:10.1021/cm5011983.

[116] P. Shen, J.C. Lofaro, W.R. Woerner, M.G. White, D. Su, A. Orlov, Photocatalytic activity of hydrogen evolution over Rh doped $SrTiO_3$ prepared by polymerizable complex method, Chem. Eng. J. 223 (2013) 200–208. doi:10.1016/j.cej.2013.03.030.

[117] R. Konta, T. Ishii, H. Kato, A. Kudo, Photocatalytic activities of noble metal ion doped $SrTiO_3$ under visible light irradiation, J. Phys. Chem. B. 108 (2004) 8992–8995. doi:10.1021/jp049556p.

[118] J.-P.P. Zou, L.-Z.Z. Zhang, S.-L.L. Luo, L.-H.H. Leng, X.-B.B. Luo, M.-J.J. Zhang, Y. Luo, G.-C.C. Guo, Preparation and photocatalytic activities of two new Zn-doped $SrTiO_3$ and $BaTiO_3$ photocatalysts for hydrogen production from water without cocatalysts loading, Int. J. Hydrogen Energy. 37 (2012) 17068–17077. doi:10.1016/j.ijhydene.2012.08.133.

[119] P. Li, C. Liu, G. Wu, Y. Heng, S. Lin, A. Ren, K. Lv, L. Xiao, W. Shi, Solvothermal synthesis and visible light-driven photocatalytic degradation for tetracycline of Fe-doped $SrTiO_3$, RSC Adv. 4 (2014) 47615–47624. doi:10.1039/c4ra06630h.

[120] J. Wang, S. Yin, Q. Zhang, F. Saito, T. Sato, Influences of the factors on photocatalysis of fluorine-doped $SrTiO_3$ made by mechanochemical method, Solid State Ionics. 172 (2004) 191–195. doi:10.1016/j.ssi.2004.05.016.

[121] F. Zou, Z. Jiang, X. Qin, Y. Zhao, L. Jiang, J. Zhi, T. Xiao, P.P. Edwards, Template-free synthesis of mesoporous N-doped $SrTiO_3$ perovskite with high visible-light-driven photocatalytic activity, Chem. Commun. 48 (2012) 8514–8516. doi:10.1039/c2cc33797e.

[122] O. Ruzimuradov, K. Sharipov, A. Yarbekov, K. Saidov, M. Hojamberdiev, R.M. Prasad, G. Cherkashinin, R. Riedel, A facile preparation of dual-phase nitrogen-doped TiO_2-$SrTiO_3$ macroporous monolithic photocatalyst for organic dye photodegradation under visible light, J. Eur. Ceram. Soc. 35 (2015) 1815–1821. doi:10.1016/j.jeurceramsoc.2014.12.023.

[123] Z. Sun, Y. Huang, X. Zheng, J. Wu, Y. Wei, L. Fan, J. Wang, J. Xu, Solvothermal synthesis nitrogen doped $SrTiO_3$ with high visible light photocatalytic activity, Ceram.

Int. 40 (2014) 10583–10591. doi:10.1016/j.ceramint.2014.03.037.

[124] Q. Kuang, S. Yang, Template synthesis of single-crystal-like porous $SrTiO_3$ nanocube assemblies and their enhanced photocatalytic hydrogen evolution., ACS Appl. Mater. Interfaces. 5 (2013) 3683–90. doi:10.1021/am400254n.

[125] X. Fan, Y. Wang, X. Chen, L. Gao, W. Luo, Y. Yuan, Z. Li, T. Yu, J. Zhu, Z. Zou, Facile method to synthesize mesoporous multimetal oxides ($ATiO_3$, A=Sr, Ba) with large specific surface areas and crystalline pore walls, Chem. Mater. 22 (2010) 1276–1278. doi:10.1021/cm903303v.

[126] P. Khunrattanaphon, S. Chavadej, T. Sreethawong, Synthesis and application of novel mesoporous-assembled $SrTi_xZr_{1-x}O_3$-based nanocrystal photocatalysts for azo dye degradation, Chem. Eng. J. 170 (2011) 292–307. doi:10.1016/j.cej.2011.03.055.

[127] T. Puangpetch, T. Sreethawong, S. Yoshikawa, S. Chavadej, Hydrogen production from photocatalytic water splitting over mesoporous-assembled $SrTiO_3$ nanocrystal-based photocatalysts, J. Mol. Catal. A Chem. 312 (2009) 97–106. doi:10.1016/j.molcata.2009.07.012.

[128] H. Liu, X. Chen, S. Yan, Z. Li, Z. Zou, Basic Molten Salt Route to Prepare Porous $SrTiO_3$ Nanocrystals for Efficient Photocatalytic Hydrogen Production, Eur. J. Inorg. Chem. 2014 (2014) 3731–3735. doi:10.1002/ejic.201402280.

[129] W. Dong, X. Li, J. Yu, W. Guo, B. Li, L. Tan, C. Li, J. Shi, G. Wang, Porous $SrTiO_3$ spheres with enhanced photocatalytic performance, Mater. Lett. 67 (2012) 131–134. doi:10.1016/j.matlet.2011.09.045.

[130] S. Ouyang, P. Li, H. Xu, H. Tong, L. Liu, J. Ye, Bifunctional-Nanotemplate Assisted Synthesis of Nanoporous $SrTiO_3$ Photocatalysts Toward Efficient Degradation of Organic Pollutant, ACS Appl. Mater. Interfaces. 6 (2014) 22726–22732. doi:10.1021/am506877b.

[131] K. Yu, C. Zhang, Y. Chang, Y. Feng, Z. Yang, T. Yang, L.L. Lou, S. Liu, Novel three-dimensionally ordered macroporous $SrTiO_3$ photocatalysts with remarkably enhanced hydrogen production performance, Elsevier B.V., 2017. doi:10.1016/j.apcatb.2016.07.049.

[132] U.S. Energy Information Administration, Annual Energy Outlook 2018 with projections to 2050, 2018. doi:DOE/EIA-0383(2017).

[133] H. Tu, U. Stimming, Advances, aging mechanisms and lifetime in solid-oxide fuel cells, J. Power Sources. 127 (2004) 284–293. doi:10.1016/j.jpowsour.2003.09.025.

[134] I.R. de Larramendi, N. Ortiz-Vitoriano, I.B. Dzul-Bautista, T. Rojo, Designing Perovskite Oxides for Solid Oxide Fuel Cells, in: Perovskite Mater. - Synth. Characterisation, Prop. Appl., 2016. doi:10.5772/61304.

[135] Y. Zhang-Steenwinkel, L.M. Van Der Zande, H.L. Castricum, A. Bliek, Step response and transient isotopic labelling studies into the mechanism of CO oxidation over $La_{0.8}Ce_{0.2}MnO_3$ perovskite, Appl. Catal. B Environ. 54 (2004) 93–103. doi:10.1016/j.apcatb.2004.02.008.

[136] Y. Yu Yao, The Oxidation of CO and Hydrocarbons over Noble Metal Catalysts, J. Catal. 87 (1984) 152–162. doi:10.1016/0021-9517(84)90178-7.

[137] S.H. Oh, C.C. Eickel, Influence of metal particle size and support on the catalytic properties of supported rhodium: CO-O_2 and CO-NO reactions, J. Catal. 128 (1991) 526–536. doi:10.1016/0021-9517(91)90310-Z.

[138] P. Mars, D.W. van Krevelen, Oxidations carried out by means of vanadium oxide catalysts, Chem. Eng. Sci. 3 (1954) 41–59. doi:10.1016/S0009-2509(54)80005-4.

[139] C. Doornkamp, V. Ponec, The universal character of the Mars and Van Krevelen mechanism, Jorn. (2015). doi:Doi 10.1039/C1cy00074h.

[140] R. Auer, F.C. Thyrion, Kinetics of the Total Oxidation of Methane over a $La_{0.9}Ce_{0.1}CoO_3$ Perovskite Catalyst, Ind. Eng. Chem. Res. 41 (2002) 680–690. doi:10.1021/ie0104924.

[141] H. Arandiyan, H. Dai, J. Deng, Y. Liu, B. Bai, Y. Wang, X. Li, S. Xie, J. Li, Three-dimensionally ordered macroporous $La_{0.6}Sr_{0.4}MnO_3$ with high surface areas: Active catalysts for the combustion of methane, J. Catal. 307 (2013) 327–339. doi:10.1016/j.jcat.2013.07.013.

[142] N.S. Nasri, E.C.A. Tatt, U.D. Hamza, J. Mohammed, H.M. Zain, Kinetic Rate Comparison of Methane Catalytic Combustion of Palladium Catalysts Impregnated onto gama-Alumina and Bio-Char, Int. J. Chem. Mol. Nucl. Mater. Metall. Eng. 9 (2015) 563–569. doi:scholar.waset.org/1999.2/10001023.

[143] J. Chen, H. Arandiyan, X. Gao, J. Li, Recent Advances in Catalysts for Methane Combustion, (2015) 140–171. doi:10.1007/s10563-015-9191-5.

[144] R. Schlögl, Heterogeneous catalysis, Angew. Chemie - Int. Ed. 54 (2015) 3465–3520. doi:10.1002/anie.201410738.

[145] M. Misono, Heterogeneous Catalysis of Mixed Oxides - Perovskite and Heteropoly Catalysts, 2013.

[146] T. Nitadori, T. Ichiki, M. Misono, Catalytic Properties of Perovskite-Type Mixed Oxides (ABO_2) Consisting of Rare Earth and 3d Transition Metals. The Roles of the A- and B-Site Ions, Bull. Chem. Soc. Jpn. 61 (1988) 621–626. doi:10.1246/bcsj.61.621.

[147] G. Kremenic, J.M.L. Nieto, J.M.D. Tascon, T. Luis G., Chemisorption and Catalysis on $LaMO_3$ Oxides, J. Chem. Soc. Faraday Trans. 1. 81 (1985) 939–949.

[148] X. Wei, P. Hug, R. Figi, M. Trottmann, A. Weidenkaff, D. Ferri, Catalytic combustion of methane on nano-structured perovskite-type oxides fabricated by ultrasonic spray combustion, Appl. Catal. B Environ. 94 (2010) 27–37. doi:10.1016/j.apcatb.2009.10.017.

[149] X. Yan, Q. Huang, B. Li, X. Xu, Y. Chen, S. Zhu, S. Shen, Catalytic performance of $LaCo_{0.5}M_{0.5}O_3$ (M=Mn, Cr, Fe, Ni, Cu) perovskite-type oxides and $LaCo_{0.5}Mn_{0.5}O_3$ supported on cordierite for CO oxidation, J. Ind. Eng. Chem. 19 (2013) 561–565. doi:10.1016/j.jiec.2012.09.026.

[150] L. Fabbrini, I. Rossetti, L. Forni, Effect of honeycomb supporting on activity of $LaBO_{3\pm\delta}$ perovskite-like catalysts for methane flameless combustion, Appl. Catal. B Environ. 63 (2006) 131–136. doi:10.1016/j.apcatb.2005.10.002.

[151] B. Kucharczyk, W. Tylus, Metallic monolith supported $LaMnO_3$ perovskite-based catalysts in methane combustion, Catal. Letters. 115 (2007) 122–132. doi:10.1007/s10562-007-9076-y.

[152] M.A. Peña, J.L.G. Fierro, Chemical structures and performance of perovskite oxides, Chem. Rev. 101 (2001) 1981–2017. doi:10.1021/cr980129f.

[153] C. Oliva, L. Bonoldi, S. Cappelli, L. Fabbrini, I. Rossetti, L. Forni, Effect of preparation parameters on $SrTiO_{3\pm\delta}$ catalyst for the flameless combustion of methane, J. Mol. Catal. A Chem. 226 (2005) 33–40. doi:10.1016/j.molcata.2004.09.023.

[154] T. Tian, W. Wang, M. Zhan, C. Chen, Catalytic partial oxidation of methane over $SrTiO_3$ with oxygen-permeable membrane reactor, Catal. Commun. 11 (2010) 624–628. doi:10.1016/j.catcom.2010.01.009.

[155] F.E. López-suárez, A. Bueno-lópez, M.J. Illán-gómez, J. Trawczyński, Potassium-copper perovskite catalysts for mild temperature diesel soot combustion, Appl. Catal. A, Gen. 485 (2014) 214–221. doi:10.1016/j.apcata.2014.07.037.

[156] B. Ura, J. Trawczyński, A. Kotarba, W. Bieniasz, M.J. Illán-Gómez, A. Bueno-López, F.E. López-Suárez, Effect of potassium addition on catalytic activity of $SrTiO_3$ catalyst for diesel soot combustion, Appl. Catal. B Environ. 101 (2011) 169–175.

doi:10.1016/j.apcatb.2010.09.018.

[157] H. Einaga, Y. Nasu, M. Oda, H. Saito, Catalytic performances of perovskite oxides for CO oxidation under microwave irradiation, Chem. Eng. J. 283 (2016) 97–104. doi:10.1016/j.cej.2015.07.051.

[158] M. Alifanti, J. Kirchnerova, B. Delmon, D. Klvana, Methane and propane combustion over lanthanum transition-metal perovskites: Role of oxygen mobility, Appl. Catal. A Gen. 262 (2004) 167–176. doi:10.1016/j.apcata.2003.11.024.

[159] S. Suthirakun, S. Cheettu, G. Xiao, F. Chen, K. Huang, H. Loye, A. Heyden, Obtaining mixed ionic/electronic conductivity in perovskite oxides in a reducing environment : A computational prediction for doped $SrTiO_3$, Solid State Ionics. 228 (2012) 37–45. doi:10.1016/j.ssi.2012.09.013.

[160] J. Canales-Vázquez, M.J. Smith, J.T.S. Irvine, W. Zhou, Studies on the reorganization of extended defects with increasing n in the perovskite-based $La_4Sr_{n-4}Ti_nO_{3n+2}$ Series, Adv. Funct. Mater. 15 (2005) 1000–1008. doi:10.1002/adfm.200400362.

[161] X. Li, H. Zhao, X. Zhou, N. Xu, Z. Xie, N. Chen, Electrical conductivity and structural stability of La-doped $SrTiO_3$ with A-site deficiency as anode materials for solid oxide fuel cells, Int. J. Hydrogen Energy. 35 (2010) 7913–7918. doi:10.1016/j.ijhydene.2010.05.043.

[162] C.D. Savaniu, J.T.S. Irvine, La-doped $SrTiO_3$ as anode material for IT-SOFC, in: Solid State Ionics, 2011: pp. 491–493. doi:10.1016/j.ssi.2010.02.010.

[163] X. Zhou, N. Yan, K.T. Chuang, J. Luo, Progress in La-doped $SrTiO_3$ (LST)-based anode materials for solid oxide fuel cells, RSC Adv. 4 (2014) 118–131. doi:10.1039/C3RA42666A.

[164] R. Mukundan, E.L. Brosha, F.H. Garzon, Sulfur Tolerant Anodes for SOFCs, Electrochem. Solid-State Lett. 7 (2004) A5. doi:10.1149/1.1627452.

[165] A.L. Vincent, J.L. Luo, K.T. Chuang, A.R. Sanger, Promotion of activation of CH_4 by H_2S in oxidation of sour gas over sulfur tolerant SOFC anode catalysts, Appl. Catal. B Environ. 106 (2011) 114–122. doi:10.1016/j.apcatb.2011.05.014.

[166] T. Zhu, D.E. Fowler, K.R. Poeppelmeier, M. Han, S.A. Barnett, Hydrogen Oxidation Mechanisms on Perovskite Solid Oxide Fuel Cell Anodes, J. Electrochem. Soc. 163 (2016) F952–F961. doi:10.1149/2.1321608jes.

[167] A. Nenning, L. Volgger, E. Miller, L. V. Mogni, S. Barnett, J. Fleig, The Electrochemical Properties of $Sr(Ti,Fe)O_{3-\delta}$ for Anodes in Solid Oxide Fuel Cells, J.

Electrochem. Soc. 164 (2017) F364–F371. doi:10.1149/2.1271704jes.

[168] J. Xu, X. Zhou, X. Dong, L. Pan, K. Sun, Catalytic activity improvement for efficient hydrogen oxidation of infiltrated $La_{0.3}Sr_{0.7}Ti_{0.3}Fe_{0.7}O_{3-\delta}$ anode for solid oxide fuel cell, Ceram. Int. 43 (2017) 10750–10756. doi:10.1016/j.ceramint.2017.05.081.

[169] S. Molin, W. Lewandowska-Iwaniak, B. Kusz, M. Gazda, P. Jasinski, Structural and electrical properties of $Sr(Ti,Fe)O_{3-\delta}$ materials for SOFC cathodes, J. Electroceramics. 28 (2012) 80–87. doi:10.1007/s10832-012-9683-x.

[170] B. Levasseur, S. Kaliaguine, Effects of iron and cerium in $La_{1-y}Ce_yCo_{1-x}Fe_xO_3$ perovskites as catalysts for VOC oxidation, Appl. Catal. B Environ. 88 (2009) 305–314. doi:10.1016/j.apcatb.2008.11.007.

[171] P. Xiao, L. Zhong, J. Zhu, J. Hong, J. Li, H. Li, Y. Zhu, CO and soot oxidation over macroporous perovskite $LaFeO_3$, Catal. Today. 258 (2015) 660–667. doi:10.1016/j.cattod.2015.01.007.

[172] K. Ji, H. Dai, J. Deng, L. Zhang, F. Wang, H. Jiang, C.T. Au, Three-dimensionally ordered macroporous $SrFeO_{3-\delta}$ with high surface area: Active catalysts for the complete oxidation of toluene, Appl. Catal. A Gen. 425–426 (2012) 153–160. doi:10.1016/j.apcata.2012.03.013.

[173] J. Xu, J. Liu, Z. Zhao, J. Zheng, G. Zhang, A. Duan, G. Jiang, Three-dimensionally ordered macroporous $LaCo_xFe_{1-x}O_3$ perovskite-type complex oxide catalysts for diesel soot combustion, Catal. Today. 153 (2010) 136–142. doi:10.1016/j.cattod.2010.01.063.

[174] Y. Wang, J. Ren, Y. Wang, F. Zhang, X. Liu, Y. Guo, G. Lu, Nanocasted synthesis of mesoporous $LaCoO_3$ perovskite with extremely high surface area and excellent activity in methane combustion, J. Phys. Chem. C. 112 (2008) 15293–15298. doi:10.1021/jp8048394.

[175] M.M. Nair, F. Kleitz, S. Kaliaguine, Kinetics of Methanol Oxidation over Mesoporous Perovskite Catalysts, ChemCatChem. 6 (2012) 387–394. doi:10.1002/cctc.201100356.

[176] R.K.C. de Lima, M.S. Batista, M. Wallau, E.A. Sanches, Y.P. Mascarenhas, E.A. Urquieta-González, High specific surface area LaFeCo perovskites-Synthesis by nanocasting and catalytic behavior in the reduction of NO with CO, Appl. Catal. B Environ. 90 (2009) 441–450. doi:10.1016/j.apcatb.2009.04.004.

[177] M. Cargnello, J.J. Delgado Jaén, J.C. Hernández Garrido, K. Bakhmutsky, T. Montini, J.J. Calvino Gámez, R.J. Gorte, P. Fornasiero, Exceptional activity for methane combustion over modular $Pd@CeO_2$ subunits on functionalized Al_2O_3, Science (80-.).

337 (2012) 713–717. doi:10.1126/science.1222887.

[178] T.R. Reina, S. Ivanova, V. Idakiev, T. Tabakova, M.A. Centeno, Q.F. Deng, Z.Y. Yuan, J.A. Odriozola, Nanogold mesoporous iron promoted ceria catalysts for total and preferential CO oxidation reactions, J. Mol. Catal. A Chem. 414 (2016) 62–71. doi:10.1016/j.molcata.2016.01.003.

[179] W.C. Conner, J.L. Falconer, Spillover in Heterogeneous Catalysis, (1995) 759–788. doi:10.1021/cr00035a014.

[180] C. Bozo, N. Guilhaume, J.M. Herrmann, Role of the ceria-zirconia support in the reactivity of platinum and palladium catalysts for methane total oxidation under lean conditions, J. Catal. 203 (2001) 393–406. doi:10.1006/jcat.2001.3320.

[181] K. An, S. Alayoglu, N. Musselwhite, S. Plamthottam, A.E. Lindeman, G.A. Somorjai, G. Melaet, A.E. Lindeman, G.A. Somorjai, Enhanced CO oxidation rates at the interface of mesoporous oxides and Pt nanoparticles, J. Am. Chem. Soc. 135 (2013) 16689–16696. doi:10.1021/ja4088743.

[182] S. Gatla, D. Aubert, G. Agostini, O. Mathon, S. Pascarelli, T. Lunkenbein, M.G. Willinger, H. Kaper, Room-Temperature CO Oxidation Catalyst: Low-Temperature Metal-Support Interaction between Platinum Nanoparticles and Nanosized Ceria, ACS Catal. 6 (2016) 6151–6155. doi:10.1021/acscatal.6b00677.

[183] M.S. Avila, C.I. Vignatti, C.R. Apesteguía, T.F. Garetto, Effect of support on the deep oxidation of propane and propylene on Pt-based catalysts, Chem. Eng. J. 241 (2014) 52–59. doi:10.1016/j.cej.2013.12.006.

[184] G. Groppi, C. Cristiani, L. Lietti, C. Ramella, M. Valentini, P. Forzatti, Effect of ceria on palladium supported catalysts for high temperature combustion of CH4 under lean conditions, Catal. Today. 50 (1999) 399–412. doi:10.1016/S0920-5861(98)00518-5.

[185] A. V. Nartova, L.M. Kovtunova, A.K. Khudorozhkov, K.I. Shefer, G. V. Shterk, R.I. Kvon, V.I. Bukhtiyarov, Influence of preparation conditions on catalytic activity and stability of platinum on alumina catalysts in methane oxidation, Appl. Catal. A Gen. 566 (2018) 174–180. doi:10.1016/j.apcata.2018.08.029.

[186] W.R. Schwartz, L.D. Pfe, Combustion of Methane over Palladium-Based Catalysts: Support Interactions, (2012). doi:10.1021/jp2119668.

[187] M. Cargnello, V.V.T. Doan-nguyen, T.R. Gordon, R.E. Diaz, E.A. Stach, R.J. Gorte, P. Fornasiero, C.B. Murray, Control of Metal Nanocrystal Size Reveals Metal-Support Interface Role for Ceria Catalysts, Science (80-.). 341 (2013) 771–774.

[188] V.P. Pakharukova, I.Y. Pakharukov, V.I. Bukhtiyarov, V.N. Parmon, Alumina-supported platinum catalysts: Local atomic structure and catalytic activity for complete methane oxidation, Appl. Catal. A Gen. 486 (2014) 12–18. doi:10.1016/j.apcata.2014.08.014.

[189] S. Lee, J. Seo, W. Jung, Sintering-resistant Pt@CeO_2 nanoparticles for high-temperature oxidation catalysis, Nanoscale. 8 (2016) 10219–10228. doi:10.1039/C6NR00170J.

[190] G. Prieto, J. Zecevic, H. Friedrich, K.P. de Jong, P.E. de Jong, Towards stable catalysts by controlling collective properties of supported metal nanoparticles, Nat. Mater. 12 (2013) 34–39. doi:10.1038/NMAT3471.

[191] J.A. Farmer, C.T. Campbell, Ceria Maintains Smaller Metal Catalyst Particles by Strong Metal-Support Bonding, Science (80-.). 329 (2010) 933–937.

[192] J.E. Park, K.B. Kim, K.W. Seo, K.S. Song, E.D. Park, Propane combustion over supported Pt catalysts, Res. Chem. Intermed. 37 (2011) 1135–1143. doi:10.1007/s11164-011-0379-7.

[193] A.A. Ramirez, S. Benard, G.-F. Anne, J.P. Jones, M. Heitz, Treatment of air polluted with methanol vapours in biofilters with and without percolation, Can. J. Civ. Eng. 36 (2009) 1911–1918. doi:10.1139/L09-144.

[194] Y. Liu, H. Dai, Y. Du, J. Deng, L. Zhang, Z. Zhao, C. Tong, Controlled preparation and high catalytic performance of three-dimensionally ordered macroporous $LaMnO_3$ with nanovoid skeletons for the combustion of toluene, J. Catal. 287 (2012) 149–160. doi:10.1016/j.jcat.2011.12.015.

[195] M. Haneda, M. Sasaki, H. Hamada, M. Ozawa, Effect of Pt dispersion on the catalytic activity of supported Pt catalysts for diesel hydrocarbon oxidation, Top. Catal. 56 (2013) 249–254. doi:10.1007/s11244-013-9962-z.

[196] A. Parinyaswan, S. Pongstabodee, A. Luengnaruemitchai, Catalytic performances of Pt-Pd/CeO_2 catalysts for selective CO oxidation, Int. J. Hydrogen Energy. 31 (2006) 1942–1949. doi:10.1016/j.ijhydene.2006.05.002.

[197] H. Arandiyan, H. Dai, J. Deng, Y. Wang, S. Xie, J. Li, Dual-templating synthesis of three-dimensionally ordered macroporous $La_{0.6}Sr_{0.4}MnO_3$-supported Ag nanoparticles: Controllable alignments and super performance for the catalytic combustion of methane, Chem. Commun. 49 (2013) 10748–10750. doi:10.1039/c3cc46312e.

[198] G. Guo, K. Lian, F. Gu, D. Han, Z. Wang, Three dimensionally ordered macroporous

Pd-$LaMnO_3$ self-regeneration catalysts for methane combustion, Chem. Commun. 50 (2014) 13575–13577. doi:10.1039/c4cc05966b.

[199] D. Segal, Chemical synthesis of ceramic materials, J. Mater. Chem. 7 (1997) 1297–1305. doi:10.1017/CBO9780511565014.

[200] N. Wang, D. Kong, H. He, Solvothermal synthesis of strontium titanate nanocrystallines from metatitanic acid and photocatalytic activities, Powder Technol. 207 (2011) 470–473. doi:10.1016/j.powtec.2010.11.034.

[201] D.D. Athayde, D.F. Souza, A.M.A. Silva, D. Vasconcelos, E.H.M. Nunes, J.C. Diniz da Costa, W.L. Vasconcelos, Review of perovskite ceramic synthesis and membrane preparation methods, Ceram. Int. 42 (2015) 6555–6571. doi:10.1016/j.ceramint.2016.01.130.

[202] R. Konta, H. Kato, H. Kobayashi, A. Kudo, Photophysical properties and photocatalytic activities under visible light irradiation of silver vanadates, Phys. Chem. Chem. Phys. 5 (2003) 3061–3065. doi:10.1039/b300179b.

[203] P. Dhanasekaran, N.M. Gupta, Factors affecting the production of H_2 by water splitting over a novel visible-light-driven photocatalyst $GaFeO_3$, Int. J. Hydrogen Energy. 37 (2012) 4897–4907. doi:10.1016/j.ijhydene.2011.12.068.

[204] H. Ziaei-Azad, A. Khodadadi, P. Esmaeilnejad-Ahranjani, Y. Mortazavi, Effects of Pd on enhancement of oxidation activity of $LaBO_3$ (B=Mn, Fe, Co and Ni) pervoskite catalysts for pollution abatement from natural gas fueled vehicles, Appl. Catal. B Environ. 102 (2011) 62–70. doi:10.1016/j.apcatb.2010.11.025.

[205] C. Zhu, A. Nobuta, I. Nakatsugawa, T. Akiyama, Solution combustion synthesis of $LaMO_3$ (M = Fe, Co, Mn) perovskite nanoparticles and the measurement of their electrocatalytic properties for air cathode, Int. J. Hydrogen Energy. 38 (2013) 13238–13248. doi:10.1016/j.ijhydene.2013.07.113.

[206] A. Civera, M. Pavese, G. Saracco, V. Specchia, Combustion synthesis of perovskite-type catalysts for natural gas combustion, Catal. Today. 83 (2003) 199–211. doi:10.1016/S0920-5861(03)00220-7.

[207] N.A. Baharuddin, A. Muchtar, M.R. Somalu, Preparation of $SrFe_{0.5}Ti_{0.5}O_{3-\delta}$ perovskite-structured ceramic using the glycine-nitrate combustion technique, Mater. Lett. 194 (2017) 197–201. doi:10.1016/j.matlet.2017.02.064.

[208] U. Schubert, N. Huesing, Synthesis of inorganic materials, 2nd editio, Vienna, 2005.

[209] C.J. Brinker, Hydrolysis and condensation of silicates: Effects on structure, J. Non.

Cryst. Solids. 100 (1988) 31–50. doi:10.1016/0022-3093(88)90005-1.

[210] K. Möller, T. Bein, Talented Mesoporous Silica Nanoparticles, Chem. Mater. (2016) acs.chemmater.6b03629. doi:10.1021/acs.chemmater.6b03629.

[211] D. Gu, F. Schüth, Synthesis of non-siliceous mesoporous oxides, Chem. Soc. Rev. 43 (2014) 313–344. doi:10.1039/C3CS60155B.

[212] S. Nakayama, $LaFeO_3$ perovskite-type oxide prepared by oxide-mixing, co-precipitation and complex synthesis methods, J. Mater. Sci. 36 (2001) 5643–5648. doi:10.1023/A:1012526018348.

[213] H. Taguchi, S. Yamada, M. Nagao, Surface characterization of $LaCoO_3$ synthesized using citric acid, Mater. Res. Bull. 37 (2002) 69–76. doi:10.1016/S0025-5408(01)00799-1.

[214] K.R. Thampi, M.S. Rao, W. Schwarz, M. Grätzel, J. Kiwi, Preparation of $SrTiO_3$ by sol-gel techniques for the photoinduced production of H_2 and surface peroxides from water, J. Chem. Soc. Faraday Trans. 1 Phys. Chem. Condens. Phases. 84 (1988) 1703–1712. doi:10.1039/F19888401703.

[215] M. Kakihana, M. Yoshimura, Synthesis and characteristics of complex multicomponent oxides prepared by polymer complex method, Bull. Chem. Soc. Jpn. 72 (1999) 1427–1443. doi:10.1246/bcsj.72.1427.

[216] M.P. Pechini, Method of preparing lead and alkaline earth titanates and niobates and coating method using the same to form a capacitor, US30443463A, 1967. https://patentimages.storage.googleapis.com/f8/63/97/d8e0d2ac042993/US3330697.pdf.

[217] M. Kakihana, T. Okubo, M. Arima, Y. Nakamura, M. Yashima, M. Yoshimura, Polymerized complex route to the synthesis of pure $SrTiO_3$ at reduced temperatures: Implication for formation of Sr-Ti heterometallic citric acid complex, J. Sol-Gel Sci. Technol. 12 (1998) 95–109. doi:10.1023/A:1008613312025.

[218] E.R. Leite, C.M.G. Sousa, E. Longo, J.A. Varela, Influence of polymerization on the synthesis of SrTiO3: Part I. Characteristics of the polymeric precursors and their thermal decomposition, Ceram. Int. 21 (1995) 143–152. doi:10.1016/0272-8842(95)90903-V.

[219] S.G. Cho, P.F. Johnson, R.A. Condrate, Thermal decomposition of (Sr, Ti) organic precursors during the Pechini process, J. Mater. Sci. 25 (1990) 4738–4744. doi:10.1007/BF01129934.

[220] R. Del Toro, P. Hernández, Y. Díaz, J.L. Brito, Synthesis of $La_{0.8}Sr_{0.2}FeO_3$ perovskites nanocrystals by Pechini sol-gel method, Mater. Lett. 107 (2013) 231–234. doi:10.1016/j.matlet.2013.05.139.

[221] A. Ianculescu, D. Berger, M. Viviani, C.E. Ciomaga, L. Mitoseriu, E. Vasile, N. Drăgan, D. Crişan, Investigation of $Ba_{1-x}Sr_xTiO_3$ ceramics prepared from powders synthesized by the modified Pechini route, J. Eur. Ceram. Soc. 27 (2007) 3655–3658. doi:10.1016/j.jeurceramsoc.2007.02.017.

[222] J.X. Wang, Y.K. Tao, J. Shao, W.G. Wang, Synthesis and properties of $(La_{0.75}Sr_{0.25})_{0.95}MnO_{3\pm\delta}$ nano-powder prepared via Pechini route, J. Power Sources. 186 (2009) 344–348. doi:10.1016/j.jpowsour.2008.09.116.

[223] M. Kuhn, J.J. Kim, S.R. Bishop, H.L. Tuller, Oxygen Nonstoichiometry and Defect Chemistry of Perovskite-Structured $Ba_xSr_{1-x}Ti_{1-y}Fe_yO_{3-y/2+\delta}$ Solid Solutions, Chem. Mater. 25 (2013) 2970–2975. doi:10.1021/cm400546z.

[224] W. Shi, S. Song, H. Zhang, Hydrothermal synthetic strategies of inorganic semiconducting nanostructures, Chem. Soc. Rev. 42 (2013) 5714–5743. doi:10.1039/c3cs60012b.

[225] D.R. Modeshia, R.I. Walton, Solvothermal synthesis of perovskites and pyrochlores: crystallisation of functional oxides under mild conditions, Chem. Soc. Rev. 39 (2010) 4303. doi:10.1039/b904702f.

[226] T. Kimijima, K. Kanie, M. Nakaya, A. Muramatsu, Solvothermal synthesis of $SrTiO_3$ nanoparticles precisely controlled in surface crystal planes and their photocatalytic activity, Appl. Catal. B Environ. 144 (2014) 462–467. doi:10.1016/j.apcatb.2013.07.051.

[227] G. Canu, V. Buscaglia, Hydrothermal synthesis of strontium titanate: Thermodynamic considerations, morphology control and crystallisation mechanisms, CrystEngComm. 19 (2017) 3867–3891. doi:10.1039/c7ce00834a.

[228] L. Dong, H. Shi, K. Cheng, Q. Wang, W. Weng, W. Han, Shape-controlled growth of $SrTiO_3$ polyhedral submicro / nanocrystals, Nano Res. 7 (2014) 1311–1318. doi:10.1007/s12274-014-0495-y.

[229] W. Zheng, R. Liu, D. Peng, G. Meng, Hydrothermal synthesis of $LaFeO_3$ under carbonate-containing medium, (2000) 20–23.

[230] S. Hosokawa, H.J. Jeon, S. Iwamoto, M. Inoue, Synthesis of rare earth iron-mixed oxide nanoparticles by solvothermal methods, J. Am. Ceram. Soc. 92 (2009) 2847–

2853. doi:10.1111/j.1551-2916.2009.03295.x.

[231] Y. Wang, H. Xu, X. Wang, X. Zhang, H. Jia, L. Zhang, J. Qiu, A General Approach to Porous Crystalline TiO_2, $SrTiO_3$, and $BaTiO_3$ Spheres, J. Phys. Chem. B. 110 (2006) 13835–13840. doi:10.1021/jp061597t.

[232] Y. Wang, G. Xu, L. Yang, Z. Ren, X. Wei, W. Weng, P. Du, Formation of single-crystal $SrTiO_3$ dendritic nanostructures via a simple hydrothermal method, J. Cryst. Growth. 311 (2009) 2519–2523. doi:10.1016/j.jcrysgro.2009.01.103.

[233] U.A. Joshi, J.S. Lee, Template-Free Hydrothermal Synthesis of Single-Crystalline Barium Titanate and Strontium Titanate Nanowires, Small. 1 (2005) 1172–1176. doi:10.1002/smll.200500055.

[234] Y. Li, X.P. Gao, G.R. Li, G.L. Pan, T.Y. Yan, H.Y. Zhu, Titanate Nanofiber Reactivity : Fabrication of $MTiO_3$ (M = Ca , Sr , and Ba) Perovskite Oxides, J. Phys. Chem. C. 113 (2009) 4386–4394.

[235] Z. He, X.Y. Sun, X. Gu, $SrTiO_3$ nanoparticles and nanofibers: synthesis and comparison of photocatalytic properties, J. Mater. Sci. Mater. Electron. 28 (2017) 13950–13955. doi:10.1007/s10854-017-7244-4.

[236] F.A. Rabuffetti, H.S. Kim, J.A. Enterkin, Y. Wang, C.H. Lanier, L.D. Marks, K.R. Poeppelmeier, P.C. Stair, Synthesis-Dependent First-Order Raman Scattering in $SrTiO_3$ Nanocubes at Room Temperature, Chem. Mater. 20 (2008) 5628–5635. doi:10.1021/cm801192t.

[237] X. Wei, G. Xu, Z. Ren, C. Xu, G. Shen, G. Han, PVA-Assisted Hydrothermal Synthesis of $SrTiO_3$ Nanoparticles with Enhanced Photocatalytic Activity for Degradation of RhB, J. Am. Ceram. Soc. 91 (2008) 3795–3799. doi:10.1111/j.1551-2916.2008.02716.x.

[238] K.G. Knauss, M.J. Dibley, W.L. Bourcier, H.F. Shaw, Ti (IV) hydrolysis constants derived from rutile solubility measurements made from 100 to 300 C, Appl. Geochemistry. 16 (2001) 115–1128. doi:0883-2927/01/$.

[239] H. Yang, K. Kan, J. Ouyang, Y. Li, Solvothermal synthesis and optical properties of Mn^{2+}-doped $SrTiO_3$ powders, J. Alloys Compd. 485 (2009) 351–355. doi:10.1016/j.jallcom.2009.05.109.

[240] B.L. Gersten, M.M. Lencka, R.E. Riman, Low-Temperature Hydrothermal Synthesis of Phase-Pure (Ba,Sr)TiO_3 Perovskite using EDTA, J. Am. Ceram. Soc. 87 (2004) 2025–2032.

[241] R.Z. Hou, A. Wu, P.M. Vilarinho, Low-Temperature Hydrothermal Deposition of $(Ba_xSr_{1-x})TiO_3$ Thin Films on Flexible Polymeric Substrates for Embedded Applications, Chem. Mater. 21 (2009) 1214–1220.

[242] N. Pal, A. Bhaumik, Soft templating strategies for the synthesis of mesoporous materials: Inorganic, organic-inorganic hybrid and purely organic solids, Adv. Colloid Interface Sci. 189–190 (2013) 21–41. doi:10.1016/j.cis.2012.12.002.

[243] G.J.D.A.A. Soler-Illia, C. Sanchez, B. Lebeau, J. Patarin, Chemical strategies to design textured materials: From microporous and mesoporous oxides to nanonetworks and hierarchical structures, Chem. Rev. 102 (2002) 4093–4138. doi:10.1021/cr0200062.

[244] S. Che, A.E. Garcia-Bennett, T. Yokoi, K. Sakamoto, H. Kunieda, O. Terasaki, T. Tatsumi, A novel anionic surfactant templating route for synthesizing mesoporous silica with unique structure., Nat. Mater. 2 (2003) 801–805. doi:10.1038/nmat1022.

[245] F. Hoffmann, M. Cornelius, J. Morell, M. Fröba, Mesoporöse organisch-anorganische Hybridmaterialien auf Silicabasis, Angew. Chemie. 118 (2006) 3290–3328. doi:10.1002/ange.200503075.

[246] C.T. Kresge, M.E. Leonowicz, W.J. Roth, J.C. Vartuli, J.S. Beck, Ordered mesoporous molecular sieves synthesized by a liquid-crystal template mechanism, Nature. 359 (1992) 710–712.

[247] Y. Ni, A. Sun, X. Wu, G. Hai, J. Hu, T. Li, G. Li, Facile synthesis of hierarchical nanocrystalline ZSM-5 zeolite under mild conditions and its catalytic performance, J. Colloid Interface Sci. 361 (2011) 521–526. doi:10.1016/j.jcis.2011.06.020.

[248] D. Grosso, C. Boissiere, B. Smarsly, T. Brezesinski, N. Pinna, P.A. Albouy, H. Amenitsch, M. Antonietti, C. Sanchez, Periodically ordered nanoscale islands and mesoporous films composed of nanocrystalline multimetallic oxides, Nat. Mater. 3 (2004) 787–792. doi:10.1038/nmat1206.

[249] Q. Liu, F. Chen, Self-rising approach to synthesize hierarchically porous metal oxides, Mater. Res. Bull. 44 (2009) 2056–2061. doi:10.1016/j.materresbull.2009.07.013.

[250] B. Lertpanyapornchai, T. Yokoi, C. Ngamcharussrivichai, Citric acid as complexing agent in synthesis of mesoporous strontium titanate via neutral-templated self-assembly sol-gel combustion method, Microporous Mesoporous Mater. 226 (2016) 505–509. doi:10.1016/j.micromeso.2016.02.020.

[251] N. Suzuki, M.B. Zakaria, N.L. Torad, K.C.W. Wu, Y. Nemoto, M. Imura, M. Osada, Y. Yamauchi, Synthesis of highly strained mesostructured $SrTiO_3/BaTiO_3$ composite

films with robust ferroelectricity, Chem. - A Eur. J. 19 (2013) 4446–4450. doi:10.1002/chem.201203421.

[252] F. Schüth, Endo- and exotemplating to create high-surface-area inorganic materials, Angew. Chemie - Int. Ed. 42 (2003) 3604–3622. doi:10.1002/anie.200300593.

[253] A.H. Lu, F. Schüth, Nanocasting: A versatile strategy for creating nanostructured porous materials, Adv. Mater. 18 (2006) 1793–1805. doi:10.1002/adma.200600148.

[254] R. Zhang, P. Li, N. Liu, W. Yue, B. Chen, Effect of hard-template residues of the nanocasted mesoporous $LaFeO_3$ with extremely high surface areas on catalytic behaviors for methyl chloride oxidation, J. Mater. Chem. A. 2 (2014) 17329–17340. doi:10.1039/c4ta03615h.

[255] R. Liu, Y. Shi, Y. Wan, Y. Meng, F. Zhang, D. Gu, Z. Chen, B. Tu, D. Zhao, Triconstituent co-assembly to ordered mesostructured polymer-silica and carbon-silica nanocomposites and large-pore mesoporous carbons with high surface areas, J. Am. Chem. Soc. 128 (2006) 11652–11662. doi:10.1021/ja0633518.

[256] S. Hashimoto, L. Kindermann, F.W. Poulsen, M. Mogensen, A study on the structural and electrical properties of lanthanum-doped strontium titanate prepared in air, J. Alloys Compd. 397 (2005) 245–249. doi:10.1016/j.jallcom.2004.11.066.

[257] R. Moos, K.H. Hardtl, Defect chemistry of donor-doped and undoped strontium titanate ceramics between 1000° and 1400°C, J. Am. Ceram. Soc. 80 (1997) 2549–2562. doi:10.1111/j.1151-2916.1997.tb03157.x.

[258] M. Cologna, B. Rashkova, R. Raj, Flash Sintering of Nanograin Zirconia in 5 s at 850°C, J. Am. Ceram. Soc. 93 (2010) 3556–3559. doi:10.1111/j.1551-2916.2010.04089.x.

[259] R.I. Todd, E. Zapata-Solvas, R.S. Bonilla, T. Sneddon, P.R. Wilshaw, Electrical characteristics of flash sintering: thermal runaway of Joule heating, J. Eur. Ceram. Soc. 35 (2015) 1865–1877. doi:10.1016/J.JEURCERAMSOC.2014.12.022.

[260] A. Gaur, V.M. Sglavo, Densification of $La_{0.6}Sr_{0.4}Co_{0.2}Fe_{0.8}O_3$ ceramic by flash sintering at temperature less than 100 °c, J. Mater. Sci. 49 (2014) 6321–6332. doi:10.1007/s10853-014-8357-2.

[261] European Commision, Reference Document on Best Available Techniques in the Ceramic Manufacturing Industry, Ceram. Manuf. Ind. (2007) 210–211. http://eippcb.jrc.ec.europa.eu/reference/BREF/cer_bref_0807.pdf.

[262] R. Raj, Joule heating during flash-sintering, J. Eur. Ceram. Soc. 32 (2012) 2293–2301.

doi:10.1016/j.jeurceramsoc.2012.02.030.

[263] J. Narayan, A new mechanism for field-assisted processing and flash sintering of materials, Scr. Mater. 69 (2013) 107–111. doi:10.1016/j.scriptamat.2013.02.020.

[264] R. Chaim, G. Chevallier, A. Weibel, C. Estournès, Flash sintering of dielectric nanoparticles as a percolation phenomenon through a softened film, J. Appl. Phys. 121 (2017). doi:10.1063/1.4980853.

[265] W. Qin, H. Majidi, J. Yun, K. van Benthem, Electrode Effects on Microstructure Formation During Flash Sintering of Yttrium-Stabilized Zirconia, J. Am. Ceram. Soc. 99 (2016) 2253–2259. doi:10.1111/jace.14234.

[266] Y. Zhang, J. Nie, J.M. Chan, J. Luo, Probing the densification mechanisms during flash sintering of ZnO, Acta Mater. 125 (2017) 465–475. doi:10.1016/j.actamat.2016.12.015.

[267] W. Ji, B. Parker, S. Falco, J.Y. Zhang, Z.Y. Fu, R.I. Todd, Ultra-fast firing: Effect of heating rate on sintering of 3YSZ, with and without an electric field, J. Eur. Ceram. Soc. 37 (2017) 2547–2551. doi:10.1016/j.jeurceramsoc.2017.01.033.

[268] J.C. M'Peko, J.S.C. Francis, R. Raj, Field-assisted sintering of undoped $BaTiO_3$: Microstructure evolution and dielectric permittivity, J. Eur. Ceram. Soc. 34 (2014) 3655–3660. doi:10.1016/j.jeurceramsoc.2014.04.041.

[269] L.A. Perez-Maqueda, E. Gil-Gonzalez, A. Perejon, J.M. Lebrun, P.E. Sanchez-Jimenez, R. Raj, Flash sintering of highly insulating nanostructured phase-pure $BiFeO_3$, J. Am. Ceram. Soc. 100 (2017) 3365–3369. doi:10.1111/jace.14990.

[270] R. Chaim, C. Estournès, Effects of the fundamental oxide properties on the electric field-flash temperature during flash sintering, Scr. Mater. 163 (2019) 130–132. doi:10.1016/j.scriptamat.2019.01.018.

[271] C. Schmerbauch, J. Gonzalez-julian, R. Roeder, C. Ronning, O. Guillon, Flash Sintering of Nanocrystalline Zinc Oxide and its Influence on Microstructure and Defect Formation, J. Am. Ceram. Soc. 97 (2014) 1728–1735. doi:10.1111/jace.12972.

[272] D. Liu, J. Liu, Y. Gao, F. Liu, K. Li, J. Xia, Y. Wang, L. An, Effect of the applied electric field on the microstructure and electrical properties of flash-sintered 3YSZ ceramics, Ceram. Int. 42 (2016) 19066–19070. doi:10.1016/j.ceramint.2016.09.065.

[273] A. Karakuscu, M. Cologna, D. Yarotski, J. Won, J.S.C. Francis, R. Raj, B.P. Uberuaga, Defect structure of flash-sintered strontium titanate, J. Am. Ceram. Soc. 95 (2012) 2531–2536. doi:10.1111/j.1551-2916.2012.05240.x.

[274] N. Shomrat, S. Baltianski, E. Dor, Y. Tsur, The influence of doping on flash sintering

conditions in $SrTi_{1-x}Fe_xO_{3-\delta}$, J. Eur. Ceram. Soc. 37 (2017) 179–188. doi:10.1016/j.jeurceramsoc.2016.07.037.

[275] W. Rheinheimer, X.L. Phuah, H. Wang, F. Lemke, M.J. Hoffmann, H. Wang, The role of point defects and defect gradients in flash sintering of perovskite oxides, Acta Mater. (2018). doi:10.1016/j.actamat.2018.12.007.

[276] E. Riedel, C. Janiak, Anorganische Chemie, 7. Aufl., de Gruyter GmbH & Co. KG, Berlin, 2007. doi:10.1016/j.eupc.2003.11.010.

[277] F.A. Kröger, H.J. Vink, Relations between the Concentrations of Imperfections in Crystalline Solids, Solid State Phys. 3 (1956) 307–435. doi:10.1016/S0081-1947(08)60135-6.

[278] F.A.A. Kröger, H.J.J. Vink, Relations between the concentrations of imperfections in solids, J. Phys. Chem. Solids. 5 (1958) 208–223. doi:10.1016/0022-3697(58)90069-6.

[279] K. Gömann, G. Borchardt, M. Schulz, A. Gömann, W. Maus-Friedrichs, B. Lesage, O. Kaïtasov, S. Hoffmann-Eifert, T. Schneller, Sr diffusion in undoped and La-doped $SrTiO_3$ single crystals under oxidizing conditions, Phys. Chem. Chem. Phys. 7 (2005) 2053–2060. doi:10.1039/b418824a.

[280] M.J. Akhtar, Z.-U.-N. Akhtar, R.A. Jackson, C.R.A. Catlow, Computer Simulation Studies of Strontium Titanate, J. Am. Ceram. Soc. 78 (1995) 421–428. doi:10.1111/j.1151-2916.1995.tb08818.x.

[281] J. Crawford, P. Jacobs, Point Defect Energies for Strontium Titanate: A Pair-Potentials Study, J. Solid State Chem. 144 (1999) 423–429. doi:10.1006/jssc.1999.8191.

[282] R. Meyer, R. Waser, J. Helmbold, G. Borchardt, Cationic surface segregation in donor-doped $SrTiO_3$ under oxidizing conditions, J. Electroceramics. 9 (2002) 101–110. doi:10.1023/A:1022898104375.

[283] U. Balachandran, Electrical Conductivity in Lanthanum-Doped Strontium Titanate, J. Electrochem. Soc. 129 (1982) 1021. doi:10.1149/1.2124008.

[284] N. Chan, R. Sharma, D. Smyth, Nonstoichiometry in $SrTiO_3$, J. Electrochem. 128 (1981) 1762–1769. doi:10.1149/1.2127727.

[285] R.A. De Souza, F. Gunkel, S. Hoffmann-Eifert, R. Dittmann, Finite-size versus interface-proximity effects in thin-film epitaxial $SrTiO_3$, Phys. Rev. B - Condens. Matter Mater. Phys. 89 (2014) 1–5. doi:10.1103/PhysRevB.89.241401.

[286] X. Guo, Comment on " Colossal Ionic Conductivity at Interfaces of Epitaxial, Science. 324 (2009) 465a. doi:10.1126/science.1168940.

[287] M. Lontsi-Fomena, A. Villesuzanne, J.P. Doumerc, C. Frayret, M. Pouchard, A density functional theory study of oxygen diffusion in $LaAlO_3$ and $SrTiO_3$, Comput. Mater. Sci. 44 (2008) 53–60. doi:10.1016/j.commatsci.2008.01.046.

[288] C.J. Shin, H.I. Yoo, Al-doped $SrTiO_3$: Part II, unusual thermodynamic factor and chemical diffusivity, Solid State Ionics. 178 (2007) 1089–1094. doi:10.1016/j.ssi.2007.05.009.

[289] I. Denk, W. Münch, J. Maier, Partial Conductivities in $SrTiO_3$: Bulk Polarization Experiments, Oxygen Concentration Cell Measurements, and Defect-Chemical Modeling, J. Am. Ceram. Soc. 78 (1995) 3265. doi:https://doi.org/10.1111/j.1151-2916.1995.tb07963.x.

[290] R. Merkle, J. Maier, Defect association in acceptor-doped $SrTiO_3$: Case study for $Fe'TiV_O^{\cdot\cdot}$ and $Mn''TiV_O^{\cdot\cdot}$, Phys. Chem. Chem. Phys. 47 (2008) 2297–2303. doi:10.1039/b300205p.

[291] V.Y. Zenou, D.E. Fowler, R. Gautier, S.A. Barnett, K.R. Poeppelmeier, L.D. Marks, Redox and phase behavior of Pd-substituted (La,Sr)CrO_3 perovskite solid oxide fuel cell anodes, Solid State Ionics. 296 (2016) 90–105. doi:10.1016/j.ssi.2016.09.006.

[292] V. Metlenko, A.H.H.H. Ramadan, F. Gunkel, H. Du, H. Schraknepper, S. Hoffmann-Eifert, R. Dittmann, R. Waser, R.A. De Souza, Do dislocations act as atomic autobahns for oxygen in the perovskite oxide $SrTiO_3$?, Nanoscale. 6 (2014) 12864–76. doi:10.1039/c4nr04083j.

[293] J.R. Jurado, F.M. Figueiredo, B. Gharbage, J.R. Frade, Electrochemical permeability of $Sr_{0.7}(Ti,Fe)O_{3-\delta}$ materials, Solid State Ionics. 118 (1999) 89–97. doi:Doi: 10.1016/s0167-2738(98)00471-8.

[294] S. Steinsvik, R. Bugge, J. Gjønnes, J. Taftø, T. Norby, The defect structure of $SrTi_{1-x}Fe_xO_{3-y}$ (x = 0–0.8) investigated by electrical doncutivity measurements and electron energy loss spectroscopy (EELS), J. Phys. Chem. Solids. 58 (1997) 969–976. doi:10.1016/S0022-3697(96)00200-4.

[295] H.D. Zhou, J.B. Goodenough, Polaron morphologies in $SrFe_{1-x}Ti_xO_{3-\delta}$, J. Solid State Chem. 177 (2004) 1952–1957. doi:10.1016/j.jssc.2004.01.015.

[296] P.R. Slater, D.P. Fagg, J.T.S. Irvine, Synthesis and electrical characterisation of doped perovskite titanates as potential anode materials for solid oxide fuel cells, J. Mater. Chem. 7 (1997) 2495–2498. doi:10.1039/a702865b.

[297] W. Menesklou, H.-J. Schreiner, K.H. Härdtl, E. Ivers-Tiffée, High temperature oxygen

sensors based on doped $SrTiO_3$, Sensors Actuators, B Chem. 59 (1999) 184–189. doi:10.1016/S0925-4005(99)00218-X.

[298] N.H. Perry, D. Pergolesi, S.R. Bishop, H.L. Tuller, Defect chemistry and surface oxygen exchange kinetics of La-doped $Sr(Ti,Fe)O_{3-\alpha}$ in oxygen-rich atmospheres, Solid State Ionics. 273 (2015) 18–24. doi:10.1016/j.ssi.2014.09.013.

[299] M. Thommes, K. Kaneko, A. V. Neimark, J.P. Olivier, F. Rodriguez-Reinoso, J. Rouquerol, K.S.W. Sing, Physisorption of gases, with special reference to the evaluation of surface area and pore size distribution (IUPAC Technical Report), Pure Appl. Chem. 87 (2015) 1051–1069. doi:10.1515/pac-2014-1117.

[300] S. Lowell, J.E. Shields, M.A. Thomas, M. Thommes, Characterization of porous solids and powders: surface area, pore size, and density, Kluwer Academic Publishers, Dordrecht, 2004. doi:10.1007/978-1-4020-2303-3.

[301] M. Thommes, Physical Adsorption Characterization of Nanoporous Materials, Chemie Ing. Tech. 82 (2010) 1059–1073. doi:10.1002/cite.201000064.

[302] J. Landers, G.Y. Gor, A. V. Neimark, Density functional theory methods for characterization of porous materials, Colloids Surfaces A Physicochem. Eng. Asp. 437 (2013) 3–32. doi:10.1016/j.colsurfa.2013.01.007.

[303] P.H. Emmett, S. Brunauer, The Use of Low Temperature van der Waals Adsorption Isotherms in Determining the Surface Area of Iron Synthetic Ammonia Catalysts, J. Am. Chem. Soc. 59 (1937) 1553–1564. doi:10.1021/ja01287a041.

[304] J. Rouquerol, P. Llewellyn, F. Rouquerol, Is the bet equation applicable to microporous adsorbents?, 2991 (2007) 49–56. doi:10.1016/S0167-2991(07)80008-5.

[305] M. Thommes, K.A. Cychosz, Physical adsorption characterization of nanoporous materials: Progress and challenges, Adsorption. 20 (2014) 233–250. doi:10.1007/s10450-014-9606-z.

[306] P.I. Ravikovitch, A. V. Neimark, Characterization of micro- and mesoporosity in SBA-15 materials from adsorption data by the NLDFT method, J. Phys. Chem. B. 105 (2001) 6817–6823. doi:10.1021/jp010621u.

[307] M. Eckert, Max von Laue and the discovery of X-ray diffraction in 1912, Ann. Phys. 524 (2012) 83–85. doi:10.1002/andp.201200724.

[308] W.H. Bragg, W.L. Bragg, The structure of some crystals as indicated by their diffraction of X-rays, Proc. R. Soc. Lond. A. 89 (1913) 248–277. doi:10.1098/rspa.1913.0083.

[309] A.W. Hull, A New Method of Chemical Analysis., J. Am. Chem. Soc. 41 (1919) 1168–1175. doi:10.1021/ja02229a003.

[310] B. Fultz, J. Howe, Transmission Electron Microscopy and Diffractometry of Materials, Fourth edi, Springer, Berlin, 2017. doi:10.1007/978-3-642-29761-8.

[311] W. Borchardt-Ott, 13 Röntgenographische Untersuchungen an Kristallen, in: Krist. - Eine Einführung Für Naturwissenschaftler, Siebte Auf, Berlin, 2009: p. 360. doi:10.1007/978-3-540-78271-1.

[312] A.C. Juhl, Poröse Kohlenstoffe für Lithium-Schwefel-Batterien : Darstellung besonderer Morphologien und Verwendung als Wirtstruktur für Schwefel, University of Hamburg, 2017.

[313] P. Debye, P. Scherrer, Bestimmung der Größe und der inneren Struktur von Kolloidteilchen mittels Röntgenstrahlen, Nachr. Ges. Wiss. Göttingen, Math.-Physik. Klasse. 2 (1918) 101–120.

[314] U. Holzwarth, N. Gibson, The Scherrer equation versus the “Debye-Scherrer equation,” Nat. Nanotechnol. 6 (2011) 534–534. doi:10.1038/nnano.2011.145.

[315] A.R. Denton, N.W. Ashcroft, Vegard’s law, Phys. Rev. A. 43 (1991) 3161–3164. doi:10.1103/PhysRevA.43.3161.

[316] K.T. Jacob, S. Raj, L. Rannesh, Vegard’s law : a fundamental relation or an approximation?, Int. J. Mater. Res. 98 (2007) 776–779.

[317] D.B. Williams, C.B. Carter, Transmission Electron Microscopy: A textbook for Materials Science, Springer, 2009. doi:10.1007/978-0-387-40093-8.

[318] D. Brandon, W.D. Kaplan, Microstructural characterization of Materials, 2nd Editio, 2008.

[319] N.F. Cheville, J. Stasko, Techniques in Electron Microscopy of Animal Tissue, Vet. Pathol. 51 (2014) 28–41. doi:10.1177/0300985813505114.

[320] H. Schatten, The role of scanning electron microscopy in cell and molecular biology, Scanning Electron Microsc. Life Sci. (2013) 1–15. doi:10.1017/cbo9781139018173.002.

[321] L.J. Allen, A.J.D. Alfonso, S.D. Findlay, J.M. Lebeau, N.R. Lugg, S. Stemmer, Elemental mapping in scanning transmission electron microscopy, J. Phys. Conf. Ser. 241 (2010) 012061. doi:10.1088/1742-6596/241/1/012061 Elemental.

[322] S. Thomas, R. Thomas, A. K. Zachariah, R.K. Mishra, Spectroscopic Methods for Nanomaterials Characterization, 2017. doi:10.1016/B978-0-323-46140-5.01001-3.

[323] Royal Society of Chemistry, Ultraviolet -Visible Spectroscopy (UV), RSC - Adv. Chem. Sci. (2009) 68. doi:10.1016/j.jpcs.2008.07.014.

[324] L.D.S. Yadav, Organic Spectroscopy, Springer-Science+Business Media, B.V., Dordrecht, 2005. doi:10.1007/978-1-4020-2575-4.

[325] T.G. Mayerhöfer, H. Mutschke, J. Popp, Employing Theories Far beyond Their Limits—The Case of the (Boguer-) Beer–Lambert Law, ChemPhysChem. (2016) 1948–1955. doi:10.1002/cphc.201600114.

[326] A.E. Morales, E.S. Mora, U. Pal, Use of diffuse reflectance spectroscopy for optical characterization of un-supported nanostructures, Rev. Mex. F´Isica S. 53 (2007) 18–22.

[327] G. Kortüm, G. Schreyer, Über die Gültigkeit der Kubelka-Munk-Funktion für Reflexionsspektren an Pulvern, Zeitschrift Für Naturforsch. Part A - Astrophys. Phys. Und Phys. Chemie. 11 (1956) 1018–1022.

[328] M.L. Myrick, M.N. Simcock, M. Baranowski, H. Brooke, S.L. Morgan, J.N. McCutcheon, The kubelka-munk diffuse reflectance formula revisited, Appl. Spectrosc. Rev. 46 (2011) 140–165. doi:10.1080/05704928.2010.537004.

[329] P. Kubelka, F. Munk, The Kubelka-Munk Theory of Reflectance, Zeitschrift Für Tech. Phys. 12 (1931) 593–601. doi:10.4236/msce.2014.28004.

[330] J. Tauc, R. Grigorovici, A. Vancu, Optical Properties and Electronic Structure of Amorphous Germanium, Phys. Status Solidi Basic Res. 15 (1966) 627–637. doi:doi.org/10.1002/pssb.19660150224.

[331] B.D. Viezbicke, S. Patel, B.E. Davis, D.P. Birnie, Evaluation of the Tauc method for optical absorption edge determination: ZnO thin films as a model system, Phys. Status Solidi Basic Res. 252 (2015) 1700–1710. doi:10.1002/pssb.201552007.

[332] J. Torrent, V. Barrón, Methods of Soil Analysis Chapter 13—Diffuse Reflectance Spectroscopy, Soil Sci. Soc. Am. J. (2008) 367–385. doi:10.2136/sssabookser5.5.c13.

[333] G. Socrates, Infrared and Raman characteristic group frequencies. Tables and charts, 2001. doi:10.1016/j.yebeh.2013.06.031.

[334] C. Perry, B. Khanna, G. Rupprecht, Infrared studies of perovskite titanates, Phys. Rev. 9 (1964) 1–5. doi:10.1103/PhysRev.135.A408.

[335] K. Loutherback, G. Birarda, L. Chen, H.-Y. N. Holman, Microfluidic approaches to synchrotron radiation-based Fourier transform infrared (SR-FTIR) spectral microscopy of living biosystems, Protein Pept. Lett. 23 (2016) 273–282. doi:10.2174/0929866523666160106154035.

[336] E. Barsoukov, J.R. Macdonald, Impedance Spectroscopy, 2005. doi:10.1002/0471716243.

[337] W. Nernst, Methode zur Bestimmung von Dielektrizitätskonstanten, Zeitschrift Für Phys. Chemie. 14U (1894) 622–663. doi:doi:10.1515/zpch-1894-144.

[338] M. Grossi, B. Ricc, Electrical impedance spectroscopy (EIS) for biological analysis and food characterization : a review, J. Sensors Sens. Syst. 6 (2017) 303–325. doi:doi.org/10.5194/jsss-6-303-2017.

[339] A. Sacco, Electrochemical impedance spectroscopy: Fundamentals and application in dye-sensitized solar cells, Renew. Sustain. Energy Rev. 79 (2017) 814–829. doi:10.1016/j.rser.2017.05.159.

[340] F. Lisdat, D. Schäfer, The use of electrochemical impedance spectroscopy for biosensing, Anal. Bioanal. Chem. 391 (2008) 1555–1567. doi:10.1007/s00216-008-1970-7.

[341] S. Tol, Causality and the Dispersion Relation: Logical Foundations, Phys. Rev. 104 (1956) 1760–1770. doi:doi.org/10.1103/PhysRev.104.1760.

[342] R.D.L. KRONIG, On the Theory of Dispersion of X-Rays, J. Opt. Soc. Am. 12 (1926) 547–557. doi:10.1364/JOSA.12.000547.

[343] P.J. Hore, Nuclear Magnetic Resonance, 2015. doi:10.1007/978-1-4612-4894-1 e-ISBN-13:

[344] M.A. Nanny, R.A. Minear, J.A. Leenheer, Nuclear Magnetic Resonance Spectroscopy in Environmental Chemistry, Oxford University Press, New York, 1997.

[345] M.J. Duer, Solid-State NMR Spectroscopy: Principles and Applications, Blackwell Science, Oxford, 2002.

[346] J. Klinowski, New Techniques in Solid-State NMR, Top. Curr. Chem. 246 (2004) 1–33. doi:10.1007/b98646.

[347] H.R. Verma, Atomic and Nuclear Analytical Methods, Springer Berlin Heidelberg, Berlin, n.d.

[348] N.N. Greenwood, T.C. Gibb, Mössbauer spectroscopy, 1971. doi:10.1080/00107517508211091.

[349] B. Fultz, Mössbauer Spectrometry, in: Charact. Mater., John Wiley & Sons, New York, 2011. doi:10.1021/ac60313a003.

[350] J.A. Weil, J.R. Bolton, Electron Paramagnetic Resonance: Elemental Theory and Practical Applications, Second Edi, John Wiley & Sons, 2007.

[351] C. Karunakaran, M. Balamurugan, Electron Paramagnetic Resonance Spectroscopy, Elsevier Inc., 2018. doi:10.1016/B978-0-12-813608-9.00004-6.

[352] D.A. Skoog, E.J. Holler, S.R. Crouch, Principles of Instrumental Analysis, Sixth Edit, David Harris, Belmont, 2007.

[353] M. Inagaki, F. Kang, Materials science and engineering of carbon : characterization, 2016. doi:10.1007/BF00426590.

[354] M.A. Reiche, M. Maciejewski, A. Baiker, Characterization by temperature programmed reduction, Catal. Today. 56 (2000) 347–355. doi:0920-586.

[355] M.M. Nair, H. Yen, F. Kleitz, Nanocast mesoporous mixed metal oxides for catalytic applications, Comptes Rendus Chim. 17 (2014) 641–655. doi:10.1016/j.crci.2014.04.005.

[356] A.M. Youssef, H.K. Farag, A. El-Kheshen, F.F. Hammad, Synthesis of Nano-Structured Strontium Titanate by Sol-Gel and Solid State Routes, Silicon. 10 (2018) 1225–1230. doi:10.1007/s12633-017-9596-z.

[357] J.F. Moulder, W.F. Stickle, P.E. Sobol, K.D. Bomben, Handbook of X-ray Photoelectron Spectroscopy, Eden Praire, 1992. doi:10.1002/sia.740030412.

[358] D.C.M. Dutoit, M. Schneider, A. Baiker, Titania – Silica Mixed Oxides, J. Catal. 164 (1996) 433–439.

[359] S. Brunauer, P.H. Emmett, E. Teller, Adsorption of Gases in Multimolecular Layers, J. Am. Chem. Soc. 60 (1938) 309–319. doi:citeulike-article-id:4074706.

[360] Y. Liu, J.Y. Su, Y.L. Xu, X.C. Zhang, The influence of pore shapes on the band structures in phononic crystals with periodic distributed void pores, Ultrasonics. 49 (2009) 276–280. doi:10.1016/j.ultras.2008.09.008.

[361] K. Wang, Y. Liu, Q.S. Yang, Tuning of band structures in porous phononic crystals by grading design of cells, Ultrasonics. 61 (2015) 25–32. doi:10.1016/j.ultras.2015.02.022.

[362] E. Monaico, V. V. Ursaki, I.M. Tiginyanu, Z. Dashevsky, V. Kasiyan, R.W. Boyd, Porosity-induced blueshift of photoluminescence in CdSe, J. Appl. Phys. 100 (2006) 1–6. doi:10.1063/1.2338833.

[363] T.K. Townsend, N.D. Browning, F.E. Osterloh, T.E.T. Al, Nanoscale Strontium Titanate Photocatalysts for Overall Water Splitting, ACS Nano. 6 (2012) 7420–7426. doi:10.1021/nn302647u.

[364] H. Zhan, Z.-G. Chen, J. Zhuang, X. Yang, Q. Wu, X. Jiang, C. Liang, M. Wu, J. Zou, Correlation between Multiple Growth Stages and Photocatalysis of $SrTiO_3$

Nanocrystals, J. Phys. Chem. C. 119 (2015) 3530–3537. doi:10.1021/jp512448p.

[365] X. Chen, S. Shen, L. Guo, S.S. Mao, Semiconductor-based Photocatalytic Hydrogen Generation., Chem. Rev. (Washington, DC, United States). 110 (2010) 6503–6570. doi:10.1021/cr1001645.

[366] T.R. Clevenger, Effect of Fe^{4+} in the System $SrFeO_3$-$SrTiO_3$, J. Am. Ceram. Soc. 46 (1963) 207–210. doi:10.1111/j.1151-2916.1963.tb19773.x.

[367] A.A. Leontiou, A.K. Ladavos, A.E. Giannakas, T. V. Bakas, P.J. Pomonis, A comparative study of substituted perovskite-type solids of oxidic $La_{1-x}Sr_xFeO_{3\pm\delta}$ and chlorinated $La_{1-x}Sr_xFeO_{3\pm\delta}Cl_\sigma$ form: Catalytic performance for CH_4 oxidation by O, J. Catal. 251 (2007) 103–112. doi:10.1016/j.jcat.2007.07.012.

[368] L. Karanovic, S. Petrovic, V. Dondur, D. Paneva, I. Mitov, V. Rakic, $LaMO_3$ (M = Mg , Ti , Fe) perovskite type oxides : Preparation , characterization and catalytic properties in methane deep oxidation, 79 (2008) 186–198. doi:10.1016/j.apcatb.2007.10.022.

[369] J. Zhu, D. Xiao, J. Li, X. Yang, Perovskite-Like Mixed Oxides ($LaSrMn_{1-x}Ni_xO_{4+\delta}$, $0\leq x\leq 1$) as Catalyst for Catalytic NO Decomposition: TPD and TPR Studies, Catal. Letters. 129 (2009) 240–246. doi:10.1007/s10562-008-9807-8.

[370] H. Falcón, J.A. Barbero, J.A. Alonso, M.J. Martínez-Lope, J.L.G. Fierro, $SrFeO_{3-\delta}$ perovskite oxides: Chemical features and performance for methane combustion, Chem. Mater. 14 (2002) 2325–2333. doi:10.1021/cm011292l.

[371] M.S.S. Khine, L. Chen, S. Zhang, J. Lin, S.P. Jiang, Syngas production by catalytic partial oxidation of methane over $(La_{0.7}A_{0.3})BO_3$ (A = Ba, Ca, Mg, Sr, and B = Cr or Fe) perovskite oxides for portable fuel cell applications, Int. J. Hydrogen Energy. 38 (2013) 13300–13308. doi:10.1016/j.ijhydene.2013.07.097.

[372] G. Pecchi, M.G. Jiliberto, A. Buljan, E.J. Delgado, Relation between defects and catalytic activity of calcium doped $LaFeO_3$ perovskite, Solid State Ionics. 187 (2011) 27–32. doi:10.1016/j.ssi.2011.02.014.

[373] H. Arai, T. Yamada, K. Eguchi, T. Seiyama, Catalytic combustion of methane over various perovskite-type oxides, Appl. Catal. 26 (1986) 265–276. doi:10.1016/S0166-9834(00)82556-7.

[374] R. Gholami, M. Alyani, K. Smith, Deactivation of Pd Catalysts by Water during Low Temperature Methane Oxidation Relevant to Natural Gas Vehicle Converters, 2015. doi:10.3390/catal5020561.

[375] R. Doshi, C.B. Alcock, J.J. Carberry, Effect of surface area on CO oxidation by the

perovskite catalysts $La_{1-x}Sr_xMO_{3-\delta}$ (M = Co, Cr), Catal. Letters. 18 (1993) 337–343. doi:10.1007/BF00765279.

[376] C. Xiulan, L. Yuan, New methods to prepare ultrafine particles of some perovskite-type oxides, Chem. Eng. J. 78 (2000) 205–209. doi:10.1016/S1385-8947(00)00132-7.

[377] D.A.J.M. Ligthart, R.A. Van Santen, E.J.M. Hensen, R.A. van Santen, E.J.M. Hensen, Supported Rhodium Oxide Nanoparticles as Highly Active CO Oxidation Catalysts, Angew. Chemie Int. Ed. 50 (2011) 5306–5310. doi:10.1002/anie.201100190.

[378] M.K.J. Park, Dispersion Improvement of Platinum Catalysts Supported on Silica , Silica-Alumina and Alumina by Titania Incorporation and pH Adjustment, (2009) 288–297. doi:10.1007/s10562-009-0188-4.

[379] M.H. Liu, Y.W. Chen, T.S. Lin, C.Y. Mou, Defective Mesocrystal ZnO-Supported Gold Catalysts: Facilitating CO Oxidation via Vacancy Defects in ZnO, ACS Catal. 8 (2018) 6862–6869. doi:10.1021/acscatal.8b01282.

[380] J. Zhu, X. Yang, X. Xu, K. Wei, Cyclic voltammetry for predicting oxidation process in heterogeneous catalysis, Zeitschrift Fur Phys. Chemie. 220 (2006) 1589–1594. doi:10.1524/zpch.2006.220.12.1589.

[381] L. Chen, J.P. McCann, S.L. Tait, A re-examination of the catalyst activation and temperature hysteresis in methane combustion on Pt/Al_2O_3, Appl. Catal. A Gen. 549 (2018) 19–30. doi:10.1016/j.apcata.2017.09.008.

[382] G. Corro, C. Cano, J.L. Garcia Fierro, Improved activity of $Pt/\gamma\text{-}Al_2O_3$ catalysts for CH_4-O_2 reaction under lean conditions due to sulfation and catalyst loading, Catal. Commun. 9 (2008) 2601–2605. doi:10.1016/j.catcom.2008.07.026.

[383] I.E. Beck, V.I. Bukhtiyarov, I.Y. Pakharukov, V.I. Zaikovsky, V. V. Kriventsov, V.N. Parmon, Platinum nanoparticles on Al_2O_3: Correlation between the particle size and activity in total methane oxidation, J. Catal. 268 (2009) 60–67. doi:10.1016/j.jcat.2009.09.001.

[384] R. Meyer, R. Waser, Resistive donor-doped $SrTiO_3$ sensors: I, basic model for a fast sensor response, Sensors Actuators, B Chem. 101 (2004) 335–345. doi:10.1016/j.snb.2004.04.004.

[385] M. Biesuz, V.M. Sglavo, Flash sintering of alumina: Effect of different operating conditions on densification, J. Eur. Ceram. Soc. 36 (2016) 2535–2542.

[386] R. Baraki, S. Schwarz, O. Guillon, Effect of electrical field/current on sintering of fully stabilized zirconia, J. Am. Ceram. Soc. 95 (2012) 75–78.

[387] L.B. Caliman, E. Bichaud, P. Soudant, D. Gouvea, M.C. Steil, A simple flash sintering setup under applied mechanical stress and controlled atmosphere., MethodsX. 2 (2015) 392–8. doi:10.1016/j.mex.2015.10.004.

[388] M.N. Rahaman, Ceramic processing and sintering, Marcel Dekker, New York, USA, 1996.

[389] B. Koo, H. Kwon, Y. Kim, H.G. Seo, J.W. Han, W. Jung, Enhanced oxygen exchange of perovskite oxide surfaces through strain-driven chemical stabilization, Energy Environ. Sci. 11 (2018) 71–77. doi:10.1039/c7ee00770a.

[390] R. Meyer, A.F. Zurhelle, R.A. De Souza, R. Waser, F. Gunkel, Dynamics of the metal-insulator transition of donor-doped $SrTiO_3$, Phys. Rev. B. 94 (2016) 1–19. doi:10.1103/PhysRevB.94.115408.

[391] A.A. Yaremchenko, E.N. Naumovich, S.G. Patrício, O. V. Merkulov, M. V. Patrakeev, J.R. Frade, Rare-Earth-Substituted Strontium Titanate: Insight into Local Oxygen-Rich Structures and Redox Kinetics, Inorg. Chem. 55 (2016) 4836–4849. doi:10.1021/acs.inorgchem.6b00350.

[392] J. Won, L.J. Vernon, A. Karakuscu, R.M. Dickerson, M. Cologna, R. Raj, Y. Wang, S.J. Yoo, S.-H. Lee, A. Misra, B.P. Uberuaga, The role of non-stoichiometric defects in radiation damage evolution of $SrTiO_3$, J. Mater. Chem. A. 1 (2013) 9235. doi:10.1039/c3ta11046j.

[393] J.O. Rubio, H.T. Tohver, Y. Chen, M.M. Abraham, Trapped-hole defects in SrO, Phys. Rev. B. 14 (1976) 5466–5472. doi:10.1103/PhysRevB.14.5466.

[394] S. Ahuja, T.R.N. Kutty, Nanoparticles of $SrTiO_3$ prepared by gel to crystallite conversion and their photocatalytic activity in the mineralization of phenol, J. Photochem. Photobiol. A Chem. 97 (1996) 99–107. doi:10.1016/1010-6030(96)04324-9.

[395] R. Moos, S. Schollhammer, K.H. Hardtl, Electron mobility of Sr1-xLaxTiO3 ceramics between 600° C and 1300° C, Appl. Phys. A Mater. Sci. Process. 65 (1997) 291–294. doi:10.1007/s003390050581.

[396] M. Danaie, D. Kepaptsoglou, Q.M. Ramasse, C. Ophus, K.R. Whittle, S.M. Lawson, S. Pedrazzini, N.P. Young, P.A.J. Bagot, P.D. Edmondson, Characterization of Ordering in A-Site Deficient Perovskite $Ca_{1-x}La_{2x/3}TiO_3$ Using STEM/EELS, Inorg. Chem. 55 (2016) 9937–9948. doi:10.1021/acs.inorgchem.6b02087.

[397] Y. Sun, J. Li, Y. Zeng, B.S. Amirkhiz, M. Wang, Y. Behnamian, J. Luo, A-site

deficient perovskite: the parent for in situ exsolution of highly active, regenerable nano-particles as SOFC anodes, J. Mater. Chem. A. 3 (2015) 11048–11056. doi:10.1039/C5TA01733E.

[398] E.Y. Konysheva, X. Xu, J.T.S. Irvine, On the existence of A-site deficiency in perovskites and its relation to the electrochemical performance, Adv. Mater. 24 (2012) 528–532. doi:10.1002/adma.201103352.

[399] J. Maier, Nanoionics: Ion transport and electrochemical storage in confined systems, Nat. Mater. 4 (2005) 805–815. doi:10.1038/nmat1513.

[400] J. Maier, Pushing nanoionics to the limits: Charge carrier chemistry in extremely small systems, Chem. Mater. 26 (2014) 348–360. doi:10.1021/cm4021657.

[401] G. Gregori, S. Heinze, P. Lupetin, H.U. Habermeier, J. Maier, Seebeck coefficient and electrical conductivity of mesoscopic nanocrystalline $SrTiO_3$, J. Mater. Sci. 48 (2013) 2790–2796. doi:10.1007/s10853-012-6894-0.

[402] P. Balaya, J. Jamnik, J. Fleig, J. Maier, Mesoscopic electrical conduction in nanocrystalline $SrTiO_3$, Appl. Phys. Lett. 88 (2006). doi:10.1063/1.2171798.

[403] Y. Kozuka, Y. Hikita, C. Bell, H.Y. Hwang, Dramatic mobility enhancements in doped $SrTiO_3$ thin films by defect management, Appl. Phys. Lett. 97 (2010) 95–98. doi:10.1063/1.3457994.

[404] K. Aika, J.H. Lunsford, Surface reactions of oxygen ions. I. Dehydrogenation of alkanes by oxygen(1-) ions on magnesium oxide, J. Phys. Chem. 81 (1977) 1393–1398. doi:10.1021/j100529a010.

[405] G. Tsekouras, J.T.S. Irvine, The role of defect chemistry in strontium titanates utilised for high temperature steam electrolysis, J. Mater. Chem. 21 (2011) 9367. doi:10.1039/c1jm11313e.

[406] V.C. Belessi, A.K. Ladavos, G.S. Armatas, P.J. Pomonis, Kinetics of methane oxidation over La–Sr–Ce–Fe–O mixed oxide solids, Phys. Chem. Chem. Phys. 3 (2001) 3856–3862. doi:10.1039/b103426j.

[407] A. Staykov, H. T??llez, T. Akbay, J. Druce, T. Ishihara, J. Kilner, Oxygen Activation and Dissociation on Transition Metal Free Perovskite Surfaces, Chem. Mater. 27 (2015) 8273–8281. doi:10.1021/acs.chemmater.5b03263.

[408] C. Oliva, S. Cappelli, I. Rossetti, A. Kryukov, L. Bonoldi, L. Forni, Effect of M ion oxidation state in $Sr_{1-x}M_xTiO_3$ perovskites in methane catalytic flameless combustion, J. Mol. Catal. A Chem. 245 (2006) 55–61. doi:10.1016/j.molcata.2005.09.037.

[409] Q. Fu, T. He, J.L. Li, G.W. Yang, Band-engineered $SrTiO_3$ nanowires for visible light photocatalysis, J. Appl. Phys. 112 (2012). doi:10.1063/1.4767229.

[410] M. Misono, Recent progress in the practical applications of heteropolyacid and perovskite catalysts: Catalytic technology for the sustainable society, Catal. Today. 144 (2009) 285–291. doi:10.1016/j.cattod.2008.10.054.

[411] A. Bisht, A. Sihag, A. Satyaprasad, S.S. Mallajosyala, S. Sharma, Pt Metal Supported and - Pt 4 + Doped - La 1 − x Sr x CoO 3 : Non-performance of - Pt 4 + and Reactivity Differences with Pt Metal, (2018) 1965–1977. doi:10.1007/s10562-018-2408-2.

[412] R. Watanabe, Y. Sekine, H. Takamatsu, Y. Sakamoto, S. Aramaki, M. Matsukata, E. Kikuchi, Pt and/or Pd supported/incorporated catalyst on perovskite-type oxide for water gas shift reaction, Top. Catal. 53 (2010) 621–628. doi:10.1007/s11244-010-9496-6.

[413] L. Millard, M. Bowker, Photocatalytic water-gas shift reaction at ambient temperature, J. Photochem. Photobiol. A Chem. 148 (2002) 91–95. doi:10.1016/S1010-6030(02)00077-1.

[414] O. Kwon, S. Sengodan, K. Kim, G. Kim, H.Y. Jeong, J. Shin, Y.W. Ju, J.W. Han, G. Kim, Exsolution trends and co-segregation aspects of self-grown catalyst nanoparticles in perovskites, Nat. Commun. 8 (2017) 1–7. doi:10.1038/ncomms15967.

[415] D.R. Rolison, Catalytic Nanoarchitectures - the Importance of Nothing and the Unimportance of Periodicity, Science (80-.). 299 (2003) 1698–1701.

[416] F. Zaera, Nanostructured materials for applications in heterogeneous catalysis, Chem. Soc. Rev. 42 (2013) 2746–2762. doi:10.1039/c2cs35261c.

[417] O. Sel, S. Sallard, T. Brezesinski, J. Rathouský, D.R. Dunphy, A. Collord, B.M. Smarsly, Periodically ordered meso- and macroporous SiO_2 thin films and their induced electrochemical activity as a function of pore hierarchy, Adv. Funct. Mater. 17 (2007) 3241–3250. doi:10.1002/adfm.200700079.

[418] S. Brunauer, P.H. Emmett, E. Teller, Adsorption of Gases in Multimolecular Layers, J. Am. Chem. Soc. 60 (1938) 309–319. doi:10.1021/ja01269a023.

[419] D. Briggs, M.P. Seah, Practical surface analysis: by auger and x-ray photo-electron spectroscopy, Wiley, 1983.

[420] D.A. Shirley, High-Resolution X-Ray Photoemission Spectrum of the Valence Bands of Gold, Phys. Rev. B. 5 (1972) 4709–4714. doi:10.1103/PhysRevB.5.4709.

[421] A. Adamski, T. Spałek, Z. Sojka, Application of EPR spectroscopy for elucidation of

vanadium speciation in VO_x/ZrO_2 catalysts subject to redox treatment, Res. Chem. Intermed. 29 (2003) 793–804. doi:10.1163/156856703322601807.

Chapter 8

Appendix

8.1 Additional Data to 'Results and Discussion'

In this section supplementary information to the presented work in Chapter 4 is given.

8.1.1 Optimization of Calcination Program in the Polymer Complex Synthesis

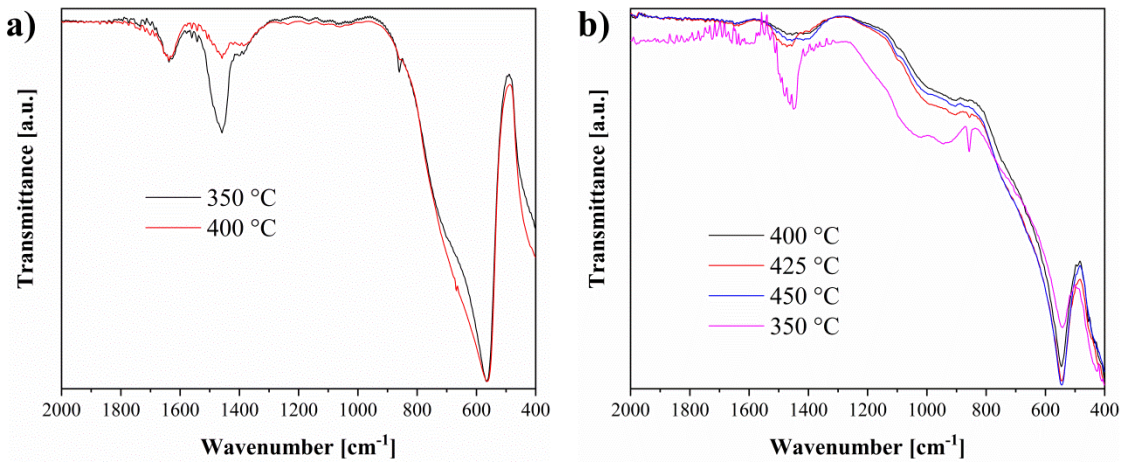

Figure 8.1: Infrared spectra of $SrTiO_3$ samples calcined with different intermediate temperature steps (a) template free STO (b) STO with 20 vol.% prehydrolyzed TEOS template.

The infrared spectroscopic analyses on $SrTiO_3$ samples prepared with different calcination programs indicate that perovskite oxides prepared with a 400 °C intermediate temperature step show the highest phase purity.

8.1.2 Choice of Precursor Strontium Salts in Polymer complex synthesis

Infrared spectra of $SrTiO_3$ obtained with different strontium precursor salts were depicted on Fig. 8.2. Both with ethylene glycol and glycerol, $SrCl_2$ engendered least amount of carbonates in polymer complex synthesis, whereas most carbonates were formed when $SrCO_3$ was employed as strontium precursor. Preparation of perovskites with high porosity were not possible with $SrCl_2$ precursor salt, since upon addition of prehydrolyzed TEOS template crystalline perovskite phase could not be obtained (Fig. 8.3b).

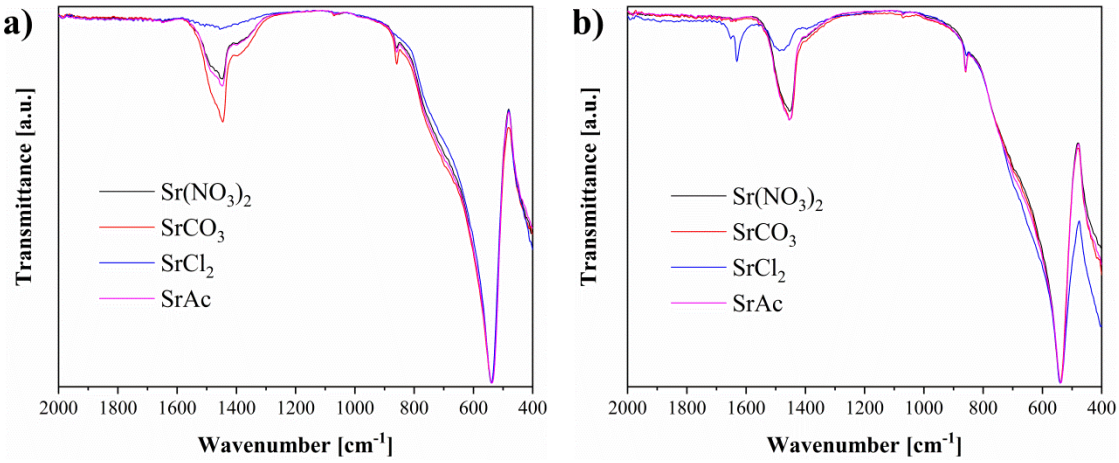

Figure 8.2: Infrared spectroscopic analysis by variation of strontium precursor in template free polymer complex synthesis with (a) ethylene glycol (b) glycerol.

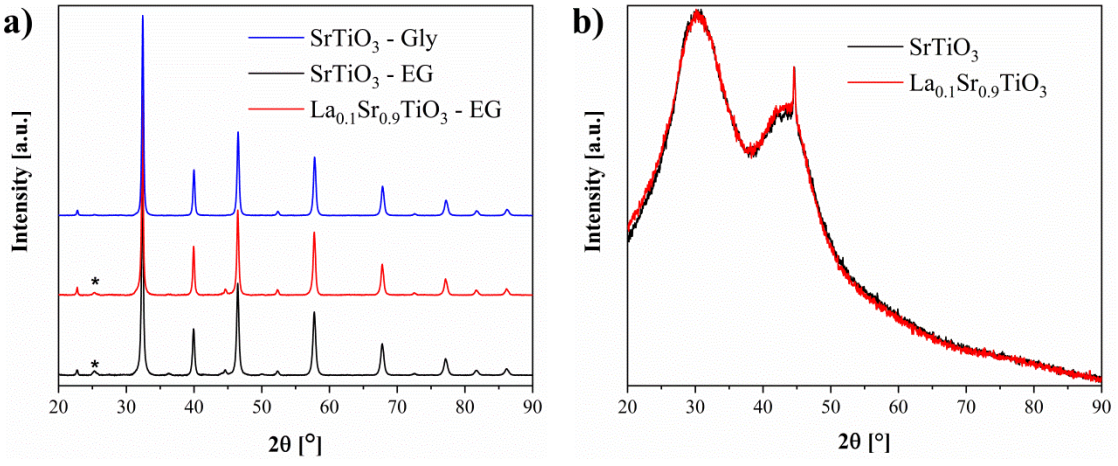

Figure 8.3: XRD analysis of perovskite oxide phase prepared with $SrCl_2$ precursor (a) template free polymer complex synthesis (b) cooperative assembly synthesis with glycerol employing 11 vol.% template.

8.1.3 Additional catalytic tests

Although cationic substitution on the A-site does not affect the performance of perovskite oxide catalysts significantly, catalytic methane oxidation tests showed minor performance loss with increasing La substitution in the investigated (La, Sr)(Ti, Fe)$O_{3\pm\delta}$ catalysts (Fig.7.4).

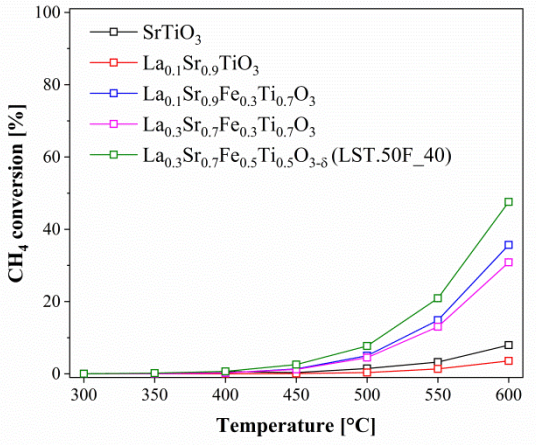

Figure 8.4: Steady state conversions obtained for the oxidation reaction of CH_4 over (La, Sr)(Ti,Fe)$O_{3\pm\delta}$ catalysts prepared by cooperative assembly synthesis route with a 40 vol.% template load. Samples show similar surface area between 230 – 250 m^2 g^{-1}.

8.1.4 Infrared spectra of LSTO nanoparticles prepared by solvothermal synthesis

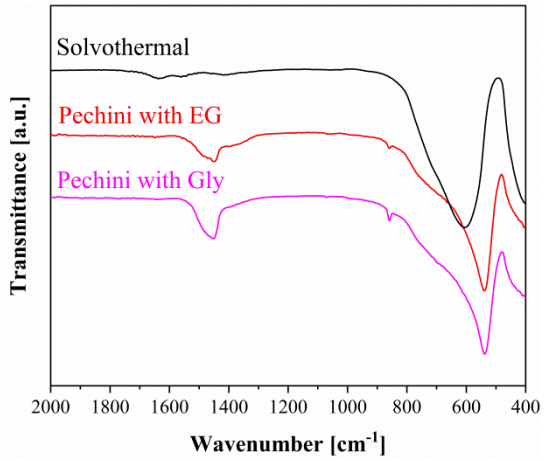

Figue 8.5: Infrared spectra of investigated LSTO ($La_{0.1}Sr_{0.9}TiO_{3+\delta}$) prepared by polymer complex and solvothermal synthesis routes

8.1 Additional data

The IR spectra of LSTO nanoparticles prepared by solvothermal synthesis work show significantly higher purity with no apparent carbonate (~ 1460 cm^{-1}) and other organic impurities (~ 870 cm^{-1}). On the other hand, LSTO powders prepared by template free polymer complex synthesis show these impurities.

Table 8.1: TEM/EDX derived local and average (avg) atomic compositions of investigated LSTO systems (Table 4.9) acquired at several survey positions normalized to nominal stoichiometric amounts in $La_{0.1}Sr_{0.9}TiO_3$ formula.

Sample		La	Sr	Ti
AP	Position 1	0.10	1.05	0.85
	Position 2	0.15	0.98	0.87
	Position 3	0.07	0.85	1.09
	Position 4	0.09	0.85	1.06
	AP avg	**0.10**	**0.93**	**0.97**
FS-300	Position 1	0.12	1.02	0.85
	Position 2	0.13	0.99	0.88
	Position 3	0.09	1.07	0.85
	FS-300 avg	**0.11**	**1.03**	**0.86**
FS-600	Position 1	0.13	0.89	0.98
	Position 2	0.12	1.04	0.84
	Position 3	0.11	0.96	0.92
	FS-600 avg	**0.12**	**0.96**	**0.92**
CS	Position 1	0.13	0.93	0.93
	Position 2	0.14	0.91	0.95
	Position 3	0.09	0.98	0.93
	CS avg	**0.12**	**0.94**	**0.94**

8.2 Preparation of pristine and La-substituted $SrTiO_3$ via methacrylic acid chelating

The excessive amount of organics containing carboxyl and hydroxyl groups in the Pechini synthesis unavoidably leads to formation of carbonate impurities in the final perovskite product. Although, these impurities can be easily removed from the final product by a mild acetic acid etching treatment, the deviations from the nominal stoichiometry that carbonates engender cannot be fully eliminated in this synthesis approach. With regard to these issues, a synthesis route based on methacrylic acid (MAA) chelating was developed to prepare pristine and La-substituted $SrTiO_3$ based perovskite oxide aggregates. In this approach, the metal cations are chelated by methacrylic acid and fixed in the polymer gel upon self-polymerization reaction of methacrylic acid to form poly(methacrylic acid) (PMAA). Finally after calcination in air, highly crystalline, pure-phase $SrTiO_3$ and $La_{0.1}Sr_{0.9}TiO_3$ samples were prepared.

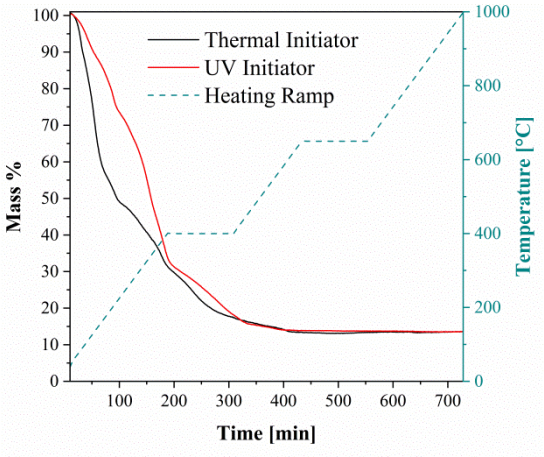

Figure 8.6: Thermograms for $SrTiO_3$ calcination by methacrylic acid chelating route

In a typical MAA chelating synthesis of $SrTiO_3$, 9.5 mL methacrylic acid ($C_4H_6O_2$, 9.72 g, 113 mmol) and 1.5 mL titanium (IV) isopropoxide (TTIP, $C_{12}H_{28}O_4Ti$, 1.47 g, 5.0 mmol) was respectively added into 7.0 mL ethanol (C_2H_6O, EtOH) under continuous stirring. A second mixture was prepared by dissolving 1.06 g strontium nitrate ($Sr(NO_3)_2$, 5.0 mmol) to 3.3 mL ammonia solution (NH_3, 25 % w/w). After 30 min stirring under air atmosphere, ammonia based solution was added dropwise to the first solution and the resulting mixture was further stirred for 45 min. Finally, either benzoyl peroxide ($C_{14}H_{10}O_4$, 0.04 g) or 1-

hydroxycyclohexyl phenyl ketone ($C_{13}H_{16}O_2$, 0.05 g) was added to the mixture as thermal and photo-induced initiator respectively. Thermal polymerization was undergone by heating the mixture to 90 °C under continuous stirring for 1 h. For UV-initiated polymerization, the solution was poured onto a petri dish which was then irradiated with a high-pressure mercury vapor lamp (Philips HPK-125W, spectra of the UV-source is given on Fig. 6.4) and kept at 50 °C simultaneously for solvent evaporation for 1 h. After drying overnight at ~ 60 °C, the polymers were grinded and obtained powders were calcined under air employing a 2 °C min^{-1} heating ramp with 2 h hold times at intermediate temperature 400 °C and final temperature 650 °C respectively. The choice of 650 °C as final temperature was due to thermogravimetric analysis of the polymers, which showed no further mass loss above this temperature (Fig. 8.6). Fig. 8.7 summarizes the synthesis scheme for methacrylic acid chelating synthesis route.

$La_{0.1}Sr_{0.9}TiO_{3+\delta}$ was prepared by modifying the stoichiometric amount of strontium nitrate precursor (0.95 g, 4.5 mmol) and dissolving 0.22 g lanthanum nitrate hexahydrate ($La(NO_3)_3 \cdot 6H_2O$, 0.5 mmol) in an additional step, right after the two initial solutions were added together.

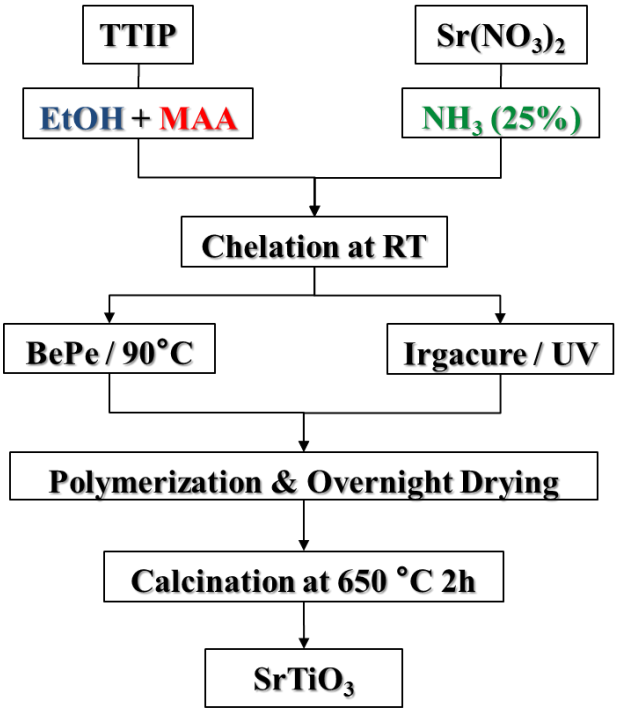

Figure 8.7: Synthesis scheme of $SrTiO_3$ by methacrylic acid (MAA) chelating route.

In this MAA chelating approach, methacrylic acid to $SrTiO_3$ product ratio, **MAA** : **STO** was set at **11.3** : **1**, whereas in a typical Pechini synthesis the organics (glycerol, citric acid) to

$SrTiO_3$ product ratio, **Gly+CA** : **STO** was employed as **17** : **1**. Moreover, considering the compositions of the respective monomer molecules, it is apparent that polyol and polycarboxylic acids associated with the Pechini approach have substantially higher amounts of oxygen in their structures which contribute to the formation of carbonates. Indeed, the X-ray diffractograms of the as-prepared $SrTiO_3$ and $La_{0.1}Sr_{0.9}TiO_{3+\delta}$ aggregates prepared with MAA chelating route show substantially high crystallinity and phase-purity without any carbonate phases (Fig. 8.7a). Crystallite sizes were calculated from [110] reflection employing Scherrer equation (3.4) and were summarized on Table 8.2. Grain sizes were between 37 – 51 nm with lowest crystallite size assigned to $SrTiO_3$ prepared with UV-polymerization.

Table 8.2: Crystallite sizes (**Φ**) retrieved from XRD, specific surface area ($\mathbf{S_{BET}}$) determined by N_2 physisorption, average atomic composition of elements determined by EDX (at. % values normalized by total nominal cation amount in $SrTiO_3$ (STO) and $La_{0.1}Sr_{0.9}TiO_{3+\delta}$ (LSTO) molecular formulas) for investigated samples prepared by MAA-chelating route.

Sample	Φ [nm]	S_{BET} [$m^2\ g^{-1}$]	La	Sr	Ti
UV/STO	37	16	-	0.82	1.00
Thermal/STO	51	13	-	0.88	1.00
Thermal/LSTO	43	19	0.11	0.93	1.00

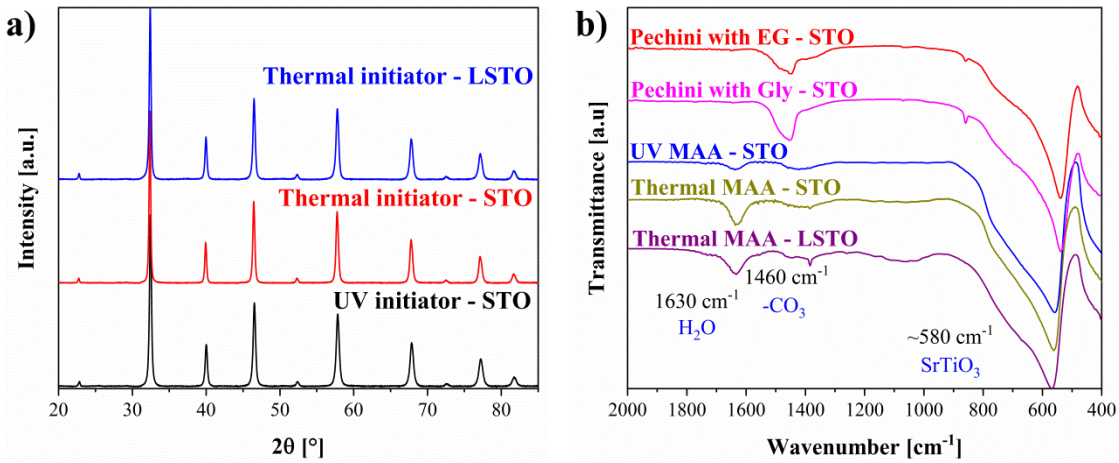

Figure 8.7: (a) X-ray diffractograms of $SrTiO_3$ and $La_{0.1}Sr_{0.9}TiO_{3+\delta}$ aggregates prepared by MAA chelating. (b) Infrared spectra of perovskites prepared by MAA route in comparison standard polymer complex synthesis with ethylene glycol (EG) and glycerol (Gly).

The infrared spectra of the perovskites prepared by this route also indicate superior purity in comparison to $SrTiO_3$ prepared by the standard polymer complex (Pechini) synthesis (Fig. 8.7b). Elemental ratios of the cations in the prepared samples determined by EDX spectroscopy were in good agreement with the nominal values (Table 8.2), whereas SEM images displayed uniformly bulk aggregates of several micrometers with only textural porosity for all investigated samples independent of the polymerization route and composition (Fig. 8.8). In accordance to the textural features observed by SEM, specific surface areas were determined by N_2 physisorption analysis to be between 13 – 19 $m^2 g^{-1}$ (Table 8.2).

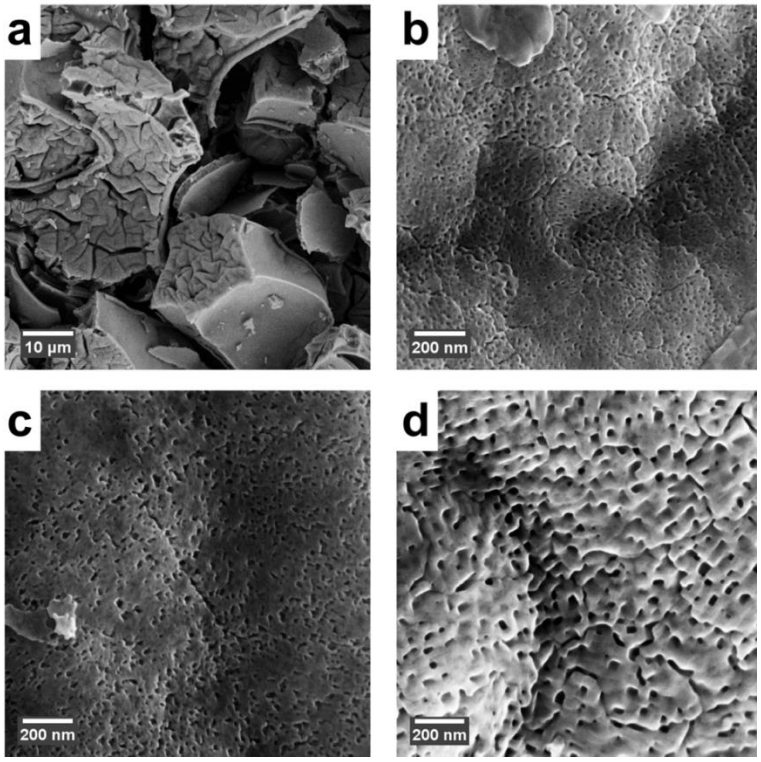

Figure 8.8: SEM images of investigated samples prepared by MAA-chelating route (a-b) Thermal/STO (c) Thermal/LSTO (d) UV/STO

The parameters in MAA chelating synthesis of $SrTiO_3$ were optimized by varying the precursor amounts and resulting perovskite oxides were assessed by X-ray diffractometry (Fig. 8.9). The phase purity of the materials was largely dependent on the initial NH_3 concentration in the mixture, which likely indicates the pH dependence of the chelation process. For the typical synthesis with **MAA** : **STO** molar ratio of **11.3** : **1**, NH_3 addition between 3.3 – 4.4 mL led to phase pure perovskites, whereas outside of this range impurity

phases started to grow (Fig. 7.5a). Pure-phase perovskite could be successfully prepared, when the **MAA** : **STO** molar ratio was decreased to **5.8** : **1** by setting NH_3 and ethanol amounts at 2.2 and 3.8 mL respectively (Fig. 8.9c). Upon further lowering **MAA** : **STO** molar ratio to **3.5** : **1** pure phase $SrTiO_3$ could not be prepared (Fig. 8.9d).

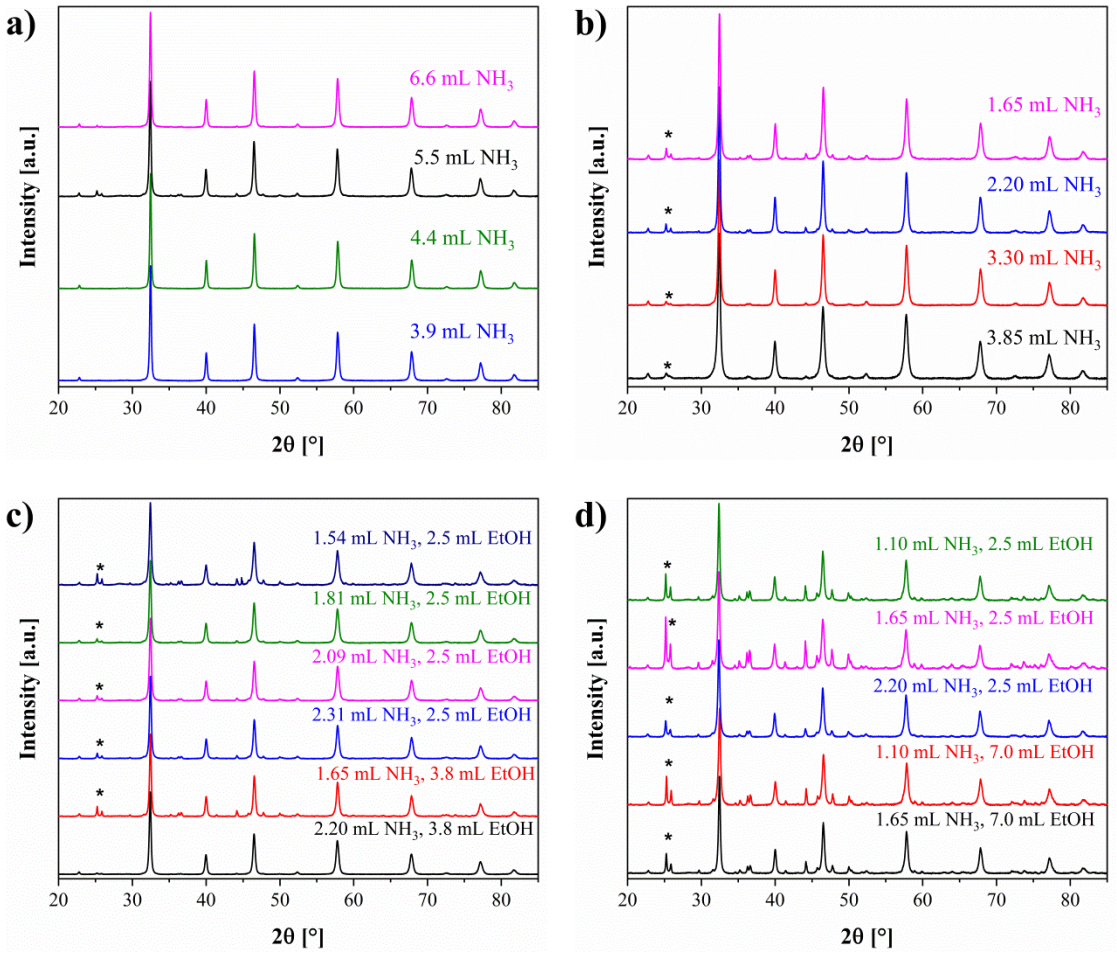

Figure 8.9: Influence of precursor amounts on phase-purity of $SrTiO_3$ samples prepared with (a) 9.5 mL MAA, 7.0 mL ethanol (EtOH) (b) 4.5 mL MAA, 7.0 mL EtOH (c) 4.5 mL MAA (d) 3.0 mL MAA. Asterisks indicate presence of impurity phase.

8.3 List of Chemicals with Safety Information

Table 8.3: Overview of used chemicals in this work with their pertaining safety information according to GHS.

Substance	GHS code	H statements	P statements
Acetic acid, glacial	02, 05	226, 303, 312, 314, 317, 331, 402	261, 280, 305+351+338, 310
Alkyltrimethlyammonium bromide (C_{18}TAB)	05	314	280, 305+351+338, 310
Ammonia (25% w/w)	05, 07, 09	314, 318, 335, 400	260, 303+361+353, 305+351+338, 310, 405, 501
Benzoyl peroxide (wet with 25% water)	02, 07, 09	242, 317, 319, 410	210, 220, 234, 280, 305, 351, 338+370, 378
Citric acid, anhydrous	07	319	264, 280, 305+351+338, 337+313
Ethanol	02, 07	225, 319	210, 240, 305+351+338, 403+233
Glycerol	not listed	not listed	not listed
Hydrochloric acid	05, 07	290, 314, 335	260, 280, 303+361+353, 304+340+310, 305+351+338
Iron (III) nitrate nonahydrate	07	315, 319	302+352, 305+351+338
1-Hydroxycyclohexyl phenyl ketone	07	315, 319	264, 280, 302+352, 305+351+338, 321, 332+313, 337+313,362

Lanthanum (III) nitrate hexahydrate	03, 07	272, 315, 319, 335	220, 261, 305+351+338
Methacrylic acid (stabilized with hydroquinone momomethyl ether)	05, 06	302+332, 311, 314, 335	280, 301+330+331, 302+352, 305+351+338, 308+310
Potassium tetrachloroplatinate (II)	05, 06, 08	301, 315, 317, 318, 334	261, 280, 301+310, 305+351+338, 342+311
Sodium borohydride	02, 05, 06, 08	360FD, 260, 301, 314	201, 280, 301+330+331, 305+351+338, 308+310, 402+404
Sodium hydroxide	05	290, 314	260, 280, 303+361+353, 304+340+310, 305+351+338
Strontium acetate hemihydrate	not listed	not listed	not listed
Strontium carbonate	not listed	not listed	not listed
Strontium chloride hexahydrate	05	318	280, 305+351+338
Strontium nitrate	03, 05, 07	272, 302, 318	210, 220, 221, 280, 305+351+338, 310, 370+378
Titanium (IV) isopropoxide	02, 07	226, 319, 336	210, 305+351+338, 370+378
Tetraethoxy orthosilicate (TEOS)	02, 07	226, 319, 322, 335	210, 261, 280, 303+361+353, 304+340+312, 370+378

No CMR substances were used in this work.

List of hazard pictograms ascribed to the GHS codes

8.4 Publications and Presentations

8.4.1 Publications

Kayaalp, B.•; Lee, S. •; Klauke, K.; Seo, J.; Nodari, L.; Kornowski, A.; Jung, W.; Mascotto, S.: Template-free mesoporous $La_{0.3}Sr_{0.7}Ti_{1-x}Fe_xO_{3\pm\delta}$ for CH_4 and CO oxidation catalysis.
Appl. Catal., B. (2019), DOI: 10.1016/j.apcatb.2018.12.077.
• These authors equally contributed to the realization of this work

Kayaalp, B.; Lee, Y.J.; Kornowski, A.; Gross, S.; D'Arienzo, M.; Mascotto, S.: Cooperative assembly synthesis of mesoporous $SrTiO_3$ with enhanced photocatalytic properties.
RSC Adv., (2016) DOI: 10.1039/C6RA13800D

Kayaalp B.; Klauke K.; Biesuz M.; Ionnaci, A.; Sglavo V. M.; D'Arienzo M., Lee, S.; Jung, W.; Mascotto, S. Triggering the reactivity of La-doped $SrTiO_3$ by flash sintering.
(*in preparation*)

Klauke K.; Kayaalp, B; Biesuz M.; Ionnaci, A.; Sglavo V. M.; D'Arienzo M., Lee, S.; Jung, W.; Mascotto, S. Effect of the Electric Field on the Reactivity of $SrTiO_3$ Nanoparticles.
(*in preparation*)

Kayaalp, B.; Lee, S.; Nodari, L.; Jung, W.; Mascotto. S.: Facile preparation of highly porous $(La,Sr)(Ti,Fe)O_{3-\delta}$ as active support for catalytic oxidation of CO and CH_4.
(*in preparation*)

Scholz, J.; Kayaalp, B.; Klauke, K.; Mascotto, S.: Radical polymerization as tool to prepare nanostructured multimetal oxides with improved textural properties.
(*in preparation*)

8.4.2 Oral Presentations

Kayaalp, B.; Lee, S.; Jung, W.; Mascotto, S. Catalytic Performance of mesoporous $La_{0.3}Sr_{0.7}Ti_{1-x}Fe_xO_{3\pm\delta}$ towards CO and CH_4 Oxidation.
ATC 2018, 27. Industrial Inorganic Chemistry Conference, Frankfurt, Germany

Kayaalp, B.; Lee, S.; Jung, W., Mascotto, S. Remarkable chemical reactivity of porous $La_xSr_{1-x}Fe_yTi_{1-y}O_3$ as potential mixed conducting anode for SOFCs.
SSI 2017, 21. International Conference on Solid State Ionics, Padua, Italy

8.4.3 Poster Presentations

Kayaalp, B.; Lee, Y.J.; Kornowski, A.; Gross, S.; D'Arienzo, M.; Mascotto, S.: Cooperative assembly synthesis of mesoporous $SrTiO_3$ with enhanced photocatalytic properties.
Energie 2016, 1. Jahrestagung Chemie und Energie, Jena, Germany

Kayaalp, B.; Lee, Y.J.; Mascotto, S.: Facile synthesis of nanoporous $SrTiO_3$ with enhanced photocatalytic activity by in situ hard-templating
DZT 2016, 28. Deutsche Zeolith Tagung, Gießen, Germany

Curriculum Vitae

– omitted due to data protection –

List of abbreviations

STO	$SrTiO_3$
LSTO	$La_ySr_{1-y}TiO_{3\pm\delta}$
STF	$SrTi_{1-x}Fe_xO_{3-\delta}$
LSTF	$La_ySr_{1-y}Ti_{1-x}Fe_xO_{3\pm\delta}$
HOMO	highest occupied molecular orbital
LUMO	lowest unoccupied molecular orbital
VB	valence band
CB	conduction band
EISA	evaporation-induced self-assembly
MIEC	mixed ionic electronic conductor
SOFC	solid oxide fuel cell
IT-SOFC	intermediate temperature solid oxide fuel cell
TPB	triple phase boundary
NHE	normal hydrogen electrode
MvK	Mars and von Krevelen
VOC	volatile organic compound
SDA	structure directing agents
CMC	critical micelle concentration
BET	Brauner-Emmet-Teller
DFT	density functional theory
NLDFT	non-local density functional theory
XRD	X-ray diffraction
WAXS	wide-angle X-ray scattering
SAXS	small-angle X-ray scattering
FWHM	full width at half maximum
SEM	scanning electron microscopy
TEM	transmission electron microscopy
HR-TEM	high resolution transmission electron microscopy

STEM	scanning transmission electron microscopy
CCD	charge-coupled device
HAADF	high-angle annular dark field
EDX	energy dispersive X-ray spectroscopy
XPS	X-ray photoelectron spectroscopy
UV-Vis	ultraviolet and visible
DR-UV	diffuse reflectance ultraviolet and visible
EIS	electrochemical impedance spectroscopy
NMR	nuclear magnetic resonance
CP-MAS	cross polarization – magic angle spinning
ESR	electron spin resonance
TGA	thermogravimetric analysis
TPD – O_2	temperature programmed desorption of oxygen
TPR – H_2	temperature programmed reduction by hydrogen
SRR	suprafacial reaction rate
IRR	intrafacial reaction rate
TRR	total reaction rate
TEOS	tetraethoxy orthosilicate
MB	methylene blue
TOF	turnover frequency
FS	flash sintering
CS	conventional sintering
3DOM	three-dimensionally ordered
MAA	Methacrylic acid
MB	Methylene blue

List of symbols

V_P	pore volume
S_{BET}	specific surface area
λ	wavelength
h	Planck's constant
E_{BG}	Band gap energy
ν	frequency
E_a^{EIS}	activation energy for charge migration obtained by electrochemical impedance spectroscopy
$E_a^{CO\ ox.}$	activation energy for CO oxidation
$E_a^{CH_4\ ox.}$	activation energy for CH_4 oxidation
m	reaction order with respect to oxidizing fuel
n	reaction order with respect to oxygen
Φ	crystallite size
P_{CH_4}	methane partial pressure
P_{O_2}	oxygen partial pressure
T	temperature
ε	dielectric permittivity